Master's thesis

NTNU
Norwegian University of Science and Technology
Faculty of Information Technology and Electrical Engineering
Department of Electric Power Engineering

Kjersti Lunde Runestad

Adaptive Protection of an Inverter-Dominated Microgrid and Testing at the Smart Grid Laboratory at NTNU

Master's thesis in Energy and Environmental Engineering
Supervisor: Hans Kristian Høidalen
June 2019

NTNU
Norwegian University of Science and Technology

Kjersti Lunde Runestad

Adaptive Protection of an Inverter-Dominated Microgrid and Testing at the Smart Grid Laboratory at NTNU

Master's thesis in Energy and Environmental Engineering
Supervisor: Hans Kristian Høidalen
June 2019

Norwegian University of Science and Technology
Faculty of Information Technology and Electrical Engineering
Department of Electric Power Engineering

Problem Description

This master thesis is a part of the ProSmart project; Power system protection in a Smart Grid perspective, which is a cooperation between the NTNU departments Electrical Power Engineering and Telecommunications, and Michigan Technological University (MTU) in the USA. The objective of the project is to enable new protection strategies that improve the power system performance and the integration of renewables by utilizing smart grid technologies.

The connection of microgrids in the existing distribution network causes the magnitude of fault current to change dynamically depending on the modes of operation (grid connected or islanded mode), type of distributed generator, the status of distributed generators and the number of distributed generators [12]. The complexity of future power systems complicates the protection strategies and the handling of faults due to the integration of distributed energy resources.

In reaction to these protection strategy challenges, this master thesis will focus on implementing an inverter-dominated AC microgrid with several distribution generation units and an adaptive protection scheme at the Smart Grid Laboratory at NTNU. The main objectives are to investigate the microgrid behavior during islanding transition and the influence of converter control strategies and parameters on the protection strategy.

Preface

This master's thesis finalizes the degree Master of Science in Energy and Environmental Engineering and completes my studies at the Norwegian University of Science and Technology (NTNU). The master's thesis is a part of the ProSmart project; Power system protection in a Smart Grid perspective. The specialization project called "A Review of Challenges and Methods for Microgrid Protection and Control of Power Converters in Microgrids" written by the same author in the fall of 2018 functions as a pre-project for this master's thesis.

The completion of this master's thesis would not have been possible without the help of several contributors. Firstly, I would like to thank my supervisor, Professor Hans Kristian Høidalen, for proposing this interesting and relevant assignment. Moreover, his guidance throughout the process has been indispensable. Additionally, I would like to thank my co-supervisor, Maciej Grebla, for always helping me, especially with the laboratory preparations and the implementation of the protection relays. His creative ideas were crucial in realizing the laboratory setup.

Furthermore, I would like to thank Research Scientists at Sintef, Salvatore D'Arco and Kjell Ljøkelsøy, for helping me implement the laboratory converters. Ljøkelsøy devoted a lot of his time to help me understand the built-in control of the laboratory converters. I also thank Vladimir Klubicka and the other people at the Service Lab at NTNU for providing the necessary equipment at all times. Finally, I express my deepest gratitude to Researcher Thomas S. Haugan. His help accelerated the implementation process of the complicated laboratory setup, and his genuine desire to help was extremely motivating.

Trondheim, 2019

Kjersti Lunde Runestad

Kjersti Lunde Runestad

Abstract

The rapid expansion of distributed electrical power generation is setting the stage for modern distribution systems to operate as microgrids. Microgrids integrate decentralized generation sources in the distribution system, which can supply local loads during grid disturbances. Subsequently, the integration of renewable energy sources is made possible, which complies with the future low-carbon society.

However, the aforementioned advantages are threatened if microgrids are not properly protected or controlled in the event of faults [27]. Traditional protection systems and regulation strategies designed for passive distribution networks are not necessarily valid in the future power with microgrids [22]. Additionally, the control strategies of power electronic converters affect the behavior of inverter-interfaced distributed generation units during short-circuits, thus complicating the microgrid protection. Overall, this supports the need for adaptive microgrid protection. Protection and control strategies for AC microgrids are therefore major subjects in this master's thesis.

An inverter-dominated microgrid is implemented at the Smart Grid Laboratory at NTNU where its protection system consists of digital protective relays. The microgrid system consists of three distributed generation units with power electronic converters and one load. Moreover, two contactors are equipped with communication-aided (IEC61850 GOOSE messaging) digital relays with adaptive protection functions based on the present operating state of the microgrid.

Local voltage measurements are conducted to examine the islanding transition during varying power contributions from the utility grid. The voltage drops in the event of islanding; however, this is also the case when the load increases and during short-circuits. Consequently, it is difficult to differentiate between these events solely based on local voltage measurements. As a result, the islanding detection method based on a direct transfer signal is implemented, which detects the islanding event in a reliable way.

Furthermore, the adaptive function of the protective relays is tested during a short-circuit. The over-current relay is configured with a pick-up setting based on the short-circuit contribution from the utility grid, and is therefore not operating for short-circuits during islanded microgrids. However, if the protection relay is adapted to a protection function that is suitable in islanded inverter-dominated microgrids, the protection system detects the short-circuit.

The correlation between the protection settings and the converter control of inverter-interfaced distributed generation units is investigated. The implemented control strategy and the parameters within each control strategy are of great importance because they affect the fault behavior of the converters. As a result, it is essential to examine the converter control while developing the protection schemes of inverter-dominated microgrids. Standardization of the converter control applied in microgrids may help to predict the converter behavior during short-circuits and subsequently help to decide which protection settings to utilize.

Sammendrag

Den raske utvidelsen av distribuert elektrisk kraftproduksjon medfører at forsyningsnettet må kunne operere som mikronett. Mikronett integrerer desentraliserte energikilder i distribusjonssystemet, og som kan levere kraft lokalt ved forstyrrelser på hovednettet. Det muliggjør integreringen av fornybare energikilder i et større distribusjonssystem, noe som er i tråd med energiforsyning i et lav-karbon samfunn.

Mulighetene til å etablere slike løsninger er imidlertid vanskeliggjort hvis mikronett ikke er skikkelig beskyttet og kontrollert i tilfelle feil [27]. Tradisjonelle beskyttelsessystemer og reguleringstrategier er designet for passive distribusjonsnett og er ikke nødvendigvis anvendbare i kraftdistribusjon som inkluderer mikronett [22]. I tillegg vil styringen og kontrollstrategien for elektriske omformere påvirke oppførselen ved kortslutninger, og dermed kompliserere beskyttelsen av mikronettet. Samlet sett støtter dette behovet for adaptive løsninger som tilpasser seg mikronettet. Vern og kontrollstrategier for vekselstrøms mikronett er derfor hovedtema i denne masteroppgaven.

Et omformer-dominert mikronett er implementert på Smart Grid laboratoriet ved NTNU hvor beskyttelsessystemet består av digitale relévern. Mikronettsystemet består av tre distribuerte genereringsenheter med omformere og én last. To kontaktorer er utstyrt med digitale releer med adaptive vernsettinger og elektronisk kommunikasjon (IEC61850 GOOSE) tilpasset driftstilstanden av mikronettet.

Spenningsmålinger utføres lokalt for å undersøke overgangen til øy-modus ved varierende kraftforsyning fra nettet. Spenningen synker ved øy-modus; dette er imidlertid også tilfelle når lasten øker og ved kortslutning. Følgelig er det vanskelig å differensiere mellom disse situasjonene utelukkende basert på spenningsmålinger. Som en konsekvens av dette implementeres en metode for pålitelig deteksjon av veksling mellom øy-modus og hovednett basert på et direkte overføringssignal.

I tillegg testes den adaptive funksjonen av relévern ved en kortslutning. Overstrømssvern som er konfigurert for nett-tilkobling tilstand fungerer ikke ved kortslutninger hvis mikronettet er i øymodus. Men hvis relévernet endrer beskyttelsesfunksjon som er egnet for omformer-basert mikronett, vil kortslutningen detekteres.

Sammenhengene mellom omformer styring og de ulike vernsettingene undersøkes. Den valgte kontrollstrategien og parametrene innenfor hver kontrollstrategi er av stor betydning da dette påvirker virkemåten til omformerne. Følgelig er det viktig å undersøke effekten av omformerkontroll når vernløsningene skal utvikles. Standardisering av omformerkontrol anvendt i mikronett kan bidra til å forutsi hvordan omformeren oppfører seg ved kortslutninger og dermed hjelpe i å avgjøre valg av reléverninnstillinger.

Contents

List of Tables

List of Figures

Abbreviations

AC Alternating current

CB Circuit breaker

CT Current transformer

DC Direct current

DER Distributed energy resource

DG Distributed generation

DSO Distribution system operator

DTT Direct transfer trip

ESS Energy storage system

FRT Fault-ride-through

GOOSE Generic object oriented substation event

HMI Human-machine interface

ICT Information and communications technology

IED Intelligent electronic device

IGBT Insulated-gate bipolar transistor

IIDG Inverter-interfaced DG

LCL Inductor-capacitor-inductor

LPF Low-pass filter

LV Low voltage

MCPU Microgrid central protection unit

PCC Point of common coupling

PI Proportional-integral

PLL Phase locked loop

PV Photovoltaics

PWM Pulse width modulation

RES Renewable energy source

RMS Root mean square

ROCOF Rate of change of frequency

STS Static transfer switch

TSO Transmission system operator

VCO Voltage source oscillator

VSC Voltage source converter

VT Voltage transformer

Nomenclature

A Ampere

F Farad

H Henry

Hz Hertz

ms millisecond

pu Per-unit

s second

V Voltage

VA Volt-ampere

W Watt

Chapter 1

Introduction

1.1 Background and motivation

Nowadays, there is a growing demand for electrical energy due to rapid population growth and an increase in personal income [18]. The utilization of conventional fossil fuels are strongly linked to causing climate change, and the scarcity of existing fossil fuels is also a major concern. As a result, it is paramount to replace the existing non-renewable energy sources with cleaner alternatives. According to the European Commission, a target for 2030 is at least 27 % renewable energy consumption and greenhouse gas reduction of 40% [34]. Integrating renewable energy sources in the electricity sector is, therefore, necessary to meet future energy needs while providing a sustainable energy production and reducing the dependence on fossil fuels. Moreover, the traditional centralized power system suffers from high transmission losses, reduced reliability, and high expansion costs [12]. As a result, the expansion of small-scale distributed energy sources into modern electricity grids is increasing in order to address the aforementioned issues [11]. Figure 1.1 shows the paradigm shift towards the 21st century; decentralized power systems with renewable energy.

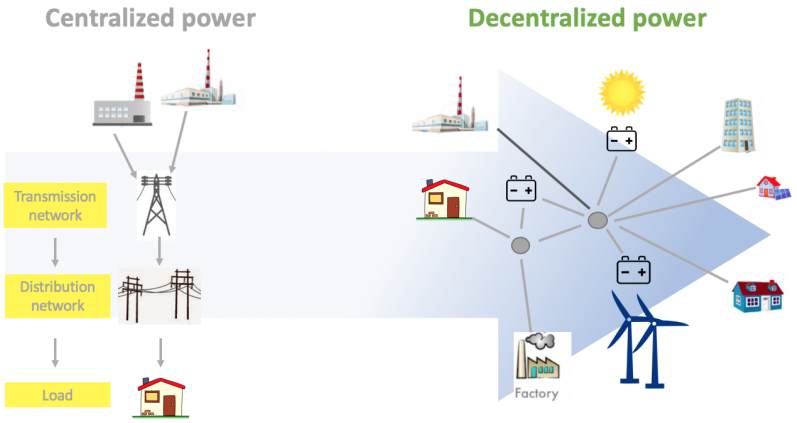

Figure 1.1: Paradigm shift from centralized towards decentralized power systems

Despite the reduced dependency on fossil fuels and limited grid investments, the stochastic and intermittent behavior of the Renewable energy source (RES) poses challenges regarding their integration into the grid. Moreover, small-scale generation units distributed at different locations in the power system brings new challenges related to bidirectional power flows and reduction in short-circuit current levels. The need for power electronic interfaces is significant with the use of RES, so the short-circuit

current contribution from such units is limited in order to protect the electronics. Additionally, the development towards intermittent renewable generation at the distribution level leads to the integration of Energy storage system (ESS). Subsequently, this introduces bidirectional power flows because customers both consume and produce energy, referred to as *prosumers*. Hence, small versions of a power system which contain Distributed generation (DG) units and ESSs, referred to as microgrids in literature, are proposed in order to face the challenges related to the integration of RES. In other words, the concept of microgrids was introduced to facilitate the integration of small-scale generation units into distribution networks. Microgrids can operate connected to the utility grid, but also as isolated grids referred to as "islanded mode". Due to the paradigm shift towards decentralized power systems, a new Smart Grid architecture is necessary in order to take advantage of the properties of Distributed energy resource (DER)s and thus realize their full potential. The possibility of momentary islanded operation of microgrids should be basic blocks of the architecture in order to secure the power supply [36].

Despite the increased integration of RESs and improved performance of electrical power systems, microgrids raise several concerns like the need for modified protection and control strategies [54]. Traditional protection schemes and control strategies are not necessarily valid in the future power grid because the strategies are based on large synchronous generators [24]. In islanded microgrids, the fault current level during short-circuits is reduced due to the disconnected utility grid [12]. Moreover, the voltage, frequency, and power flow control are assigned to the generation units within the isolated microgrid. However, the utility grid maintains the voltage and frequency during grid-connected mode. Consequently, new control and protection schemes have to be developed to meet these challenges and exploit the advantages related to DG units integrated with power electronic converters.

Adaptive microgrid protection and control strategies of power converters in microgrids are addressed in this thesis through laboratory experiments at the Smart Grid laboratory at NTNU. Necessary background information about microgrids as a power system and the microgrid elements are explained first in chapter 2 before microgrid protection and control schemes are investigated.

1.2 Relation to Specialization Project

This thesis is based on the specialization project called "A Review of Challenges and Methods for Microgrid Protection and Control of Power Converters in Microgrids" written by the same author in the fall of 2018 [51]. Some sections in this thesis contain reused or modified material from the specialization project. The list below itemizes the sections or chapters that contain reused material.

- Some parts of the introduction in section 1.1 are obtained from the specialization project.
- Chapter 2 is based on the specialization project, especially sections 2.1 and 2.4 about the general microgrid system and microgrid components.
- Chapter 3 is considerably based on the specialization project, especially section 3.3 about protection issues in microgrids, and the explanations of the protection functions in sections 3.4 and 3.5. Moreover, section 3.6 about adaptive microgrid protection is based on the specialization project.
- Chapter 4 is a continuation of the chapter about power flow control in the specialization project, thus much material from the that chapter is reused and modified in this thesis.

1.3 Objectives

The general objectives of this master thesis is to:

- Investigate an adaptive protection scheme with digital relays applicable in microgrids.
- Investigate the control strategies of power converters in AC microgrids.

The general objective is achieved by:

- Implementing an inverter-dominated microgrid system with adaptive digital protection relays at the Smart Grid Laboratory.
- Conducting experiments to investigate the transition between grid-connected and islanded operation.
- Conducting experiments to investigate the coordination between converter settings and the internal converter protection.
- Investigate the influence of inverter-interfaced distributed generation and its control settings on microgrid protection.

1.4 Methodology and scope of work

An inverter-dominated microgrid will be investigated in this thesis to achieve the aforementioned objectives. The laboratory setup is based on an adaptive protection scheme with two digital ABB relays, three laboratory power converts, five Alternating current (AC) bus-bars, two Direct current (DC) bus-bars provided with DC voltage from Egston, line impedance, and a load. The protective relays are implemented with a communication scheme and adaptive protective function blocks. Local control of the converters integrating three DG units is utilized, and the control systems include current, power, and voltage control loops. The control systems of the laboratory converters are changed to study their fault behavior during different conditions.

The scope of this thesis is to investigate adaptive microgrid protection and how power converters behave during short-circuits. The hypotheses are that the fault current level is reduced in islanded mode and that the control strategies and control parameters affect the behavior of Inverter-interfaced DG (IIDG) units during short-circuits. The main research questions are listed below and are examined at the laboratory to investigate the aforementioned assumptions.

1. What happens during the islanding transition of the microgrid?
2. What happens during a three-phase short-circuit?
3. What is the correlation between converter settings and the internal converter protection?
4. How does the implemented control scheme affect the IIDG behavior during a short-circuit?
5. How does the control settings within the control scheme affect the IIDG behavior during a short-circuit?

1.5 Limitations

The main purpose of this thesis is to implement, test, and verify an inverted-dominated microgrid at the Smart Grid laboratory at NTNU. The overall laboratory setup has a high degree of complexity with many components and potential test cases. The practical execution of this complex setup with the available time and resources prompted the need to reduce the number of test variables.

The adaptive protection scheme is limited to two protective functions, so only the over-current and the under-voltage protection functions are investigated. Moreover, only one setting group is applied to each protection function. The ABB digital relays have never been utilized in the Smart Grid laboratory before, so the main focus is to get the relays working. The functionality of the ABB relays is established, namely by performing this simplified protection testing, which might initialize more advanced testing and research of this technology in the future.

The advanced control system of the laboratory converters facilitates numerous possibilities. However, the control strategies tested in the laboratory are limited to active and reactive power control, direct active and reactive current control, and AC voltage regulation due to time constraints and the high demand on the laboratory converter units. Consequently, the DC-link voltage regulator is omitted, and the control of the DC-side of the converter is considered out of scope. Moreover, harmonic oscillations or losses related to the converters are beyond the scope of this thesis.

Furthermore, the effect of external factors, e.g., duration and type of short-circuit, is omitted to limit the number of test cases. Additionally, only the voltage is investigated during the islanding transition. Several islanding detection methods are proposed in the literature; however, only the local detection method based on voltage measurements are examined.

1.6 Thesis outline

The outline of the thesis is presented in this section.

- Chapter 2 presents background information about microgrids as a power system. Additionally, the system description of the microgrid configuration utilized in this thesis is provided.
- Chapter 3 presents the protection challenges introduced by integrating DG units in the existing networks. Moreover, several protection functions are described, and the proposed microgrid protection scheme is presented.
- Chapter 4 explains the power flow control in microgrids. The classification of the power converters and strategies of converter control in AC microgrids are emphasized.
- Chapter 5 describes the laboratory setup and the approach to perform the tests in the Smart Grid Laboratory at NTNU.
- Chapter 6 presents the results from the laboratory tests.
- Chapter 7 summarizes the final remarks in the thesis and suggests further work.

Chapter 2

Microgrids as a power system and System Description

This chapter presents background information about microgrids as a power system with its associated elements. Moreover, a specific microgrid system is utilized throughout this thesis to examine adaptive microgrid protection and control strategies of power converters at the laboratory. Consequently, the system description of this microgrid system is additionally included in this chapter.

2.1 Microgrid systems

Microgrids can be defined as small-scale distribution systems containing distributed energy resources, power electronic converters, and local loads that can operate connected to the main power network or islanded (Cigré WG C6.22). Figure 2.1 illustrates the different components constructing a microgrid, and the microgrid unit is connected and disconnected from the utility grid through a Static transfer switch (STS) at the Point of common coupling (PCC). Consequently, an important linkage between DER units and the utility grid is formed through the microgrid unit during grid-connected mode at PCC [16].

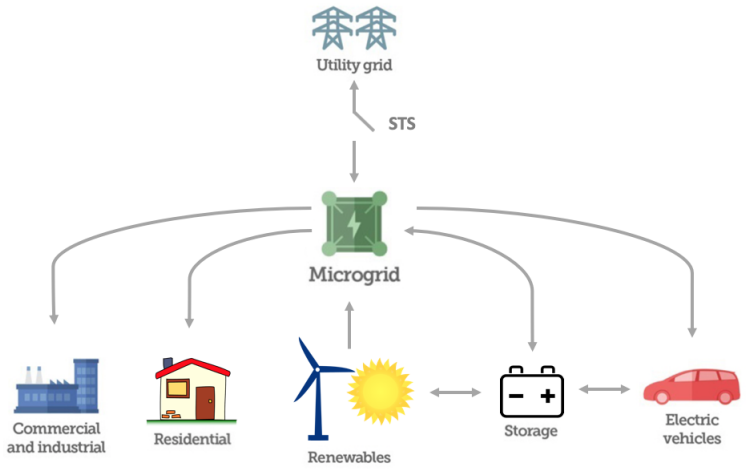

Figure 2.1: Generic diagram of microgrid

The controlled and coordinated operation of DER units makes the microgrid operate as a single controllable unit at the PCC [54]. In other words, the microgrid unit is seen as one single generator or load from the perspective of the main electricity grid. The bidirectional power flow from the utility grid and the microgrid depends on the net load demand and generation supply within the microgrid. The microgrid is thereby designed to provide a reliable power supply with the help of local controllers and distributed protection units [12].

Figure 2.2 illustrates the microgrid system examined in this thesis. The microgrid elements in this system are the resistive load, distribution lines, and two DG units connected through Voltage source converter (VSC)s. The DG units are supplied from ideal DC sources, so VSC units are utilized for the DC-AC conversion. Each VSC unit is connected to an Inductor-capacitor-inductor (LCL)-filter in order to reduce harmonics. The working principle of a VSC unit is explained in section 2.4, together with the other microgrid elements. Moreover, a communication infrastructure is necessary to monitor the status of the STS, i.e., if the microgrid is grid-connected or islanded. Accordingly, digital protection relays are crucial in order to adapt their protection settings depending on the microgrid configuration.

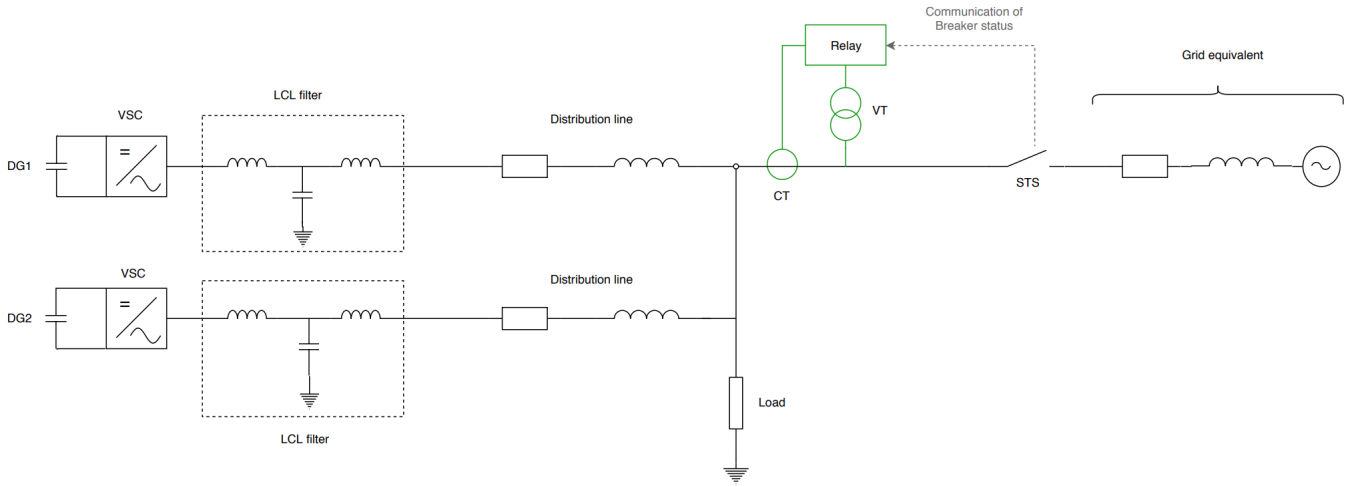

Figure 2.2: The investigated system

2.2 Benefits with microgrids

The microgrid concept is expected to play a major role in future power systems to allow the integration of DG units in the electricity network [36]. The main advantages with microgrids and associated DG units are summarized in the list below:

1. Microgrids facilitate the integration of DER units, which subsequently enables the integration of RESs. So, future microgrids are in compliance with the future low-carbon society [25].
2. By integrating DG sources into the existing power system, transmission losses will be reduced, and the need for grid reinforcements is postponed.
3. As a result of the islanding capability, local micro-sources can continue to supply local load during disturbances in the main utility grid. Hence, the power supply is not interrupted, and the overall reliability of the system increases.
4. The islanded microgrid operation can bring electricity to remote areas.

2.3 Challenges with microgrids

Technical challenges related to microgrids need to be addressed to obtain the aforementioned benefits. Reference [36] presents the key technical challenges of Low voltage (LV) microgrids, which are summarized in the list below:

1. Stability issues, especially during the transition from grid-connected to island operation.
2. Frequency deviations due to low inertia in inverter-dominated microgrids. Moreover, the power quality is affected by the volatile power production and the harmonics produced by power electronics [25].
3. Voltage and frequency control in islanded microgrids. Normally, the utility grid preservers a stable voltage and frequency; however, the local control of microgrids is required to maintain the voltage and frequency during the islanded operation. Hence, structured control systems of the power converters in microgrids are required to ensure a proper microgrid operation during both modes and in the event of faults [48].
4. Microgrid protection during island operation and normal operation. The protection issues mainly concern bi-directional power flows and reduced fault current level during islanded mode if the microgrid consists of low capacity IIDG sources.

The encountered non-technical obstacles, e.g., the need for new market structures and regulatory policies, are beyond the scope of this thesis. However, the challenges related to microgrid protection and control strategies are of particular relevance, and subsequently further examined in chapter 3 and chapter 4, respectively.

2.4 Microgrid elements

In this section, some of the main components of the microgrid system in figure 2.2 will be introduced.

2.4.1 Distributed generation

Distributed generation is defined as small-scale generation of electricity integrated at distribution system level [45]. The difference between DER and DG is that the distributed energy resources also include storage devices and controllable loads along with generator units [2]. Main generation units are separated between controllable and non-controllable resources, also referred to as dispatchable and variable [25]. According to [44], there are three types of DG sources; synchronous generator, induction generator, and inverter interfaced generator. Renewable power sources like Photovoltaics (PV) and wind turbines are integrated to the microgrid through an inverter, and evidently, the presence of power electronics in microgrids is considerable. This thesis focuses on the inverter-dominated microgrid in figure 2.2, hence the distributed generation units are inverter-interfaced, i.e., IIDGs.

2.4.2 Distribution lines

Distribution lines deliver electricity to the consumers and are dependent on the voltage level used for the power transfer. Microgrids are defined as a group of interconnected loads and generation units at the distribution level, so this thesis focuses on the low-voltage power transfer. The distribution lines in low-voltage microgrids will be typically dominated by resistive components as illustrated in table 2.1 [48]. In other words, the grid impedance is mainly resistive in LV networks because the resistive component is much higher than the inductive component of the line impedance [48].

Type of line	R [Ω/km]	X [Ω/km]	$\frac{R}{X}$ [pu]
Low-voltage line	0.642	0.083	7.7
Medium-voltage line	0.161	0.190	0.85
High-voltage line	0.06	0.191	0.31

Table 2.1: Typical line impedances values for different voltage levels rendered from [48]

2.4.3 Load

The load in the microgrid system (figure 2.2) is shared between two VSCs and represented as a linear, resistive component. Normally, microgrid loads are categorized into conventional loads or power electronics loads which are controllable [25]. In order to maintain the energy balance, flexible loads can be adjusted to match the supply [25]. The adjustment is made by control signals which enable a demand-side response. Undesired load shedding of fixed loads might be necessary during abnormal operations. However, the objective of an islanded microgrid is to serve as a power source and supply micro loads during grid disturbances as long as the micro-generation is sufficient.

2.4.4 Voltage source converter

Nowadays, the VSC is a commonly used power electronic converter for high-power-applications [58]. As a result, the extent of this section is limited by a brief description of the two-level VSC configuration.

Two-level voltage source converter

A two-level VSC is the interface between a DC and an AC system, and can be operated as a rectifier (AC to DC) or as an inverter (DC to AC). The VSC is a central component in this thesis since the DG units in the microgrid system are based on DC-voltages. Additionally, the local control of the microgrid is achieved through the control system for each VSC in the microgrid. Figure 2.3 shows the representation of a three-phase, two-level VSC during the inverter-mode of the VSC. The input voltage is a DC-voltage, V_{DC}, whereas the output voltage is the AC voltage.

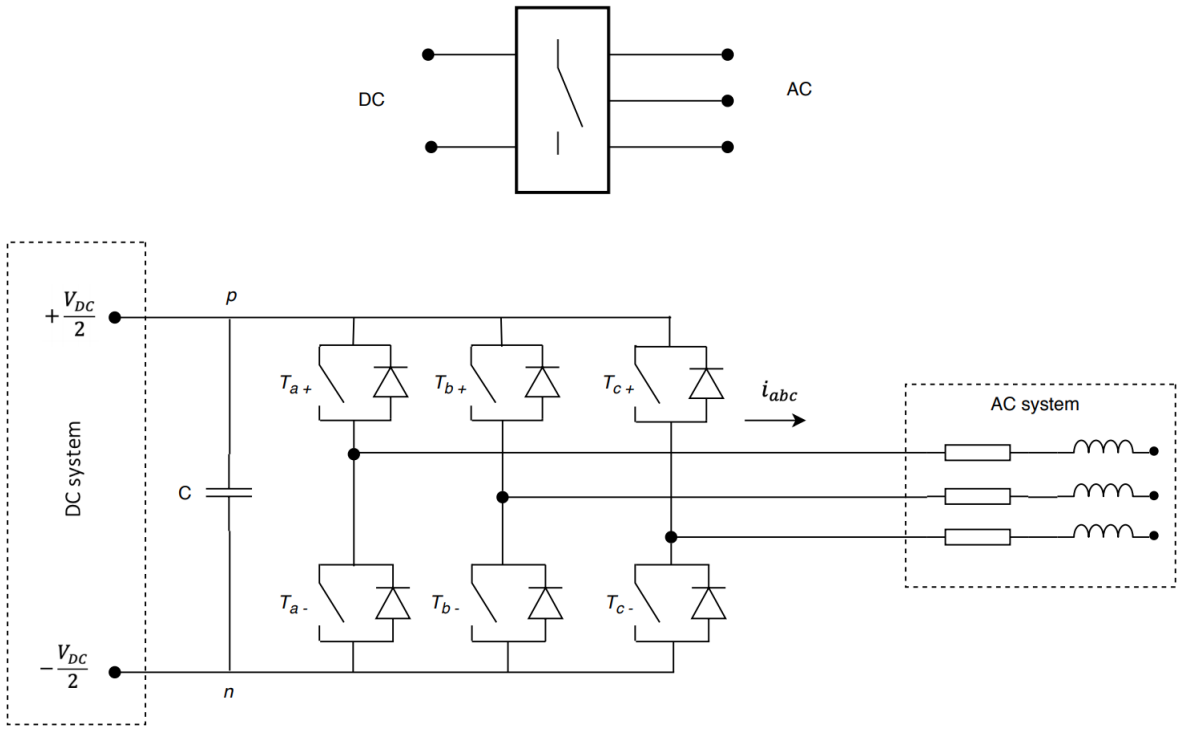

Figure 2.3: Schematic diagram and representation of a two-level VSC

By performing switching actions, the VSC creates an AC voltage, and facilitates the energy exchange between the DC- and the AC-system [25]. As illustrated in figure 2.3, the two-level VSC consists of three legs where each leg is connected in one phase. Moreover, one leg integrates two switches which are constructed by Insulated-gate bipolar transistor (IGBT)-valves [20]. A diode is placed in anti-parallel with the IGBT to conduct current in the opposite direction since IGBTs cannot conduct in the reverse direction. The converter in figure 2.3 is called a two-level VSC since the voltage level varies between two voltage levels. The output voltage is equal to $+\frac{V_{dc}}{2}$ during conduction of the upper switch, whereas the output voltage is negative and half of the DC voltage, $-\frac{V_{dc}}{2}$, when the lower switch is conducting [20], [53]. A separate control circuit controls the semiconducting switches in the VSC, and the pulse-width modulation switching technique is described in the next section 2.4.4.

Pulse-width modulation

The sinusoidal Pulse width modulation (PWM) technique controls the VSCs in the investigated microgrid system. The PWM technique provides switching signals which control the IGBT-valves in the VSC in figure 2.3. The reference voltage signal, also called the modulating signal, is compared with a high-frequency carrier which typically has a symmetrical triangle waveform [ref. MathWorks Support]. In other words, the modulating signal ($v_{control}$) is compared to a high-frequency triangular waveform (v_{tri}). When the modulating signal is greater than the carrier, the upper group of switches in each converter leg will conduct, whereas the lower group conducts when the reference voltage is lower than the carrier [20]. In reference to figure 2.3, the T_{a+} switch conducts if $v_{control} > v_{tri}$, whereas the switch is open if $v_{control} < v_{tri}$.

The output voltage signal is affected by harmonic components, switching losses, blanking time, and on-state losses [26]. However, the harmonic components and converter losses are both out of scope of this thesis, so the semiconducting switches associated to the converters are not examined during the laboratory experiments.

2.4.5 Control system

The VSCs in the microgrid consist of several control systems to obtain a proper power flow control with satisfying voltage and frequency levels [26]. Moreover, a proper control of VSCs in microgrids enable IIDG units to meet the wide-ranging demands of their integration with the existing distribution network [23]. The different levels of control and the inner control loops regulating the PWM signals to the VSC are therefore elaborated in chapter4.

2.4.6 Low-pass filter

As elaborated in section 2.4.4, the output voltage of the VSC in inverter-mode is a sinusoidal wave including high-frequency components. Consequently, low-pass filters are located at the output of the converter to reduce the high-frequency harmonics [58]. Harmonics can be filtered by a simple inductor which is referred to as an L-filter [26]. However, the combination of inductors and capacitors, i.e., LC- or LCL-filters, is another common alternative for filtering harmonics. The LCL-filter is commonly utilized for grid-connected applications. Moreover, the laboratory converters are connected to the AC grid via an LCL-filter. Consequently, the selected Low-pass filter (LPF) for this thesis is the LCL-filter in figure 2.2, and the values of the parameters are listed below.

Parameters	**Value**
Inverter-side inductor: L_1	500 [μH]
Grid-side inductor: L_2	200 [μH]
Capacitor: C	50 [μF]

Figure 2.4 illustrates the schematics of a LPF LCL-filter where C is the capacitor and L_1 is the inverter-side inductor, whereas L_2 denotes the grid-side inductor.

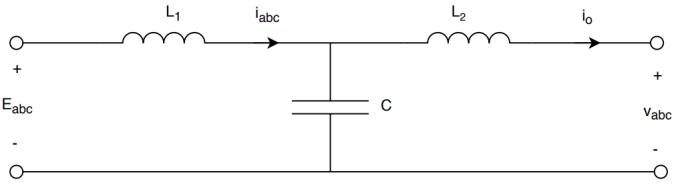

Figure 2.4: Schematics of a low-pass LCL-filter

2.4.7 Protection system

Proper protection of microgrids is crucial in order to protect people against electrical hazards and prevent damage on installations and equipment [14]. Traditional protection systems that are designed for passive distribution networks are no longer suitable for microgrids because DG units disrupt the coordination of over-current protective relays and switch-gear such as fuses and reclosers [22]. Evidently, the need for adaptive microgrid protection emerges where the relay can adapt its protection settings and functions whenever a change in the network configuration is noticed. The protection strategies for microgrids are therefore elaborated in chapter 3.

2.4.8 Communication

Microgrid protection and control schemes need to react to local changes in configuration, thus a new kind of Information and communications technology (ICT) infrastructure is required to meet the communication needs of future microgrids [36]. According to [36], the IEC 61850 is the most promising communication standard for microgrids. The IEC 61850 standard defines communication protocols for Intelligent electronic device (IED)s at electrical substations, and the Generic object oriented substation event (GOOSE) service of IEC 61850 makes the direct information exchange between IEDs possible [36]. GOOSE is a suitable communication protocol regarding protection functions since it contains either binary or analog data like network status, Circuit breaker (CB) status, adaptive protection settings, etc. The implementation of an adaptive microgrid protection scheme with GOOOSE communication is further elaborated in section 5.1.5.

Chapter 3

Microgrid Protection

Proper protection of electrical power systems is crucial to protect people against electrical hazards, prevent damage to electrical equipment, and maintain stability and reliability in power systems [14]. However, the wide deployment of microgrids at LV distribution networks causes protection challenges because conventional protection practices are based on static protective settings [7]. According to [24], most conventional protection schemes are based on short-circuit current sensing. The presence of microgrids changes the magnitude and direction of fault currents [12]. Hence, problems related to selectivity (unnecessary tripping), sensitivity (undetected faults), and speed (delayed tripping) of the protection system may arise for many operating conditions of microgrids [24]. Moreover, the protection system must now respond both to faults in the utility grid and faults within the microgrid, where the desired response depends on the fault location.

Section 3.1 briefly outlines the power system protection with its protection components. Additionally, the type of short-circuits are listed in section 3.2. The microgrid protection challenges regarding DG units and conventional protective schemes are discussed in section 3.3. Different protective relays protect each feeder and all DG units within microgrids from abnormal situations. The adaptive protection scheme implemented at the laboratory consists of the over-current and under-voltage protection functions. Subsequently, this chapter explains the over-current and the under/over- voltage/frequency relays in section 3.4 and section 3.5, respectively. Appendix A describes the principles of the directional over-current, distance, and differential protective relays. Moreover, islanding detection methods are explained in section 3.5 because this feature is crucial to adapt the protection scheme to the present microgrid configuration. Furthermore, the adaptive relay coordination with the over-current and under-voltage relays is presented with a flowchart in section 3.6.

3.1 Power system protection components

The power system protection scheme is constructed by several components working together with the common objective; to disconnect short-circuits as quickly and accurately as possible. Figure 3.1 illustrates the key components of the protection scheme; transducers (Current transformer (CT)s/Voltage transformer (VT)s), protection relays, power supply, and CBs [40]. The instrument transformers change the currents and voltages to acceptable levels for the relays. Moreover, the relay is the "brain" in the protection system, which ensures that the correct circuit breaker trips at the right time. The circuit breakers receive commands to either open or close to isolate faults or enable restoration, respectively.

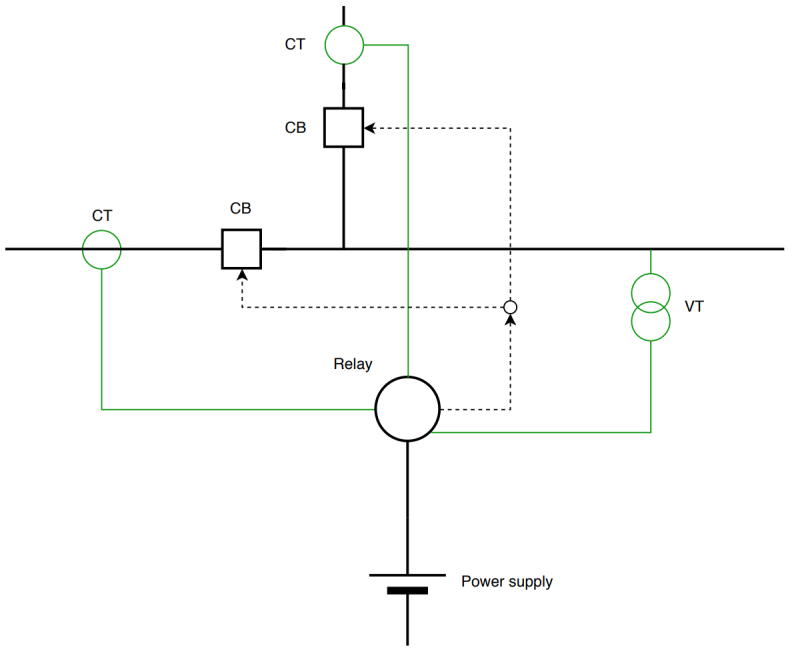

Figure 3.1: Main components of the power system protection rendered from [17]

3.2 Types of short-circuits

Short-circuits are a result of unwanted connections between points with different potential in the power system [17]. In the event of short-circuits, the fault current can be several orders of magnitude larger than normal operating currents, while the voltage levels at the fault location will be lowered [21]. However, in reference to Ohm's law ($I_{sc} = \frac{V_{sc}}{Z_F}$), the fault current magnitude is determined by the fault impedance. The impedance between two connection points during a short-circuit is not necessarily zero, and the fault impedance may vary depending on the cause of the fault [17]. In other words, the type of short-circuit affects the fault impedance, and accordingly, the fault current level. If the fault impedance is low or negligible, it can cause high fault currents, whereas a high fault impedance will lead to lower fault currents. Moreover, the fault occurrence also depends on the type of power system (e.g., overhead lines vs. underground cables) and local weather conditions [10]. However, the effect of such external factors on the fault current level is omitted from this thesis.

Short-circuits are classified by whether they are symmetrical or asymmetrical, i.e., balanced or unbalanced [21]. The different fault types can be divided into four groups, and the list below represents the approximate percentages of occurrence [21]:

- Single phase-to-ground faults: 70%–80%
- Phase-to-phase-to ground faults: 10%–17%
- Phase-to-phase faults: 8%–10%
- Three-phase(-to-ground) faults: 2%–3%

Although the three-phase short-circuit does not occur frequently, this type of fault is further examined

at the laboratory. Three-phase short-circuits generally yield the maximum short-circuit current values. Hence, the serve consequences from the three-phase short-circuit are used for protective device selection because the protection system should be dimensioned for this worst-case scenario. Accordingly, the three-phase short-circuit is applied during the laboratory testing in chapter 5. Figure 3.2 illustrates the fault current contribution from all phases, which is fed to the short-circuit. The reader is referred to [21, chapter 7] regarding the calculation of fault currents during three-phase short-circuits.

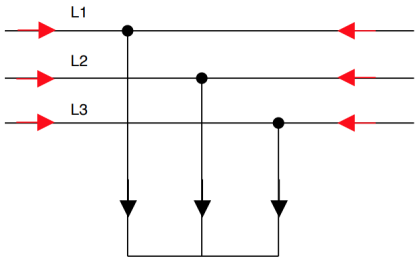

Figure 3.2: Three-phase short-circuit

3.3 Protection Issues in Microgrid

Literature [12, 14, 28, 41, 53, 54] states that the existence of DG units in distribution networks and the two operation modes of microgrids will affect the operation of protective devices. Thus, problems related to namely selectivity, sensitivity, and speed of protection systems may arise during different microgrid typologies. The fault current contribution from DGs differs from "conventional" energy resources in the following ways:

(i) **Reduction in fault current level**

If the main utility grid and the microgrid share the fault current, the measured fault current by an over-current relay is reduced [22]. Additionally, the type of interfacing scheme between the DG unit and the grid effects the level of fault current in the system, thereby having a fundamental impact on the protection scheme. The fault current contribution from IIDGs differs from traditional machine-based DGs [3]. The control scheme of the converters determines the fault current level, and the internal control loops limit the current to protect the power electronics [14]. The fault current magnitude from IIDGs is usually limited to 1.5 times the rated current during a short-circuit [12]. In contrast, DG units based on rotating generators will produce a fault current about 200 to 400 % of the nominal current during a short-circuit [14]. Accordingly, the different fault current capabilities make the protection of microgrids a difficult task.

(ii) **Frequent changes in microgrid typologies and islanding capability**

In the event of a short-circuit during grid-connected operation, both the utility and the DG units within the microgrid will contribute with fault currents. As a result, the fault current will be very high. However, the fault current is very low during stand-alone mode if the microgrid consists of low capacity IIDG sources [12]. Article [27] states that the short-circuit capacity of the utility grid can be more than one order of magnitude larger than the relatively small DER units forming the microgrid. Accordingly, the fault currents in an islanded inverter-dominated microgrid may not have adequate magnitudes to trip traditional over-current protection [42, 57].

Moreover, the frequent connection/disconnection of DG units affects the short-circuit current capacity of the system [4, 22]. Thus, the operating status is essential information as a DG source

only contributes with fault current during its ON state [12]. Generation sources based on renewables will rapidly change its operation mode due to their intermittent behavior; hence it is difficult to accurately predict the fault current.

(iii) **Bidirectionality**

The connection of DG units in the LV network introduces a bidirectional power flow in the distribution network [54]. Besides supplying local loads, microgrids also export power to the utility grid during excess generation, and the power thereby flows in reverse direction [22]. Consequently, the implementation of microgrids causes a bidirectional power flow between the microgrid and the utility grid. Conventional protection schemes designed for radial power flow will therefore not operate faithfully to microgrids [12].

Evidently, the presence of DGs within microgrids changes the magnitude and the direction of fault current. The Borrego Spring project in article [54] demonstrates that the fault current is significantly low in islanded mode, which affects the performance of the existing over-current protection devices. Furthermore, new grid codes like the fault ride through capability prevent the disconnection of DGs during faults, which challenges the well-established protection schemes. The Fault-ride-through (FRT) capability is explained in the next section.

3.3.1 Fault ride through capability

Traditionally, protection devices were set to automatically disconnect DG units whenever a fault in the network was detected [14]. Despite the obvious advantages of feeding isolated parts of the grid, the standards required automatic disconnection to maintain the existing protection schemes [12]. However, if DG units are disconnected following a voltage dip, the loss of generation would lead to an even greater voltage dip. Consequently, modern grid codes prevent unnecessary disconnection of DER units to ensure network supporting functionalities such as FRT [27]. This specification requires that DG units must remain connected to the grid during voltage dips even if the voltage is well below the nominal voltage [47]. The typical FRT trip curve is shown in figure 3.3.

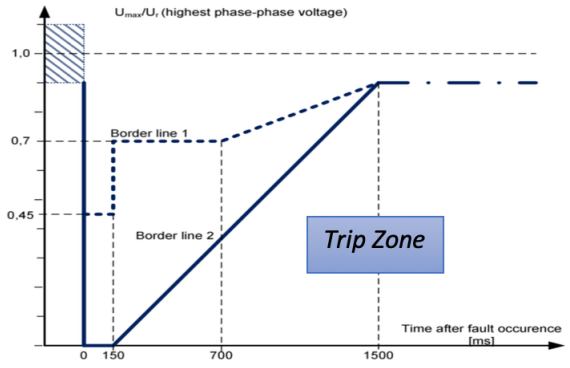

Figure 3.3: A typical FRT capability curve [14]

The FRT requirement is explained in reference to figure 3.3. When the voltage drops to values between borderline 1 and borderline 2, generating units shall pass through the fault without disconnecting from the network [6]. For voltage values below borderline 2, a short-time disconnection of the DG unit might

be carried out regardless. Accordingly, the permissible disconnection range is voltage values below borderline 2 on the FRT capability curve in figure 3.3. Otherwise, the generation units are required to stay connected to support the grid. The FRT requirements vary among different grid codes and national guidelines [27]. Additionally, voltage and time requirements depend on the generator type and the characteristics of the protection system [6]. Figure 3.3 illustrates the FRT capability curve for type-2 generators which consist of IIDG units [6].

The protection relays must disconnect the DGs during permanent faults to ensure stable operation, whereas the DG units should ride-through temporary faults. Despite the transients that may occur during the transition between grid-connected and isolated microgrid, the DGs have to stay connected and supply power to the grid. This requirement will have an impact on protection settings for the generating units following FRT [14].

It becomes evident that the microgrid protection system is complicated by the increased expansion of DG units together with the FRT requirement. A significant challenge is thereby to implement a protection scheme compatible with the protection characteristics of IIDGs, while operating faithfully in both operation modes of microgrids. Accordingly, the need for adaptive microgrid protection emerges. The next sections explain the protection functions which are applied in the microgrid protection scheme implemented at the Smart Grid laboratory. Figure 3.10 illustrates the flowchart of the implemented protection scheme.

3.4 Feeder protection of distribution networks or Distribution system protection

Reference [14] identifies over-current protection, directional over-current protection, and distance protection with impedance pick-up as short-circuit protection of outgoing feeders. However, only the basic principle of the over-current protective relay is explained in this section because this relay is implemented at the laboratory. The explanation of the over-current relay is based on the specialization project "A Review of Challenges and Methods for Microgrid Protection and Control of Power Converters in Microgrids" conducted by the same author during the fall of 2018 [51].

3.4.1 Over-current protection

Over-current protection is a wide deployed protective relay that protects against high fault currents. The working principle of over-current relays is based on the fact that fault currents are significantly higher than load currents during normal operation of the network. In the event of a persistent fault, the over-current relay is calibrated to trip the circuit breaker if the current level exceeds its pickup value. According to [17], over-current relays operate with inverse- and definite- time and instantaneous characteristics, and the relationships between current and time magnitude are illustrated in figure 3.4. Accordingly, the relay trips the circuit breaker if the current exceeds the specified pickup current, I_S, for a time interval given by the definite- or inverse time characteristic [19]. The definite time is given by t_D in figure 3.4. The current must exceed its pickup value for t_D amount of time in order to trip the circuit breaker. The inverse time characteristic is not constant, and the operating time of the circuit breaker depends on the current value. So, high currents will trip over-current relays faster since the inverse time characteristic will decrease the operating time value if the current increases [17]. There are three types of inverse time characteristics: normal inverse, very inverse, and extremely inverse time over-current relay. If the current reaches the instantaneous trip current, I_H, the relay trips after t_H which is set as low as practically possible [19], as illustrated on the graph in figure 3.4.

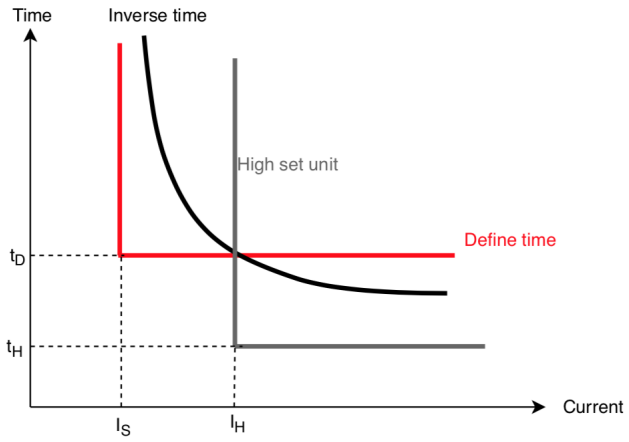

Figure 3.4: Definite-, inverse- and instantaneous time characteristic of over-current protective relays reproduced from [19]

According to the Norwegian specific protection approach, the coordination time is typically set to 0.2-0.3 seconds, while the starting current is typically set to $1.2 \cdot I_n$ of the current transformers [14]. Furthermore, feeders with distributed sources are given an additional coordination time delay. Hence, over-current relays with an extra time delay are applicable considering feeder protection in microgrids.

Figure 3.5 shows a simplified single line diagram of the over-current outgoing feeder protection scheme obtained from [14]. The trip characteristics for protection feeder 1 (FP1) is $I > 1.2 \cdot I_{n,min}$ and $t = 0.2sec$, while protection feeder 2 (FP2) has $I > 1.2 \cdot I_{n,min}$ and $t = 0.3sec$ as current and time settings. Evidently, FP2 is given an extra coordination time delay due to the DG unit on feeder 2, which contributes with additional fault current. Additionally, figure 3.5 illustrates the under/over-voltage/frequency DG protection implemented at the connection point of the DG. These protective relays are described in section 3.5.1. Moreover, an over-current relay is supplemented at the DG feeder. The coordination between the over-current feeder relay and the lateral over-current relay is archived by setting a time delay above regulator response time at the lateral [14].

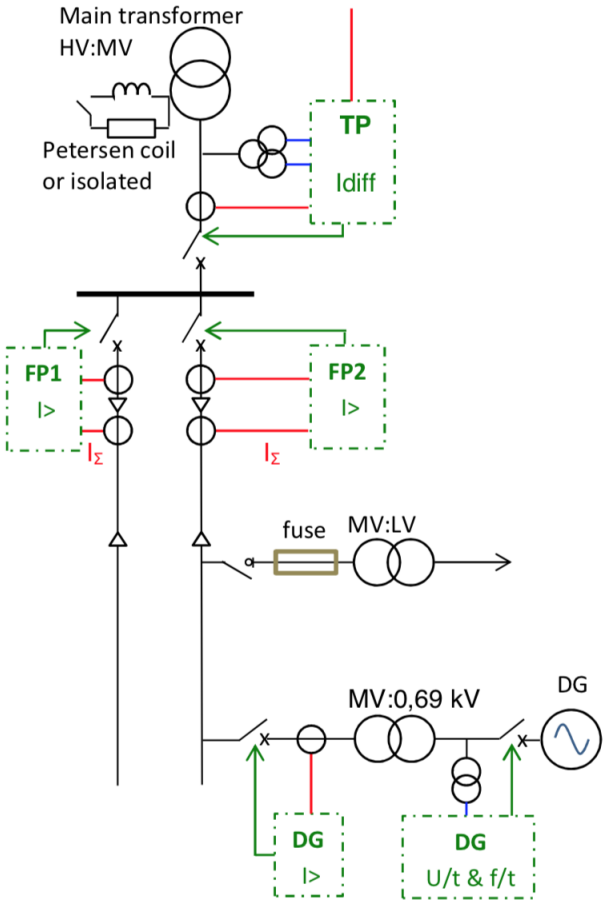

Figure 3.5: Over-current protection of outgoing feeder [14]

Despite the coordination with additional time delays, the over-current protection function utilized in the microgrid protection scheme is configured with zero time delay. The reason for implementing the over-current relay with immediately response is to make the relay operate before the internal protection functions of the laboratory converters. This is further elaborated in section 5.1.5.

3.5 Distributed generation protection

All DG units in the microgrid should be equipped with local voltage/frequency protection elements, so they are protected from abnormal conditions [15]. Typically, DG units are also equipped with over-current protective relays which disconnect internal faults in the DG unit [14]. Figure 3.6 shows the protection devices and the interaction between the over-current relay and the U/f f/t elements to provide proper DG protection.

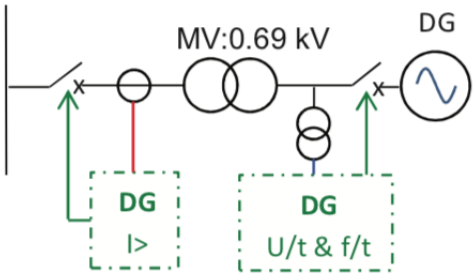

Figure 3.6: Simplified single line diagram of DG protection elements [14]

3.5.1 Under/over-voltage/frequency protection

Voltage/frequency-based protection schemes are independent of both the magnitude and direction of the fault current, which improves the fault detection in microgrids. Nevertheless, the aforementioned protective relays do not offer any selectivity since the DG units are disconnected once the frequency or voltage has reached certain threshold values.

Under/over voltage or under/over frequency protections operate following an unbalance between generation and load. A change in voltage or frequency is a result of a network topology change because the generation sees it as a load change [14]. The transition between grid-connected and islanded mode is an example of topology change due to the loss of generation from the utility grid. Over-frequency results from excess generation, whereas under-frequency operations occur during an overload [5]. Reduced power output is the corrective approach to handle over-frequency. In the case of overload, the frequency is adjusted to its rated value by load shedding. Furthermore, over-voltage occurs due to a sudden loss of generation, and the speed of the prime mover increases [5]. Under-voltage occurs if other generators try to supply the additional load. Consequently, the generators experience a sudden increase in current, and the terminal voltage decreases [5]. Moreover, under/over voltage or under/over frequency protections are based on local measurements, and face problems if the load condition matches the islanded DG generation because there is no significant change in voltage and frequency [50]. The voltage during the islanding transition is investigated at the laboratory, and presented in section 6.1.1, to recognize the change in voltage levels in the event of different network topology changes.

Under/over-voltage/frequency protection schemes require that the DG units are disconnected if the voltage or frequency have reached their threshold values, i.e., a predefined limit [46]. The disconnection is activated after a defined time-period to allow microgrid relays to isolate the fault [15]. The regulatory threshold is determined based on the network voltage and associated standards. Table 3.1 shows the requirements regarding the protection response to voltage deviations. The table sources from a report made by Sintef about technical guidelines of production units in reference [46].

Voltage range in [%] of nominal voltage	**Maximum disconnection time [s]**
U > 115	0.2
U > 110	1.5
U < 85	1.5
U < U_{limit}	0.2

Table 3.1: Disconnection times for under/over voltage protection rendered from [46]

Where U_{limit} is the voltage limit set by the utility company [14]. Furthermore, the DGs should automatically disconnect according to the standards of frequency deviations in table 3.2, based on [46].

Frequency range [Hz]	**Maximum disconnection time [s]**
f > 51	0.2
f < 48	0.2

Table 3.2: Disconnection times for under/over frequency protection rendered from [46]

3.5.2 Islanding detection

Unintentional islanding occurs when DG units continue to supply loads even though the main power network is disconnected [41]. The safety of maintenance personnel may be jeopardized because parts of the network are energized while de-energization is expected [14]. Due to the aforementioned issue, European standards require protection against uncontrolled islanding, i.e., islanding detection. In contrast to the FRT requirement, the protection system must subsequently disconnect the DG sources to shut down the isolated microgrid [27] [31]. Moreover, a reliable detection method is crucial because IIDG units have to comply with control and protection requirements for the islanded mode of operation. Methods for islanding protection are explained in this section.

Generally, active and passive techniques are utilized to detect unintentional islanding [14]. The passive methods are based on measurement schemes such under/over-voltage/frequency protection in section 3.5.1. Furthermore, the Rate of change of frequency (ROCOF) and the voltage vector shift are passive methods to assure detection. The direct transfer trip is an active method and a communication-assisted approach. These techniques are briefly discussed in this section.

Rate of change of frequency (ROCOF)

A frequency deviation indicates an unbalance between the generated power and the load demand [14]. The frequency changes rapidly if the unbalance between supply and demand is large, for example, during the transition between islanded and grid-connected modes. The rate of the frequency is given by equation 3.1 from [13]:

$$\frac{df}{dt} = ROCOF = \frac{\Delta P}{2} \cdot \frac{f}{G \cdot H} \tag{3.1}$$

Where ΔP is the power imbalance, G is the system capacity, and H is the system inertia. Islanding is detected if the ROCOF value is higher than a threshold value. The ROCOF method is not further discussed because it not applied in the laboratory setup.

Direct transfer trip (DTT)

The Direct transfer trip (DTT) method is a reliable anti-islanding protection compared to the passive methods based on local measurements because it is not affected by the local power balance [14]. The circuit breaker initiates a signal to disconnect the generator during the islanded operation. Nevertheless, expensive communication links are required, and the protection system becomes complex if the transfer trip is supplied from more than one location [14]. Even though communication-based island detection methods are reliable, the cost and complexity related to the communication structure may be prohibitive. Despite the required communication, the laboratory experiments are based on the DTT islanding detection method. The implementation of the communicated-assisted digital relays and the

signal transfer with the status of the STS are explained in section 5.1.5 and section 5.1.6, respectively. The typical arrangement of the DTT is illustrated schematically in 3.7, whereas figure 3.8 illustrates the the transfer of the trip signal of the STS.

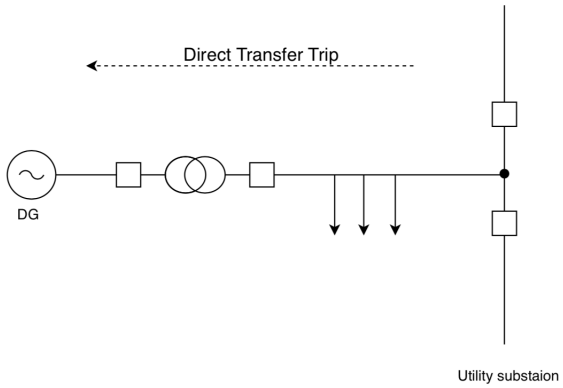

Figure 3.7: The direct transfer trip principle reproduced from [14]

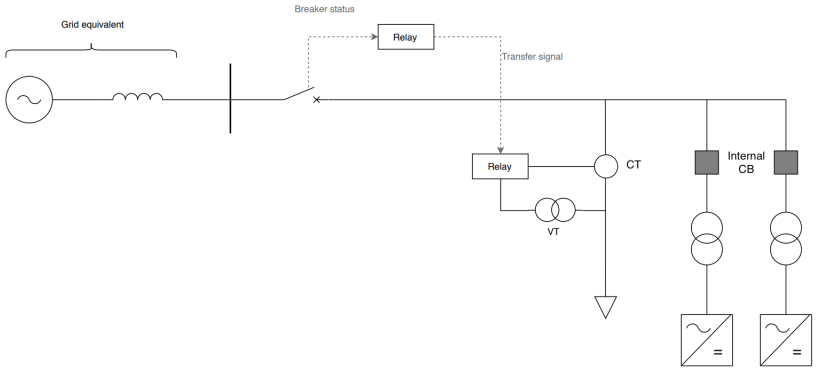

Figure 3.8: Direct transfer signal of the breaker status, which is implemented at the Smart Grid laboratory

---

In this section, the purpose of a reliable islanding detection is to shut down isolated microgrids during faults. The disconnection of DG units enables the use of existing protection equipment based on conventional over-current protective relays [54]. Nevertheless, new grid codes requirements, like the FRT capability, prohibit the disconnection of DG units during faults to support the stability of the grid [55]. Furthermore, the advanced control of microgrids permit a paradigm shift towards *intentional* islanding where microgrids operate isolated from the main power network [48]. Subsequently, island detection is essential to adapt protection and control settings to the present operational state of microgrids. Adaptive microgrid protection is discussed in the next section.

3.6 Adaptive microgrid protection

Reference [27] stress that the existing distribution protective systems cannot reliably protect microgrids, and the protection relays must therefore be adaptable to the present operational state and the status and number of DGs. In this regard, an adaptive protection scheme considering the over-current and under-voltage protective functions is suggested. The adaptive protection system considers the microgrid configuration, and accordingly change the relay settings to ensure the proper protection of the whole microgrid at all times.

Adaptive protection is defined as "an online activity that modifies the preferred protective response to a change in system conditions or requirements in a timely manner by means of externally generated signals or control action" in [24, p.125]. Thus, the relay can change its settings online whenever a change in the network configuration is noticed [22]. However, reliable communication and fast data acquisition systems are required to protect the system against faults. According [28], the use of microprocessor based, i.e., digital relays, is inevitable. Moreover, the digital relays should have several group settings with different tripping characteristics that can be parameterized locally or remotely [24]. The use of secure communication infrastructure and communication protocols such as IEC61850 is also required. As a result, the individual relays can communicate and exchange information with a central control unit or between different protective relays to facilitate a reliable performance [28], [24].

The technical requirements of the adaptive protection scheme are associated with relatively high investment costs compared to the conventional protection system based on fuses, electro-mechanical, or standard solid state relays [24]. Consequently, a cost-benefit analysis considering potential benefits over the microgrid protection system lifetime and investment and operating costs should to be conducted [36]. However, this thesis focuses on the technical realization of the adaptive microgrid protection system.

Generally, adaptive protection can be implemented by two infrastructures; centralized structure and decentralized structure (called multi-agents) [12]. In both structures, the protective settings are adaptive to any network changes, and the parameters are updated online or offline. The online modification is based on real-time calculated settings, whereas the offline method is based on pre-calculated settings [28]. The principle of centralized protection is discussed in section 3.6.1, while the decentralized adaptive protection is omitted because the adaptive protection implemented at the laboratory relates more to the centralized protection scheme. Subsequently, the proposed solution for microgrid protection is presented in section 3.7. The protection scheme adapts between over-current protection during grid-connected operation and under-voltage protection when the microgrid is islanded.

3.6.1 Centralized adaptive protection system

In centralized protection, network changes, such as status of the DGs and operational state, are updated continuously to a central controller to devise proper protection schemes [12]. In other words, the centralized control unit instructs the protective IED units based on the received information. Modern relays are logic devices, constantly processing input values to check whether they represent a normal or faulted system [17]. Noticeably, to monitor the overall network situation, the centralized adaptive protection schemes require substantial communication infrastructure. Based on the exchanged information, the controller transmits protective signals to all components in the microgrid, such as DG units, relays, and circuit breakers. Regarding online coordination, a control signal is sent to the Microgrid central protection unit (MCPU) to do new online calculations for any network topology change. The MCPU thereby updates the operational settings of each relay [28]. However, in the offline database, all possible configurations are stored offline in the memory of MCPU.

Figure 3.9 illustrates an example from [29] where the monitors the network, and selects the correct protective settings based on the DG status. Consequently, communication infrastructure and digital relays with group settings are necessary to implement this adaptive protection scheme. According to reference [29], the different operation modes and settings are:

1. Setting 1: no DG units connected
2. Setting 2: DG unit at bus 12 operating
3. Setting 3: DG unit at bus 19 operating
4. Setting 4: DG units at buses 12 and 19 are both operating
5. Setting 5: Communication failure
6. Setting 6: Spare

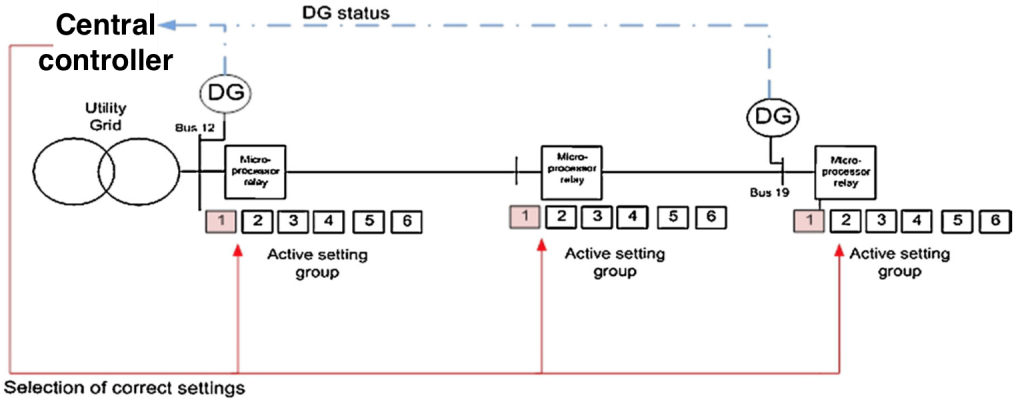

Figure 3.9: Proposed centralized adaptive protection scheme [29]

However, fast data acquisition is challenged by the dynamic behavior of microgrids, and consequently, this method cannot cover all changes in microgrid topologies [28]. Especially bigger systems with more than two DG units, have a huge set of operating conditions and thereby require a collection of an enormous amount of data.

3.7 Proposed solution for microgrid protection

The performance of the aforementioned protective relays applied in microgrids is yet to be analyzed [27]. Technical literature proposes several microgrid protection schemes which consist of both conventional protection relays and new solutions broadly categorized as adaptive protection schemes. Adaptive protection will play a central role in the protection of *future networks* due to new technologies like digital relays and communication links [28]. However, adaptive protection is not widely deployed in distribution grids today. Many authors only presented the idea of adaptive microgrid protection, but specific testing and simulations are carried out in some cases. According to [22], a complete solution is yet to be developed, and consequently, the adaptive protection schemes are not widely deployed in the power system industry. Additionally, reference [27] confirms that the research on microgrid protection has not led to a commercially available microgrid relay to date.

The specialization project "A Review of Challenges and Methods for Microgrid Protection and Control of Power Converters in Microgrids" conducted by the same author presents some protection methods applied in existing microgrids and adaptive microgrid protection schemes proposed in the literature. However, this is omitted in this master's thesis to focus on the actual protection scheme implemented at the Smart Grid laboratory. Figure 3.10 is a flowchart of the working principle of the protection scheme; however, the practical configuration is described in the laboratory setup in chapter 5.

The proposed protection scheme is based on an adaptation between over-current protection during grid-connected operation and under-voltage protection when the inverter-dominated microgrid is islanded. Figure 3.10 illustrates the flowchart of the protection scheme implemented at the Smart Grid laboratory. The configuration of the protection relays is explained more in detail in section about the laboratory setup.

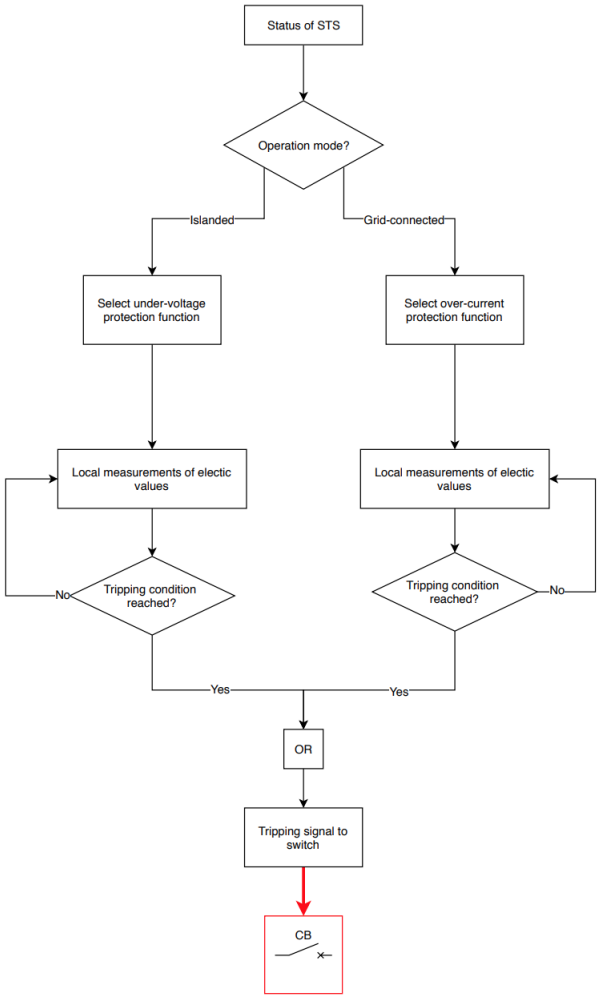

Figure 3.10: Flowchart of proposed microgrid protection scheme

Chapter 4

Power Flow Control of Converters in Microgrids

Power electronic IIDG units are of special interest concerning distribution network protection as their controllers affect the DG behavior [23]. The control strategy of a power converter depends on its role in microgrids, and it might be changed according to the present operation mode. Accordingly, the power converters are classified into grid-forming, grid-feeding, and grid-supporting converters. In this chapter, the control strategies of different power converters in AC microgrids are investigated. This is necessary to gain knowledge about the fault behavior of microgrids with a considerable presence of power electronics.

PV arrays, storage batteries, and fuel cells are examples of DC units, and a power electronic converter must facilitate the energy exchange between the DC- and the AC system. Although microturbines and wind energy conversion systems are AC units, they are connected to an AC microgrid bus-bar through power electronic converters to match the grid frequency and voltage [23]. In other words, the diverse characteristics of DERs make power electronic converters necessary to facilitate the energy exchange between subsystems [25]. Figure 4.1 illustrates the power electronic interface between a DER unit and the utility grid, which in general consists of four modules; the source input converter module, the DC-AC converter module, the output interface module, and the controller module [35]. Depending on the DER unit, the input converter module is either an AC-DC or a DC-DC converter as depicted in figure 4.1.

The input-side controller and grid-side controller represent the main control features of a distributed power generation system [56]. In reference to figure 4.1, the AC-DC or DC-DC converter will be the input-side converter, whereas the DC-AC converter represents the grid-side converter. The input-side controller is responsible for extracting maximum power from the DER unit while protecting the input-side converter [56]. On the other hand, the grid-side controller manages the interaction between a DG unit and the utility grid by controlling active power and reactive power generated to the grid [11]. This thesis focuses on the grid-connected converter, i.e. the DC-AC converter module in figure 4.1, since its features are important when implementing microgrids. Subsequently, the two-level VSC configuration explained in section 2.4.4 limits the extent of this thesis as the VSC is nowadays a commonly used grid-connected converter for high-power-applications [25]. The VSCs in microgrids consist of several control systems. First, the different levels of control are mentioned in section 4.1, while the inner control level is elaborated further in section 4.2. Furthermore, the different control strategies, together with their inner control loops, are explained by classifying the power converter into grid-forming, grid-following, and grid-supporting converters in section 4.3. Thereby, this thesis emphasizes the local control embedded in power converters belonging to microgrids.

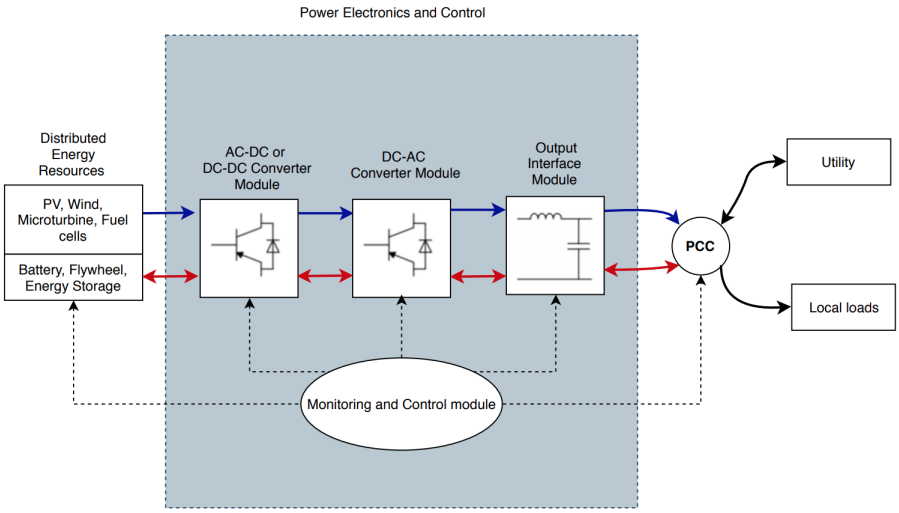

Figure 4.1: Illustration of a generalized power electronic interface topology

4.1 Hierarchical Control Structure

A hierarchical control structure aims to optimize and standardize the operation of microgrids [11]. The hierarchical control scheme is divided into four levels; from zero to three, and consists of inner, primary, secondary, and tertiary control levels [8, 11, 48] as illustrated in figure 4.2. Table 4.1 lists the control levels according to their response time where the regulation speed decreases with the increasing control level.

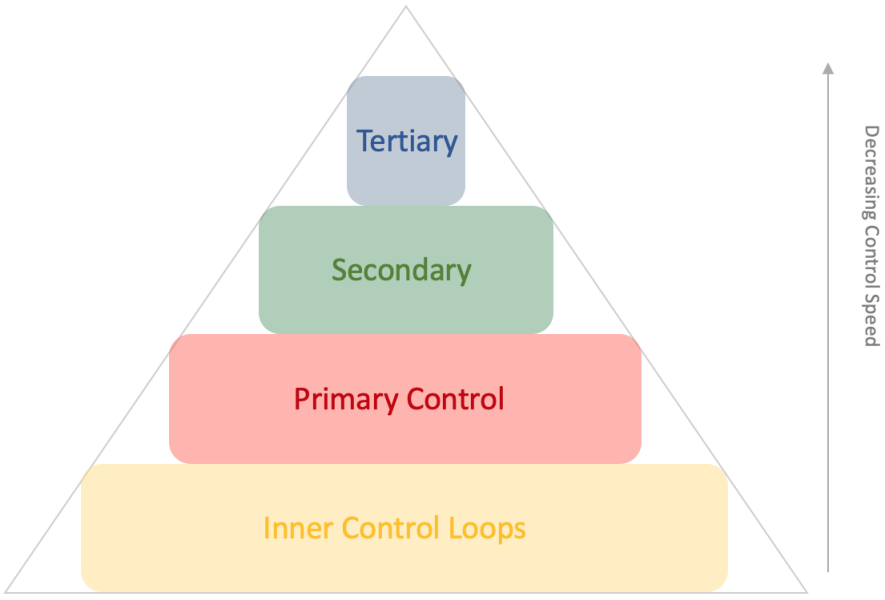

Figure 4.2: Hierarchical control structure

Level	Type	Response
0	Current control loop	Short-term
0	Voltage control loop	Short-term
1	Droop control loop	Long-term
2	Secondary control	Long-term
3	Tertiary control	Longer-term

Table 4.1: Hierarchical control strategy for the controllers of VSCs from reference [52]

The hierarchical control strategy regulates the VSCs in microgrids with the multiple control loops in figure 4.3, to maintain the voltage and frequency stable [52].

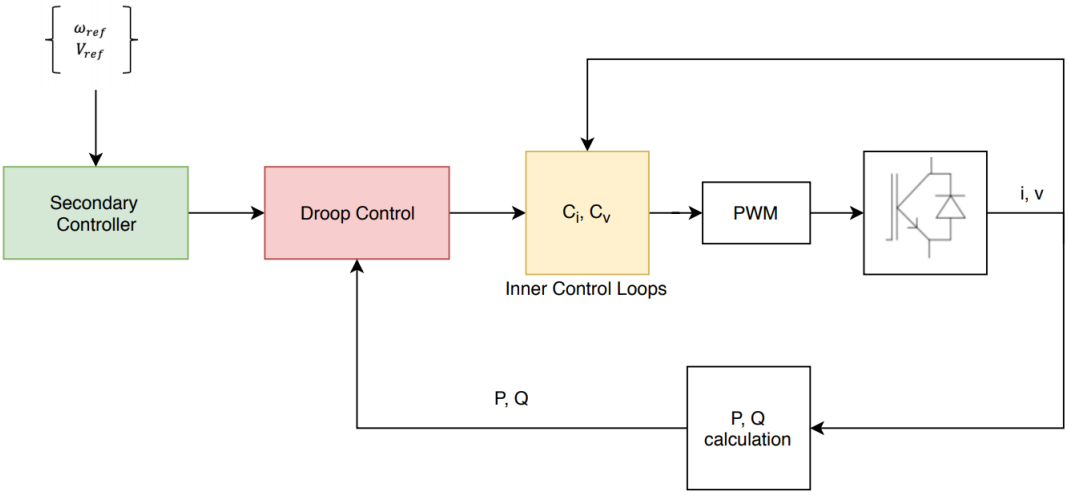

Figure 4.3: Hierarchical management strategy of primary and secondary control reproduced from [52]

The low-level inner control loops in figure 4.3 are responsible for the local control for each VSC and represent the current and voltage control loops at the zero control level in table 4.1. These controllers should have high bandwidths and performance to guarantee a fast time response under generic operating conditions [48]. Evidently, the inner controllers regulate the currents and voltages of the storage elements; the filter inductor and capacitor [8].

The primary controllers take care of the short-term stability of microgrids at a higher control level. The primary control manages the power-sharing among the DGs by implementing droop control techniques for each power converter connected to the microgrid [48]. Thus, the primary control level is referred to as the droop control loop at control level 1 in table 4.1. Droop control is essential to maintain short-term stability due to the lack of inertia from power electronic devices [52]. Section 4.3.3 describes the classical droop control in the grid-supporting power converters, which utilizes the P/f and Q/V relationships.

The secondary control level in the grid-supporting converter adjusts the droop characteristic coefficients to restore the microgrid voltage and frequency to the rated values [48]. Secondary control is a centralized approach that sets the power references to minimize the voltage and frequency deviations caused by the primary control [8]. The tertiary control considers the market and the demands from the Transmission system operator (TSO) or Distribution system operator (DSO), and regulates the

import or export of power between the microgrid and the main grid [8], [48]. The secondary and tertiary control levels require communication channels to coordinate the action of all the generation units within a given area, whereas droop controllers do not require any communication among the power converters in the microgrid.

As illustrated in figure 4.3, the hierarchical control strategy is organized by multiple control loops. However, this thesis focuses on the control of VSCs, i.e., the inner controllers and the primary droop control level. Section 4.2 describes the inner control, while section 4.3 explains the different control strategies, together with their inner control loops, by classifying the power converter into grid-forming, grid-following, and grid-supporting power converters.

4.2 Inner control

The inner control loops regulate the PWM signals to the VSC, and the inner control is established with a cascade of two single control loops, as illustrated in figure 4.4 [44]. The inner control scheme regulates the current through the converter-side inductor, L_1, and the voltage across the capacitor C in the LCL-filter. Figure 4.4 illustrates the location of voltage- and current measurements in the VSC and LCL-filter configuration.

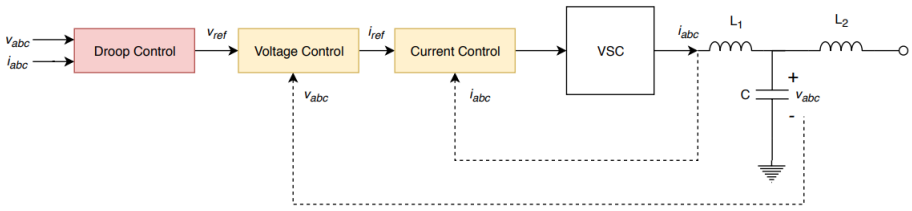

Figure 4.4: Cascaded control of the inner control loops

In technical literature, power converters are categorized based on their control schemes, and the converter output is mainly regulated by the current control or voltage control strategy [23], [44]. Generally, the application of the VSC determines the control scheme. Current-controlled converters are desired in grid-connected microgrids, whereas voltage-controlled converters are necessary to set the amplitude and frequency reference of the voltage in islanded microgrids. The inner controllers, namely the outline of control steps of the current and voltage controller, are explained accordingly by classifying the power converters into grid-following, grid-forming, and grid-supporting power converters. Consequently, the current controller is explained in section 4.3.1 for the current-controlled grid-following converter, while the voltage controller is explained in section 4.3.2 for the voltage-controlled grid-forming converter.

The implementation of the control strategy can be done in different reference frames [56]. This thesis focuses on converters implemented in the synchronous reference frame, with Proportional-integral (PI) controllers, because the *dq* PI regulator is commonly used for converter control [38]. Vector control is therefore explained first in section 4.2.1 as the *abc* to *dq* transformation is relevant for both the current and voltage controller.

4.2.1 Vector control

The control structures for a grid-connected converter are implemented in different reference frames; the synchronous reference frame (dq-frame), the stationary reference frame ($\alpha\beta$-frame), and the natural frame (abc-frame) [56]. Figure 4.5 illustrates the relation between the dq, $\alpha\beta$, and abc reference frames. The natural frame is ideally transformed to dq or $\alpha\beta$ in order simplify the controller design [9]. As elaborated, the extent of this thesis is limited to the PI regulator in the synchronous reference frame. Subsequently, the synchronous reference frame and the PI-regulator are explained in sections 4.2.1 and 4.2.2, respectively.

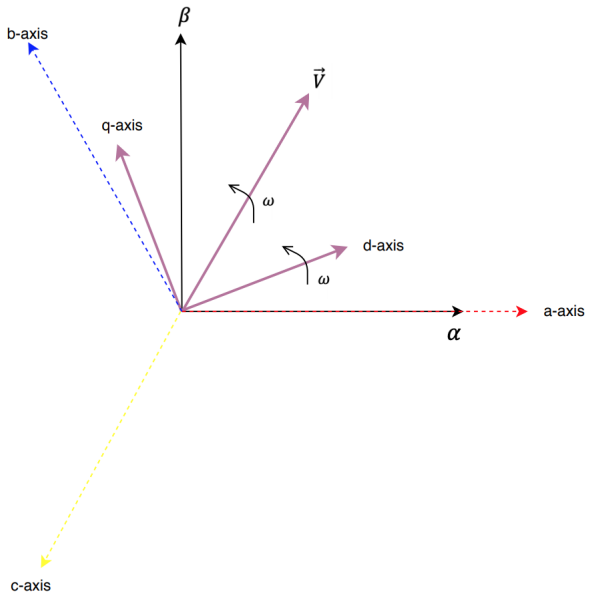

Figure 4.5: The synchronous, stationary, and natural reference frame

Synchronous reference frame control

The synchronous reference frame rotates with a rotational speed equivalent to the electrical frequency of the AC-system. The measured AC voltage and current signals are translated to DC signals for the synchronous dq reference frame [53]. The $abc \rightarrow dq$ transformation module, referred to as Park transformation, translates the control variables from their natural frame to the dq reference frame that synchronously rotates with the frequency of the grid voltage [9, 56]. As a result, the control variables become DC values in steady state, which makes the regulation easier.

The following relations between synchronous and natural reference frame are obtained when the rotating frame is aligned with A axis:

$$\begin{bmatrix} u_q \\ u_d \\ u_0 \end{bmatrix} = \frac{2}{3} \cdot \begin{bmatrix} cos(\omega t) & cos(\omega - \frac{2\pi}{3}) & cos(\omega t + \frac{2\pi}{3}) \\ -sin(\omega t) & -sin(\omega t - \frac{2\pi}{3}) & -sin(\omega t + \frac{2\pi}{3}) \\ \frac{1}{2} & \frac{1}{2} & \frac{1}{2} \end{bmatrix} \begin{bmatrix} u_a \\ u_b \\ u_c \end{bmatrix}$$

A three-phase AC signal can be represented by a set of three rotating vectors which are summarized to a single space-phasor. $\vec{V}$ in figure 4.5 denotes the single space-phasor that synchronously

rotates with the frequency of the AC grid voltage in the counter-clockwise direction [25]. The d- and q-axis components of $\vec{V}$ are stationary with perfect synchronization between the rotating frame and the space-phasor velocities. Equation 4.1 gives the amplitude of the voltage, $\hat{V}$, in the dq-frame [58]:

$$\hat{V} = \sqrt{V_d^2 + V_q^2} \tag{4.1}$$

The length of $\vec{V}$ is given by $\hat{V}$, while V_d and V_q are the d- and q-axis components of $\vec{V}$, respectively.

The dq reference frame is decoupled, so it facilitates independent control of the active and reactive power exchanged between the DC and AC systems. This is done by exploiting the relationship between the active power and the direct current component (i_d), and secondly the correspondence between the reactive power and the quadrature current component (i_q) [53].

The VSC must determine the frequency of the microgrid voltage in the event of islanding. Hence, the angular velocity of the dq-reference frame is set to 50 Hz [58]. However, the frequency of the microgrid voltage is controlled by the utility grid during grid-connected operation. Consequently, a synchronization mechanism is required, so the synchronous dq-frame matches the angular speed of the AC system [25]. $\vec{V}$ is synchronized with the d-axis of the rotating frame by phase locking, i.e., Phase locked loop (PLL). Thus, in steady state, the q-component of the voltage is omitted as illustrated in equation 4.2.

$$V_d = \hat{V} \tag{4.2a}$$
$$V_q = 0 \tag{4.2b}$$

4.2.2 PI-Controllers

As elaborated, the control system involves the use of several PI regulators. Reference [56] gives the typical transfer function of a PI controller, which is rendered in equation 4.3:

$$G_{PI}^{(dq)}(s) = K_p + \frac{K_i}{s} \tag{4.3}$$

where K_p is the proportional gain, whereas K_i is the integral gain of the PI controller. Figure 4.6 illustrates the block diagram with the PI controller in series with an electrical system.

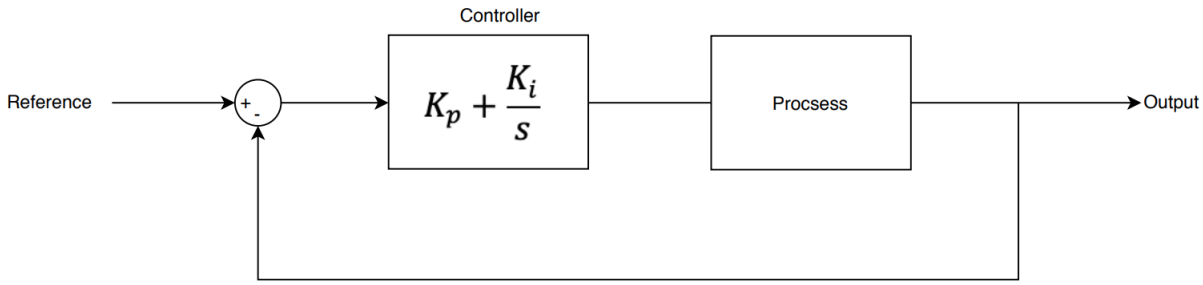

Figure 4.6: PI regulator

The current and voltage controllers utilize PI regulators in order to obtain zero steady state deviation between the reference value and measured value. The proportional gain, K_p, and the integral gain, K_i, have to be tuned in each regulator to secure a fast and accurate response. The K_p regulator gain is adjusted for the grid-forming converter during the laboratory testing, but this is further elaborated in chapters 5 and 6.

According to literature [9, 48, 56], the objective of the Park transformation is to obtain control loops with PI control. However, the phase angle of the utility voltage is necessary in order to perform the dq transformation [9]. Consequently, every voltage deviation will be reflected in the direct and quadrature components during unbalanced conditions, and PI controllers are unable to regulate these oscillations [48, 53, 56]. Furthermore, its poor compensation capability of low-order harmonics is another disadvantage with PI control in grid-connected systems [9].

4.2.3 Phase locked loop technique

The overall performance of grid-connected power converters is dependent on the estimation of AC grid voltage parameters [48]. In other words, the estimation of voltage amplitude, frequency, and phase angle is necessary to conduct an accurate control of the active and the reactive power delivered to the grid. As elaborated, the grid frequency is estimated by the PLL technique, which synchronizes grid-connected power converters with the grid voltage. Figure 4.7 depicts the structure of the closed control loop working on the synchronous reference frame. The feedback control loop regulates the angular position of the dq reference and forces the v_q component to zero [48]. The Voltage source oscillator (VCO) finds the estimated phase angle, $\theta^{'}$, by integrating the estimated grid frequency, $\omega^{'}$. References [55, 49] also propose a decoupled double synchronous reference frame PLL since the performance of a synchronous reference frame PLL is exposed during faults.

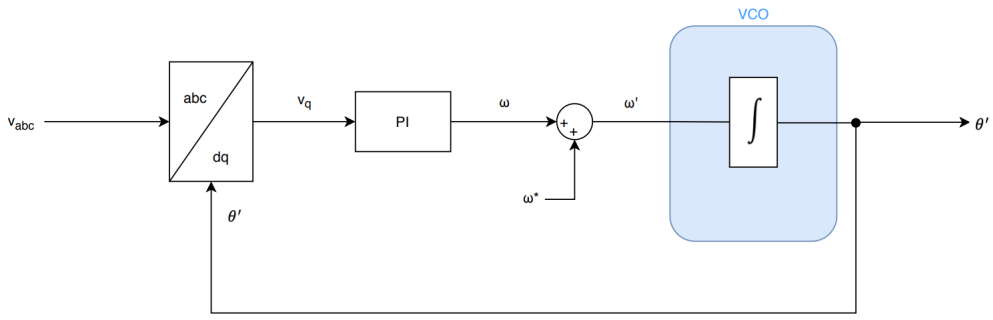

Figure 4.7: Block diagram of the synchronous reference frame phase-locked loop

4.3 Classification and control schemes of power converters in microgrids

The power converters in AC microgrids are classified into grid-following, grid-forming, and grid-supporting power converters [11], [48]. The control strategy, which depends on their operation in an AC microgrid, is the main distinction between the power converters. In grid-connected operation, the microgrid units are responsible for balancing active and reactive power by delivering or absorbing power (P/Q control), while the utility grid regulates the voltage and frequency. However, the microgrid must additionally maintain the voltage at the PCC to its nominal magnitude and frequency during islanded mode [12]. Thus, the microgrid units must also engage in voltage-frequency control (V/f control). Structured controllers with cascaded control loops are thereby required to ensure a proper microgrid operation during both modes and in the event of faults [48]. The implemented control loops in the aforementioned power converters are discussed in this section. The control design is of great importance since the fault current contribution from a IIDG source is determined by VSC's control system. Moreover, it is important to recognize the classification of power converters because these definitions are frequently used in the laboratory setup. The practical implementation of the laboratory converters and the necessary modifications to obtain grid-forming, grid-following, and grid-supporting power converters at the laboratory are explained in chapter 5.

Figure 4.8 illustrates a simplified representation of the power converters, while sections 4.3.1, 4.3.2, and 4.3.3 explains the control strategies more in detail. Variables denoted with * represent the reference values of the variables, while the d- and q-axis components of the variable are denoted with subscript d and q, respectively.

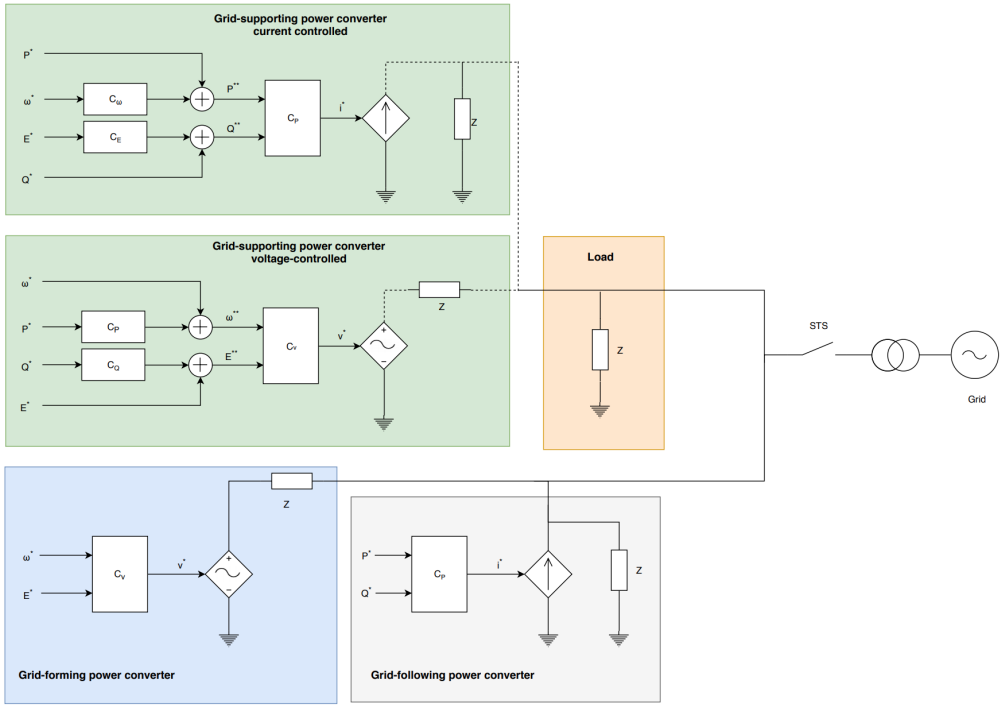

Figure 4.8: Simplified representation of the power converters in AC microgrids

4.3.1 Grid-following power converter control

The cascaded system of the grid-following power converter consists of multiple controllers which aim to perform power control (P/Q control). The inner control loop consists of a current controller, while the power controller constructs the outer control loop. The current control loop regulates the current injected into the grid based on the reference current received from the power controller. As illustrated in figure 4.8, the grid-following power converter is controlled as a current source. Thus, a grid-following VSC depends on the utility grid or other voltage-controlled DGs to form the grid voltage to be able to operate [48]. Therefore, this kind of converter cannot operate independently in island mode [23], and the VSC is connected to the utility grid at PCC in figure 4.9. Figure 4.9 illustrates the developed control system of a grid-following power converter.

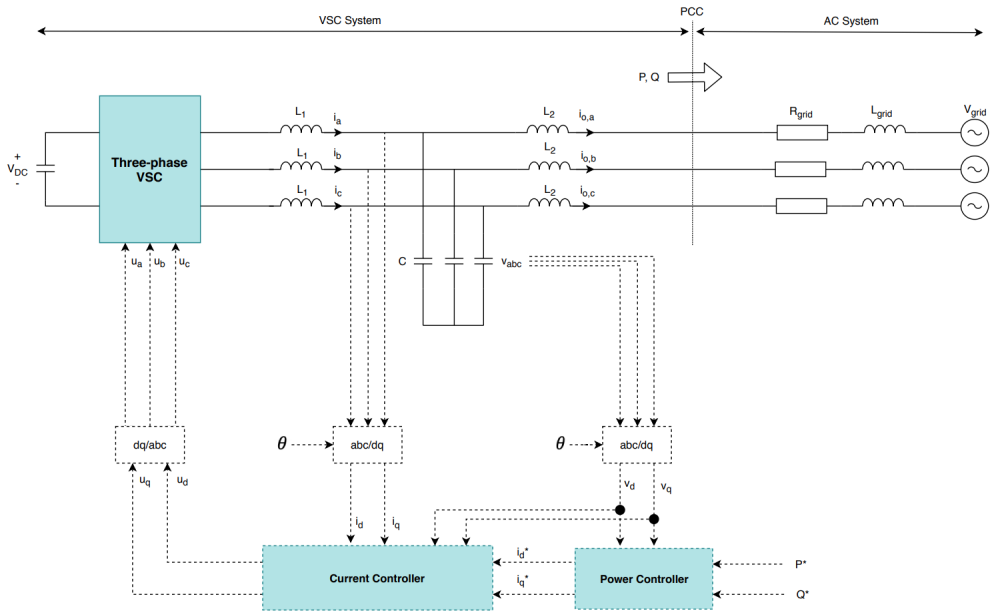

Figure 4.9: Schematic diagram of the grid-following power converter where the dotted lines denote control signals and measurements

The outline of the control steps for the grid-following control strategy is listed below in reference to [48].

1. The references for active and reactive power to be delivered are set directly as input values. Thus, the MPPT controller, which adjusts the power references according to the DC-side of the converter, is omitted. In other words, the input-side controller is not included, and the DG units are represented as ideal DC voltage sources.

2. The power controller receives the selected reference values for active power and reactive power, P^* and Q^* respectively. These input parameters are utilized to obtain the reference currents. Based on the power reference inputs, the power controller regulates the current references to keep the active and reactive power constant.

3. The current controller receives the reference currents, i_d^* and i_q^*. Depending on the input, the controller adjusts the switching signals, which affect the voltage at the AC-side of the converter, u_{abc} [58].

The measurement signals needed by the controllers are obtained from various places in the system. Figure 4.10 shows a simplified representation of the converter and the LCL-filter, where the location of the measurement signals is emphasized. Moreover, the *abc/dq*-transformation of the AC measurement signals is illustrated.

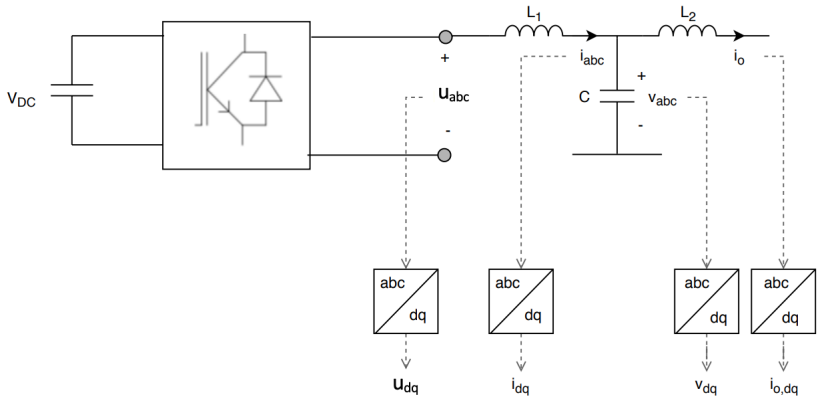

Figure 4.10: Representation of the three-phase converter and the LCL-filter

The control system is explained by focusing on the control loops individually. Regarding the grid-following power converter, the current controller and the power controller are explained in this section.

Current controller

The current controller is the innermost control loop in figure 4.9. By regulating the switching signals, the current controller modulates the current flowing in the converter-side inductor to match the reference current inputs, i^*_{dq} [23]. The converter-side inductor is denoted as L_1 in figure 4.10. In other words, the current controller ensures that $i^*_d \approx i_d$ and $i^*_q \approx i_q$ by performing changes to the converter switching signals [25]. The voltage at the capacitor is found by applying Kirchoff's voltage law on the system in figure 4.10:

$$u_{abc} = R \cdot i_{abc} + L_1 \cdot \frac{di_{abc}}{dt} + v_{abc} \tag{4.4}$$

The voltage level before and after the LCL-filter is respectively u_{abc} and v_{abc}, while R and i_{abc} are denoted as the resistor and current through the converter-side inductor, L_1 [26]. The equations of the AC current in the synchronous reference frame is given by equation 4.5, obtained from reference [52]. The assumption of a balanced system makes the 0-component omitted, thus only the d- and q-components of the synchronous reference frame are subsequently considered.

$$L_1 \cdot \frac{d}{dt}\begin{bmatrix} i_d \\ i_q \end{bmatrix} = \begin{bmatrix} u_d \\ u_q \end{bmatrix} - \begin{bmatrix} v_d \\ v_q \end{bmatrix} - R\begin{bmatrix} i_d \\ i_q \end{bmatrix} + \begin{bmatrix} 0 & \omega L_1 \\ -\omega L_1 & 0 \end{bmatrix}\begin{bmatrix} i_d \\ i_q \end{bmatrix} \tag{4.5}$$

where ω is the angular velocity [58]. Important realizations are listed below:

1. The current dynamic is affected by the converter switching signals, u_d and u_q [58]. Thus, the switching signals, i.e., the output of the current controller, regulate i_d and i_q.

2. Voltages v_d and v_q affect the current dynamics so i_d and i_q may be altered without the control signals in the current controller initializing the change [25]. The capacitor voltage is therefore categorized as a disturbance that must be counteracted because it is not controllable.

3. The dynamics of i_d and i_q are cross-coupled which indicate that a change in i_d imposes a change in i_q and vice versa [25]. The current should be decoupled by eliminating these cross-coupling terms, so it is possible to change i_d or i_q without altering a change in i_q or i_d, respectively.

4. Normally, the DC-side of the converter affects the current dynamics because u_d and u_q depend on the converter switching signals and the DC voltage [58]. However, the DG units are represented as constant DC voltages, so the influence of varying V_{DC} is not considered.

The current controller should take the decoupling terms, $\omega L_1 i_d$ and $\omega L_1 i_q$, into account in order to control i_d and i_q individually. Furthermore, the current controller should additionally feedforward the capacitor voltage, so the current dynamics are only affected by the control signals. The control signals, u_d and u_q, aim to adapt to the changes in the current reference signals and counteract all other disturbances affecting the current dynamics [58]. Moreover, the PI controller is necessary to obtain a zero steady-state deviation between the reference and measured current. Thus, the controllers are given by the control signals in equation 4.6. Accurate current responses are secured by designing the current controller based on these equations.

$$u_d = v_d - \omega L_1 i_q + K_{p,i} e_d + K_{i,i} \int e_d dt \tag{4.6a}$$

$$u_q = v_q + \omega L_1 i_d + K_{p,i} e_q + K_{i,i} \int e_q dt \tag{4.6b}$$

The error, e, is the difference between the reference and measured current, and is the input to the PI controller. The proportional term is denoted as $K_{p,i}$, whereas the integral term is equivalent to $K_{i,i}$ for the PI current controller. By inserting equations 4.6a and 4.6b into equation 4.5, the equations are given by:

$$L_1 \cdot \frac{di_d}{dt} = K_{p,i} e_d + K_{i,i} \int e_d dt - R i_d \tag{4.7a}$$

$$L_1 \cdot \frac{di_q}{dt} = K_{p,i} e_q + K_{i,i} \int e_q dt - R i_q \tag{4.7b}$$

Laplace is applied, and the block diagram in figure 4.11 represents the Laplace domain equation 4.8.

$$i_d = \frac{1}{L_1 \cdot s + R} \cdot (K_{p,i} + \frac{K_{i,i}}{s}) \cdot e_d \tag{4.8a}$$

$$i_q = \frac{1}{L_1 \cdot s + R} \cdot (K_{p,i} + \frac{K_{i,i}}{s}) \cdot e_q \tag{4.8b}$$

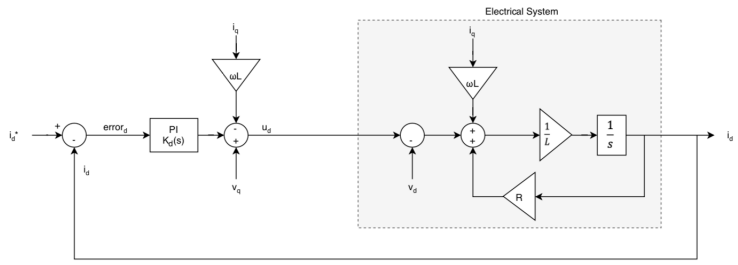

((a)) d-axis

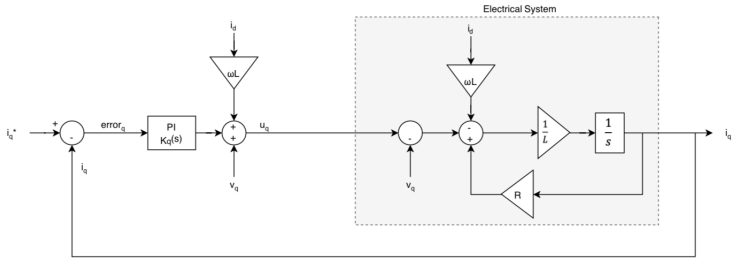

((b)) q-axis

Figure 4.11: Block diagram of the current controller based on [26]

The block diagram of the current controller in figure 4.11 is simplified to the block diagram in figure 4.12, which is rendered from [58]. The feedback measurement signals served to counteract the disturbances affecting the current dynamics are omitted in the 4.12 block diagram. To summarize, the control signals, i_d^* and i_q^*, control the actual current in the system. In all, the expectations are:

1. i_d^* and i_q^* can separately regulate i_d and i_q.
2. The regulation of i_d will not disturb the regulation of i_q, and vice versa.
3. The current will not be affected by the capacitor voltage, v_{abc}.

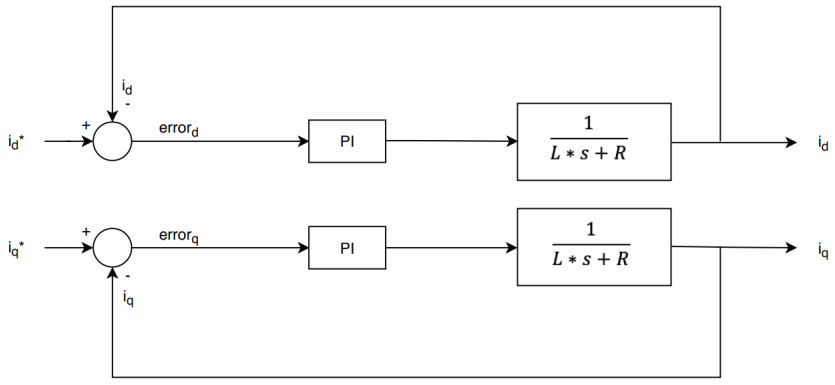

Figure 4.12: Simplified version of the current controller block diagram

Two PI regulators are utilized to achieve reference tracking since i_d and i_q are DC quantities in the synchronous reference frame [48]. The $K_d(s)$ PI regulator in figure 4.11(a) process the error signal $(i_d^* - i_d)$, while the $K_q(s)$ PI regulator in figure 4.11(b) process the error signal $(i_q^* - i_q)$. As the block diagram for the d- and q-axis control loops are identical, the two PI regulators are identical [25]. The PI controllers are therefore given by equation 4.9, which are obtained from equation 4.8 and the simplified block diagram in figure 4.12:

$$K_d(s) = K_q(s) = K_{p,i} + \frac{K_{i,i}}{s} \tag{4.9}$$

where $K_{p,i}$ and $K_{i,i}$ are the proportional and integral gains of the PI in the current regulator, respectively.

The power controller

The power controller establishes the reference currents, i_d^* and i_q^*, based on the active power and reactive power references, P^* and Q^*, respectively. Hence, the power controller regulates the active and reactive power delivered to the grid [48]. The regulated active and reactive power by the VSC are denoted as P and Q in figure 4.9. According to reference [58, p.218], the real and reactive power delivered to the AC system at PCC, *P(t)* and *Q(t)*, are calculated by equation 4.10:

$$P(t) = \frac{3}{2} \cdot [V_d(t)i_d(t) + V_q(t)i_q(t)] \tag{4.10a}$$

$$Q(t) = \frac{3}{2} \cdot [V_d(t)i_q(t) - V_q(t)i_d(t)] \tag{4.10b}$$

Where V_d and V_q are the d- and q- components of the V_{abc} voltage, whereas i_d and i_q are the d- and q-components of the i_{abc} current in reference to figure 4.9. Equation 4.10 is the non per-unitized version of the power equation. However, the per-unitized version of the instantaneous active and reactive power components is given in equation 4.11 obtained from [48, p.4739]:

$$P = V_d i_d + V_q i_q \tag{4.11a}$$

$$Q = V_d i_q - V_q i_d \tag{4.11b}$$

Equation 4.11 can be rewritten to equation 4.12 as $V_q = 0$ when the dq-frame is synchronized with the AC system [58].

$$P = V_d i_d \tag{4.12a}$$

$$Q = V_d i_q \tag{4.12b}$$

Consequently, V_d is the only non-controllable signal present, and subsequently accounted for in the power controller design. Based on equation 4.12, the active and reactive power is controlled by i_d and i_q, respectively. The d-component of the V_{abc} is considered by defining the reference currents:

$$i_d^* = \frac{1}{V_d} \cdot P^* \tag{4.13a}$$

$$i_q^* = \frac{1}{V_d} \cdot Q^* \tag{4.13b}$$

Hence, if the currents are equal to the reference values, the powers subsequently equal their reference value. The active and reactive power are regulated separately by changing their reference values, P^* and Q^*, respectively.

The control structure of the grid-following converter with the current- and power cascaded control loops is illustrated in figure 4.13.

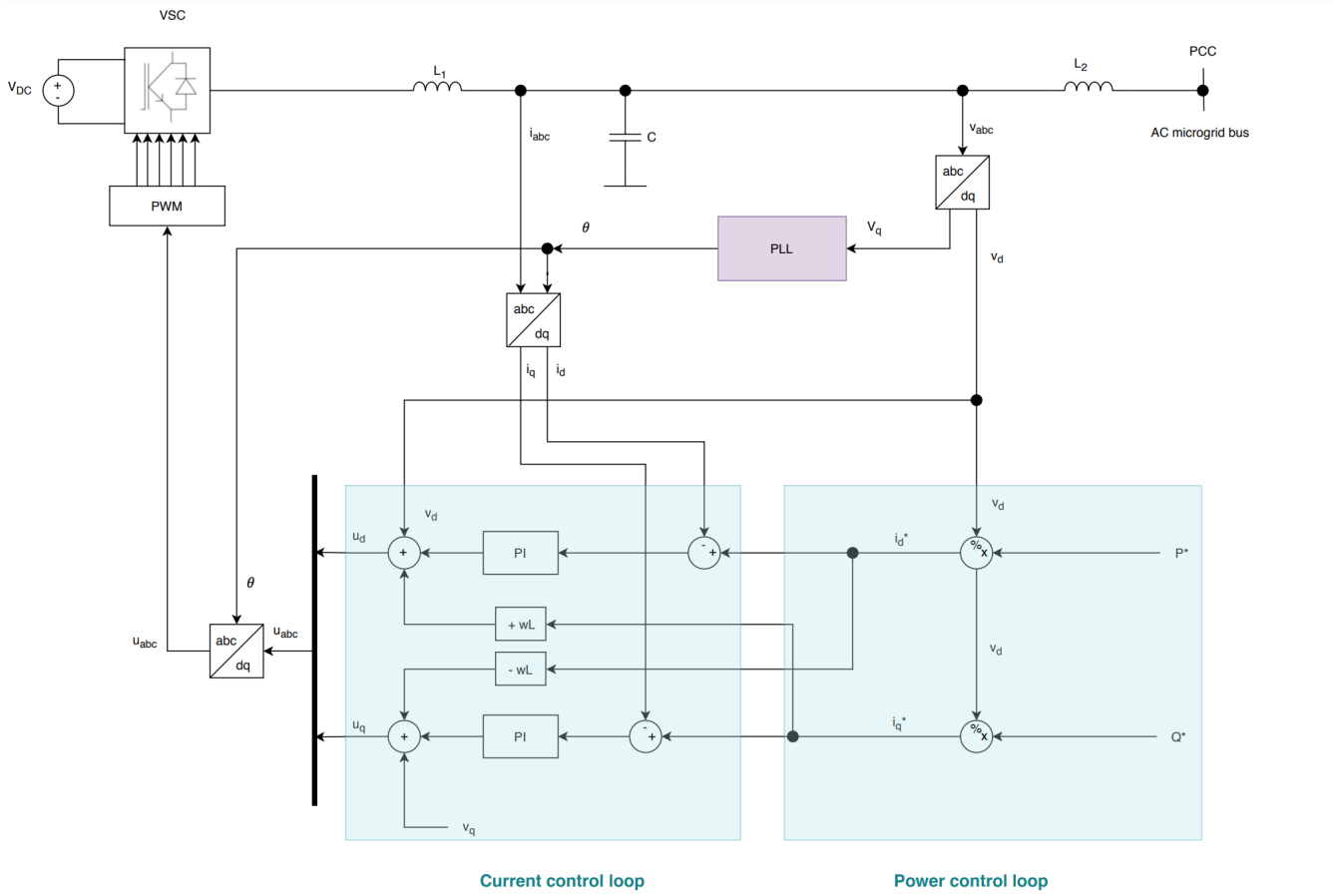

Figure 4.13: Control strategy of a grid-following power converter

4.3.2 Grid-forming power converter

The grid-forming power converters are represented as ideal voltage sources with a low-output impedance and are designed for autonomous operation [11]. The simplified representation is illustrated in figure 4.8. Grid-forming converters are voltage-controlled with a given voltage amplitude, E^*, and frequency, ω^* [48]. Grid-forming power converters therefore usually operate in islanded mode, in contrast to grid-following converters. In the event of a grid failure, a grid-forming converter sets the amplitude and frequency reference of the microgrid voltage, and the other grid-following power converters in the microgrid follow this reference [11]. Due to the low output impedance, the grid-forming converter needs an extremely accurate synchronization system to operate in parallel with other grid-forming converters or the stiff utility grid [48]. Consequently, the grid-forming converter is applied in an islanded microgrid and remains disconnected from the main utility when the microgrid is grid-connected.

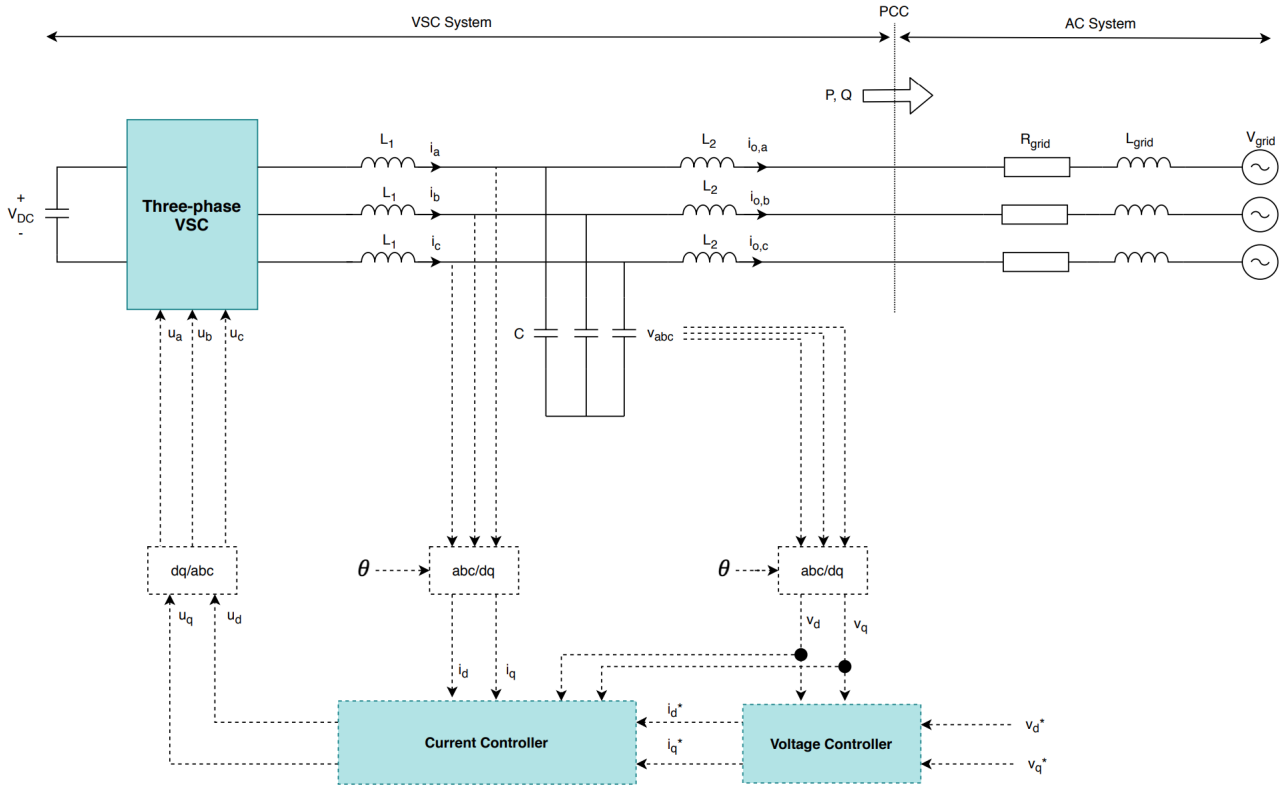

Figure 4.14: Schematic diagram of the grid-forming power converter where the dotted lines denote control signals and measurements

As illustrated in figure 4.14, the control scheme consists of two cascade control loops; an inner current control loop and an outer voltage control loop, working in the dq synchronous reference frame. The voltage controller regulates the output voltage to match its reference value, whereas the current controller regulates the injected current from the converter to the grid [11]. The outline of the control steps for the grid-forming control strategy is listed below in reference to [48].

1. The voltage controller calculates the reference currents, i_d^* and i_q^*, based on the input voltages, v_d^* and v_q^*. The voltage PI controller receives the difference between the reference and measured voltage, and accordingly establishes the current reference.

2. The current controller receives the reference currents and subsequently regulates the converter switching signals, u_d and u_q, based on this input.

The controlled inductor current flowing through L_1, charges the capacitor, C, so the output voltage is kept close to the reference provided by the voltage controller [48]. Figure 4.10 illustrates the locations of the measurement signals needed by the grid-forming control strategy. The current control loop is the same controller as developed in section 4.3.1, whereas the voltage controller is explained in this section.

Voltage Controller

The voltage controller is the outer control loop in figure 4.14, which adjusts the reference currents to control the voltage across the three-phase capacitor. In other words, the voltage controller ensures that $v_d^* \approx v_d$ and $v_q^* \approx v_q$ by performing changes to the reference currents, i_d^* and i_q^*, respectively. Kirchoff's current law is applied on the system in figure 4.10 in order to express the voltage dynamics:

$$i_{abc} - i_o = C\frac{dv_{abc}}{dt} \tag{4.14}$$

Where i_{abc} is the current flowing through the converter-side inductor, L_1, while i_o is the output current. Furthermore, v_{abc} is the voltage across the filter capacitor, C. The equations of the AC voltage in the synchronous reference frame is given by equation 4.15:

$$C \cdot \frac{d}{dt}\begin{bmatrix} v_d \\ v_q \end{bmatrix} = \begin{bmatrix} i_d \\ i_q \end{bmatrix} - \begin{bmatrix} i_{d,o} \\ i_{q,o} \end{bmatrix} + \begin{bmatrix} 0 & \omega C \\ -\omega C & 0 \end{bmatrix} \begin{bmatrix} v_d \\ v_q \end{bmatrix} \tag{4.15}$$

where ω is the electrical angular velocity [58]. Important realizations are:

1. The voltage dynamics depend on the current. Hence, the voltage behavior can be controlled by i_d^* and i_q^*.
2. The output current from the converter, $i_{d,o}$ and $i_{q,o}$, also contributes to the voltage dynamics. Consequently, v_d and v_q might be altered without the reference currents from the voltage controller initializing the change [25]. This disturbance signal should therefore be counteracted.
3. The dynamics of v_d and v_q are cross-coupled which indicate that a change in v_d imposes a change in v_q and vice versa [25]. The voltage should therefore be decoupled by eliminating these cross-coupling terms so it is possible to control the v_d and v_q voltages separately.

Subsequently, the voltage controller should take the decoupling terms, $\omega C v_d$ and $\omega C v_q$ into account, and additionally feedforward the output current. The control signals, i_d^* and i_q^*, aim to adapt to the changes in the voltage reference signals and account for all disturbances affecting the voltage dynamics. Moreover, the voltage PI controller is necessary in order to obtain a zero steady state deviation between the reference and measured voltage. Thus, the control signals from the voltage controller are given in equation 4.16 which account for the disturbance from the output current and the voltage-cross-coupling:

$$i_d = i_{d,o} - \omega C v_q + K_{pv} e_d + K_{iv} \int e_d dt \tag{4.16a}$$

$$i_q = i_{q,o} + \omega C v_d + K_{pv} e_q + K_{iv} \int e_q dt \tag{4.16b}$$

The error, e, is the difference between the reference and measured voltage, and is the input to the PI controller. The proportional term is denoted as $K_{p,v}$, whereas the integral term is equivalent to $K_{i,v}$ for the PI voltage controller. By inserting equations 4.16a and 4.16b into equation 4.15, the equation is given by:

$$C \cdot \frac{dv_d}{dt} = K_{pv} e_d + K_{iv} \int e_d dt - R i_d \tag{4.17a}$$

$$C \cdot \frac{dv_q}{dt} = K_{pv} e_q + K_{iv} \int e_q dt - R i_q \tag{4.17b}$$

Applying Laplace gives equation 4.18 and the block diagram in figure 4.15:

$$v_d = \frac{1}{C \cdot s}(K_{pv} + \frac{K_{iv}}{s}) \cdot e_d \tag{4.18a}$$

$$v_q = \frac{1}{C \cdot s}(K_{pv} + \frac{K_{iv}}{s}) \cdot e_q \tag{4.18b}$$

$$\tag{4.18c}$$

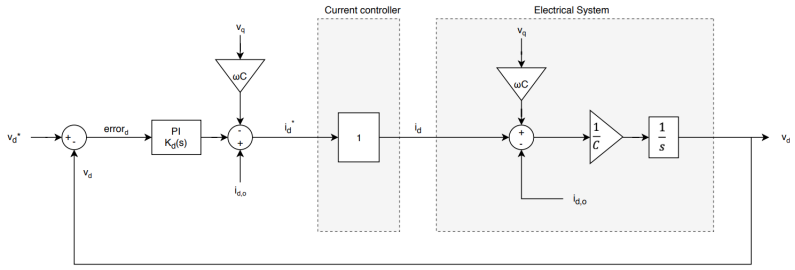

((a)) d-axis

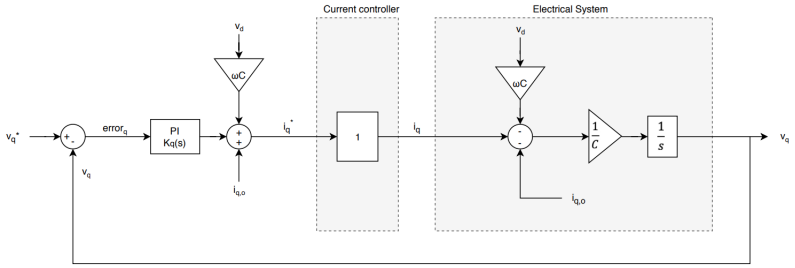

((b)) q-axis

Figure 4.15: Block diagram of the voltage controller based on [26]

Assuming that the current controller is much faster than the voltage controller, the dynamics of the current control loop is represented as unity in figure 4.15 seen from the voltage control level [26].

The block diagram of the current controller in figure 4.15 is simplified to the block diagram in figure

4.16, which is rendered from [58]. The feedback measurement signals served to counteract the disturbances affecting the voltage dynamics are omitted in the 4.16 block diagram. To summarize, the control signals, i_d^* and i_q^*, control the actual voltage in the system. In all, the expectations are:

1. v_d^* and v_q^* can separately regulate v_d and v_q.
2. When v_d and v_q are regulated, they will not disturb each other.
3. The voltage will not be affected by the output current, i_o.

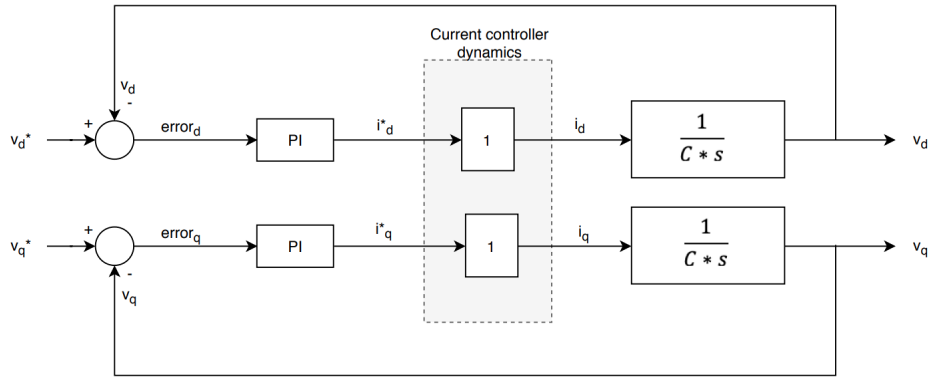

Figure 4.16: Simplified version of the voltage controller block diagram

Two PI regulators are utilized to achieve reference tracking since v_d and v_q are DC quantities in the synchronous reference frame [58]. The $K_d(s)$ PI regulator in figure 4.15(a) process the error signal $(v_d^* - v_d)$, while the $K_q(s)$ PI regulator in figure 4.15(b) process the error signal $(v_q^* - v_q)$. As the block diagram for the d- and q-axis control loops are identical, the two PI regulators are identical [25]. The PI controllers are therefore given by equation 4.19, which are obtained from equation 4.18 and the simplified block diagram in figure 4.16:

$$K_d(s) = K_q(s) = K_{p,v} + \frac{K_{i,v}}{s} \tag{4.19}$$

where $K_{p,v}$ and $K_{i,v}$ are the proportional and integral gains of the PI in the voltage regulator, respectively.

The control structure of the grid-forming converter with the current- and voltage cascaded control loops is illustrated in figure 4.17.

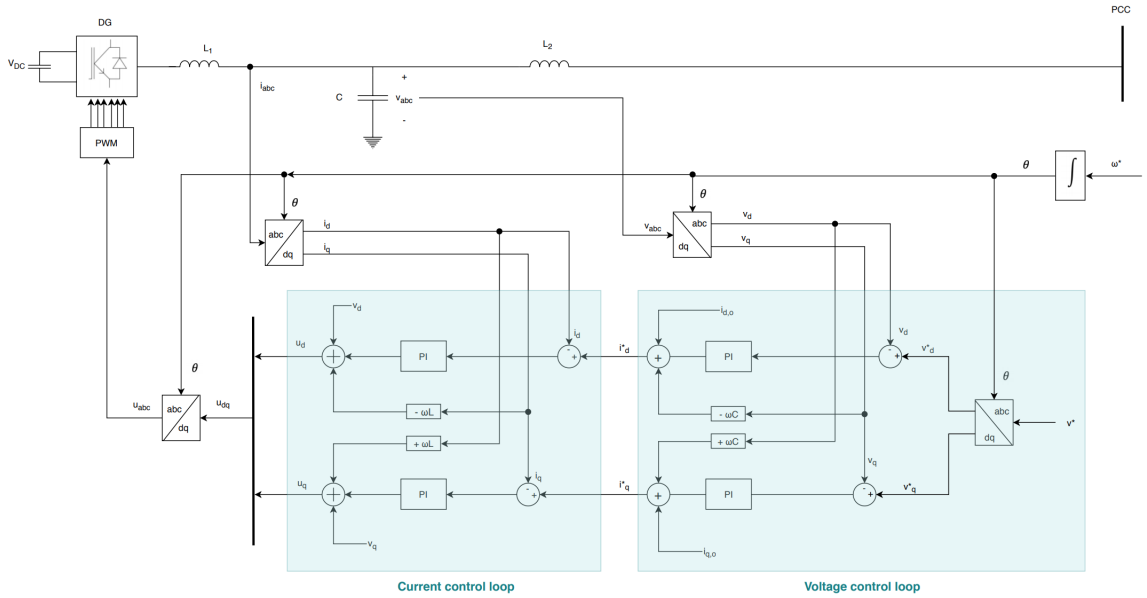

Figure 4.17: Control strategy of a grid-forming power converter

4.3.3 Grid-supporting power converter

Grid-supporting converters regulate the amplitude and frequency of the AC grid voltage to their rated values by controlling the active and reactive [48]. As illustrated in figure 4.8, a grid-supporting converter can be controlled as a current source with an impedance in parallel or as a voltage source with link impedance [11]. Accordingly, the control scheme of the grid-following and grid-forming power converters can be modified to grid-supporting power converters, including droop control as illustrated in figure 4.18. Droop control is needed for grid-supporting operation and utilized in islanded application to achieve load sharing among the converters.

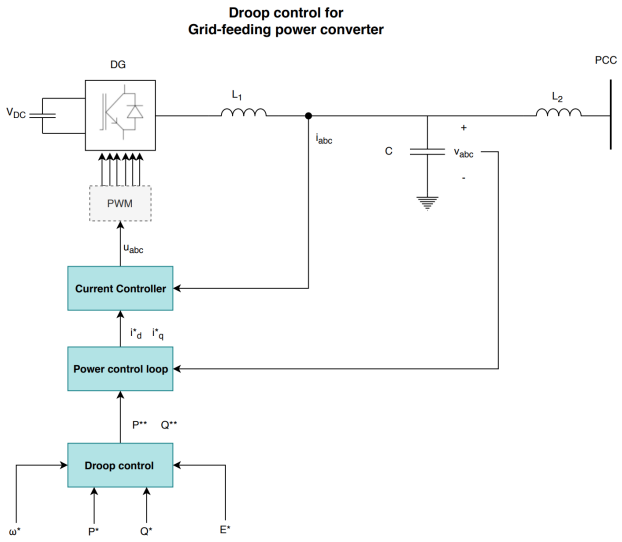

((a)) The grid-following control scheme modified with droop control to achieve grid-supporting control operating as a current source

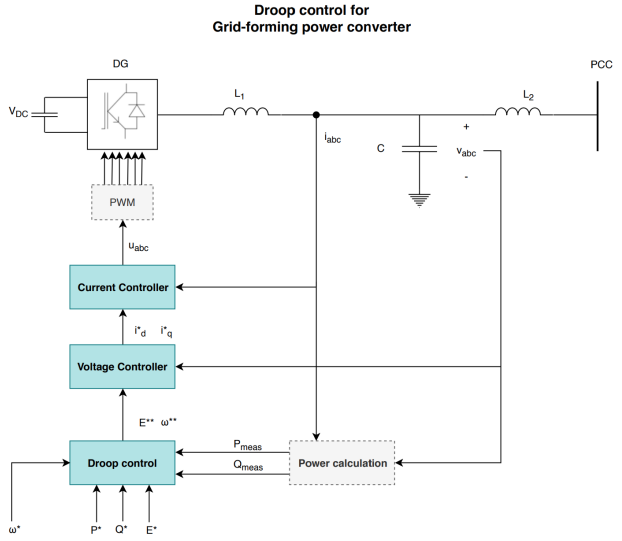

((b)) The grid-forming control scheme modified with droop control to achieve grid-supporting control operating as a voltage source

Figure 4.18: Representation of grid-supporting operation

The definition of a grid-supporting converter differs in technical literature, e.g., the explanations of the grid-supporting converter in [48] and [38] are not in compliance. Article [48] by Rocabert *et al.* emphasizes that the grid-supporting converter can both be current-controlled and voltage-controlled with virtual impedance. Reference [48, p.4738] states that the voltage-controlled converter can participate in regulating the amplitude and frequency of the grid voltage, with no need of connecting any grid-forming converter in the microgrid. The project memo [38] by Ljøkelsøy explains the practical control system for the three-phase grid connected converters employed at the Smart Grid Laboratory at NTNU. The grid-connected laboratory converter is assigned with grid-supporting capabilities by selecting the voltage controller as reactive control. However, it is still the current regulator regulating the voltage [38]. Hence, the grid-supporting converter implemented at the laboratory is not able to set the amplitude and frequency of the voltage in islanded microgrids [38]. The practical configuration is explained more in detail in section 5.1.4. Nevertheless, the grid-supporting configuration with the voltage control loop in figure 4.18(b) is the most relevant control structure regarding the actual implementation of the grid-supporting converter at the laboratory. Hence, the grid-supporting converter with the voltage control loop is further discussed in this thesis in line with the laboratory grid-supporting converter. The practical configuration of the grid-supporting converter is further elaborated in section 5.1.4 about converter control.

The outline of the control steps for the grid-supporting control strategy with the voltage control loop is based on the outline of the grid-forming converter. However, the droop control loop in figure 4.18(b) is additionally assigned.

1. Power calculation is performed based on the local measurements of i_{abc} and v_{abc}.
2. The droop control loop receives the reference values of the active and reactive power, P^* and Q^*. The error between the reference values and the measured values of the active and reactive power are subsequently multiplied with their respective droop coefficients. The droop frequency reference and droop voltage reference are thus obtained, and sent to the voltage control loop.
3. The voltage controller calculates the reference currents, i_d^* and i_q^*, based on the input voltages, v_d^* and v_q^*. The voltage PI controller receives the difference between the reference and measured voltage, and accordingly establishes the current reference.
4. The current controller receives the reference currents and subsequently regulates the converter switching signals, u_d and u_q, based on this input.

Figure 4.19 shows the control structure of the grid-supporting converter with the cascaded control loops, and this control structure is based on the voltage-controlled grid-supporting power converter in reference [48]. However, the virtual impedance in [48] is omitted because this control technique is not implemented in the laboratory testing. In short, the effect of virtual impedance improves the power sharing among the droop controlled converters in dominant resistive microgrids with a high R/X ratio [11].

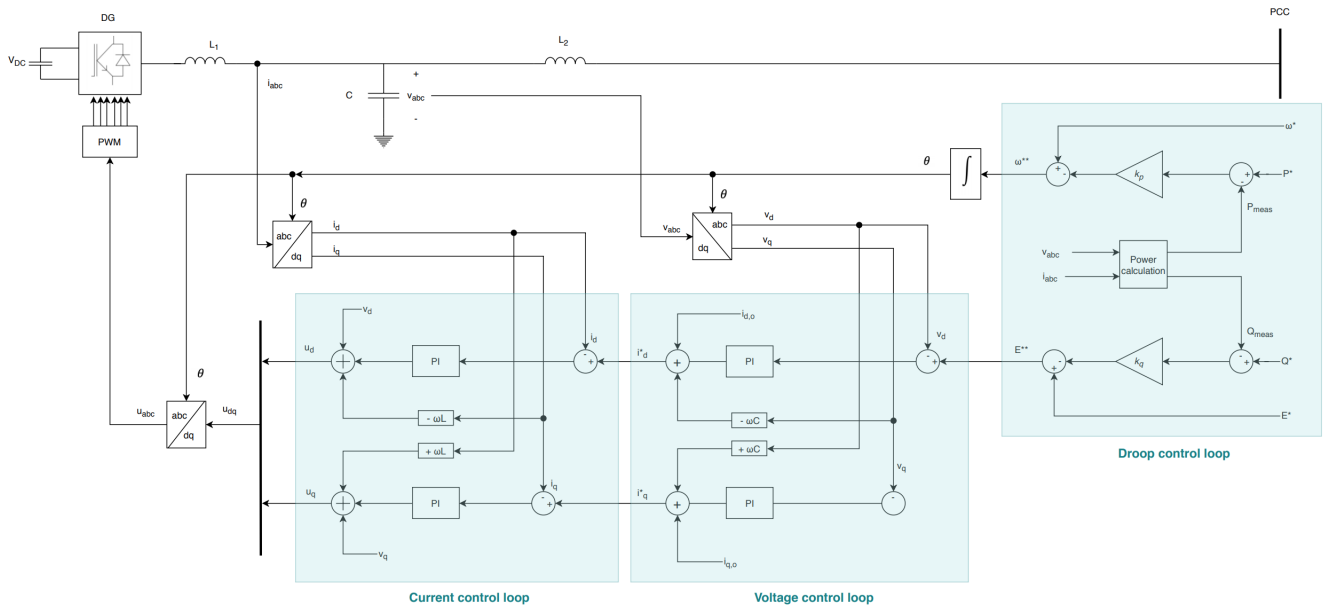

Figure 4.19: Control structure of a grid supporting power converter controlled as a voltage source

The current control loop and voltage control loop are the same controllers as developed in section 4.3.1 and section 4.3.2, respectively. However, the droop controller is explained in this section.

Droop control

In order to participate in voltage and frequency regulation, the grid-supporting converters adjust their active and reactive power references by a droop regulation technique [48]. A droop control algorithm is referred to the second level of hierarchical control and is implemented to regulate the power sharing in microgrids without communication-assisted devices. In other words, the droop control is a decentralized approach for power sharing based on local measurements performed at the converters. Despite the small impedance angle of a distribution line due to the low X/R line ratio in microgrids, the conventional P/f and Q/V droop characteristics are emphasized in this thesis. The classical droop control can be performed with the LCL-filters at the converter terminals because the inductor connected to the grid provides the inductive characteristic of the network [52]. Thus, the active power controls the frequency, while the reactive power controls the voltage at the grid connection point. The active power reference is increased if a higher frequency is desired, whereas the reactive power reference is increased if a higher voltage is desired.

The objective of the droop controller is to find the frequency reference, ω^{**} and the voltage amplitude reference, E^{**}, as depicted in figure 4.19. First, the measured active and reactive powers are calculated and subsequently subtracted from the corresponding reference values. Next, these deviations are multiplied with their corresponding droop coefficients; k_p and k_q in equation 4.20. Finally, the difference between the droop voltage and the reference voltage and the difference between the droop frequency and the reference frequency are obtained. The droop frequency, ω^{**}, is integrated to find the phase angle, whereas the droop voltage, E^{**}, is the input to the voltage control loop.

$$\begin{aligned} \omega^* - \omega^{**} &= -k_p \cdot (P - P^*) \\ E^* - E^{**} &= -k_q \cdot (Q - Q^*) \end{aligned} \tag{4.20}$$

The grid frequency and voltage deviations are respectively represented as $\omega^* - \omega^{**}$ and $E^* - E^{**}$ in equation 4.20. Moreover, k_p and k_q are the droop parameters utilized in the P/f and Q/V control, respectively. P and Q in equation 4.20 are the measured values of the real and reactive power, while $P - P^*$ and $Q - Q^*$ represent the variations in the active and reactive powers delivered by the power converter to compensate for the frequency and voltage deviations [11]. Figure 4.20 shows the frequency and voltage droop characteristics in grids with dominant inductive behavior.

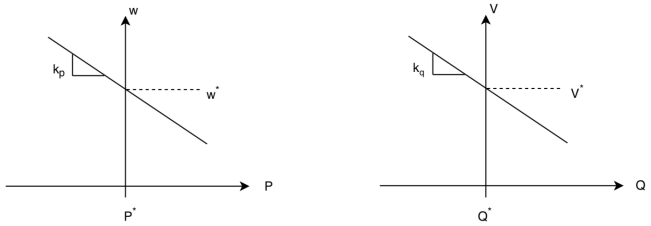

Figure 4.20: Droop characteristics in inductive networks

To summarize, the P/Q controller consists of an inner current control loop and an outer power control loop, while the V/f control system is based on an inner current control loop and an outer voltage control loop. In other words, the difference is assigned to the outer control loop which feeds the reference current to the inner current controller. Regarding grid-following power converters, the external power controller sends the reference currents, $[i_d^*, i_q^*]$, to the inner current controller. However, the voltage control loop provides the reference currents to the current controller for grid-forming converters. Lastly, regarding grid-supporting converters, the reference currents is found by the voltage control loop which is based on the voltage references from the droop controller. The aforementioned control types and other characteristics of the grid-following, grid-forming, and grid-supporting power converters are summed up in table 4.2, based on reference [11].

Contribution to the grid	**Grid-following**	**Grid-forming**	**Grid-supporting**
Source type	Ideal current source	Ideal voltage source	Current or voltage source
Control type	PQ control	Constant frequency/voltage control	Droop control
Combination	Parallel	Series	Parallel or series
Output frequency	Grid synchronized	Fixed frequency	Frequency droop
Output impedance	$Z = \infty$	$Z = 0$	Finite, non-zero
Application	Grid-connected	Islanded	Grid-connected or islanded

Table 4.2: Classification of grid-connected power converters rendered from [11]

Implementing the aforementioned control schemes is necessary in order to configure the microgrid system at the Smart grid laboratory. Chapter 5 explains the laboratory setup constructed by grid-following, grid-forming, and grid-supporting converters. The converter control of the laboratory converter units is described in the section 5.1.4, and the regulation systems of the laboratory units may differ from the control structures presented in this chapter. Testing the operation of the different power converters in the Smart Grid laboratory is one of the objective in this thesis.

Chapter 5

Laboratory Setup and Procedure

The laboratory setup implemented at the Smart Grid Laboratory at NTNU is presented in this chapter, together with the test procedure. The aim to utilize the digital ABB relays in the Smart Grid Laboratory for the first time, initialized this laboratory setup. Subsequently, further examination of the digital relay at the Smart Grid laboratory can be conducted in the future. The purpose of doing laboratory experiments is to examine an adaptive protection scheme of an IIDG-dominated microgrid in a practical way. Moreover, the influence of converter control schemes is investigated by conducting experiments with different control parameters. The outline of this chapter is the description of the laboratory setup in section 5.1, the parameter settings in section 5.2, and the approach in section 5.3.

5.1 Laboratory setup

The objective of the laboratory tests is to implement an adaptive protection scheme for a microgrid consisting of IIDG units and a load. In short, the protection scheme is based on adaptable protection functions where the breaker status of the STS indicates if the microgrid is grid-connected or islanded. Subsequently, the right protection function is selected based on the microgrid configuration, i.e., depending on the status of STS.

Figure 5.1 shows the examined microgrid system, which is based on the microgrid in figure 2.2 explained throughout this thesis.

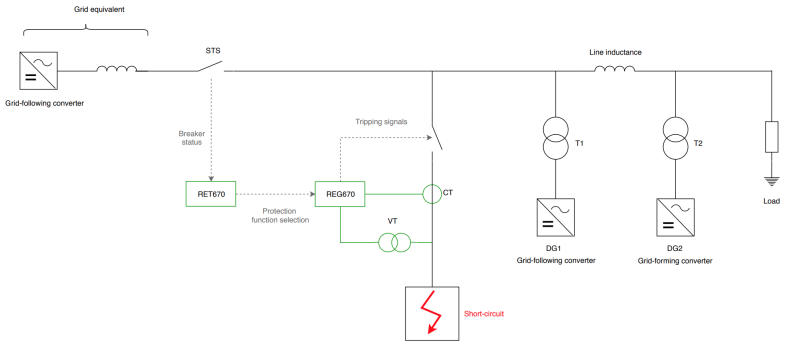

Figure 5.1: The investigated microgrid system

Testing of the microgrid system in figure 5.1 is done by implementing the setup illustrated in figure

5.2 based on the schematics of the Smart Grid Laboratory. The simplified hierarchical overview and the schematics of the Smart Grid Laboratory are illustrated in figure B.1 in appendix B.1. As illustrated in figure 5.2, the investigated microgrid system consists of three converters with their respective transformers. Converter B and converter D in figure 5.2 represent two DG units, whereas converter C represents the utility grid. The grid emulator supplies the DC voltage to the converters. Additionally, the system consists of a load, a short-circuit emulator, and line inductance. The instrument-list is given in table 5.1.

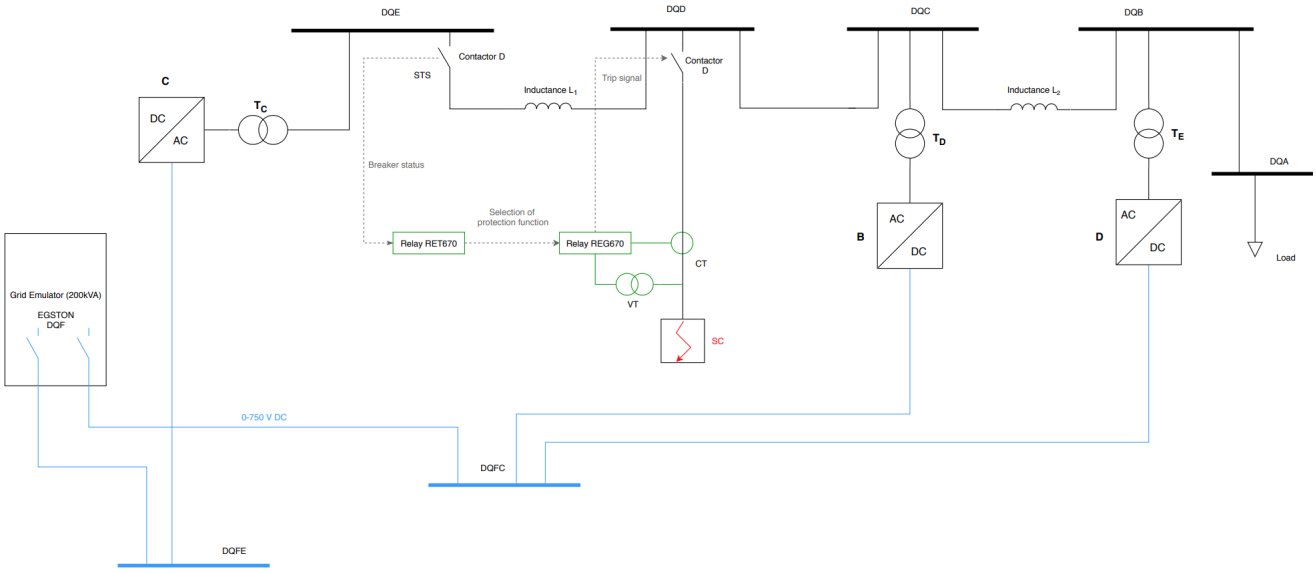

Figure 5.2: Illustration of the laboratory setup in the Smart Grid Laboratory at NTNU

Instrument type	Name in figure 5.2	Lab number
Grid emulator	EGSTON DQF	B03-0552
Bus-bar	DQE	B03-0538
Bus-bar	DQD	B03-0537
Bus-bar	DQC	B03-0536
Bus-bar	DQB	B03-0535
Bus-bar	DQA	B03-0534
Bus-bar	DQFE	B03-0545
Bus-bar	DQFC	B03-0543
Load	Load	K01-0505
Converter	B	B03-0432
Converter	C	B03-0430
Converter	D	B03-0431
Transformer	T_C	B01-1082
Transformer	T_D	B01-0991
Transformer	T_E	B01-0992
Inductor	L_1 (1mH)	K02-0134
Inductor	L_2 (1mH)	L-050082
Short-Circuit Emulator	SC	R04-0126
Short-Circuit Inductor	SC (3mH)	L-050085
Series Inductor	SC (1mH)	K02-0135
Transformer differential protection	RET670	-
Generator protection	REG670	-
Oscilloscope 1	-	G04-0373
Oscilloscope 2	-	G04-0372

Table 5.1: Instrument lists

5.1.1 Supply grid and model grid

The supply grid in the Smart Grid Laboratory has an AC voltage level equal to 400 V, and a maximum current rating of 225 A. As illustrated in figure B.1 in appendix B.1, the supply grid can be connected to several bus-bars, and subsequently feeds the model grid. The bus-bars are referred to as the model grid which has an AC voltage level equal to 400 V, with a maximum current rating of 125 A.

The supply grid is omitted in this laboratory setup, and the grid-following converter C in figure 5.2 represents the main utility grid. This adjustment is necessary because converter D in figure 5.2 is a grid-forming converter. Accordingly, converter D is not PLL-based and provides the magnitude and frequency reference of the voltage for the rest of the system. As elaborated in section 4.3.2, the grid-forming converter is applied in islanded microgrids, so the system remains operating when the stiff utility grid is disconnected. During grid-connected microgrids, however, the grid-forming converter and the supply grid will both provide references and thereby collide. Hence, the supply grid has to be represented by a grid-following converter as a result of converter D forming the amplitude and frequency of the voltage.

The microgrid configuration with a grid-forming converter is artificial because currently, the converters connecting renewables into the power system are mainly controlled as current sources. In order to protect electrical systems against potential damages as well as avoiding any risk to maintenance personnel, it is not currently allowed to form energized islands when the main power network experiences

an outage [48]. So the creation of islanded microgrids is not employed, and the grid-forming capability is not required as microgrids are forced to shut down during blackouts. Subsequently, the energy supply to consumers is interrupted because local generators could in fact feed local load [48]. With the the time available it was not considered to considered to implement adaptive control strategy from grid-following to grid-forming during the island transition. Consequently, converter D is implemented with the grid-forming control strategy throughout the tests and the supply grid is omitted.

As depicted in figure 5.2, bus-bars DQE, DQD, DQC, DQB, and DQA are of interest. The grid-following converter C, which represents the utility grid, is connected to the DQE bus-bar through a transformer. Moreover, the other grid-following converter (converter B) is connected to bus-bar DQC, whereas the grid-forming converter (converter D) is connected to bus-bar DQB through a transformer. Figure 5.3 is a picture of the DQC bus-bar.

Figure 5.3: Picture of the DQC bus-bar

5.1.2 DC grid

Egston provides the DC supply to the VSCs at the DQFC and DQFE DC bus-bars. Figure 5.4 illustrates the Egston grid emulator, whereas the DQFC bus-bar is showed in figure 5.5. Egston is a grid emulator which in practice is a high bandwidth converter able to replicate the dynamics of a grid. In this laboratory experiment, Egston is utilized as a controlled DC source which can supply up to 700 V DC. As depicted in figure 5.2, converter C is connected to bus-bar DQFE, while converter B and converter D are connected to bus-bar DQFC.

Figure 5.4: Grid emulator

Figure 5.5: Bus-bar DQFC

5.1.3 Converter Interface

The 60 kVA laboratory converter unit can be utilized for various applications, and it is dimensioned for:

- Rated power: 60 kVA.

- DC voltage: 0-750 V.
- Main supply voltage: 0-460 V AC.
- Output current: 100 A RMS.
- Adjustable current trip level: 0-800 A peak.
- Switching frequency: 0-8 kHz.
- LCL-filter: 500 μH, 50 μF, 200 μH.

Figure 5.6 is a picture of the box containing the 60 kVA laboratory converter unit, while the integrated grid interface is shown in figure 5.7(a). The converter and filter can be configured in different ways, and the active rectifier configuration is utilized for the grid-connected purpose in this laboratory experiment. The active rectifier configuration of the converter core module, LCL-filter, and the switchgear is illustrated in figure 5.7(b). The LCL-filter is connected to the transistor bridgeleg for the use as a grid-connected converter [37]. Each inverter module leg consists of two IGBTs of the type SKM 400GB126D which have a maximum voltage tolerance of 1200 V, and the maximum switching frequency is restricted to 6 kHz [37]. The LCL-filter components are divided into the converter-side filter inductor, $L_{filter1}$, the capacitor (C_{filter}), and the grid-side filter inductor ($L_{filter2}$).

Figure 5.6: Picture of the VSC laboratory unit

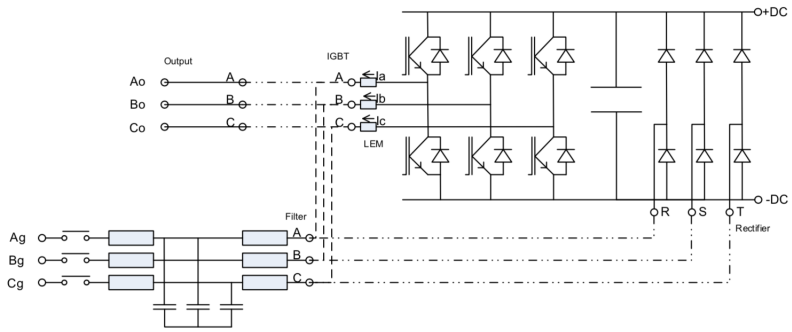

((a)) Power circuit of the converter with alternative configurations [37]

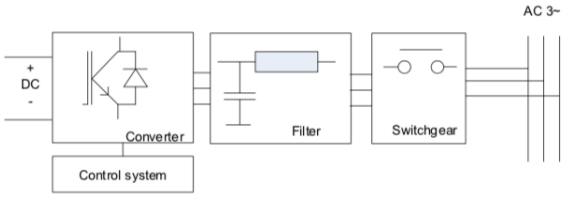

((b)) Grid-connected converter with the active rectifier configuration [37]

Figure 5.7: Laboratory converter unit

The main parts of the 60 kVA VSC are:

- Converter core module (Semikron SEMIKUBE) which consists of IGBT bridges, DC-link capacitor, drivers, heatsink, and diode rectifier [37]).
- LCL filter with the values: 500 μH, 50 μF (Y), 200 μH, respectively.
- Switchgear (contactor, DC link charging circuit, discharging circuit).
- Control system where the control electronics is not part of the converter itself, but is mounted in the top of the converter cabinet as a separate unit [37].

5.1.4 Converter control

As elaborated, the converters facilitate the energy exchange between the DC system and the AC system and subsequently control the power output from DG sources. The behavior of microgrids with converter-connected DG units is therefore affected by the implemented control system. Consequently, the control scheme is a crucial factor regarding network protection and stability issues. The control system is mounted in the top of the converter cabinet as a separate unit for the 60 kVA laboratory converters. The explanation of the laboratory converter control is solely based on reference [38], which is the documentation of the converters implemented at the Smart Grid laboratory. This project memo provides a comprehensive description of the control system for the three-phase grid-connected active rectifier converter. However, the explanations of the power flow control of converters in chapter 4 are an indispensable tool in order to understand the practical implementation of the laboratory converters. Section 5.1.4 briefly summarizes how the laboratory converters relate to the theoretical concepts regarding the classification of the power converters.

The control system runs on a Xilinx Zynq 7030 based processor system. Time critical parts are implemented as FPGA blocks, while the rest is implemented as processor software routines [38]. In

this laboratory setup, the converters are controlled by the built-in control to allocate the control parameters. The user interface is based on the LCD display and the buttons in figure 5.8. The built-in control is enabled when the control signal source is assigned to "menu". The converter can also be controlled remotely via a CAN bus, or via a high-speed fiber link using OPAL-RT [38].

Figure 5.8: Picture of the local display of control signals

While the converter is not operation, the user can set parameter values and control signals. The LCD display shows an actual value list and an input list, as well as status code, power code, and driver code when the converter is operation. The flexibility of the control system and the wide range of operational possibilities are indicated by the amount available of control signal lists. Appendix B.2 lists all available parameter value and the control signal lists. Moreover, table B.1 shows some of the assigned converter control parameters within the control signal lists. In the first list, Control Signal Parameters, the built-in control is selected.

Figure 5.9 shows the signal flow of the converter control system.

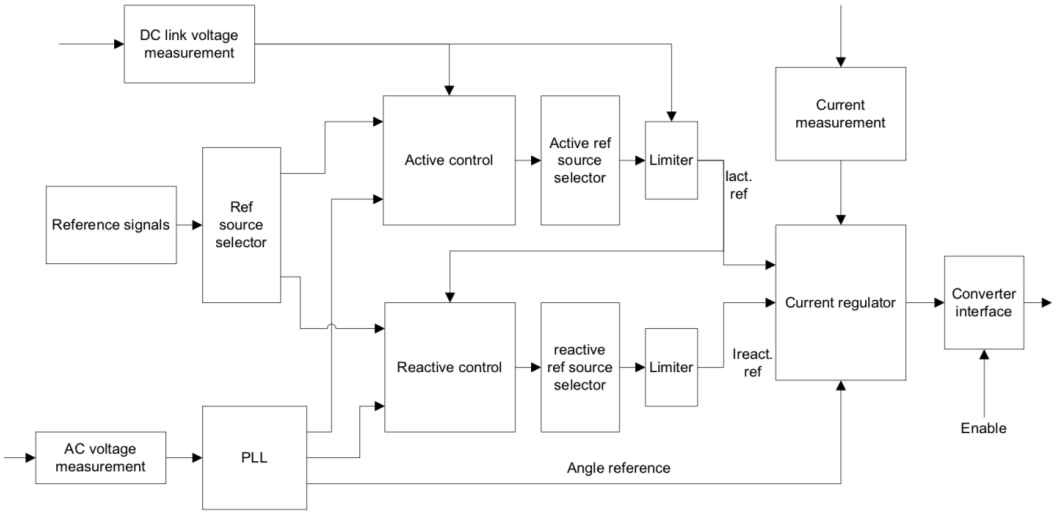

Figure 5.9: Overview of the signal flow in the control system of the laboratory converter [38, p.15]

The converter system has three main signal paths:

1. Active control
2. Reactive control
3. Angle reference

In this vector oriented converter control system, the angle reference is a fundamental signal because it defines the direction of the active and reactive currents vectors and the voltages vectors [38]. As depicted in figure 5.9, the angle reference is obtained from the AC voltage measurement and the PLL block. The angle reference is subsequently sent to the active and reactive control blocks, and to the current regulator. The PLL utilized by the control system of the laboratory converter unit is explained in section 5.1.4.

The main measurement signals; AC currents, DC link voltages, and AC voltages, together with the reference signals, are required by the control system. Most signals are scaled in a pu system, however, some are scaled in real units. The pu values are defined as 1000 as 1 pu [38]. In the laboratory tests, the reference signals are selected in the LCD because the converters are controlled manually by the built-in control. The current references are obtained based on selected active and reactive control, and sent to the current regulator. The active and reactive control methods are explained in section 5.1.4.

PI regulators

The PI regulator is applied in the active and reactive control and the current regulator. Figure 5.10 shows the structure of the PI regulator.

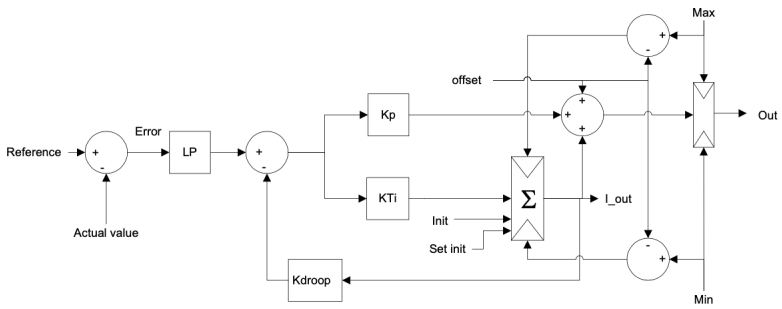

Figure 5.10: Structure of the PI regulator [38, p.19]

The actual value is subtracted from the reference value in order to obtain the error, which is subsequently low-pass filtered. In other words, the error signal in figure 5.10 is the difference between the reference and actual value. The LPF smooths out transients from the error signal and reduces the amount of noise in the output signals from the regulator [38]. As illustrated, the error is sent to the proportional and integral block in separate signal paths. However, the droop signal (K_{droop} in figure 5.10) is first subtracted from the input error signal fed to the proportional and integral block. Consequently, it is important to emphasize that the droop control is implemented in the PI regulator for the laboratory converter unit. Hence, the separate external droop control loop e.g., illustrated in figure 4.19, is eliminated. In contrast, the droop is applied in the PI regulator and thereby limits the proportional and integrator gains in the regulator. Consequently, the time delays associated with the separate droop control loop are avoided. Moreover, the droop feedback signal is obtained from the integrator output instead of the PI regulator output in figure 5.10 in order to avoid any instability at high droop gain settings [38]. The droop mechanism thereby limits the integrator action. Moreover, the droop mechanism gives a finite DC gain which transforms the integrator into a LPF. The DC gain

of the PI regulator is determined by the value of the droop feedback gain, and the proportional gain has zero effect at DC. Additionally, it is important to emphasize that the *Kdroop* factor is zero in the PI regulator applied to the current regulation system.

The error signal in the proportional path is multiplied with the proportional gain, K_P, and the equation for the P-term is: $K_p \cdot error$. In the integrator path, the error signal is multiplied with KTi, which is a factor derived from the proportional gain, the integrator time constant, and the sample rate [38]. The equation for the I-term is $\frac{K_P}{T_i} \int_0^t error\ dt$. The output signals of the proportional and integrator are summarized, and the result is limited by the maximum and minimum values. These values are based on the allowed signal range output [38]. For example, the active and reactive current limits are set in list nr. 20 called Static control signal (see appendix B.2). Additionally, an output offset signal can be added to the output signal as a setpoint for the droop action, which shifts the output signal away from zero when the error between the reference and actual value is zero [38].

By setting the time constant T_i to zero, the integrator action is disabled, which transforms the regulator into a pure proportional regulator [38]. Hence, converter D in this laboratory setup is configured as a grid-forming converter by disabling the integrator action in the PI controller for the current regulation system. Furthermore, the current reference value in figure 5.10 is set to zero, while the proportional gain parameter, I reg K_P, is changed during different test cases. So, the droop effect in section 5.3 is obtained by changing K_p in the current regulator for converter D because the droop control, Kdroop, in the P-regulator is disabled due to the zero integrator action. The proportional gain, K_p, thus provides the droop effect when the PI-regulator is a proportional regulator where the integrator action is disabled. It is important to emphasize that the proportional gain, K_P, is referred to as the proportional gain in the current regulator for the grid-forming converter D, I reg K_P, throughout section 5.3.

The PI parameter inputs for the current regulator are selected in the forth control signal list in appendix B.2. Moreover, the PI parameter inputs for the AC voltage regulator are assigned in list number 9, whereas the power regulator parameters are selected in list number 11 in appendix B.2.

Active and reactive control

The active control mode and reactive control mode are selected in the operation mode parameter list, i.e., the second list in appendix B.2. The active current reference is obtained in four different ways. The first method is direct current control where the active current is controlled directly. The second method includes a DC-link voltage regulator where the converter controls the DC link voltage. Frequency control is the third option where the active current is selected based on the AC frequency. The fourth method is active power control where a PI regulator keeps the active power is constant, following a active power reference [38]. A converter with active power control may act as a negative resistance seen from the grid since a reduction in voltage results in an increase in current [38].

The reactive current reference can also be selected in four ways; direct current control, proportional to active current reference, AC voltage regulator, and reactive power control [37]. The first method obtains the current reference by directly controlling the reactive current. Moreover, the second method determines a reactive current reference, which is proportional to the active current reference in order to achieve a constant phase angle operation. Regarding the AC voltage regulator, the converter tries to keep the AC voltage stable by adjusting the reactive current reference. Lastly, a PI regulator keeps the reactive power constant, following a reactive power reference, regarding the reactive power control. A converter with reactive power control may act as a negative dynamic reactance seen from the grid

since a reduction in voltage results in an increase in current [38].

The power is calculated in calculated in the same way as the power controller in equation 4.11. The FPGA hardware calculates the active power, while the reactive power is calculated by software. The active and reactive reference signals from the reference selector are kept within an allowed range by a set of limiters. In other words, the active and reactive references are restricted based on their respective limit values, which are determined by independent control signals. The user specifies the reference values in the LCD when the converter is operating.

Table 5.2 lists the active and reactive control sources utilized in this laboratory experiment to configure different control strategies.

Control strategy	Active control mode	Reactive control mode	VOC operation mode
Grid-following converter	P reg	Q reg = 0	PLL
Grid-supporting converter	P reg	U AC reg	PLL
Grid-forming converter	Iact	Ireact	Open-loop

Table 5.2: Active and reactive control determining the control strategies of the converter

Phase-locked loop

The PLL structure is illustrated in figure 5.11 where the time critical components in the shaded area are implemented in FPGA. As elaborated, the PLL generates the angle reference from the grid voltage, and the angle reference is a fundamental signal in this vector oriented converter control system [38]. The angle generator (VCO) is an integrator implemented in the FPGA which converts a frequency signal to a rotating angle [38]. The VCO can also be implemented as the open loop in figure 5.12. Both operation modes of the VCO are applied to the converters utilized the laboratory tests.

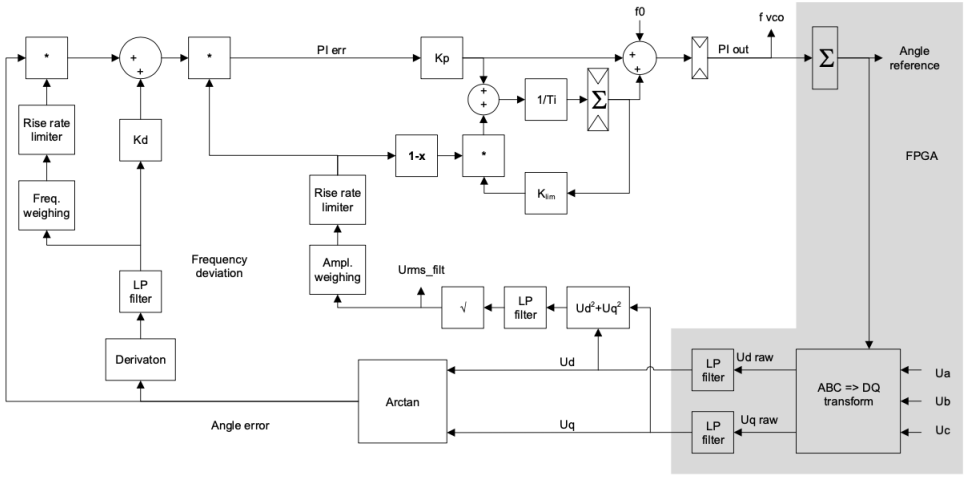

Figure 5.11: Structure of the PLL [38, p.26]

The PLL in figure 5.11 is quite complex because it contains features that are not common in a standard PLL [38]. Consequently, this section only explains the basic functioning. The reader is referred to the documentation of the converter control system in [38] for detailed explanations. As illustrated in figure 5.11, the measured grid voltages are transformed to voltages in the *dq*-frame by a Park transformation.

The *dq* voltages are filtered by a set of LPFs in FPGA in order to remove most of the high frequency components in the input signals [38]. The angle error signal, i.e., the deviation between the reference angle and the phase angle, is provided by the Arcus Tangens function in figure 5.11. Subsequently, the angle error signal is fed to the PI regulator controlling the VCO frequency. The PI regulator changes the frequency until the angle error is zero. Moreover, the angle error signal is fed to a derivator in an additional signal path. The angle error signal is subsequently low-pass filtered in order to obtain the frequency deviation signal. Subsequently, the frequency error is added to the error input signal of the PI regulator [38]. This derivative effect improves the phase margin in the feedback loop when the PLL is in a locked state. However, when the PLL is out of lock, the frequency deviation signal gives a steady error signal that guides the PLL frequency towards the right AC frequency [38].

VCO open loop mode

On the contrary to the PLL with a PI regulator in figure 5.11, the VCO is governed by a frequency reference signal during its open-loop mode as illustrated in figure 5.12.

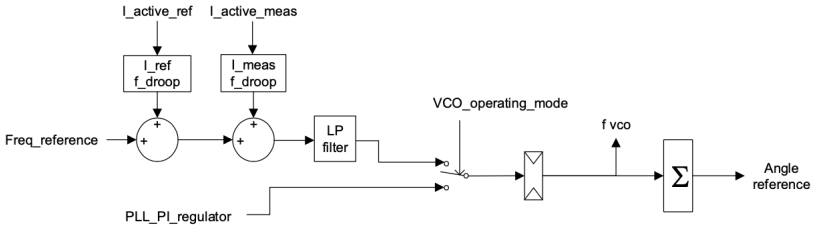

Figure 5.12: VCO [38, p.28]

The measured active current and the resulting active current reference can both provide frequency droop [38]. Moreover, the frequency droop signal passes through a LPF that emulates the effect of inertia. The grid-forming converter D is implemented with an open loop mode of the VCO, where the AC rated frequency is selected in the VCO parameter list (list nr. 12 in appendix B.2).

Current regulator

The current regulator represents the inner loop of the control system in figure 5.9. A large part of the current controller is implemented as FPGA IP modules and the high FGPA sampling rate facilities the modules to work continuously. Hence, the regulator output signal will vary instantaneously with the current error [38]. There are three options available for current regulation; the phase current PI regulator, the DQ (active and reactive) current regulator, and the DQ hysteresis regulator [38]. Figure 5.13 shows the current regulator system, where the aforementioned regulation options are included. In the laboratory tests, the current regulation is performed by the PI regulator in the *dq*-frame. Consequently, the DQ current regulator with PWM is illustrated in figure 5.14.

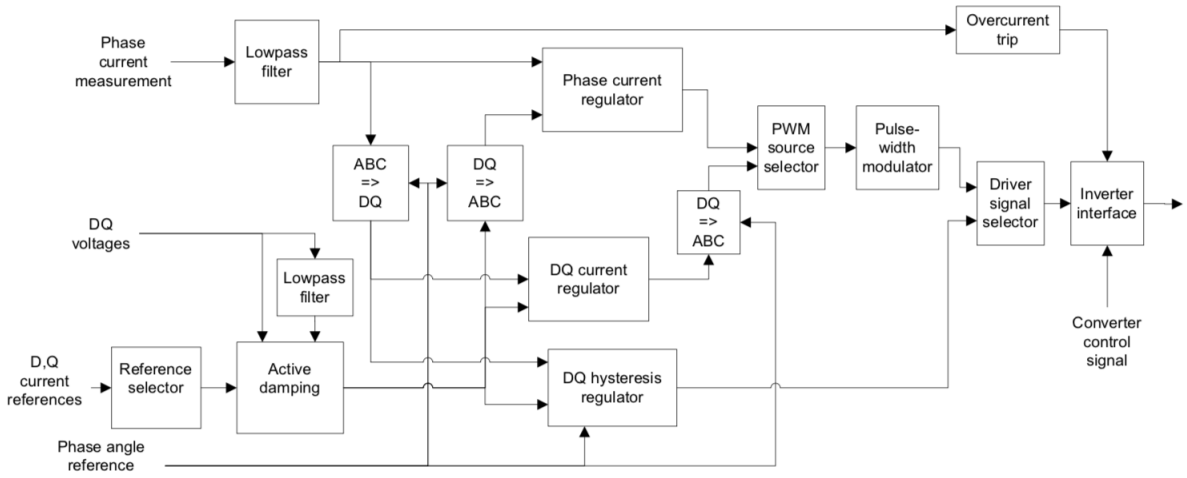

Figure 5.13: Current regulators [38, p.30]

The current regulator receives the active current and reactive current reference signals, denoted as "D, Q current references" in figure 5.13. Additionally, the phase angle reference signal from the VCO is needed to govern the Park transformations. Moreover, an active damping regulator is necessary due to the poorly damped resonance circuit introduced by the LCL-filter. The resonant circuit might cause severe oscillation triggered by transient events or signal components at resonance frequency [38]. The PWM module in figure 5.13 is based on the triangle carrier wave generator explained in section 2.4.4 and a set of compensators [38]. The triangle wave has a fixed amplitude independent from the switching frequency due to the independent amplitude and frequency control.

Figure 5.14 illustrates the DQ PI current regulator utilized in the laboratory experiment. Three individual PI regulators construct the three-phase current regulator. The measured phase currents are transformed into input signals in the dq-frame. In contrast, the output voltage signals are transformed into phase voltage references in the natural reference frame, U_{abc}, which are fed to the PWM module.

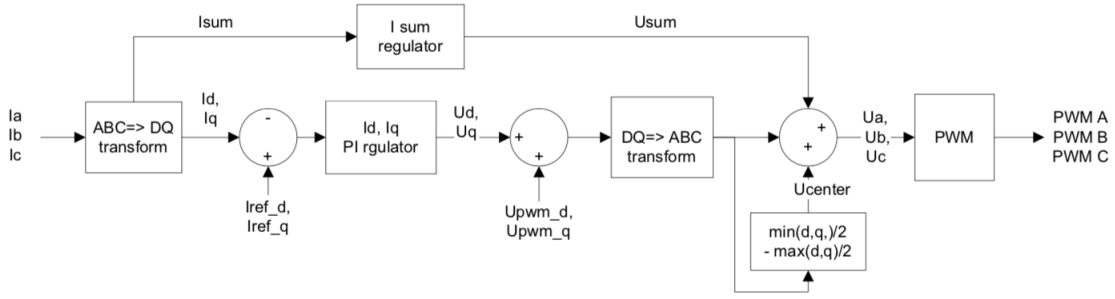

Figure 5.14: DQ PI current regulator [38, p.33]

The d- and q-components of the voltage reference are added to the regulator output signals to give a direct output voltage signal when the PIs in the current regulator are implemented as a P-regulators [38]. Hence, converter D is configured as a grid-forming converter by assigning the U_{pwm_d} value

in figure 5.14 to the preferred voltage. U_{pwm_d} is called "U PWM act ref" in the LCD display. Consequently, the grid-forming converter establishes the selected voltage reference for the rest of the system. As elaborated, the integrator gain in the PI regulators applied to the current regulation system is deactivated by setting the integrator time constant to zero. The I reg T_i parameter is found in the fourth control signal list in appendix B.2. In this operation with P-regulators, the K_p gain works as a series resistance.

Relation to the classification of the power converters

Figure 5.15 illustrates the sequence of the working principle of the grid-following configuration of the laboratory converter unit.

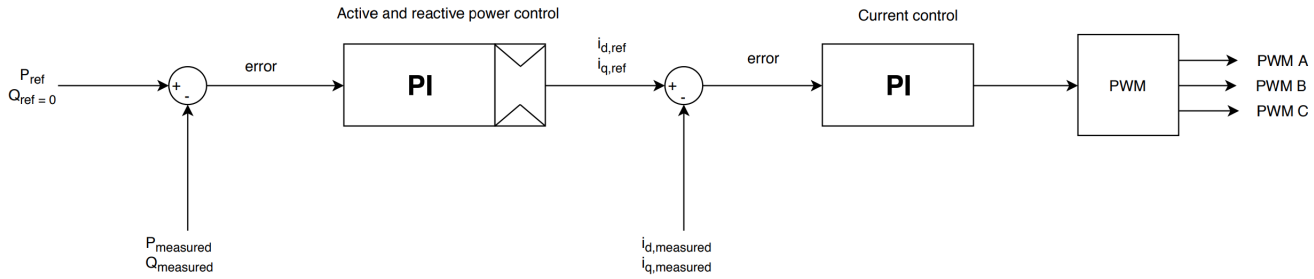

Figure 5.15: Simplified representation of the grid-following configuration of the laboratory converter

This configuration is achieved by selecting the active and reactive control mode in the operation mode parameters list to respectively active and reactive power control. As summarized in table 5.2, the PLL operating mode of the VCO is selected. The implementation of the grid-following laboratory converter consists of the same control loops in figure 4.13 in section 4.3.1

Figure 5.16 illustrates the sequence of the working principle of the grid-forming configuration of the laboratory converter unit.

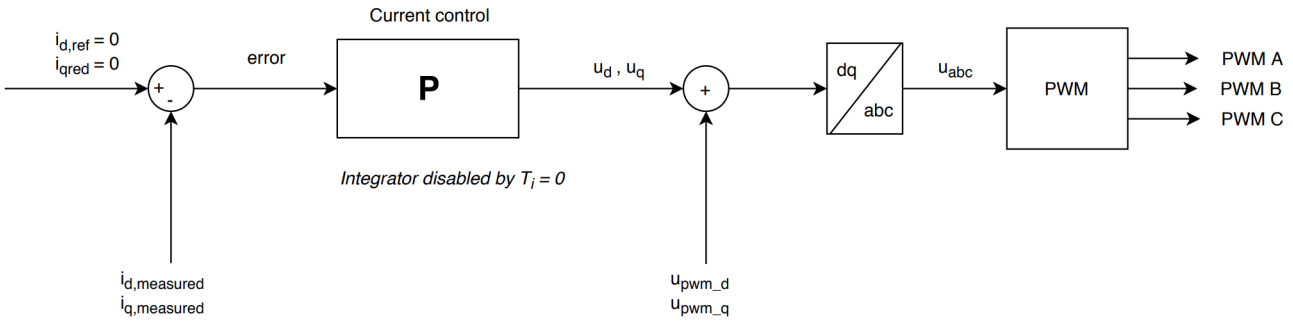

Figure 5.16: Simplified representation of the grid-forming configuration of the laboratory converter

This configuration is achieved by selecting the active and reactive control mode in the operation mode parameters list to respectively direct active current control and direct reactive current control. As summarized in table 5.2, the open operating mode of the VCO is selected. Compared to the grid-forming

converter in figure 4.17 in section 4.3.2, the configuration of the grid-forming laboratory converter differs. First, the voltage control loop is omitted, so the laboratory grid-forming converter solely consists of the current regulator. Consequently, this converter does not contribute with voltage regulation. Moreover, the PI-regulator in the current control loop is changed to a proportional regulator by disabling the integrator loop. As a result, the grid-forming converter implemented at the laboratory is very straightforward and only sets the microgrid nominal voltage and frequency without any regulation support.

Figure 5.17 illustrates the sequence of the working principle of the grid-supporting configuration of the laboratory converter unit.

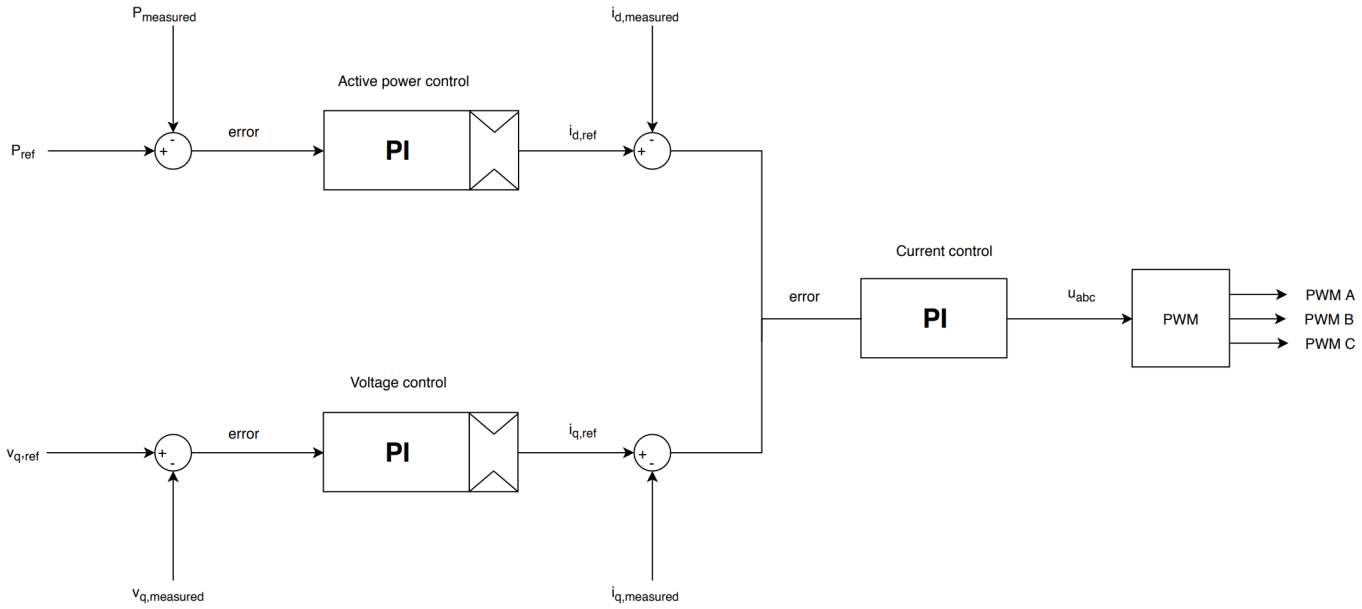

Figure 5.17: Simplified representation of the grid-supporting configuration of the laboratory converter

This configuration is achieved by selecting the active and reactive control mode in the operation mode parameters list to respectively active power control and AC voltage regulator. As summarized in table 5.2, the PLL operating mode of the VCO is selected. Compared to the the grid-supporting converter in figure 4.19 in section 4.3.3, the configuration of the grid-supporting laboratory converter is quite similar, but the outer droop control loop is assigned to the PI regulators.

Table 5.3 lists the crucial control parameters differentiating the principles of the grid-following converter, grid-forming converter, and the grid-supporting converter. Additional control signal settings in the built-in control are given in table B.1 in appendix B.2.

Parameters	**Grid-following**	**Grid-supporting**	**Grid-forming**
Active control mode	P reg	P reg	Iact
Reactive control mode	Q reg	U AC reg	Ireact
VOC operation mode	PLL	PLL	Open mode
P act ref [pu]	Varied	Varied	Not relevant
U AC ref [V AC]	Not relevant	400	Varied
U PWM act ref	Not relevant	Not relevant	Varied
I reg Kp [%]	400	400	Varied
I reg Ti [μs]	1000	1000	0

Table 5.3: Converter control parameters of special interest in order to obtain grid-following and grid-forming converters

5.1.5 Protection relays

The microgrid protection system consists of two ABB digital relays from the Relion 670 series. More specifically, one transformer differential protection relay called *RET670* and one generator protection relay referred to as *REG670*. The REG670 and RET670 relays utilized in the laboratory experiment are mounted in a mobile rack, which is illustrated in figure 5.18.

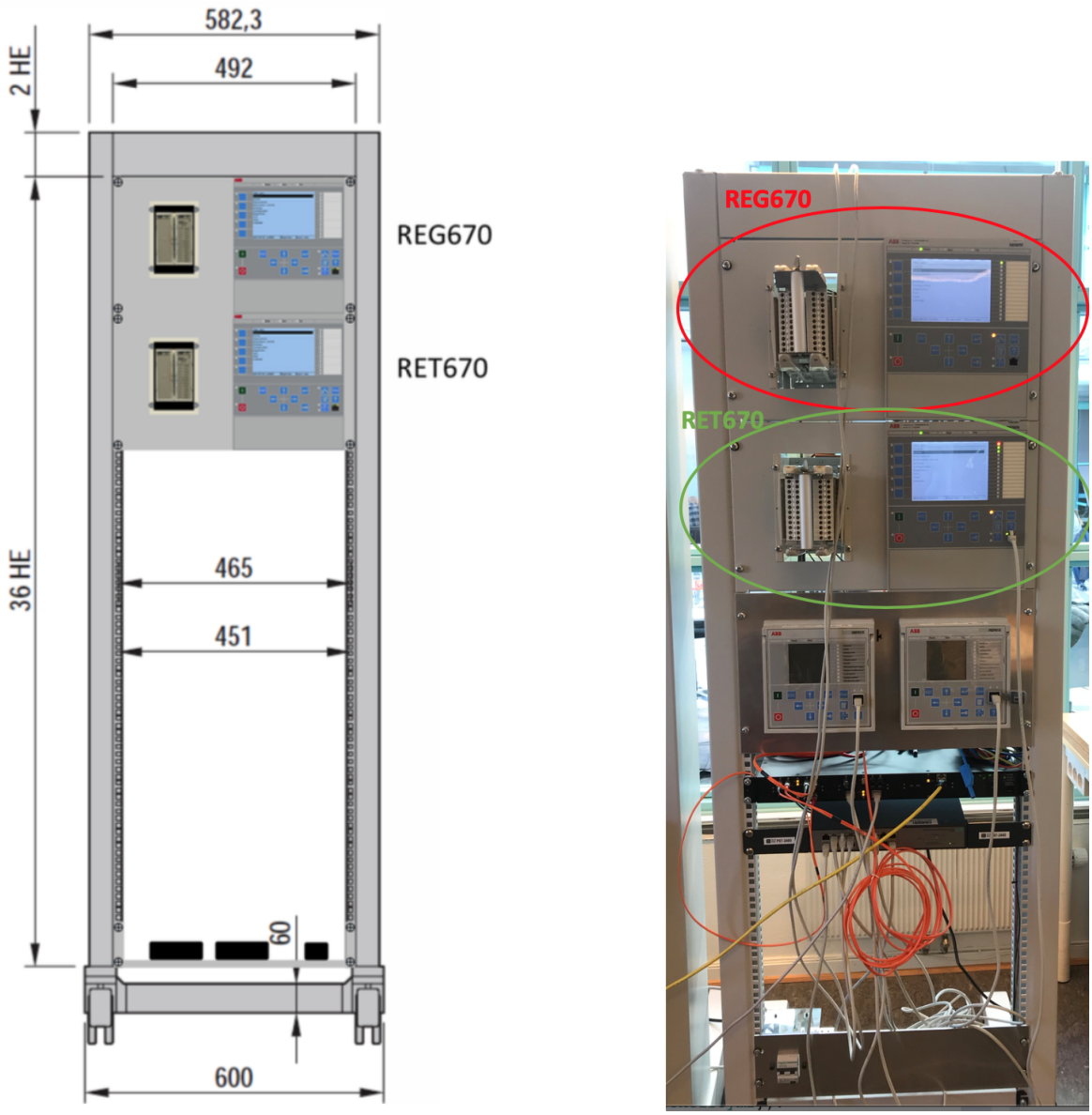

((a)) Illustration of REG670 and REG670 relays in the mobile rack

((b)) Picture of the mobile rack

Figure 5.18: Mobile rack mounted with the REG670 and RET670 relays

Moreover, the backside of the relays is displayed in figure 5.19(a), while figure 5.19(b) illustrates the card slot for the Relion 670 relays. The following modules of the card slot are relevant [17]:

1. X11 - Power Supply Module - Connection of 48 V DC supply.
2. X31/X32 - Binary Input Module (BIM) - input of binary signals
3. X41/X42 - Binary Output Module (BOM) - output of binary signals
4. X401 - Transformer Input Module (TRM) - input of currents and voltages

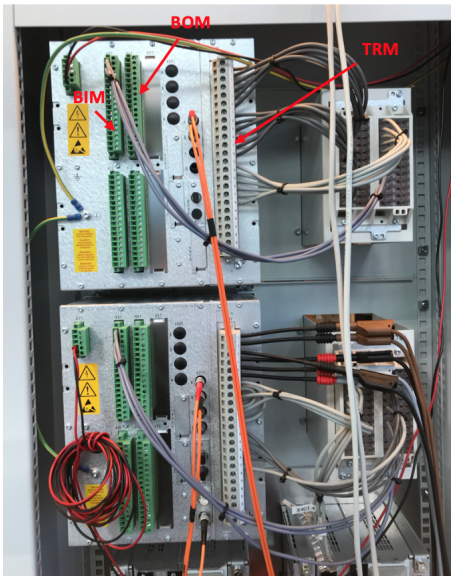

((a)) Backside of the relays

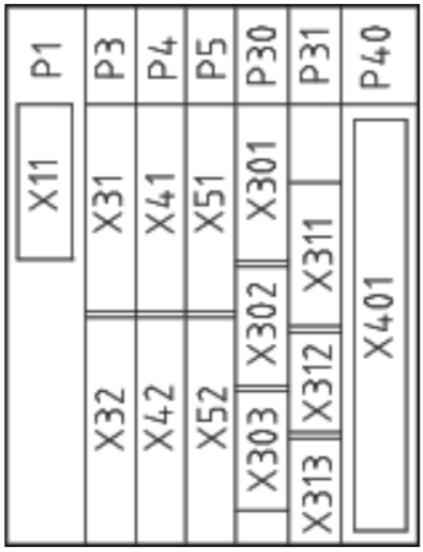

((b)) Card Slots - ABB Relion 670

Figure 5.19: ?

The transformer input modules (X401), i.e., current and voltage measurements, are the white terminals located on the right side of the relay in figure 5.18(a). Furthermore, the green terminal blocks are the binary input modules and the binary output modules (X31/X31 and X41/X42, respectively). The BOM module is located at the right-hand side, whereas the BIM module is on the left.

Protection application configuration

Figure 5.20 shows the configuration of the RET670 digital relay. The digital input is a binary signal, which indicates the position of the contact, i.e., if the CB is open or closed. The inputs are DC voltage signals, with a low/high(0/1) value, indicating open/closed [17]. An applied voltage in the range of e.g., 48-60 V DC will be interpreted by a corresponding transistor in the relay as high (1), while no applied voltage will equal low (0) [1]. The binary input value is processed in the apparatus control function blocks with a fixed time interval giving the sampling rate of the value. Subsequently, the signal is processed in the evaluation of position block. The position indication is communicated between the relays through GOOSE communication, and the data set entries for the GOOSE communication is:

- LD0.SXCBR1.pos.q (ST)
- LD0.SXBR1.pos.stval (ST)

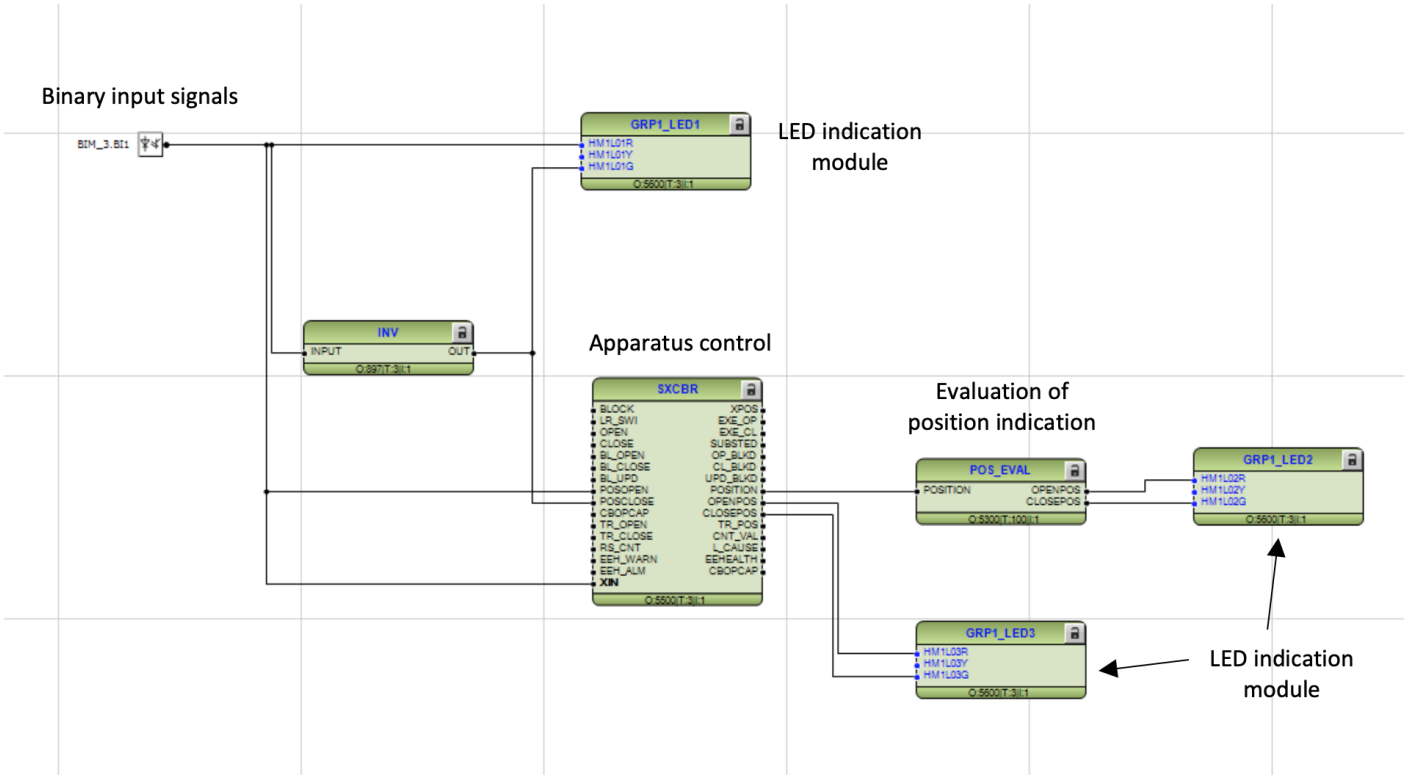

Figure 5.20: Signal and function blocks for detection of breaker status in ABB RET670 Relay

As illustrated in figure 5.20, the signals are also connected to other function blocks (GRP1_LED) which control the LEDs on the Human-machine interface (HMI). Table 5.4 specifies the color indication, where the LED lights are green if the microgrid is grid-connected, while red lights indicate an islanded microgrid.

RET670	**Green**	**Red**
LED1	Conductor D on bus-bar DQE closed	Conductor D on bus-bar DQE open
LED2	Conductor D on bus-bar DQE closed	Conductor D on bus-bar DQE open
LED3	Conductor D on bus-bar DQE closed	Conductor D on bus-bar DQE open

Table 5.4: LED indication for relay RET670

Figure 5.21 shows the configuration of the REG670 digital relay.

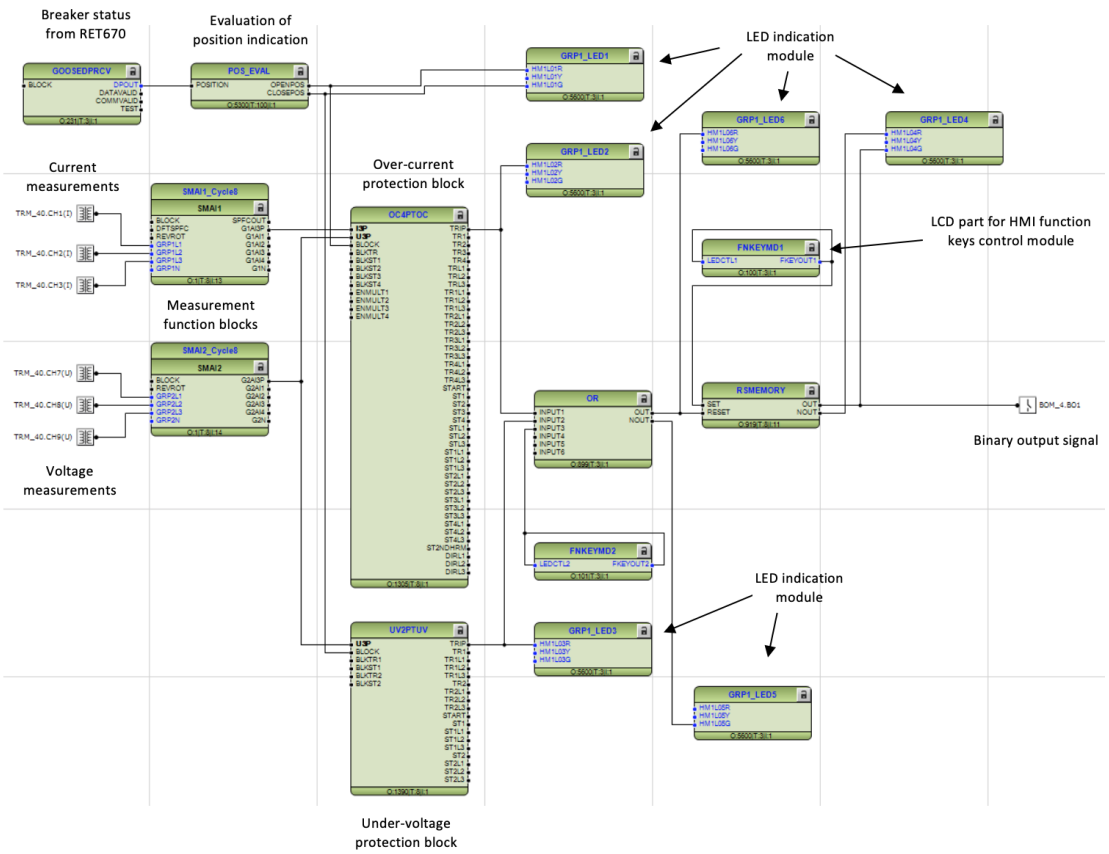

Figure 5.21: Signal and function blocks in ABB REG670 Relay for receiving the breaker status from RET670, selecting the right protection function, and sending a trip signal if the threshold value is exceeded

REG670 relay continuously processes the GOOSE message from the RET670 relay to check whether the STS is open or closed. The GOOSE function block receives the GOOSE message, and the position is subsequently evaluated. Next, the right protection function is selected based on the received GOOSE message, i.e., if the microgrid is grid-connected or islanded. As illustrated in figure 5.21, the under-voltage protective function is blocked if the contactor is closed, whereas the over-current protective function is blocked if the contactor is open. Besides the block signals, the protective function blocks additionally receive voltage and current measurements. Hence, the REG670 relay measures the currents and voltages with the measurement function blocks in figure 5.21). The input values are processed with a fixed time interval, and the protective function blocks will thereby compare the measured values with the respective threshold values. The protective functions contain advanced algorithms designed to operate with the highest possible speed and reliability [17]. Subsequently, a binary output signal is sent to remotely control contactor D on the DQD bus-bar in figure 5.2. The REG670 relay sends a binary output signal (1) if the measured value exceeds the embedded threshold value, whereas the binary out is (0) if the measured value is below the threshold limit.

The relay is configured with global base values of 125 A and 400 V. The threshold value for the over-current relay is 120 % of the base current value due to the $I > 1.2 \cdot I_n$ over-current protective setting in [14]. Moreover, the under-voltage relay is configured with a threshold value equal to 85% of the base voltage value. According to [46], all DG units that are not transiently stable should be

disconnected within 0.2 s for all voltages below 85%.

The control system of the laboratory converter has several protection functions in order to shut off the converter when the threshold values are exceeded. Most of the protection functions are handled by the software module, while the over-current protection function is implemented in hardware, by IP modules in the FPGA, so it operates quickly independent of the software execution [38]. In order words, the internal converter protection of the laboratory converters operates extremely fast to protect the power electronics. Consequently, both the over-current and under-voltage protective relays are implemented with zero time delays in order to obtain an immediate protective response. The define time characteristic of the over-current relay is explained for a given time delay t_D in section 3.4.1 with figure 3.4. So, immediately after the current or voltage exceeds its pickup value, the over-current or under-voltage relay trips the circuit breaker. However, the internal converter protection might disconnect the converter before the protection relay detects and isolates the fault. This is illustrated in section 6.3.1, and specific converter settings to avoid the immediate disconnection of the converters are subsequently evaluated in section 6.3.

The REG670 relay is also configured with local HMI functions. The FNKEY function blocks are utilized for parameter settings on the HMI. As a result, it is possible to control contactor D on busbar DQD through the HMI. Figure 5.22 illustrates the parameter setting functions on the HMI. The contactor is closed by activating the first FNKEY function block by local control on the LCD display. In contrast, the contactor is opened by activating the second FNKEY function block by local control on the LCD display. The local closing of contactor D is indicated with a green light on LED4 on the HMI, whereas the opening of the contactor is indicated with a red light.

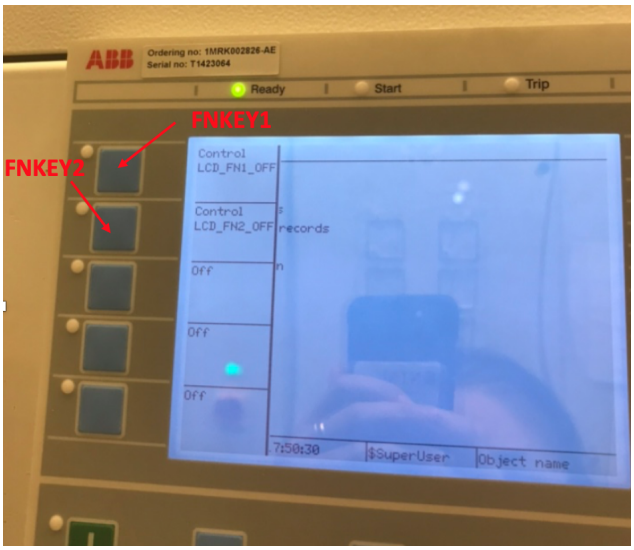

Figure 5.22: Local control of the contactor

As illustrated in figure 5.21, the signals are also connected to other function blocks (GRP1_LED) which control the LEDs on the HMI. Table 5.5 specifies the color indication.

RET670	Green	Red
LED1	Conductor D on bus-bar DQE closed	Conductor D on bus-bar DQE open
LED2	-	Overcurrent relay tripped
LED3	-	Undervoltage relay tripped
LED4	Contactor D on bus-bar DQD is closed	Contactor D on bus-bar DQD is open

Table 5.5: LED indication for relay REG670

To summarize, relay RET670 processes information about the open/closed status of the CB as a binary input, while relay REG670 receives the breaker status from relay RET670 as a GOOSE message. Subsequently, relay REG670 switches between protection functions based on the microgrid configuration. If a fault is detected, the REG670 sends a tripping signal to contactor D on bus-bar DQD.

5.1.6 Signal transfer

In the laboratory setup, bus-bar DQE is connected to bus-bar DQD through a line impedance, hence the bus-bars are connected via contactor D in reference to figure B.2. The RET670 protection relay receives the binary input from multiplug -X5 at pin 12. Figure 5.23(a) illustrates the multiplugs for external control of the DQE cabinet. Multiplug -X5, pins 01 and 02, provide a +24 V DC auxiliary voltage, which is utilized by the protection relay in order to access the open/closed status of contactor D. However, the digital relay RET670 interpreters DC voltage signals above 48 V DC as high (1). An additional DC voltage source is thus connected in series to achieve a 48 V DC voltage signal which is subsequently translated to a binary input signal. The implementation is illustrated in figure 5.23(b).

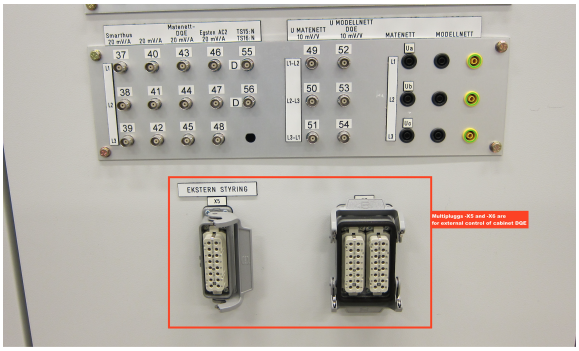

((a)) Measurements and external control of the DQE cabinet

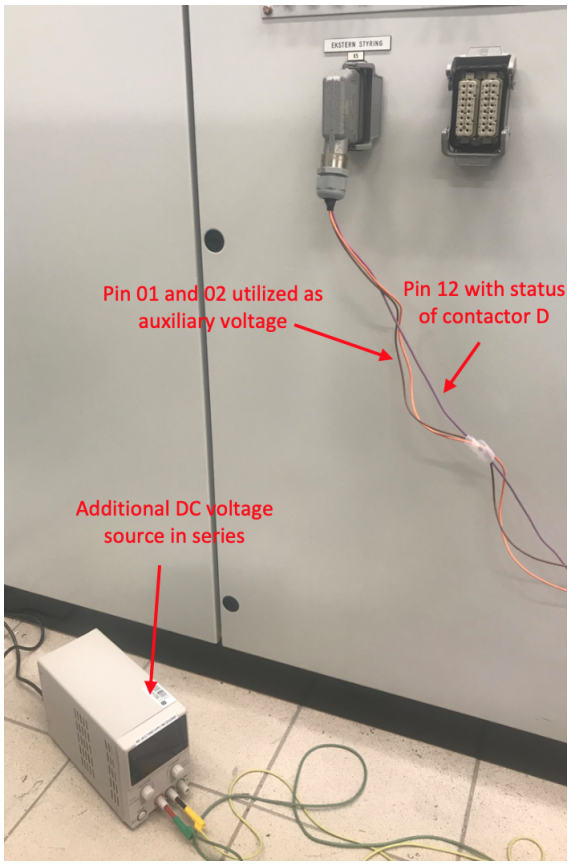

((b)) Implementation in order to access the status of contactor D at bus-bar DQE

Figure 5.23: External control of the DQE cabinet

Next, the REG670 relay selects the correct protection function based on the GOOSE message from RET670. If the fault currents or voltages exceed the threshold protection settings, the REG670 relay will send a trip to the contactor between the DQD bus-bar and the DQA bus-bar. In reference to figure B.3, the short-circuit is disconnected by opening contactor D on the DQD bus-bar, and the microgrid can thereby operate as an active island. The external control of contactor D is accessed via multiplug -X5 at the DQD bus-bar, at pin 06, which is shown in figure 5.24. Remote control of contactor D (feeder DQD $\rightarrow$ DQA) is possible by applying a voltage control signal of 24 V DC to the coil. The REG670 digital relay sends a binary output signal (0 or 1) which closes or opens the contactor, respectively. The +24 V DC auxiliary voltage, provided by multiplug -X5 at pins 01 and 02, is again utilized in order to obtain a DC voltage signal to remotely control the contactor.

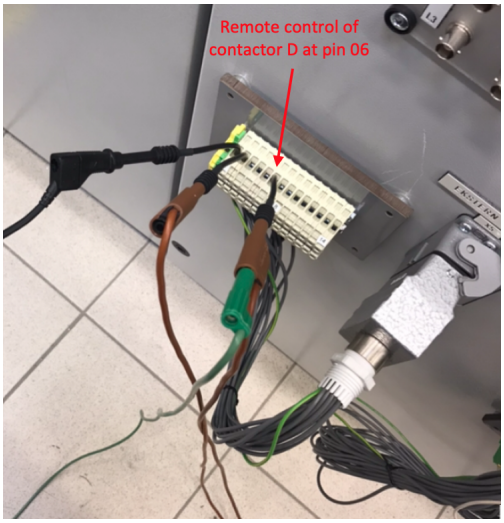

Figure 5.24: Multiplug -X5 at bus-bar DQD where contactor D is remotely controlled at pin 06

5.1.7 Measurements

The current measurements must be obtained through current transformers because the relay cannot tolerate high current levels as inputs. The initial idea was to obtain the fault currents measurements through current transformer TS22 at the DQD bus-bar, which measures the current between the DQD and DQA bus-bars. These signals are available via multiplug -X6, pins 07-12, in figure 5.27. However, this current transformer within the bus-bar cabinet measures the current behind the line inductor as denoted in figure 5.25. Consequently, it is not possible to measure the fault current with the TS22 transformer because the short-circuit emulator is implemented at the DQD-side as an open end. The current transformer TS23 measures the currents between the DQD and DQC bus-bars. Nevertheless, converter C connected at bus-bar DQE also contributes with fault current during grid-connected operation. Hence, the current measurement from the TS23 transformer only measures the current contribution from converter B and converter D. This emphasizes the problem with the bidirectional current flow due to the contributions from the utility grid and the microgrid generation units. As a result, separate current transformers are utilized with a CT ratio equal to 200/5 A for the primary and secondary side, respectively. The contactor cabinet (figure 5.26(a)) with the currents transformers (5.26(b)) is thereby connected in series between the short-circuit emulator and the DQD bus-bar. Subsequently, the digital relay obtains the fault current measurements via the banana plugs in figure 5.26(a).

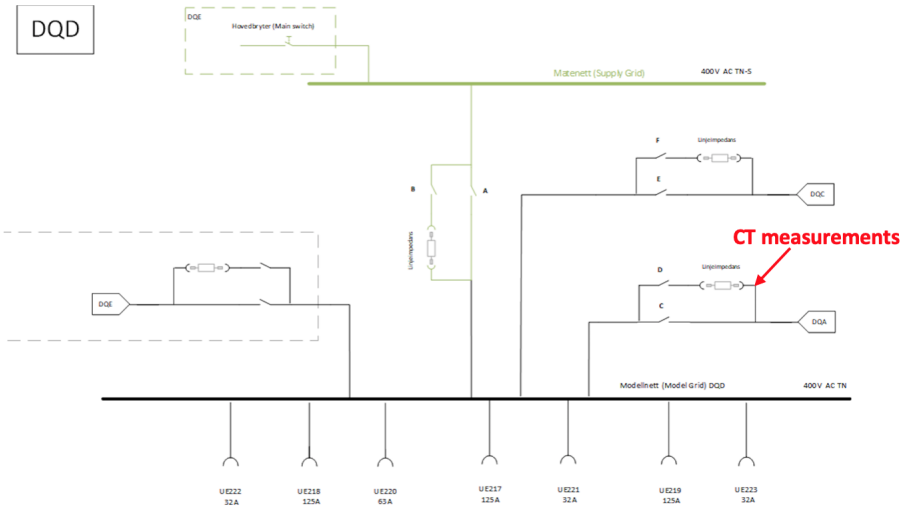

Figure 5.25: Schematics of the DQD bus-bar

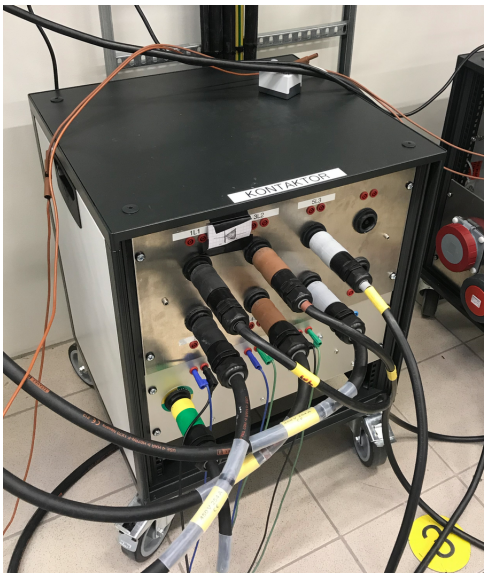

((a)) Contactor cabinet with separate current transformers

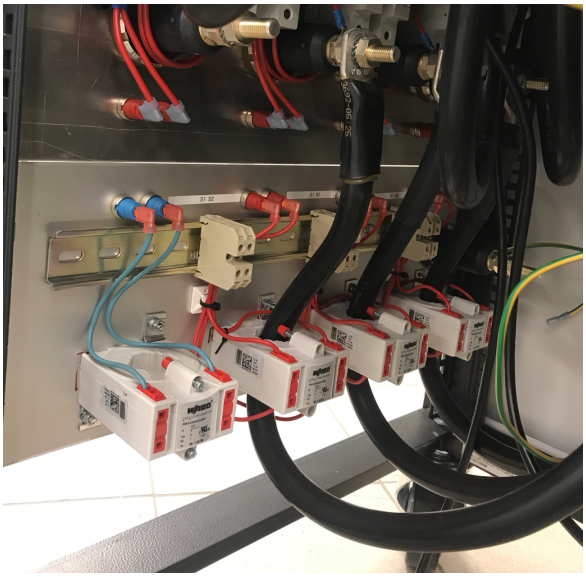

((b)) Separate current transformers

Figure 5.26: Fault current measurements to the digital relay

The voltage measurements are accessed from the -X6 multiplug (pins 22-24) at the DQD bus-bar, where the short-circuit is applied. Figure 5.27 shows how the voltage measurements at the DQD bus-bar are accessed.

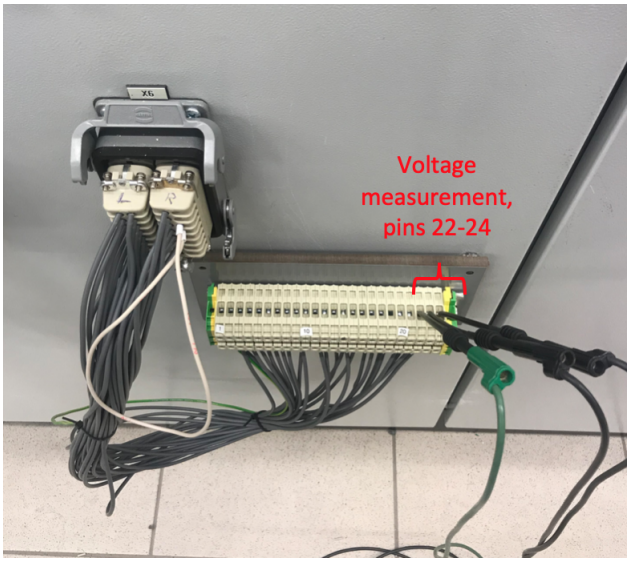

Figure 5.27: Voltage measurements at the DQD bus-bar fed to the digital relay

Furthermore, additional current and voltage measurements are made with BNC connectors and two oscilloscopes of the model type MSO2024B. Each oscilloscope can measure four different signals at the same time. The triggering output of the short-circuit emulator is logged in order to capture the changes in the other measurements when the short-circuit is applied. The fault current for phase A is additionally measured with an oscilloscope and a current prope at the output cable of the short-circuit emulator. The converter C current is measured at the measuring outtake "DQC" at bus-bar DQD. Moreover, the converter B current is measured at outtake "UE218" at bus-bar DQC, while the converter D current is measured at outtake "DQBE" at bus-bar DQE. Additionally, the voltages at the bus-bars are measured at the outtakes named "MODELLNETT" on the cabinets.

5.1.8 Short-circuit emulator

The short-circuit emulator in picture 5.28(a) is utilized in the laboratory tests in order to apply a fault in the microgrid. The rating voltage of the short-circuit emulator is 400 V AC, while the nominal current is 225 A Root mean square (RMS). The power circuit and the construction of the short-circuit emulator are shown in figure 5.28(b).

((a)) Picture of the short-circuit emulator

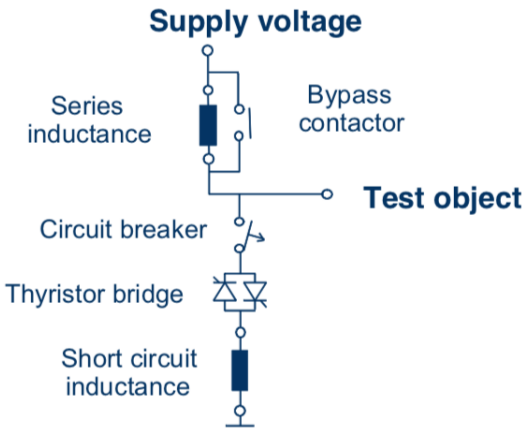

((b)) Circuit diagram of the short-circuit emulator [39]

Figure 5.28: Short-circuit emulator at the laboratory

The short-circuit emulator consists of two external inductors, $L_{emulator,series}$ and $L_{emulator,SC}$, connected in series with a triac connected thyristor bridge [39]. The inductors are accessible because they are placed outside the short-circuit emulator unit, so it is easy to change them. This is important because the inductors affect the short-circuit behavior. The series inductor between the supply and the test object limits the supplied current during short-circuits, while the short-circuit inductor determines the short-circuit impedance and voltage dip depth [39]. The series inductance is in normal operation shorted by the bypass contactor, which is connected in parallel to the series inductance. Hence, the contactor ensures a low impedance path when no fault is present. In reference to table 5.7, the implemented short-circuit inductance is 4 [μH] to limit the short-circuit contribution, and subsequently protecting the laboratory equipment.

The parameter settings can be changed through the display in figure 5.29 with the corresponding set of control buttons.

Figure 5.29: Display of the short-circuit emulator

According to [39], the short-circuit event is performed as the sequence:

- Blocked: something blocks the short-circuit sequence.

- Armed: the short-circuit emulator is waiting for the start signal.
- T_{pre}: delay to ensure that the bypass contactor is open before the shorting is applied.
- T_{sync}: synchronization, waiting for the zero-voltage crossing before the short-circuit is applied.
- T_{SC}: time interval and duration of the actual short-circuit.
- T_{post}: delay related to the closing of the contactor after the short-circuit is finished. This enables the thyristors to have time to turn off when the current reaches zero.

5.1.9 Load

The load utilized in the laboratory experiment is illustrated in figure 5.30(a), while figure 5.30(b) shows the possible combinations of the resistor banks.

((a)) Picture of the load at the laboratory

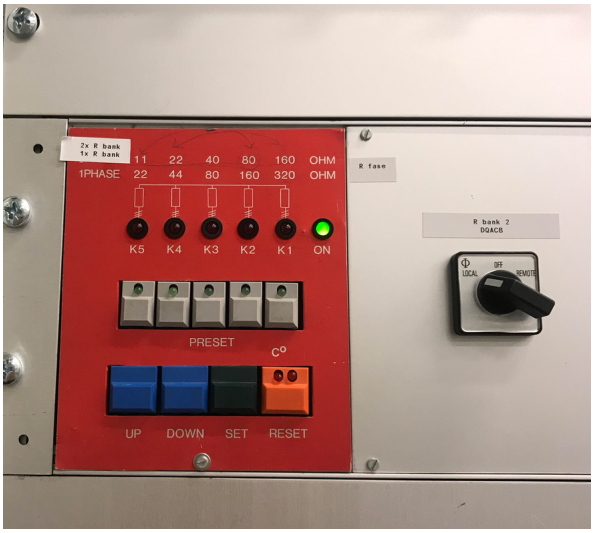

((b)) Load settings

In this laboratory experiment, the load varies between two values: low load and high load. K3 and K4 in figure 5.30(b) are activated for the low load operation which is equivalent to the calculated resistance in equation 5.1:

$$K4 \parallel K3 = \frac{1}{(\frac{1}{22} + \frac{1}{22}) + (\frac{1}{40} + \frac{1}{40})} = \underline{7.1\Omega} \tag{5.1}$$

Low load is thereby equivalent to the calculated load in equation 5.2:

$$P_{normal} = 3 \cdot VI = 3 \cdot 230V \cdot \frac{230V}{7.1\Omega} = \underline{22.4kW} \tag{5.2}$$

In contrast, K5, K4, K3, K2 are activated for the high load operation which is equivalent to the calculated resistance in equation 5.3:

$$K5 \parallel K4 \parallel K3 \parallel K2 = \frac{1}{(\frac{1}{11} + \frac{1}{11}) + (\frac{1}{22} + \frac{1}{22}) + (\frac{1}{40} + \frac{1}{40}) + (\frac{1}{80} + \frac{1}{80})} = \underline{2.9\Omega} \tag{5.3}$$

High load is thereby equivalent to the calculated load in equation 5.4:

$$P_{high} = 3 \cdot VI = 3 \cdot 230V \cdot \frac{230V}{2.9\Omega} = \underline{54.7kW} \tag{5.4}$$

5.2 Parameter settings

The parameter settings of the laboratory equipment are presented in this section. Table 5.6 gives the rated values of the converters, whereas the different impedance parameters are presented in table 5.7. Table 5.8 summarizes the time settings of the short-circuit emulator.

Parameter	Value
$V_{AC\_rated\_rms}$	400 [V]
I_{rated_rms}	90 [A]

Table 5.6: Rated value settings of the converters

Parameter	Value
L_{filter_1} [μH]	500
L_{filter_2} [μH]	200
C_{filter} [μF]	50
L_1 [μH]	1
L_2 [μH]	1
$L_{emulator,SC}$ [μH]	3+1

Table 5.7: Inductor and capacitor settings

Parameter	Value
T_{short}	1000 [ms]
T_{pre}	50 [ms]
T_{post}	20 [ms]
T_{sync}	13 [ms]

Table 5.8: Time settings of the short-circuit emulator

The duration of the short-circuit is selected to 1 s to guarantee that the digital relay is able to operate and disconnect the fault.

Crucial control parameters differentiating the laboratory converters are listed in table 5.3. Additional control settings in the built-in control are given in table B.1 in appendix B.2. As mentioned, most signals and parameters in the converter control system are scaled in the pu system with 1000 as 1 pu. In other words, 100% equals 1000 pu. Normally, 100% usually equals 1 pu.

5.3 Laboratory approach

The laboratory procedure is explained in this section. First, experiments related to islanding detection based on local voltage measurements are conducted. The system voltage at bus-bar DQD is investigated to examine the research question regarding the voltage during islanding transition. The voltage is also examined during different power contributions from the utility grid in the event of islanding. Moreover, the voltage is investigated in the event of a short-circuit and when the load is increased. Subsequently, the implementation of the direct transfer trip detection method is validated.

Next, the fault current level during grid-connected mode versus islanded mode is compared. Furthermore, the response of the protective relays is examined. In other words, the fault current levels against the settings of the ABB relay is examined and the need for adaptive protection functions is emphasized. The protection relay response with no adaptive protection function is compared with the relay response with adaptive protection.

Influence of control parameters on protection in island mode

The implemented control system is a crucial factor affecting the behavior of the IIDGs during short-circuits, and subsequently complicating the microgrid protection. In order to illustrate the influence on microgrid protection, different converter control strategies are implemented and tested during short-circuits. The influence is investigated in islanded mode due to simplifications. So, the active and reactive control, i.e., the signal path for obtaining the current references, are therefore varied to implement different control strategies. Table 5.9 summarizes the control scheme scenarios examined during short-circuits. Converter D will have the same control scheme throughout the tests, whereas converter B will be controlled with two different control schemes. For each control strategy, different control parameters are additionally altered for comparison purposes. Consequently, the behavior of the IIDGs converters is compared for different control parameters within each control scheme. Table 5.10 summarizes the parameter changes within each control scenario.

Control Scheme Scenario 1	**Converter B Grid-following**	**Converter D Grid-forming**
Active control mode	P reg	I act
Reactive control mode	Q reg	I react
VCO operating mode	PLL	Open loop
Control Scheme Scenario 2	**Converter B Grid-following**	**Converter D Grid-forming**
Active control mode	P reg	I act
Reactive control mode	U AC reg	I react
VCO operating mode	PLL	Open loop

Table 5.9: Configurations of the converters

Converter B is controlled as a grid-following converter with active and reactive power control in the first scenario, whereas converter B is configured as a grid-supporting converter in control scenario 2. The control strategy of converter D is not changed throughout the tests because the grid-forming converter is required to set the voltage and frequency reference for the rest of the system. However, the control parameters within the grid-forming control strategy are changed. The parameters in table 5.10 are varied within each control scenario. The proportional gain for the current regulator, I reg K_p, and the overcurrent trip level, I trip level, are parameters changed for the grid-forming converter. Subsequently, the active power reference and the separate positive and negative limits for active and reactive currents

are adjusted parameters for the grid-following converter. Additionally, the load changes between the low load operation (equation 5.2) and the high load operation (equation 5.4) for both control scenarios.

Case	**Varying parameter**	**Original setting**	**Values**					
1	K_p [%]	25	0	15	50	100	150	200
2	P_{B_ref} [pu]	0.3	0.5	1	-	-	-	-
3	Load [Ω]	K3//K4	K2//K3//K4//K5	-	-	-	-	-
4	I limit [pu]	$< -1, 1 >$	$< -0.5, 0.5 >$	$< -0.25, 0.25 >$	-	-	-	-

Table 5.10: Varied parameters for each control scenario

The original current trip level for converter D is 245 A for the base test case. However, it is necessary to increase the I trip level for some test cases to prevent the disconnection of converter D, e.g., when the proportional gain is substantially decreased or when the active power reference is substantially increased. This is further elaborated in section 6.3.

Chapter 6

Laboratory Results

The testing described in the previous section has resulted in a substantial amount of data, and the most important findings from the laboratory tests are presented in this chapter. Moreover, supplementary results are given in C. In the following, section 6.1.1 shows the difficulties with island detection based on voltage measurements, while section 6.1.2 presents the islanding detection based on the direct transfer signal method. Next, the functional adaptive microgrid protection scheme is illustrated in section 6.2. Furthermore, section 6.3 describes the impact of the converter control settings in table 5.10 within the control strategies in table 5.9. The utilized comparison parameters for testing the influence are summarized in table 6.1. The results will be discussed throughout this chapter, and a summary of the results is presented in section 6.4. The following should be noted before presenting the results:

- The current and voltage measurements are expressed in real values. However, the current and voltage base values in the built-in control of the converters are 90 RMS A and 400 RMS V, respectively.
- The positive direction of the converter currents is defined out the converters, whereas the positive direction of the fault current is defined into the short-circuit because the laboratory power converters feed the short-circuit.
- The noise in the measurement signals makes it difficult to determine the magnitude precisely. The values are obtained with the Data Cursor in MATLAB, and it is difficult to measure the exact values due to the noise and spikes. In this regard, all measurements should be considered as an approximation of the actual values.

6.1 Islanding detection

Reliable islanding detection methods are crucial so the microgrid protection scheme can adapt its protective settings according to the operation mode of the microgrid. First, the local detection method based on voltage measurements is presented to examine the voltage behavior during islanding transition, which is one of the research questions. Despite the obvious advantages of local detection, a communication-based detection method is implemented and presented in section 6.1.2. Implementing an adaptive microgrid protection scheme that detects the operation mode is the general objective of this thesis.

6.1.1 Passive local detection based on voltage measurements

The voltage is examined during the transition between grid-connected and islanded microgrid to investigate the validity of the passive island detection method. Converter B and converter C are controlled as grid-following converters, whereas converter D is grid-forming and provides the amplitude and frequency of the voltage. The active power reference of converter B is 300 pu for all test cases, but the

active power output of converter C is changed to examine the islanding transition during varying power contributions from the utility grid. Moreover, the current trip level is 345 A and the proportional gain constant is 25 % for the current regulator of converter D. The voltage measurements are obtained at bus-bar DQD during the transition to the islanded microgrid. Figure 6.1 illustrates the voltage drop during islanding when the active power output from the converter C is 500 pu, 800 pu, and 1000 pu. The islanding event occurs at differed times in figure 6.1. Edge triggering is utilized as a trigger function of the oscilloscope to capture single-shot waveforms. The inherent time delay between data acquired and the trigger position is inevitable since data and trigger acquisition have different paths. Consequently, the disconnection of converter C occurs at different times in figure 6.1 for different active power references. Note that the signals are scaled in a per-unit system with 1000 as 1 pu.

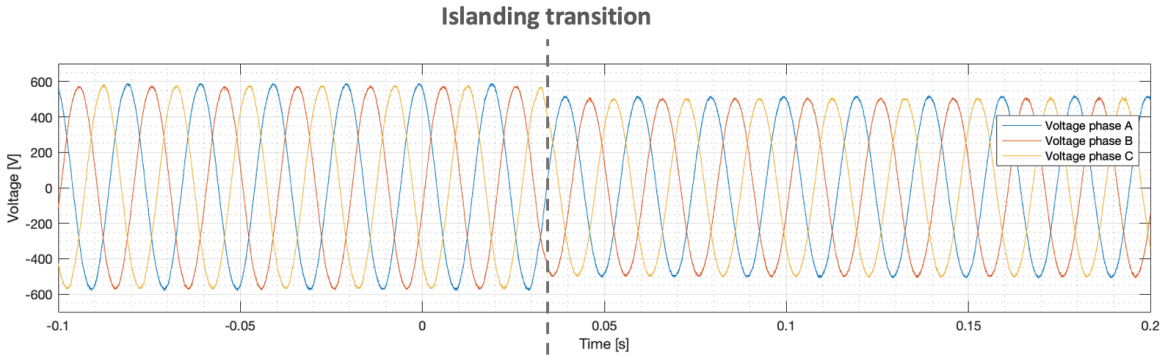

((a)) Islanding of microgrid at t = 35 ms when the active power reference is 500 pu for grid-emulating converter C

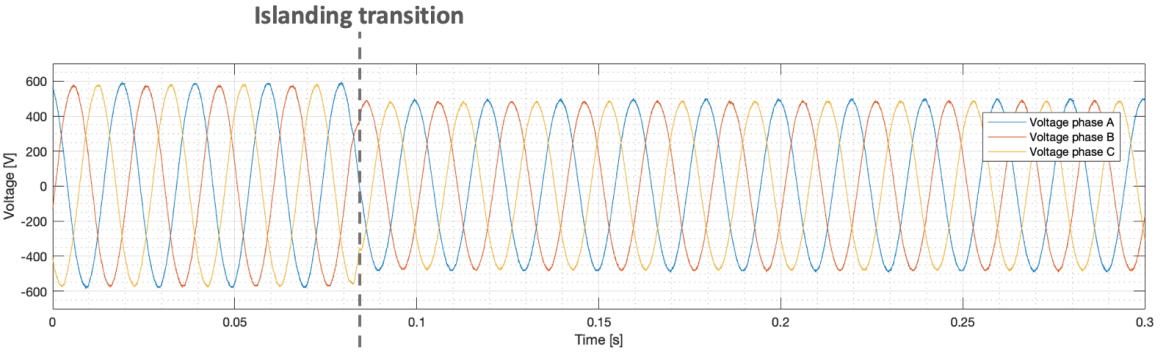

((b)) Islanding of microgrid at t = 84 ms when the active power reference is 800 pu for grid-emulating converter C

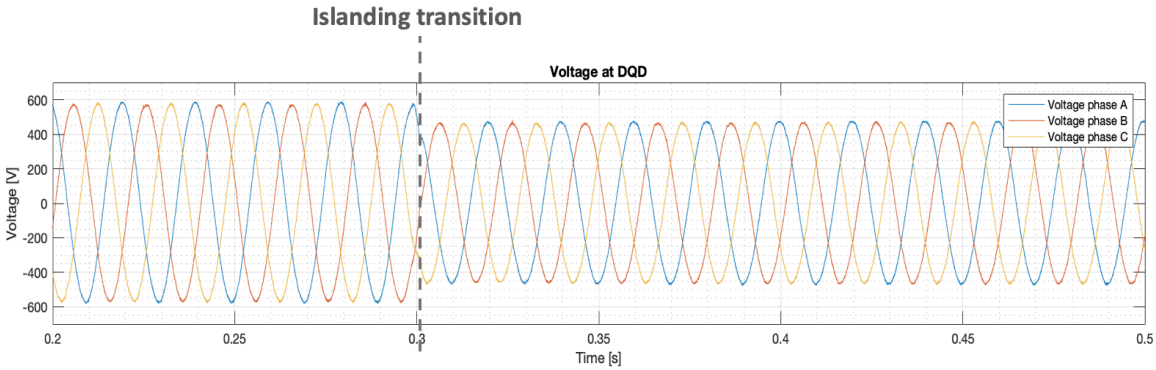

((c)) Islanding of microgrid at t = 0.3 s when the active power reference is 1000 pu for grid-emulating converter C

Figure 6.1: Voltage drop during islanding transition

After the disconnection of converter C, the voltage is not maintained constant at 400 V AC by the grid-forming converter D. As elaborated in section 5.1.4, the grid-forming laboratory converter is not equipped with voltage regulation, so the voltage drops during the islanding event. Subsequently, the voltage is reduced with approximately 50 RMS V, 70 RMS V, and 80 RMS V after islanding when P_{ref} of converter C is 500 pu, 800 pu, and 1000 pu, respectively. The loss of generation from converter C causes approximately a 20 % voltage drop when P_{ref} is 1000 pu as illustrated in figure 6.1(c). The under-voltage relay utilized in the laboratory experiments is implemented with a protective setting

of 85 %. In other words, the relay detects any abnormal situation if the voltage drops below 85% of the nominal voltage. Hence, the under-voltage relay might misinterpret the voltage drop in figure 6.1(c) as a fault condition. The voltage drop during islanding depends on the power contribution from the utility grid, i.e., from the grid-emulating converter C. Accordingly, if the active power reference of converter C is reduced, the voltage drop decreases. Thus, the voltage behavior in the event of islanding is difficult to predict because the active power output affects the reduction.

Additionally, the voltage at bus-bar DQD is affected by other events than islanding. Figure 6.2 illustrates the change in load from approximately 22 kW to 55 kW as calculated in equations 5.1 - 5.4. Converter C and converter B have active power outputs of 1000 and 300 pu, respectively, so the converter settings are equivalent to the situation in figure 6.1(c). The increased load is connected at t = 0.13 s and the voltage drops with approximately 40 RMS V. Compared to the islanding event in figure 6.1, the voltage reduction due to the increased load is smaller than the loss of generation from converter C.

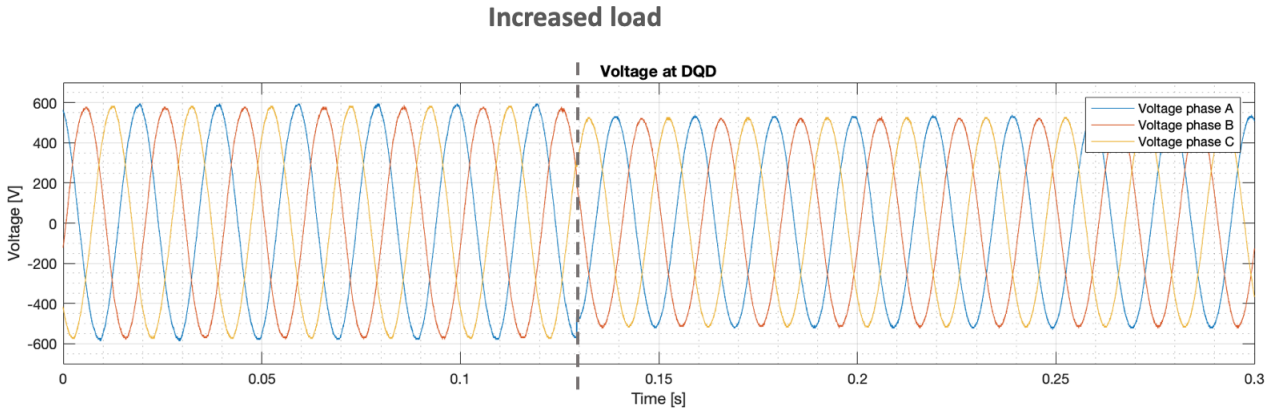

Figure 6.2: Increased load in the grid-connected microgrid at approximately t = 0.13 s

In the event of a three-phase short-circuit, however, the voltage drop is more substantial compared to the islanding event. Figure 6.3 shows the voltage drop during a short-circuit where the active power outputs of converter C and converter B are 1000 pu and 300 pu, respectively. The voltage decreases with approximately 160 RMS V.

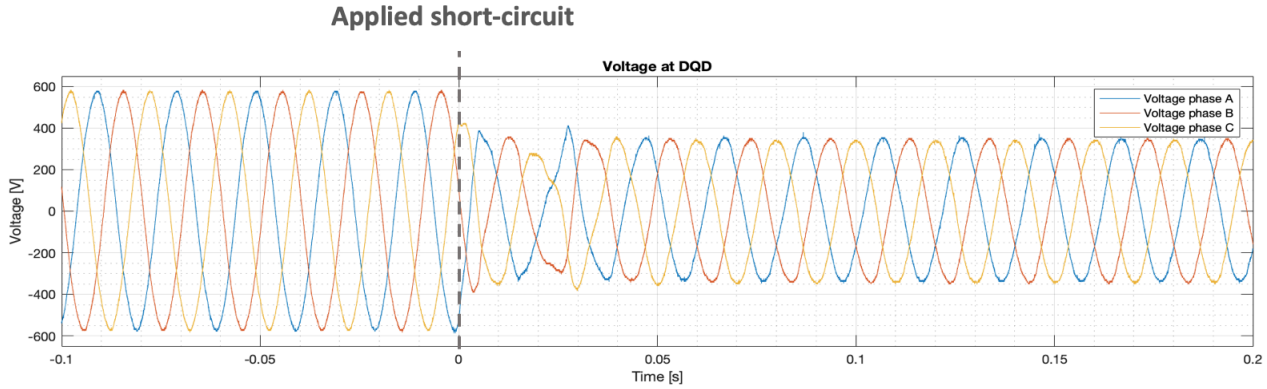

Figure 6.3: Applying a short-circuit at t = 0 s in the grid-connected microgrid

From the observations in figure 6.1, figure 6.2, and figure 6.3, the system voltage is not maintained constant at a 400 AC RMS voltage level following a change in the network topology. In other words, the voltage changes if the microgrid is islanded (i.e., disconnection of converter C), if the load is changed, or if a short-circuit is applied. The aforementioned events are seen as a load change by the generation [14], and the voltage decreases subsequently. The change in voltage magnitude can be used as an islanding detection method; however, the voltage drops significantly for all events. Consequently, it is difficult to differentiate the events solely based on the voltage magnitude. As a result, the general voltage measurement scheme cannot separate the islanding event from the increased load event or the occurrence of a short-circuit.

Moreover, the islanding detection method based on voltage measurements faces problems if the load condition matches the islanded DG generation because there is no significant change in voltage and frequency [50]. Additionally, it should be noted that proper voltage and frequency control by the VSC can keep the voltage stable during configuration changes and thereby delay the islanding detection [14]. So, the time response of these active regulations must be strongly studied before implementation [14]. Other local islanding detection methods based on ROCOF or other measurement schemes would be interesting to test, however, considered out of scope for this thesis due to time constraints.

6.1.2 Direct transfer trip

In this laboratory testing, a communication-based islanding detection method is implemented because it is difficult to differentiate the islanding event, the increased load, and the applied short-circuit solely based on the voltage magnitude. Hence, the direct transfer signal described in section 5.1.6 is implemented. Consequently, the protection system properly protects the microgrid because the relay adapts to the correct protection function according to the operation mode of the microgrid. Relay RET670 monitors contactor D on bus-bar DQE in figure 5.2 through multiplug -X5 as explained in section 5.1.6. The voltage across contactor D is 0 V DC when the contactor is closed, whereas the voltage across contactor D is 24 V DC when the contactor is open. However, the digital relay needs a 48 V DC signal to register the opening of the contactor, so a voltage source is connected in series to supply the additional 24 V DC. As a result, the relay receives a binary input signal which is either +24 V DC or +48 VDC. In reference to figure 6.4, the red graph illustrates the opening of the breaker where the voltage signal increases to 48 V DC, while the closing of the breaker is illustrated by the green graph where the voltage signal decreases to 24 V DC.

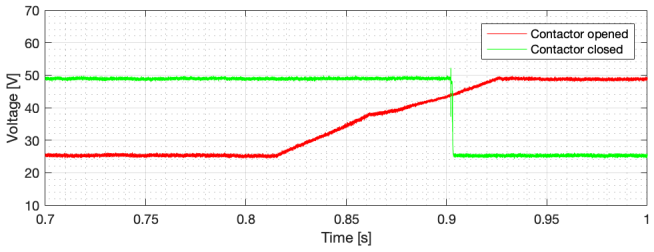

Figure 6.4: Switching of breaker status of contactor D on bus-bar DQE

Figure 6.5 is a picture of the HMI which confirms that the RET670 digital relay receives the breaker status. Green lights indicate that the breaker is closed, whereas red lights indicate that the breaker is open.

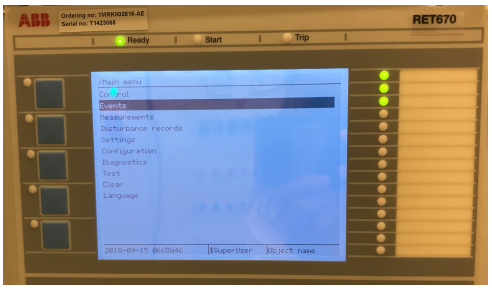

((a)) Green lights on LED1, LED2, LED3 indicate that contactor D is closed

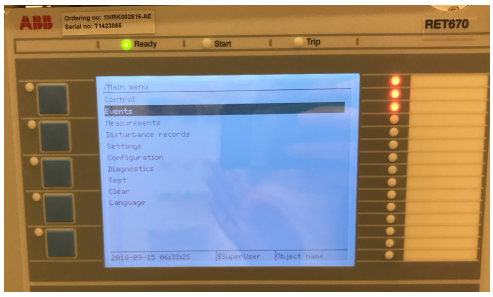

((b)) Red lights on LED1, LED2, LED3 indicate that contactor D is open

Figure 6.5: HMI of the RET670 relay

Relay RET670 communicates the breaker status to relay REG670 via GOOSE-communication. The first light on the HMI in figure 6.6 expresses the breaker status of contactor D on bus-bar DQE.

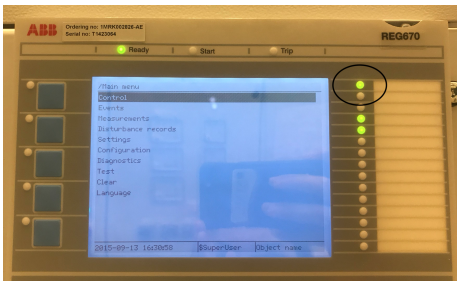

((a)) Green light on LED1 indicates that contactor D closed

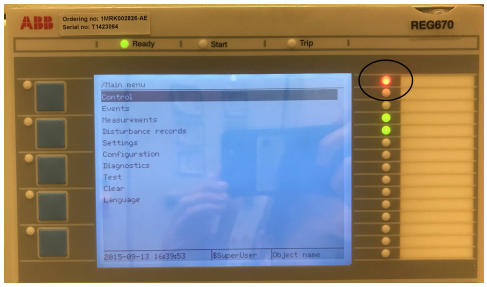

((b)) Red light on LED1 indicates that contactor D is open

Figure 6.6: HMI of the REG670 relay

6.2 Adaptive microgrid protection

A preliminary selection of graphs that illustrates different fault current levels is presented in this section to demonstrate the need for an adaptive microgrid scheme. Figure 6.7 compares the fault current magnitude during grid-connected mode and islanded mode. The load in the system is equivalent to 22.4 kW, which is calculated in equation 5.2, while the converter settings are listed below:

- Converter B is grid-following with $P_{ref} = 300$ pu
- Converter C is grid-following with $P_{ref} = 500$ pu. This converter represents the utility grid, and is thereby only connected during grid-connected operation.
- Converter D is grid-forming with a current trip level of 245 A and the proportional gain of its current regulator is I reg $K_P = 100\%$.

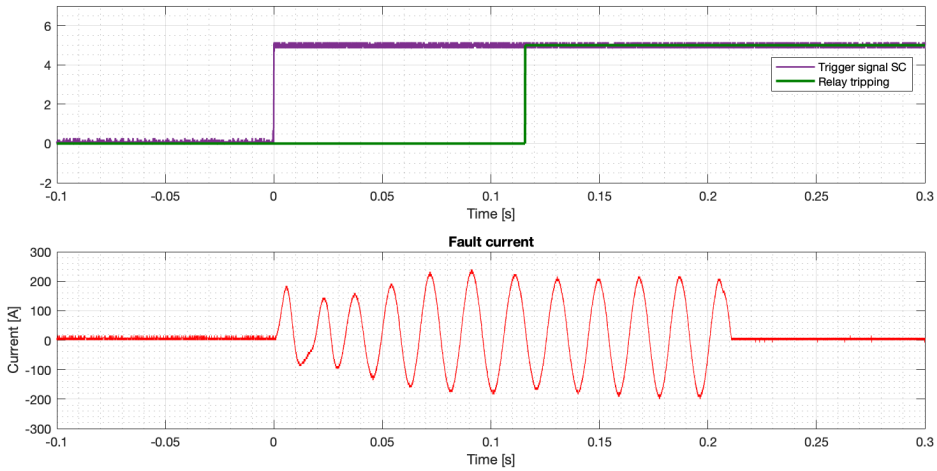

((a)) Grid-connected microgrid where the over-current relay trips after approximately 116 ms and the fault is disconnected at approximately t = 212 ms

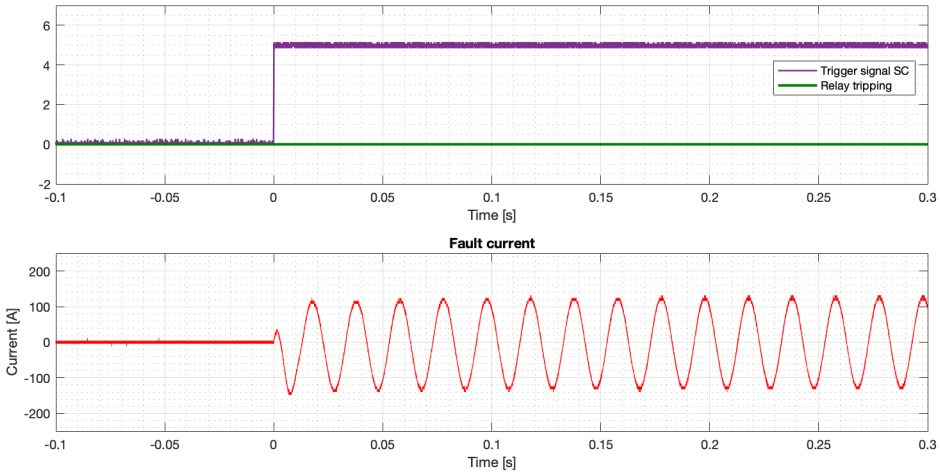

((b)) Islanded microgrid where the over-current relay does not trip

Figure 6.7: Fault currents for a 1000 ms three-phase fault during grid-connected mode and islanded mode

The purple graphs in figure 6.7 are the triggering of the short-circuit emulator at t = 0 s, whereas the green graphs are the output signal from the digital relay. Moreover, the red graphs are the fault current levels during grid-connected operation and islanded operation.

For the converter settings listed above, the static over-current relay only detects and disconnects the fault during the grid-connected mode. The green graph in figure 6.7(a) shows the tripping of the relay after approximately 116 ms, whereas the green graph in figure 6.7(b) illustrates the lack of the tripping signal. The maximum short-circuit current is approximately $I_{SC,max} \simeq 240$ A during grid-connected mode, whereas $I_{SC,max} \simeq 140$ A when the microgrid is islanded. Consequently, the relay is not tripping in figure 6.7(b) because the fault current level is below the threshold value.

Hence, the need for adaptive protection functions is demonstrated because the fault current level depends on the microgrid operation mode. However, it is important to mention that the utility grid is represented by another power electronic converter with limited current output. The grid-emulator converter cannot provide large short-circuit contributions compared to the supply grid at the laboratory. The fault current contribution from the main supply at the Smart Grid laboratory at NTNU is examined in reference [20]. During a short-circuit with a 2 [mH] fault-impedance, the current contribution from the supply grid is almost 23 times larger than the converter current [20]. The converter is controlled with direct active and reactive current control, and the active current reference is in this case 100 pu [20]. Note that the signals in the built-in converter control are scaled in a per-unit system with 1000 as 1 pu. Thus, the over-current relay will not detect short-circuits during islanded microgrid if the pick-up setting in the over-current relay is based on the large short-circuit contribution from the main supply.

Subsequently, relay REG670 selects the under-voltage protection function when contactor D on bus-bar DQE is open, i.e., when the microgrid is islanded. Figure 6.8 shows that the under-voltage relay disconnects the short-circuit applied in the islanded microgrid after 107 ms, in contrast to the over-current relay in figure 6.7(b). In reference to figure 6.7(a) and figure 6.8, the under-voltage protection function sends a tripping signal after one current cycle, whereas the over-current protection function reacts to the short-circuit after approximately six cycles. Hence, the under-voltage function detects the short-circuit faster compared to the over-current relay. The voltage drops immediately below the threshold limit of the under-voltage relay, whereas the fault current increases and exceeds the threshold limit of the over-current rely longer into the short-circuit. Additionally, there is a time delay related to opening the mechanical contactor in the bus-bar cabinet to isolate the fault.

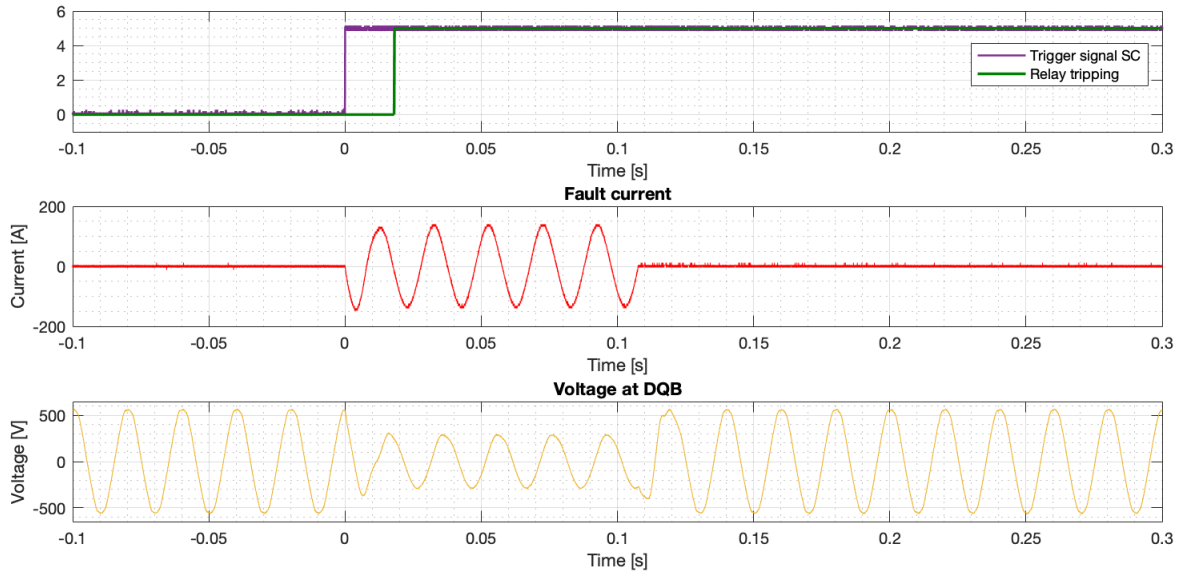

Figure 6.8: Islanded microgrid where the under-voltage protection function trips after approximately 17.8 ms and the fault is disconnected at t = 107 ms

To summarize, figure 6.7 illustrates the different fault current levels during the grid-connected and islanded microgrid. Subsequently, the need for adaptive protection functions is demonstrated. The fault current level in the islanded microgrid, which is constructed by DGs with power electronics interfaces, is not sufficient to trip the static over-current relay. Consequently, the under-voltage protection function is selected during the islanding operation, and the short-circuit is isolated after approximately 107 ms.

Nevertheless, it is not accurate to determine the protective settings solely based on the operating mode of the microgrid. Figure C.1 in appendix C.1 indicates that the fault current also depends on the implemented control strategy. When converter B is grid-supporting instead of grid-following, but the rest of the converter settings are equivalent to the situation in figure 6.7(a), the fault current level is not sufficient to trip the over-current relay even though the microgrid is grid-connected. The lack of tripping and the reduced fault current are illustrated in figure C.1. Evidently, the control strategy of converter B is crucial regarding microgrid protection because the static over-current relay trips when I reg $K_P = 100\%$ if converter B is following, but it does not trip if converter B is grid-supporting for the same proportional gain value. However, figure C.2 in appendix C.1 shows that the over-current relay trips when I reg $K_P = 50\%$ if converter B is supporting, but it does not trip if converter B is grid-following for the same proportional gain value. Hence, the control settings within the control strategy are also of great importance.

Thus, the fault current level is also affected by the converter control, not only by the network configuration. As a result, the control strategies and their control settings must be studied when implementing the microgrid protections scheme. The influence of the aforementioned control strategies, along with other converter settings, is therefore examined in greater detail in the next section.

6.3 Influence of converter control in islanded microgrid

As discussed in the previous section, the fault currents in the microgrid also depend on the selected control strategy and control parameters. This section therefore systematically examines how the converter control affects the system voltage and converter currents. In order to simplify the comparisons, the influence of the converter control is investigated in islanded mode. Thus, the relation between the grid-forming converter D and the grid-following or grid-supporting converter B is examined during islanded mode where the under-voltage protection function is activated. The impact of the different control settings will be described separately for the grid-following and grid-supporting control scheme described in table 5.9. The following should be noted before presenting the results:

- The current and voltage measurements are expressed in real values. However, the current and voltage base values used in the built-in control of the converters are 90 RMS A and 400 RMS V, respectively.
- The set of parameters in table 6.1 is utilized to easily compare the results.
- The currents are asymmetrical at the beginning of the short-circuit because the waveform does not have symmetry above and below the time axis. As a result, all RMS-values are calculated from the average values of the positive and negative peak in the momentary measurement at the end of the short-circuit. The DC component, which occurs right after the short-circuit is applied, is added to the sine wave causing the current to reach a much larger value than the sine wave alone [30]. The current in the system inductance cannot instantly change from its value before the short-circuit to its steady state fault value [30]. Thus, a DC component is introduced to compensate for this. The initial value of the DC component depends on the cycle and value of the current when the short-circuit takes place.

Parameter	Explanation
I_{B_normal}	The RMS-value of the converter B current during normal operating conditions
I_{D_normal}	The RMS-value of the converter D current during normal operating conditions
V_{normal}	The RMS-value of the voltage during normal operating conditions
I_{fault}	The RMS-value of the fault current at the end of the short-circuit
I_{B_SC}	The RMS value of the converter B current at the end of the short-circuit
I_{D_SC}	The RMS value of the converter D current at the end of the short-circuit
V_{fault}	The RMS-value of the voltage at the end of the short-circuit
V_{drop}	The percentage decrease between V_{normal} and V_{fault}
$R_{\frac{I_{B\_SC}}{I_{D\_SC}}}$	The ratio between the converter currents at the end of the short-circuit

Table 6.1: Parameter set

6.3.1 Coordination between converter settings and converter protection functions

The coordination between converter settings and internal converter protection functions needs to be examined. As elaborated in section 5.1.5, the laboratory converters are equipped with protection functions to protect the power electronics. If the threshold values are exceeded, the protection function might disconnect the converter before the protection relay isolates the fault. The converter settings are thereby important to prevent the immediate disconnection of the converter and subsequently enable the DG unit to stay connected during short-circuits. The loss of generation during short-circuits would lead to greater voltage dips and additionally stability issues if the grid-forming converter D disconnects. Modern grid codes therefore require that the DG units remain connected to the grid during voltage dips to ensure network supporting functionalities [27]. Moreover, if the grid-forming converter

disconnects before the digital relay clears the fault, the remaining grid-following converters lose their voltage magnitude and voltage frequency reference.

The disconnection of the grid-forming converter D is illustrated in figure 6.9 when a 1000 ms three-phase short-circuit is applied at t = 0. The converter settings are equal to the original parameters in table 5.10; however, the proportional gain in the current regulator of converter D is zero to trigger the disconnection of the converter. As illustrated in figure 6.9, the under-voltage relay sends a tripping signal after approximately 21 ms and the fault is disconnected at approximately t = 120 ms. However, the converter D current (orange graph in figure 6.9) immediately increases, and the converter immediately disconnects due to over-current. The grid-forming converter is disconnected after half a current cycle because its current output is zero after that. Hence, the digital relay is not operating fast enough, i.e., detecting the short-circuit and sending a corresponding trip signal to disconnect the fault.

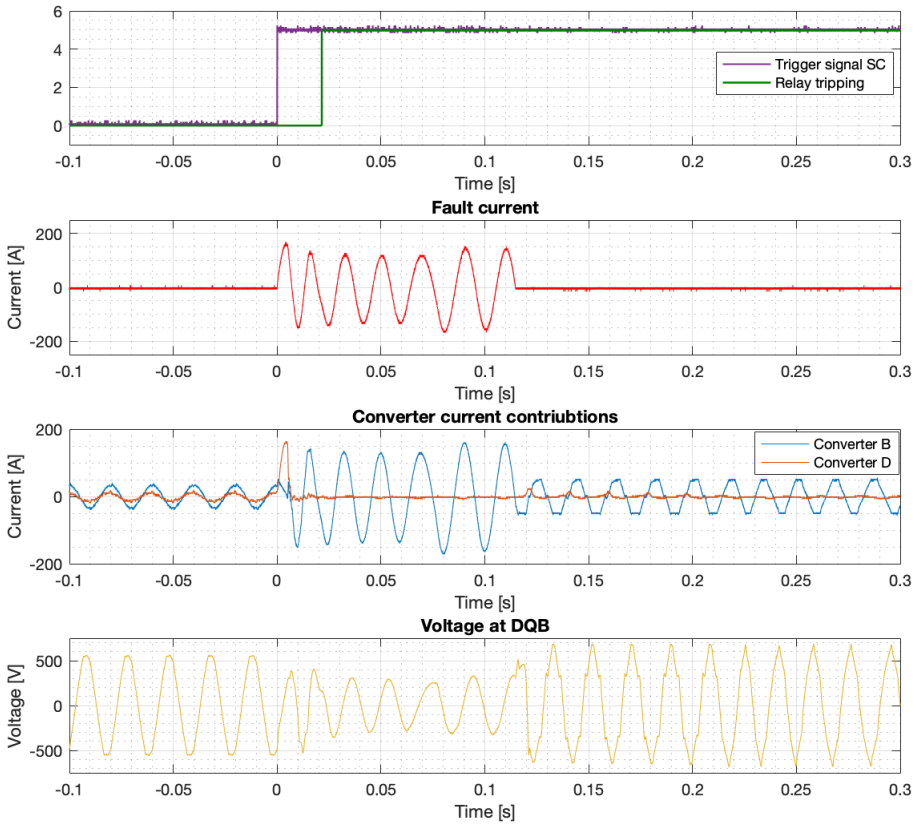

Figure 6.9: Disconnection of the grid-forming converter D due to over-current when I reg K_P is zero

The grid-forming converter D is crucial to provide the voltage reference of 400 AC V at the frequency of 50 Hz. However, the grid-following converter B continues to stay connected, but the current and voltage are not sinusoidal waves anymore. Moreover, the voltage magnitude and frequency are not kept at 400 V AC and 50 Hz. By decreasing the high AC frequency trip level of converter B to 57 Hz, the grid-following converter will disconnect at approximately t = 0.26 s. The disconnection by the

over-frequency protection function is illustrated in figure C.3 in appendix C.2.1.

The immediate disconnection of converter D in figure 6.9 for I reg $K_P = 0$ % demonstrate the need to examine the impact of control parameters so the DG units stay connected during short-circuits. First, the base cases with the original settings in table 5.10 are presented for each control strategy.

6.3.2 Original settings

The base cases with the original settings in table 5.10 for control strategy 1 and control strategy 2 are presented in this section. Consequently, it is easier to investigate the influence of control parameters by comparing to the base case. The proportional gain in the current regulator of the grid-forming converter D is selected to 25 %. This proportional gain value is more suitable regarding the coordination of protection functions, so the immediate disconnection of the converter is avoided. It is important to emphasize that the proportional gain, K_P, is referred to as the proportional gain in the PI current regulator of the grid-forming converter D, I reg K_P, throughout this chapter.

Control strategy 1

Figure 6.10 illustrates the same case as figure 6.9, however, the proportional gain constant is now I reg $K_P = 25\%$.

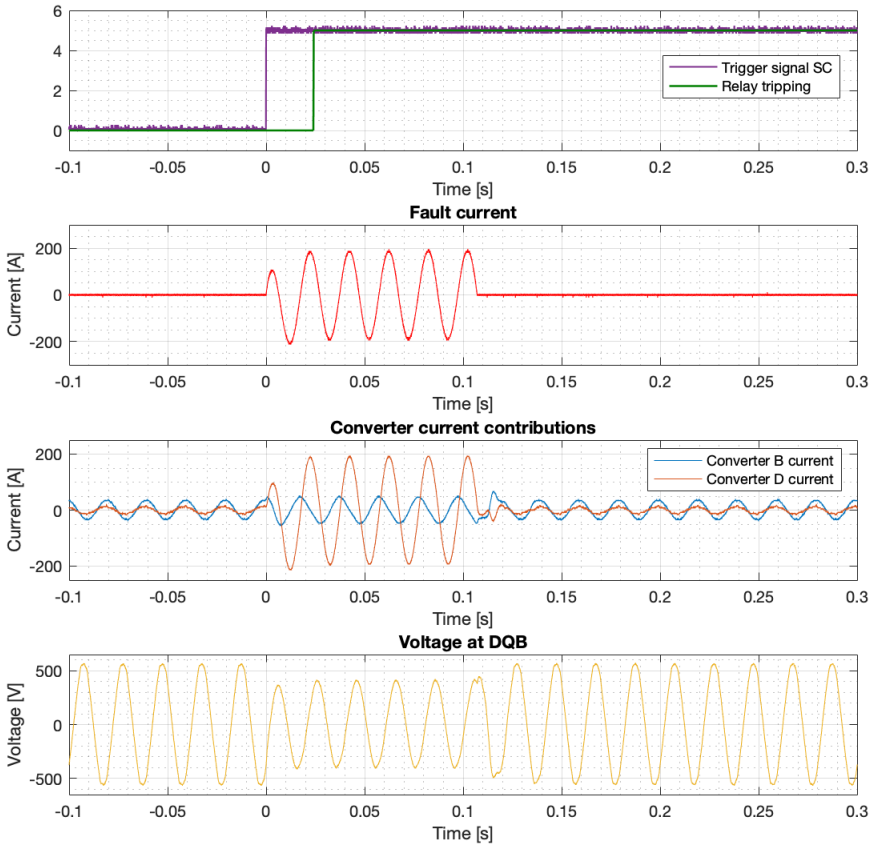

Figure 6.10: Control strategy 1 with the original settings in table 5.10

The increased proportional gain increases the power-sharing between the converters, which prevents the disconnection of converter D. During normal operation, the current contributions from converter B and D are approximately 25 and 10 RMS A at the converter filters, respectively. The system voltage is only plotted at bus-bar DQB in figure 6.10 because the voltage at bus-bar DQC is identical. As illustrated in figure 6.10, the negative and positive peak-values differ after the short-circuit occurs. Hence, the mean amplitude is displaced from zero due to the DC-component in the current transient. Longer into the short-circuit, the sine waves start to stabilize, but the fault is cleared before the DC-component completely disappears. As a result, the momentary values obtained from the graphs in figure 6.10 are average values between the positive and negative peaks at the end of the short-circuit. Next, the average momentary values are transformed to RMS values at the end of the short-circuit to compare the measurement signals for different control parameters. The average RMS currents at the end of the short-circuit are given by equations 6.1-6.3:

$$I_{B\_SC} = \frac{1}{\sqrt{2}} \cdot \frac{44 + 48}{2} = 32.5A \tag{6.1}$$

$$I_{D\_SC} = \frac{1}{\sqrt{2}} \cdot \frac{194 + 194}{2} = 137.2A \tag{6.2}$$

$$I_{fault} = \frac{1}{\sqrt{2}} \cdot \frac{196 + 196}{2} = 138.6A \tag{6.3}$$

Moreover, the voltage decreases immediately, and the measured RMS voltage is at the end of the short-circuit:

$$V_{fault} = \frac{1}{\sqrt{2}} \cdot \frac{408 + 416}{2} = 291.3V \tag{6.4}$$

Hence, the voltage drop is:

$$V_{drop}[\%] = [1 - \frac{V_{SC}}{V_{normal}}] \cdot 100 = [1 - \frac{291.3}{396}] \cdot 100 = 26.4\% \tag{6.5}$$

For I reg $K_P = 25$ %, the ratio between the converter currents during the short-circuit is:

$$R_{\frac{I_{B\_SC}}{I_{D\_SC}}} = \frac{32.5A}{137.2A} = 0.24 \tag{6.6}$$

Control strategy 2

Figure 6.11 illustrates the base case of control strategy 2. The converter settings are equivalent to the previous base case; however, the reactive control of converter B is changed to AC voltage regulation that supports the voltage by controlling the reactive current.

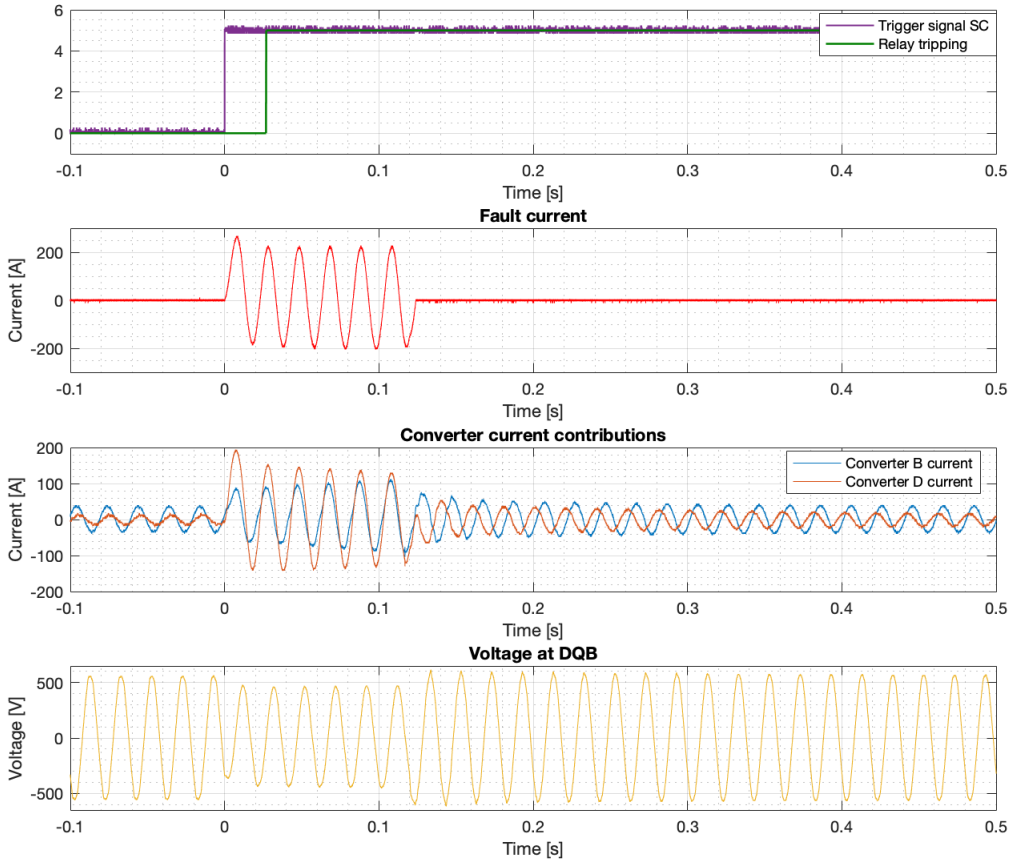

Figure 6.11: Control strategy 2 with the original settings in table 5.10

During normal operation, the grid-supporting converter B with $P_{ref} = 300$ pu has an AC RMS current of approximately 25 A at the converter filter, whereas the converter contribution from the grid-forming converter D is approximately 10 RMS A. Similar to control strategy 1, the negative and positive peaks differ during the short-circuit. Consequently, the average value between the negative and positive momentary peaks is utilized to calculate the RMS-value at the end of the short-circuit. The fact that the RMS-values are calculated based on the momentary values at the end of the short-circuit is especially important to emphasize for the second control strategy. Due to the grid-supporting control scheme, converter B slowly regulates its output current during the short-circuit. The reactive current from converter B and the voltage therefore increases during the short-circuit. However, the fault is cleared by the under-voltage relay before the voltage and converter B current are finished stabilizing. It is thus important to stress that the current and voltage values are obtained at the end of the short-circuit. The average RMS currents at the end of the short-circuit are given by equations 6.7-6.9:

$$I_{B\_SC} = \frac{1}{\sqrt{2}} \cdot \frac{112 + 88}{2} = 70.7A \tag{6.7}$$

$$I_{D\_SC} = \frac{1}{\sqrt{2}} \cdot \frac{130 + 134}{2} = 93.3A \tag{6.8}$$

$$I_{fault} = \frac{1}{\sqrt{2}} \cdot \frac{224 + 208}{2} = 152.7A \tag{6.9}$$

Moreover, the voltage decreases immediately, and the measured RMS voltage is at the end of the short-circuit:

$$V_{fault} = \frac{1}{\sqrt{2}} \cdot \frac{472 + 448}{2} = 325.3V \tag{6.10}$$

Hence, the voltage drop is:

$$V_{drop}[\%] = [1 - \frac{V_{SC}}{V_{normal}}] \cdot 100 = [1 - \frac{325.3}{402}] \cdot 100 = 19.1\% \tag{6.11}$$

For I reg $K_P = 25$ %, the ratio between the converter currents during the short-circuit is:

$$R_{\frac{I_{B\_SC}}{I_{D\_SC}}} = \frac{70.7A}{93.3A} = 0.76 \tag{6.12}$$

After the fault is disconnected, control scheme 2 requires more time to correlate with the new state of the system compared to control strategy 1 in figure 6.10. Hence, the x-axis is extended to plot the regulation behavior of control strategy 2 for a longer period of time. After approximately 0.4 s, the converter currents are equal to their initial values before the short-circuit. Moreover, the voltage at bus-bar DQB is also modulated back to its rated value. For control strategy 2, the $R_{\frac{I_{B\_SC}}{I_{D\_SC}}}$ ratio is much higher compared to control strategy 1. Hence, the power-sharing between the converters is increased by implementing converter B as a grid-supporting converter. Moreover, the voltage drop during the short-circuit is reduced for control strategy 2 due to the voltage support from converter B.

The regulation behavior of the grid-supporting converter is not fully evolved in figure 6.11 because the protection relay disconnects the fault and limits the duration of the short circuit. As a result of the slow regulation of converter B, one test with reduced PI time constants in the active power control and the reactive AC voltage control is conducted to illustrate a faster regulation. Figure C.4 in appendix C.2.2 shows the base case of control strategy 2, but the time constants in the PI regulators are reduced to P reg Ti = 10 ms and U AC reg Ti = 10 ms. It is important to know about these time constants in the PI-regulators, and it would have been interesting to experiment with the regulation time of the active and reactive controllers. However, the regulation time of the converters is not further investigated due to limited time and high demand for the laboratory converters. The further test results have the original time constants in table B.1; I reg Ti = 1000 ms, P reg Ti = 500 ms, Q reg Ti = 500 ms, and U AC reg Ti = 100 ms.

In the next sections, different parameters are systematically changed to examine the correlation between the converter settings and the current and voltage characteristics during a three-phase short-circuit. The influence of the I reg K_P parameter is examined in section 6.3.3 for both control strategies. Next, the active power reference of converter B is increased in section 6.3.4. Moreover, the load is changed from low load to high load (equations 5.1-5.4) in section 6.3.5. Lastly, section 6.3.6 documents the influence of changing the active and reactive current limits of converter B for both control strategies. Note that the signals are scaled in a per-unit system with 1000 as 1 pu for the laboratory converters.

6.3.3 Changing the proportional gain parameter

The importance of the proportional gain parameter in the current PI-regulator is illustrated in figure 6.10 and figure 6.11 because converter D does not trip when the proportional gain is 25 %. Consequently, the influence of the I reg K_P parameter is examined in great detail in this section for both control strategies.

Control strategy 1

Figure 6.12 illustrates the converter currents, the fault current, and the voltage drop during the short-circuit when I reg $K_P = 0$ %. It is necessary to increase the original current trip level of converter D from 245 A to 445 A to prevent its immediate disconnection when the proportional regulator gain is zero. Hence, the tolerance for currents is over-dimensioned for converter D in order to handle the high current contribution during the short-circuit.

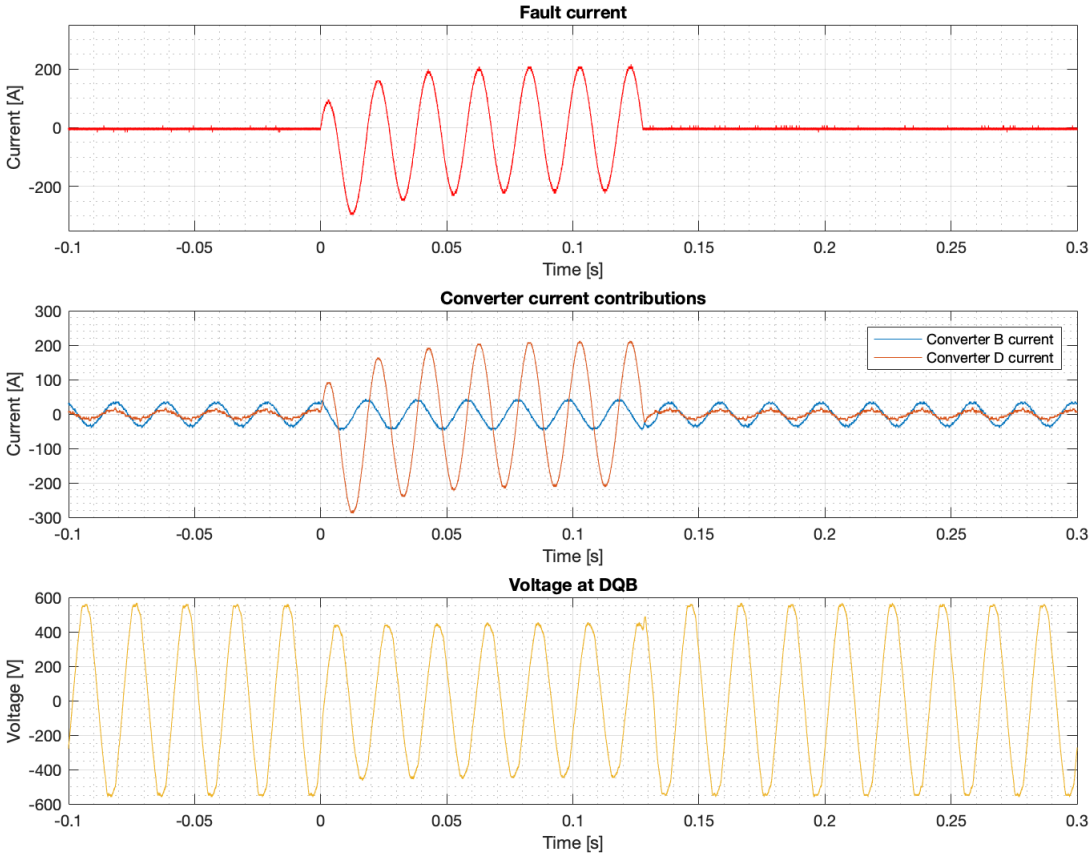

Figure 6.12: Control strategy 1 with I reg $K_P = 0$ %, I trip = 445 A

Before the short-circuit is applied, the grid-following converter B with $P_{ref} = 300$ pu has a current of approximately 25 RMS A at the converter filter, whereas the converter contribution from the grid-forming converter D is approximately 10 A. After the short-circuit is applied, the converter B current is measured to $I_{B\_SC} = 31.1$ RMS A at the end of the short-circuit. The DC-component is especially evident in the converter D current, but the current starts to oscillate around zero at the end of the short-circuit. At this point, the RMS-value is $I_{D\_SC} = 149.9$ A. Furthermore, the voltage is decreased

to approximately $\frac{452}{\sqrt{2}} = 319.6$ RMS V at the end of the short-circuit. The 452 V momentary voltage value is the average value of the positive and negative peaks because the voltage is still not oscillating around zero at the end of the short-circuit. Hence, the voltage drop is [1 - $\frac{319.6}{396}$] ·100 [%]= 19.3 %. The RMS value of the fault current is $I_{SC} = \frac{212}{\sqrt{2}} \cdot = 149.9$ A at the end of the short-circuit. Moreover, the ratio between the converter currents is $R = \frac{31.1A}{149.9A} = 0.21$. The calculations of the comparison parameters are summarized in table 6.2:

Parameter	Value
I_{B_normal}	25 RMS [A]
I_{D_normal}	10 RMS [A]
I_{B_SC}	$\frac{1}{\sqrt{2}} \cdot$ 44 = 31.1 RMS [A]
I_{D_SC}	$\frac{1}{\sqrt{2}} \cdot$ 212 = 149.9 RMS [A]
I_{fault}	$\frac{1}{\sqrt{2}} \cdot \frac{208+216}{2} = 149.9$ RMS [A]
V_{drop}	[1 - $\frac{319.6}{396}$] · 100% = 19.3 %
$R_{\frac{I_{B\_SC}}{I_{D\_SC}}}$	$\frac{31.1}{150} = 0.21$

Table 6.2: Comparison parameters for control strategy 1 when I reg $K_P = 0\%$

Interesting observations are made by comparing this case with zero proportional gain to the base case in figure 6.10. Firstly, the power-sharing between the converters is limited, so the ratio between the converter currents is reduced when the proportional gain is zero. Hence, the current output from converter B is reduced, while the converter D current is increased compared to the base case. The fault current is overall increased due to the higher current contribution from converter D. Furthermore, the voltage is stiffer during the short-circuit because the droop effect from the proportional gain is decreased. The voltage should in theory be completely stiff when I reg K_P is zero. However, there is a voltage drop across the inductors in the transformer and the LCL-filter connecting the converter to the grid. So when the current from converter D rapidly increases during the short-circuit, the voltage drops significantly across these series-connected inductors. The current from the grid-forming converter would probably exceed its current limits, but this feature is not properly governed in the grid-forming mode of the converter. The lack of an accumulator with top and bottom current limiters is illustrated in figure 5.16 of the grid-forming converter.

Figure 6.13 illustrates the converter currents, the fault current, and the voltage drop during the short-circuit when I reg $K_P = 15$ %. It is necessary to increase the current trip level to avoid immediate disconnection of converter D. However, a trip level of 345 A is sufficient when the proportional gain is 15 %. Thus, converter D is equipped with a lower current trip level compared to the test case with zero proportional gain. Table 6.3 summarizes the comparison parameters for control strategy 1 when I reg K_P is 15 %.

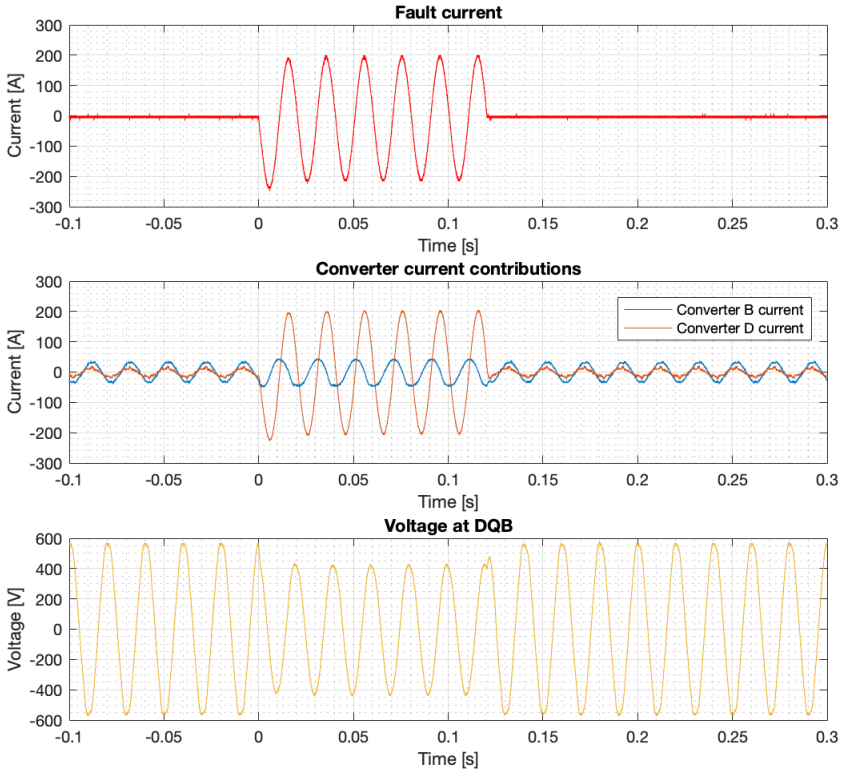

Figure 6.13: Control strategy 1 with I reg K_P = 15 %, I trip = 345 A

Parameter	Value
I_{B_normal}	25 RMS [A]
I_{D_normal}	10 RMS [A]
I_{B_SC}	$\frac{1}{\sqrt{2}} \cdot \frac{44+48}{2}$ = 32.5 RMS [A]
I_{D_SC}	$\frac{1}{\sqrt{2}} \cdot \frac{204+208}{2}$ = 145.7 RMS [A]
I_{fault}	$\frac{1}{\sqrt{2}} \cdot \frac{200+216}{2}$ = 147.1 RMS [A]
V_{drop}	$[1 - \frac{308.3}{402}] \cdot 100\%$ = 23.2 %
$R_{\frac{I_{B\_SC}}{I_{D\_SC}}}$	$\frac{32.5}{145.7}$ = 0.22

Table 6.3: Comparison parameters for control strategy 1 when I reg K_P = 15%

Compared to figure 6.12 with zero proportional gain, the power-sharing between the converters is increased due to the given droop effect. Nevertheless, the converter D current is still more than four times higher than the converter B current. Hence, the droop effect from K_p = 15 % is not particularly substantial.

Figure 6.14 illustrates the fault current, the converter currents, and the voltage drop during the

short-circuit when I reg $K_P = 50$ %.

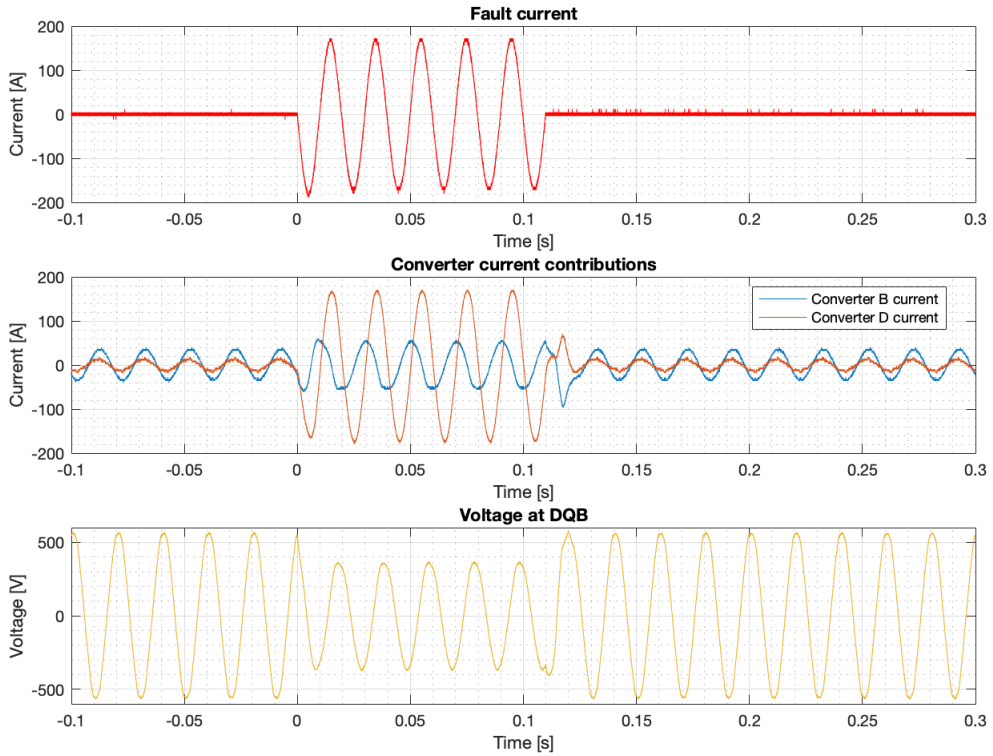

Figure 6.14: Control strategy 1 with I reg $K_P = 50$ %

The DC-component is less evident in figure 6.14 because the difference between the positive and negative peaks is smaller. Nevertheless, the average values between the momentary peaks are utilized to obtain the RMS-values at the end of the short-circuit. Table 6.4 summarizes the comparison parameters.

Parameter	Value
I_{B_normal}	25 RMS [A]
I_{D_normal}	10 RMS [A]
I_{B_SC}	$\frac{1}{\sqrt{2}} \cdot 52 = 36.8$ RMS [A]
I_{D_SC}	$\frac{1}{\sqrt{2}} \cdot \frac{167+175}{2} = 120.9$ RMS [A]
I_{fault}	$\frac{1}{\sqrt{2}} \cdot 172 = 121.6$ RMS [A]
V_{drop}	$[1 - \frac{263}{402}] \cdot 100\% = 34.5$ %
$R_{\frac{I_{B\_SC}}{I_{D\_SC}}}$	$\frac{36.8}{120.9} = 0.30$

Table 6.4: Comparison parameters for control strategy 1 when I reg $K_P = 50\%$

Compared to the base case in figure 6.10, the voltage drop is more significant when I reg K_p is 50 %. Moreover, the power-sharing between the converter is increased, so the ratio between the converter currents during the short-circuit is higher.

Figure 6.15 illustrates the fault current, the converter currents, and the voltage drop during the short-circuit when I reg $K_P = 100$ %. Moreover, table 6.5 summarizes the comparison parameters.

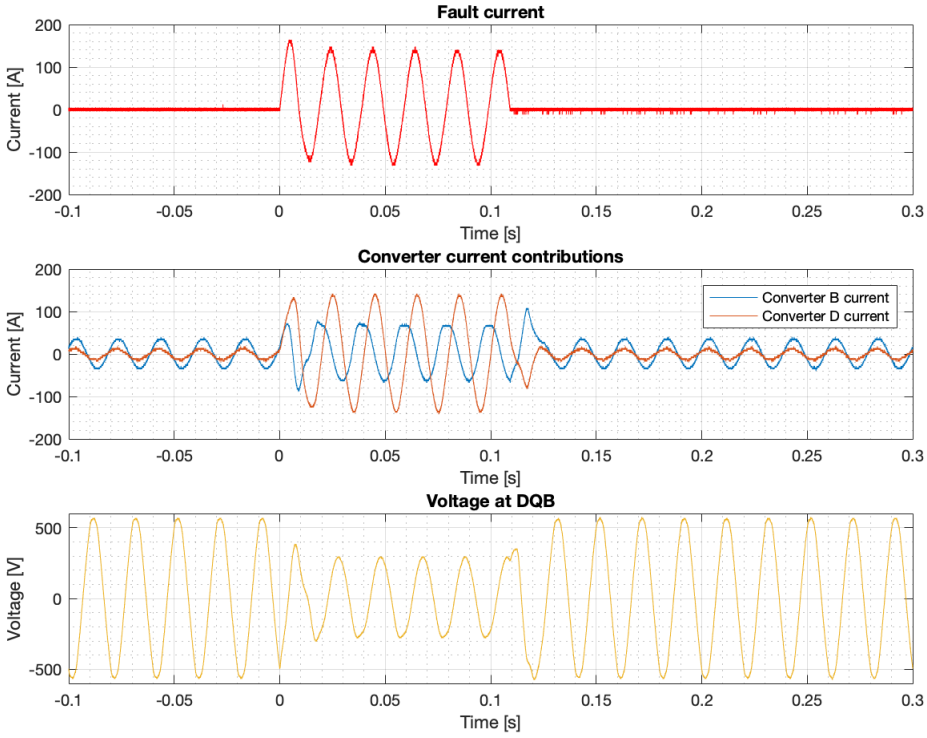

Figure 6.15: Control strategy 1 with I reg $K_P = 100$ %

Parameter	Value
I_{B_normal}	25 RMS [A]
I_{D_normal}	10 RMS [A]
I_{B_SC}	$\frac{1}{\sqrt{2}} \cdot 68 = 48.1$ RMS [A]
I_{D_SC}	$\frac{1}{\sqrt{2}} \cdot 138 = 97.6$ RMS [A]
I_{fault}	$\frac{1}{\sqrt{2}} \cdot 132 = 93.3$ RMS [A]
V_{drop}	$[1 - \frac{203.6}{402}] \cdot 100\% = 49.3$ %
$R_{\frac{I_{B\_SC}}{I_{D\_SC}}}$	$\frac{48.1}{97.6} = 0.49$

Table 6.5: Comparison parameters for control strategy 1 when I reg $K_P = 100\%$

By comparing figure 6.15 to the base case in figure 6.10, the characteristics of increasing the I reg K_P parameter are further confirmed. Firstly, the voltage drops more during the short-circuit when the proportional gain is higher. Secondly, the power-sharing between the converters increases when

the proportional gain is higher. Hence, the current output from each converter is shared more equally compared to figure 6.10.

Figure 6.16 illustrates the fault current, converter current contributions, and the voltage drop during the short-circuit when I reg $K_P = 200$ %. Moreover, table 6.6 summarizes the comparison parameters.

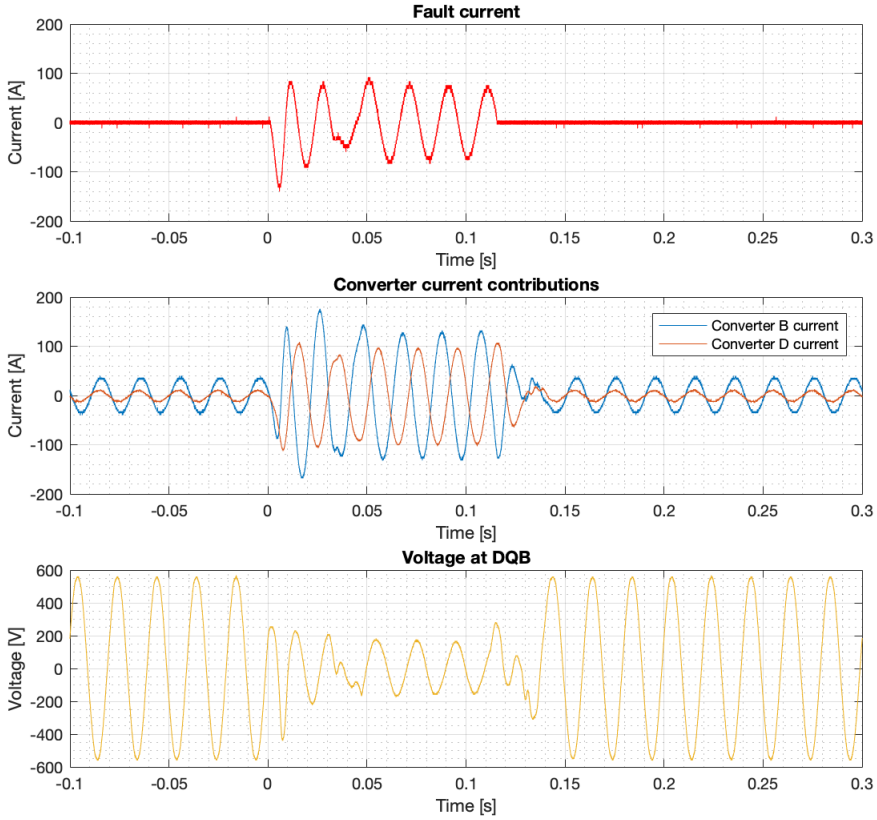

Figure 6.16: Control strategy 1 with I reg $K_P = 200$ %

Parameter	Value
I_{B_normal}	25 RMS [A]
I_{D_normal}	10 RMS [A]
I_{B_SC}	$\frac{1}{\sqrt{2}} \cdot$ 132 = 93.3 RMS [A]
I_{D_SC}	$\frac{1}{\sqrt{2}} \cdot \frac{107+103}{2}$ = 74.2 RMS [A]
I_{fault}	$\frac{1}{\sqrt{2}} \cdot$ 76 = 53.7 RMS [A]
V_{drop}	[1 - $\frac{113.1}{396}$] $\cdot$ 100% = 71.4 %
$R_{\frac{I_{B\_SC}}{I_{D\_SC}}}$	$\frac{93.3}{74.2} = 1.26$

Table 6.6: Comparison parameters for control strategy 1 when I reg K_P = 200%

The voltage level during the short-circuit is reduced compared to the previous test cases with lower I reg K_P values. Moreover, the converter B current even exceeds the current contribution from converter D during the short-circuit, in contrast to the previous test cases. The ratio between the converter currents is $R = \frac{93.34A}{74.25A} = 1.26$ when the proportional gain is 200 %.

The regulation systems of the converter takes a longer time to correlate to the new operating conditions when the proportional gain is 200 %. In reference to figure 6.16, the system voltage and the converter currents are unstable at the beginning of the short-circuit and right after the short-circuit is cleared. Thus, the converter regulation struggles to adjust to the new operating conditions when I reg K_P = 200 %. This converter behavior suggests that there is an upper limit of suitable proportional gain parameters. Hence, it is problematic if the PI controller in the grid-forming converter overcompensates for the deviation. The proportional gain of 200 % is therefore not particularly beneficial. Moreover, the converter B current also exceeds its current limit of 1000 pu, i.e., 90 RMS A. The current limit is further examined in section 6.3.6.

The effect of the proportional gain in the PI current regulator is equivalent to a resistor in series with the converter. This is illustrated in equation 6.13. So, a current deviation of 1 pu will give 1 pu voltage when K_p equals 100%. The relation between the proportional gain and resistance explains why the voltage is reduced when the proportional gain parameter increases. Hence, the grid-forming converter is made softer by increasing the proportional gain.

$$\Delta U = \Delta I \cdot R \tag{6.13a}$$

$$\Delta U = \Delta I \cdot Kp \tag{6.13b}$$

The proportional gain parameter also depends on the DC-voltage of the converter. The scaling error between the AC- and DC-side of the converter should therefore be accounted for. Equation 6.14 calculates the scaling error. However, the control of the DC-voltage is considered beyond the scope of this thesis, assuming Egston provides a stiff DC-voltage of 600 V DC to the converters.

$$Scalingerror = \frac{600VDC}{\sqrt{2} \cdot 400VAC} \approx 1.1 \tag{6.14}$$

This section presents the results when I reg K_p equals 0 %, 15 %, 50 %, and 200 % for control strategy 1. By comparing several plots with different I reg K_P values, the same tendencies are observed for control strategy 1. Firstly, the voltage level during the short-circuit inclines to drop when the proportional gain increases. Moreover, the power-sharing between the converters increases for higher proportional gain values. Another interesting observation is that the overall fault current is reduced when the proportional gain increases. It is therefore safe to say that I reg K_P affects the fault current and voltage level during short-circuits. Subsequently, this control parameter must be accounted for when implementing protective relays based on current and voltage measurements. Appendix C.2.3 presents additional test results when the proportional gain is 150 % for control strategy 1. The same characteristics are observed for this I reg K_p value, so this result supplements the main findings presented in this section. Table 6.20 summarizes all comparison parameters.

Control strategy 2

Figure 6.17 illustrates the fault current, the converter currents, and the voltage drop during the short-circuit when I reg $K_P = 0$ %. It is necessary to increase the original current trip level of converter D from 245 A to 345 A to prevent its immediate disconnection. The required current trip limit is lower compared to the first control strategy with the same I reg K_P value because the power-sharing between the converters is initially higher when converter B is grid-supporting.

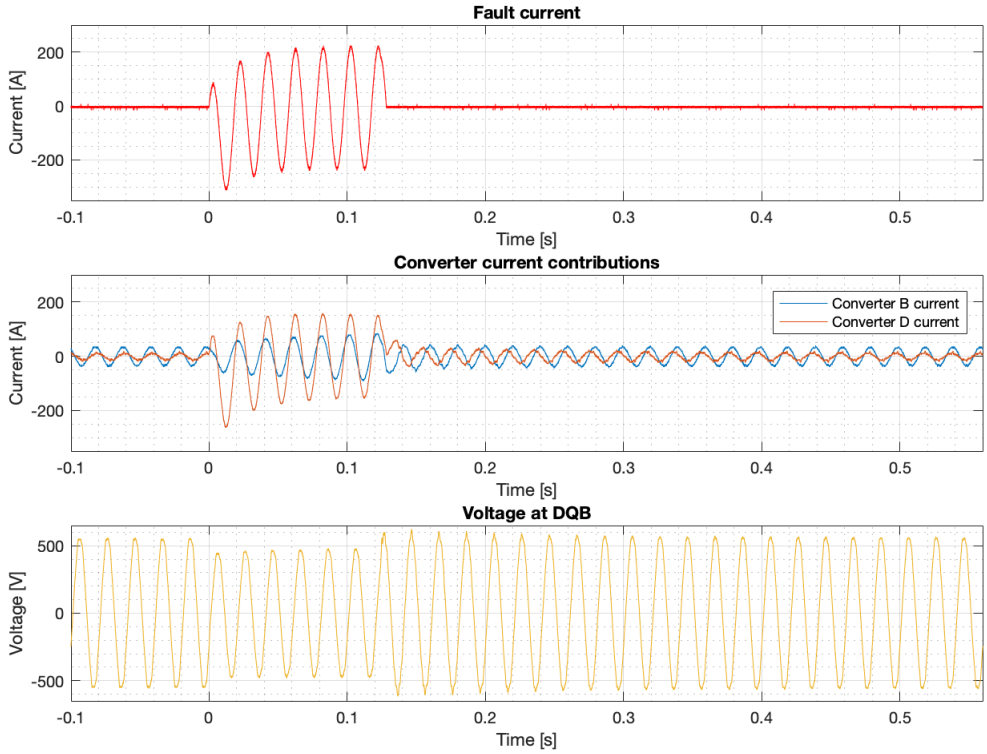

Figure 6.17: Control strategy 2 with I reg $K_P = 0$ %, I trip = 345

Similar to control strategy 1, the current from the grid-supporting converter is approximately 25 RMS A, whereas the converter contribution from the grid-forming converter D is approximately 10 A during normal operation. The other comparison parameters are summarized in table 6.7.

Parameter	Value
I_{B_normal}	25 RMS [A]
I_{D_normal}	10 RMS [A]
I_{B_SC}	$\frac{1}{\sqrt{2}} \cdot \frac{84+92}{2} = 62.2$ RMS [A]
I_{D_SC}	$\frac{1}{\sqrt{2}} \cdot \frac{152+156}{2} = 108.9$ RMS [A]
I_{fault}	$\frac{1}{\sqrt{2}} \cdot \frac{224+240}{2} = 164.0$ RMS [A]
V_{drop}	$[1 - \frac{339.4}{396}] \cdot 100\% = 14.3$ %
$R_{\frac{I_{B\_SC}}{I_{D\_SC}}}$	$\frac{62.2}{108.9} = 0.57$

Table 6.7: Comparison parameters for control strategy 2 when I reg $K_P = 0\%$

Compared to the base case in figure 6.11, the converter D current is increased, whereas the converter B current is reduced when I reg K_p is zero. Furthermore, the reduced proportional gain, i.e., the series resistance equivalent, explains the reduced voltage drop during the short-circuit. The aforementioned consequences of reducing I reg K_p for control strategy 2 are the same compared to control strategy 1. However, by comparing control strategy 1 and control strategy 2 during zero proportional gains in figure 6.12 and figure 6.17, it is evident that the power-sharing between the converters is improved during control strategy 2. The increased power-sharing during the second control strategy is reflected in the higher ratio between the converter currents. Additionally, the voltage drop is reduced for control strategy 2 because converter B produces reactive current to support the voltage. Moreover, the fault current is higher during the second control strategy and zero proportional gain.

Figure 6.18 illustrates the fault current, the converter currents, and the voltage drop during the short-circuit when I reg K_P is 15%. In contrast, it is not necessary to increase the original current trip level of converter D when I reg $K_P = 15$ % because converter B is now grid-supporting. Moreover, table 6.8 summarizes the comparison parameters.

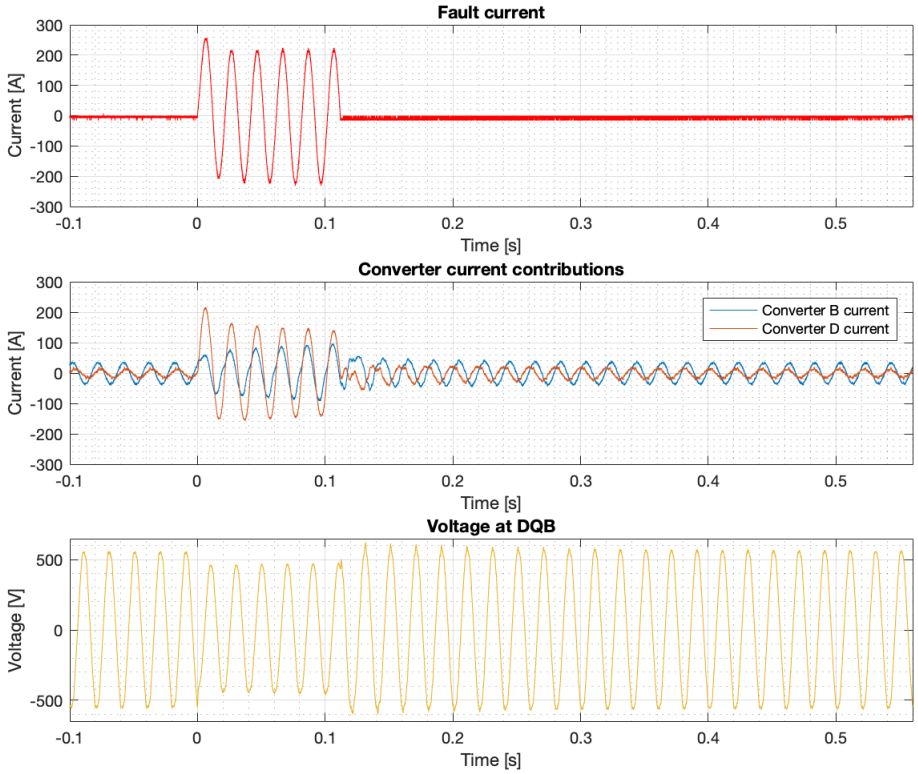

Figure 6.18: Control strategy 2 with I reg $K_P = 15$ %

Parameter	Value
I_{B_normal}	25 RMS [A]
I_{D_normal}	10 RMS [A]
I_{B_SC}	$\frac{1}{\sqrt{2}} \cdot \frac{96+92}{2} = 66.5$ RMS [A]
I_{D_SC}	$\frac{1}{\sqrt{2}} \cdot \frac{140+144}{2} = 100.4$ RMS [A]
I_{fault}	$\frac{1}{\sqrt{2}} \cdot \frac{224+232}{2} = 161.2$ RMS [A]
V_{drop}	$[1 - \frac{328.1}{396}] \cdot 100\% = 17.1$ %
$R_{\frac{I_{B\_SC}}{I_{D\_SC}}}$	$\frac{66.5}{100.4} = 0.66$

Table 6.8: Comparison parameters for control strategy 2 when I reg $K_P = 15\%$

The higher power-sharing between the converters is clearly illustrated by comparing figure 6.13 (control strategy 1) with figure 6.18 (control strategy 2) when I reg $K_P = 15$ %. Evidently, the $R_{\frac{I_{B\_SC}}{I_{D\_SC}}}$ ratio is 0.22 and 0.66 for control strategy 1 and control strategy 2, respectively. Additionally, the voltage drop is also reduced due to the voltage-support from converter B in the second control strategy.

Figure 6.19 illustrates the fault current, the converter currents, and the voltage drop during the short-circuit when I reg $K_P = 50\%$. Moreover, table 6.9 summarizes the comparison parameters.

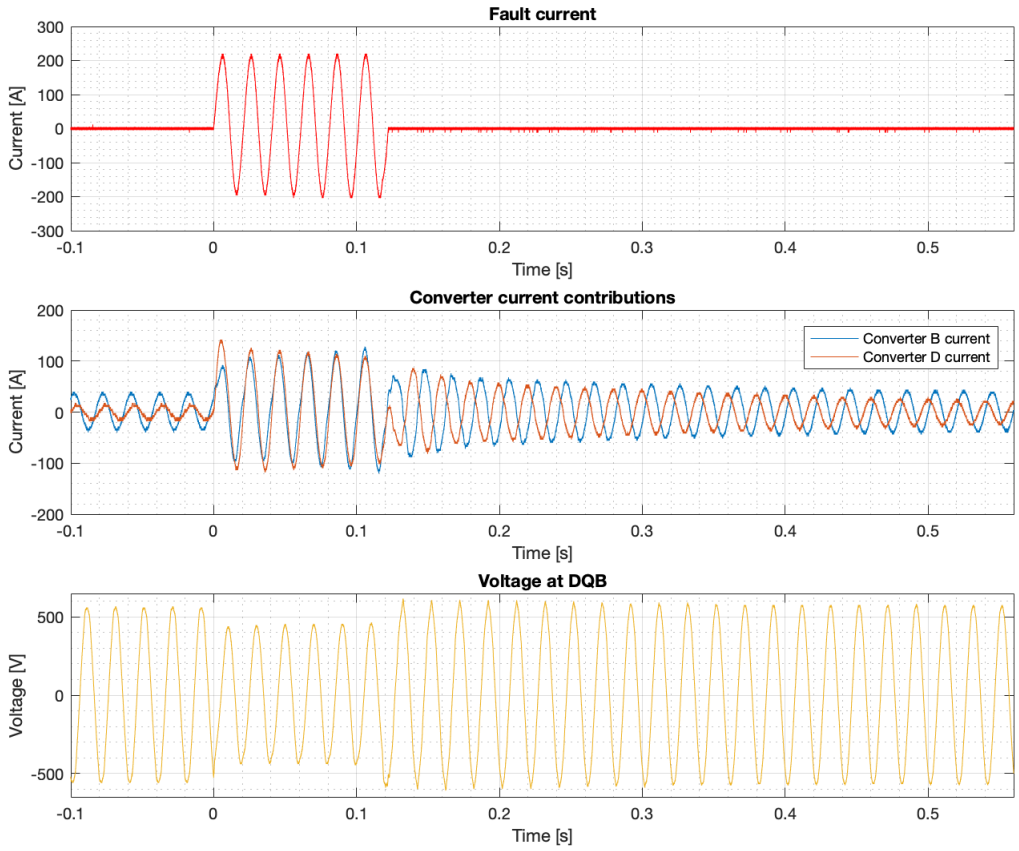

Figure 6.19: Control strategy 2 with I reg $K_P = 50$ %

Parameter	Value
I_{B_normal}	25 RMS [A]
I_{D_normal}	10 RMS [A]
I_{B_SC}	$\frac{1}{\sqrt{2}} \cdot \frac{128+112}{2} = 84.9$ RMS [A]
I_{D_SC}	$\frac{1}{\sqrt{2}} \cdot \frac{110+106}{2} = 76.4$ RMS [A]
I_{fault}	$\frac{1}{\sqrt{2}} \cdot \frac{220+204}{2} = 149.9$ RMS [A]
V_{drop}	$[1 - \frac{322.4}{402}] \cdot 100\% = 19.8$ %
$R_{\frac{I_{B\_SC}}{I_{D\_SC}}}$	$\frac{84.9}{76.4} = 1.11$

Table 6.9: Comparison parameters for control strategy 2 when I reg $K_P = 50\%$

For I reg $K_P = 50$ % during the second control strategy, the current outputs from converter B increases towards the end of the short-circuit. Thus, the voltage also increases during the short-circuit because the AC voltage regulator in converter B delivers more reactive current to support the voltage and feed the inductive fault.

Figure 6.20 illustrates the fault current, the converter currents, and the voltage drop during the short-circuit when I reg K_P is 100%. Moreover, table 6.10 summarizes the comparison parameters.

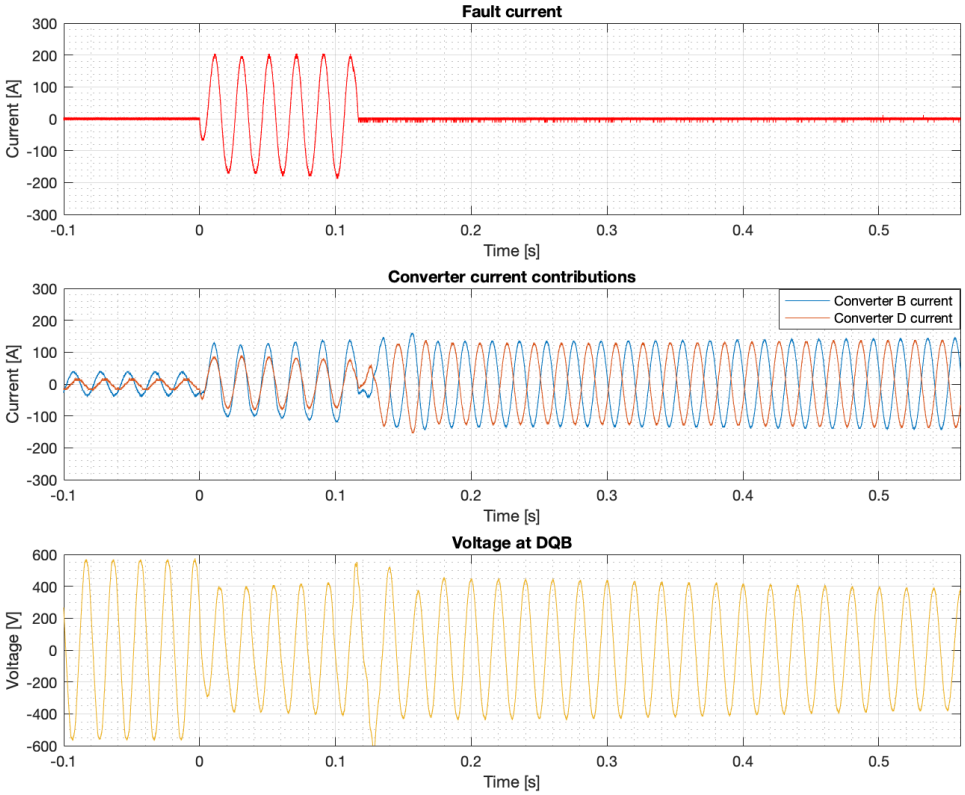

Figure 6.20: Control strategy 2 with I reg $K_P = 100$ %

Parameter	Value
I_{B_normal}	25 RMS [A]
I_{D_normal}	10 RMS [A]
I_{B_SC}	$\frac{1}{\sqrt{2}} \cdot \frac{140+120}{2} = 91.9$ RMS [A]
I_{D_SC}	$\frac{1}{\sqrt{2}} \cdot 78 = 55.2$ RMS [A]
I_{fault}	$\frac{1}{\sqrt{2}} \cdot \frac{204+180}{2} = 135.8$ RMS [A]
V_{drop}	$[1 - \frac{294.2}{402}] \cdot 100\% = 26.8$ %
$R_{\frac{I_{B\_SC}}{I_{D\_SC}}}$	$\frac{91.9}{55.2} = 1.66$

Table 6.10: Comparison parameters for control strategy 2 when I reg $K_P = 100\%$

After the under-voltage relay clears the short-circuit, the converters struggle to correlate to the new operating condition when the proportional gain is 100 %. In reference to figure 6.20, the system voltage is not maintained at 400 RMS A and decreases after the short-circuit is cleared. Moreover, the

converter currents are not back to their initial values before the short-circuit. Thus, the converter regulation struggles when I reg $K_P = 100$ % for control strategy 2, which indicates that there is an upper limit of suitable proportional gain values.

The same tendencies by changing the proportional gain are observed for control strategy 2; the voltage drop and the power-sharing between the converters decreases when the proportional gain is reduced. Additionally, the overall fault current level increases when the proportional gain is reduced.

By comparing the different control strategies for the same proportional gain values, it is evident that the grid-supporting strategy improves the power-sharing between the converters. Hence, the desired power-sharing between the converters are obtained for lower I reg K_P values if converter B is grid-supporting. In other words, a lower proportional gain is necessary if the second control strategy is implemented. Furthermore, the voltage during a short-circuit is much more maintained, and the fault current level is much higher during the second control strategy. All comparison parameters are summarized in table 6.20 and table 6.21 for control strategy 1 and control strategy 2, respectively.

There are thus two methods to achieve power-sharing between the converters in the system; increase the proportional gain when converter B is grid-following or change the control strategy of converter B to grid-supporting. Power-sharing is necessary to avoid the immediate disconnection of the grid-forming converter. So, unless the current tolerance is extremely exaggerated for the converter, a droop should be implemented to make the grid-forming converter softer.

The droop effect from I reg K_p increases the power-sharing between the converters. However, the droop also reduces the fault current and voltage level during short-circuits. In other words, the proportional gain parameter affects crucial measurement signals to the protective system. Subsequently, the protection relays must account for the proportional gain for each control strategy because it affects the fault current and voltage level during short circuits. In this testing, a 1000 ms three-phase short-circuit is applied, but the fault current is zero before the duration of the short-circuit has passed for every test case. Consequently, the under-voltage operates for all test cases and is a suitable protection function for islanded inverter-dominated microgrids because the voltage immediately drops during a short-circuit. Nevertheless, the lack of selectivity from the under-voltage relay is the main drawback.

6.3.4 Changing the active power reference of converter B

This section investigates the impact of increasing the active power reference of converter B for each control strategy independently. Subsequently, this section tests if P_{ref} affects the currents and voltages during short-circuits. The active power reference is now 500 pu, so the active power output from converter B is ideally:

$$P = 500pu \cdot \frac{1}{1000pu} \cdot \sqrt{3}(90A \cdot 400V) = 31.2kW \tag{6.15}$$

Note that the signals are scaled in a per-unit system with 1000 as 1 pu.

Control strategy 1

Figure 6.21 illustrates the converter currents, the fault current, and the voltage drop when P_{ref} of converter B is 500 pu. The other control settings are equal to the original settings in table 5.10.

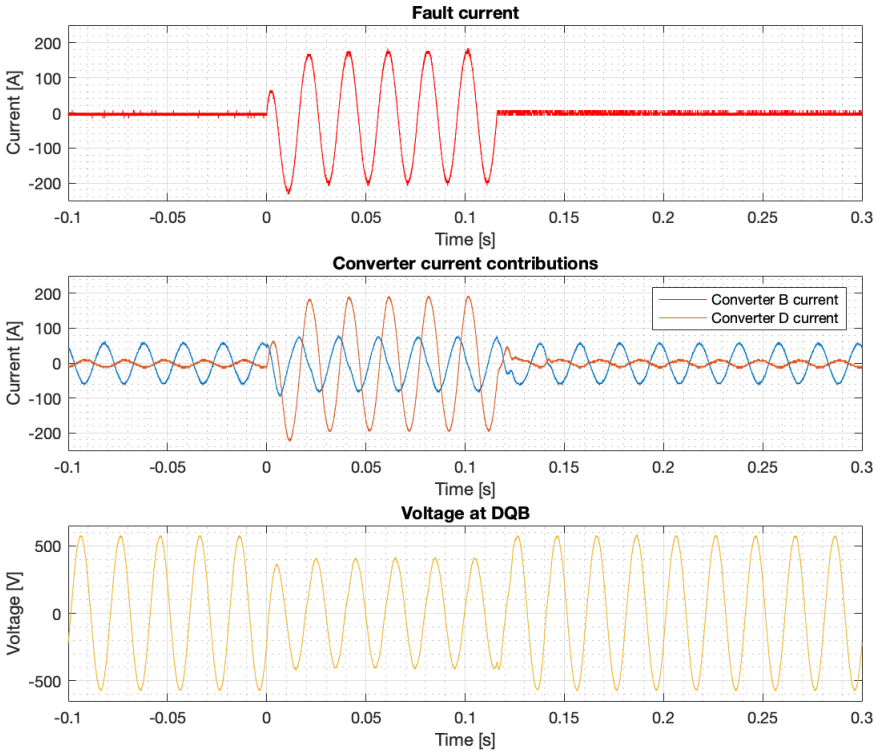

Figure 6.21: Control strategy 1 with $Pref$ = 500 pu of converter B

During normal operation, the grid-following converter B with P_{ref} = 500 pu has an AC RMS current of approximately 40 A at the converter filter due to the increased active power output. Subsequently, the converter contribution from the grid-forming converter D is reduced to approximately 8 RMS A. Table 6.11 summarizes the comparison parameters.

Parameter	Value
I_{B_normal}	40 RMS [A]
I_{D_normal}	8 RMS [A]
I_{B_SC}	$\frac{1}{\sqrt{2}} \cdot \frac{76+84}{2} = 56.6$ RMS [A]
I_{D_SC}	$\frac{1}{\sqrt{2}} \cdot \frac{192+196}{2} = 137.2$ RMS [A]
I_{fault}	$\frac{1}{\sqrt{2}} \cdot \frac{184+208}{2} = 138.6$ RMS [A]
V_{drop}	$[1 - \frac{291.3}{396}] \cdot 100\% = 26.4$ %
$R_{\frac{I_{B\_SC}}{I_{D\_SC}}}$	$\frac{56.6}{137.2} = 0.41$

Table 6.11: Comparison parameters for control strategy 1 when $Pref$ of converter B is 500 pu

Compared to the base case of control strategy 1 in figure 6.10, the current output from converter B increases because its active power reference is increased. On the other hand, the fault current and voltage level during the short-circuit are not affected by the increased active power reference. Hence, this input parameter is not of great interest because the input measurement signals to the protective relay remain unaffected.

Control strategy 2

Figure 6.22 illustrates the converter currents, the fault current, and the voltage drop when P_{ref} of converter B is 500 pu. The other control settings are equal to original settings in table 5.10.

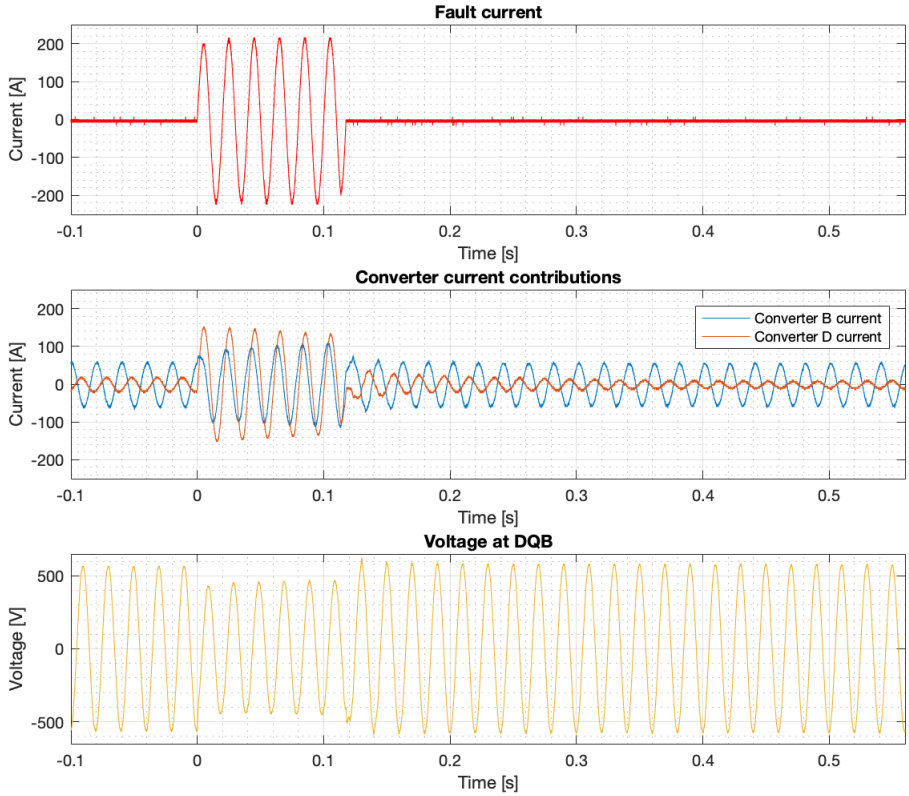

Figure 6.22: Control strategy 2 with $Pref$ = 500 pu of converter B

During normal operation, the grid-supporting converter B with $P_{ref} = 500$ pu has an AC RMS current of approximately 42 A at the converter filter due to the increased active power output. Table 6.12 summarizes the comparison parameters.

Parameter	Value
I_{B_normal}	42 RMS [A]
I_{D_normal}	11 RMS [A]
I_{B_SC}	$\frac{1}{\sqrt{2}} \cdot 112 = 79.2$ RMS [A]
I_{D_SC}	$\frac{1}{\sqrt{2}} \cdot 136 = 96.2$ RMS [A]
I_{fault}	$\frac{1}{\sqrt{2}} \cdot \frac{216+224}{2} = 155.6$ RMS [A]
V_{drop}	$[1 - \frac{328.1}{402}] \cdot 100\% = 18.4$ %
$R_{\frac{I_{B\_SC}}{I_{D\_SC}}}$	$\frac{79.2}{96.2} = 0.82$

Table 6.12: Comparison parameters for control strategy 2 when $Pref$ of converter B is 500 pu

Compared to the base case of control strategy 2 in figure 6.11, the current output from converter B increases because its active power reference is increased. However, the fault current and voltage level during the short-circuit are not significantly affected by the increased active power reference, which is similar to the first control strategy. Hence, this input parameter is not of great interest because the input measurement signals to the protective relay remain unaffected. The reactive control of the grid-supporting converter B is constructed by the AC voltage regulator. Even though the active power reference is increased, converter B does not produce more reactive current because the active power control and the AC voltage regulator are two separate controllers. Hence, the increased active power reference leads to a higher active current, but the reactive current output, which supports the voltage, is unaffected.

To summarize, the fault current and voltage level during the short-circuit are not significantly affected by the active power reference for both control strategies. Consequently, this input parameter is not of great importance regarding the protection strategy. However, the available active power output is crucial information in order to meet the load demand at all times.

6.3.5 Changing the load

This section examines the influence of increasing the load to the high load in equation 5.4. The converter behavior is described separately for each control strategy. The system load is not a converter control parameter; however, it is interesting to test how the increased load affects the converter behavior because the overall load in the system dynamically changes.

Control strategy 1

Figure 6.23 shows the fault current, the converter currents, and the voltage drop during the short-circuit for the original settings in table 5.10, but the load is increased to 55 kW. Moreover, it is important to mention that the current trip level of converter D is increased to 345 A to avoid the immediate tripping of the over-current converter function. Table 6.13 summarizes the comparison parameters.

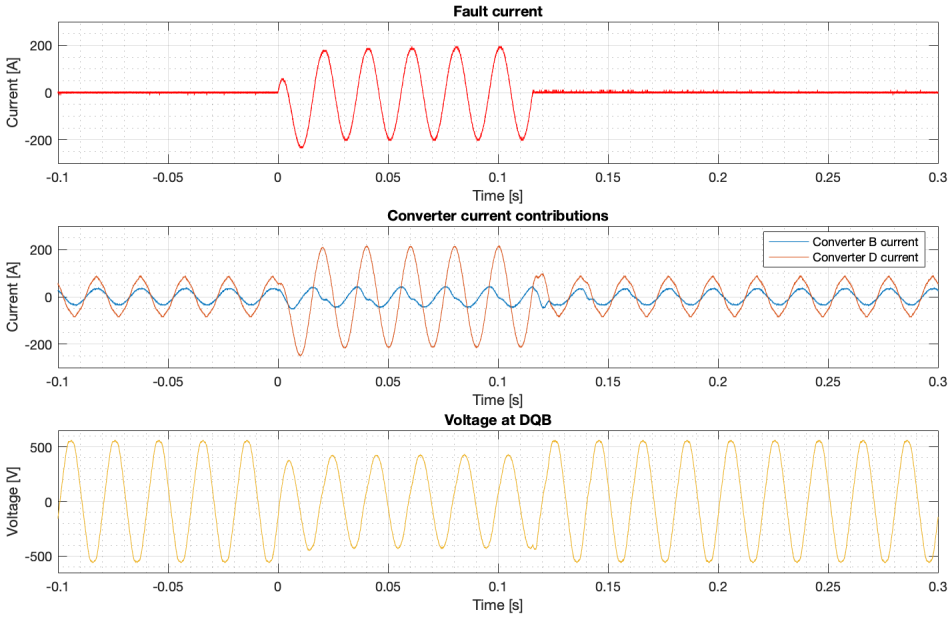

Figure 6.23: Control strategy 1 with original settings during high load

Parameter	Value
I_{B_normal}	25 RMS [A]
I_{D_normal}	58 RMS [A]
I_{B_SC}	$\frac{1}{\sqrt{2}} \cdot 44 = 31.1$ RMS [A]
I_{D_SC}	$\frac{1}{\sqrt{2}} \cdot 218 = 154.1$ RMS [A]
I_{fault}	$\frac{1}{\sqrt{2}} \cdot 196 = 138.6$ RMS [A]
V_{drop}	$[1 - \frac{299.8}{402}] \cdot 100\% = 25.4$ %
$R_{\frac{I_{B\_SC}}{I_{D\_SC}}}$	$\frac{31.1}{154.1} = 0.20$

Table 6.13: Comparison parameters for control strategy 1 with original settings during high load

The low load draws approximately 32 RMS A, whereas the high load draws approximately 79 RMS A (see the calculations in equation 5.1 to 5.4). During normal operation, the grid-following converter

B with P_{ref} = 300 pu has an AC RMS current of approximately 25 A at the converter filter. The converter contribution from the grid-forming converter D is increased to approximately 58 RMS A in order to feed the high load. Accordingly, the current contribution from converter D is increased to supply the additional 50 RMS A during high load. The initial power-sharing effect from setting I reg K_p to 25 % is not sufficient during high load due to the additional current contribution from converter D. The increased current output explains the required current trip level of 345 A of converter D.

The current contribution from converter B is equivalent to the base case in figure 6.10 due to equal active power references. The control system keeps the active power constant to 300 pu regardless of the increased load or other input parameters. The active power control is also evident during the short-circuit because the current output from converter B only increases concerning the voltage drop, and the active power output is kept constant. The grid-following converter with P/Q control only responds to the changes in the power reference and is thus not affected by the increased load.

Despite the increased converter D current and subsequently the decreased ratio between the converter currents, this test case is otherwise quite similar to the base case with the original values. The fault current and voltage level during the short-circuit, which are important parameters regarding the microgrid protection scheme, are not affected by the increased load. Hence, this input parameter is not of great interest as long as the fault current and voltage level during the short-circuit remain unaffected.

Control strategy 2

Figure 6.24 shows the fault current, the converter currents, and the voltage drop during the short-circuit for the original settings in table 5.10, but the load is increased to 55 kW. The current trip level of converter D is increased to 345 A, similar to control strategy 1 with the high load. Moreover, table 6.14 summarizes the rest of the comparison parameters.

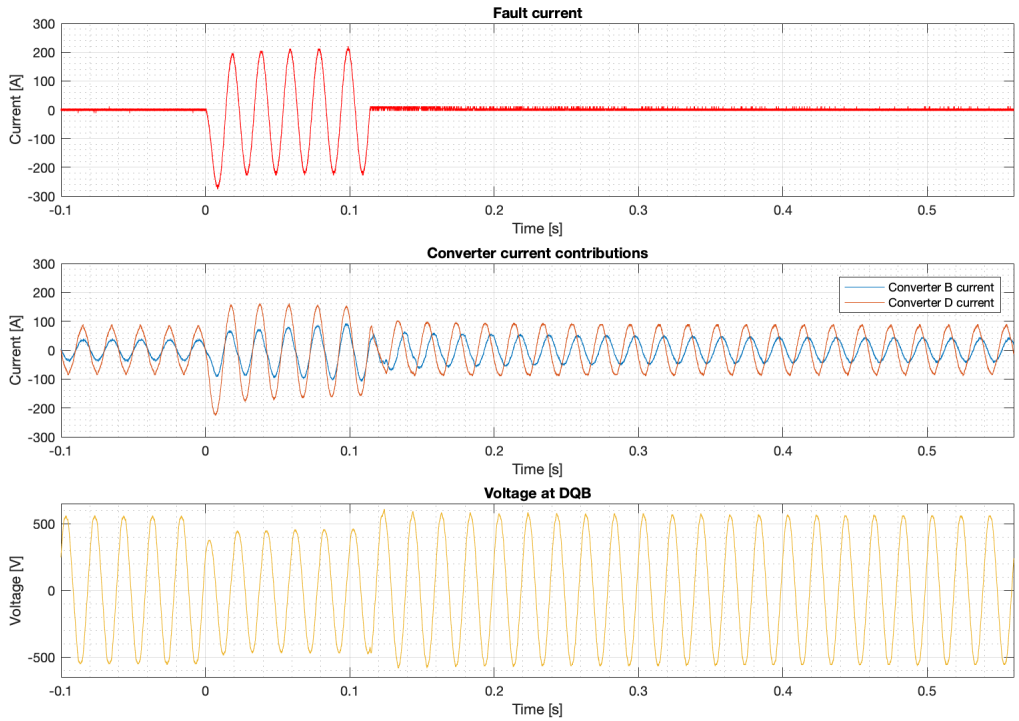

Figure 6.24: Control strategy 2 with original settings during high load

Parameter	Value
I_{B_normal}	25 RMS [A]
I_{D_normal}	58 RMS [A]
I_{B_SC}	$\frac{1}{\sqrt{2}} \cdot \frac{92+104}{2} = 69.3$ RMS [A]
I_{D_SC}	$\frac{1}{\sqrt{2}} \cdot \frac{154+162}{2} = 111.7$ RMS [A]
I_{fault}	$\frac{1}{\sqrt{2}} \cdot \frac{220+228}{2} = 158.4$ RMS [A]
V_{drop}	$[1 - \frac{330.9}{402}] \cdot 100\% = 17.6$ %
$R_{\frac{I_{B\_SC}}{I_{D\_SC}}}$	$\frac{69.3}{111.7} = 0.62$

Table 6.14: Comparison parameters for control strategy 2 when original settings during high load

Converter B is now grid-supporting with an AC regulator as reactive control. Thus, the reactive current output is not kept constant at zero in contrast to the grid-following converter. Nevertheless, the increased load is purely resistive, so only active current is fed to the load. Consequently, the reactive control is not affected by the increased load, and the reactive current output from converter B remains unaffected. Moreover, the active power output from converter B is kept constant concerning the voltage drop regardless of the increased load. As a result, the increased load does not affect the behavior of converter B.

This test case is quite similar to the base case of control strategy 2, despite the reduced power-sharing between the converters, which explains the required current trip level of converter D. The fault current and voltage level during the short-circuit, which are important parameters regarding the microgrid protection scheme, are hardly affected by the increased load. Hence, this input parameter is not of great interest as long as the fault current and voltage level during the short-circuit remain unaffected.

The microgrid control system should continuously evaluate and prioritize loads in order to maintain the balance between supply and demand. However, the active power output from converter B is constant for both control strategies due to the active power control. So, converter B cannot increase its power output during high active power demand, i.e., during a high resistive load. The voltage and fault current level during increased load are similar to the base case for both strategies, so this input parameter is not of great interest.

6.3.6 Changing the current limits of converter B

In this section, the positive and negative limits of the active and reactive currents are changed to investigate if this control parameter affects the voltage and fault current. Normally the current limit is -1000 and 1000 pu, i.e., ± 90 RMS A. Hence, if the current limit is reduced to -500 and 500 pu, the upper and lower current limit is ± 45 RMS A. Note that the signals are scaled in a per-unit system with 1000 as 1 pu.

Control strategy 1

Figure 6.25 shows the fault current, the converter currents, and the voltage drop during the short-circuit for the original settings in table 5.10, but the current limit of converter B is reduced to ± 250 pu. Consequently, the AC RMS current limit is around ± 22.5 A.

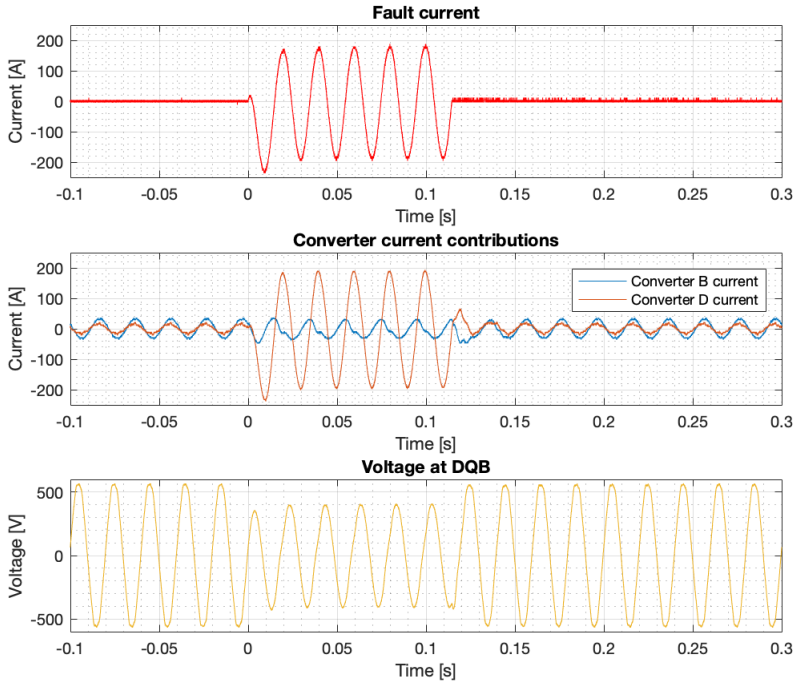

Figure 6.25: Control strategy 1 when the current limit is ± 250 [pu] and I reg $K_P = 25\%$

During normal operation, the current output from the grid-following is approximately 23 RMS A, whereas the converter contribution from the grid-forming converter D is approximately 13 RMS A. Compared to the base case in figure 6.10, the converter B current is decreased due to the current limit, whereas the converter D current is increased to provide the voltage reference of 400 RMS V and meet the load demand of 24.4 kW. Table 6.15 summarizes the comparison parameters.

Parameter	Value
I_{B_normal}	23 RMS [A]
I_{D_normal}	13 RMS [A]
I_{B_SC}	$\frac{1}{\sqrt{2}} \cdot$ 32 = 22.6 RMS [A]
I_{D_SC}	$\frac{1}{\sqrt{2}} \cdot$ 194 = 137.2 RMS [A]
I_{fault}	$\frac{1}{\sqrt{2}} \cdot \frac{188+196}{2}$ = 135.8 RMS [A]
V_{drop}	$[1 - \frac{288.5}{396}] \cdot 100\%$ = 27.1 %
$R_{\frac{I_{B\_SC}}{I_{D\_SC}}}$	$\frac{22.6}{137.2} = 0.16$

Table 6.15: Comparison parameters for control strategy 1 when the current limit is ± 250 [pu] and I reg K_P = 25%

After the short-circuit is applied, the converter B current is still limited to approximately I_{B_SC} = 22.6 RMS A, whereas the RMS-value of the converter D current is I_{D_SC} = 137.2 A at the end of the short-circuit. Converter B is implemented as a grid-following converter with P/Q control for P = 300 pu and Q = 0. In order to keep its active power output constant, the current output changes concerning the voltage. However, its current output is now restrained to the current limit. Compared to the base case, the voltage drop and the fault current are hardly affected by the decreased current limit of converter B. Consequently, this control parameter is so far not of great importance for control strategy 1.

The ± 500 pu current limit of converter B is also tested when the active current reference is 300 pu. However, the current output from converter B never exceeds its current limit during the short-circuit, so this case is more or less identical to the base case in figure 6.10. Figure C.6 in appendix C.2.4 illustrates the measurements during the ± 500 pu current limit of converter B, while table C.2 lists the comparison parameters. Table 6.20 also summarizes the comparison parameters for this case.

It is also interesting to validate the current limit when the active power reference of converter B is increased to 1000 pu. Figure C.7 in appendix C.2.4 shows the test case when the active power reference and the current limit of converter B are 1000 pu and ± 250 pu, respectively. Nevertheless, the current output is reduced before and during the short-circuit due to the current limit of ± 250 pu. Thus, this situation is more or less equivalent to figure 6.25 due to the same current limit. The comparison parameters are listed in table C.3 in the appendix, but also summarized in table 6.20.

Figure 6.26 shows the fault current, the converter currents, and the voltage drop when I reg K_p is 100 % to validate the effect of the current limit during control strategy 1. The active power reference and the current limit of converter B are 300 pu and ± 250 pu, respectively. Consequently, the AC RMS current limit is around ± 22.5 A. Table 6.16 summarizes the comparison parameters.

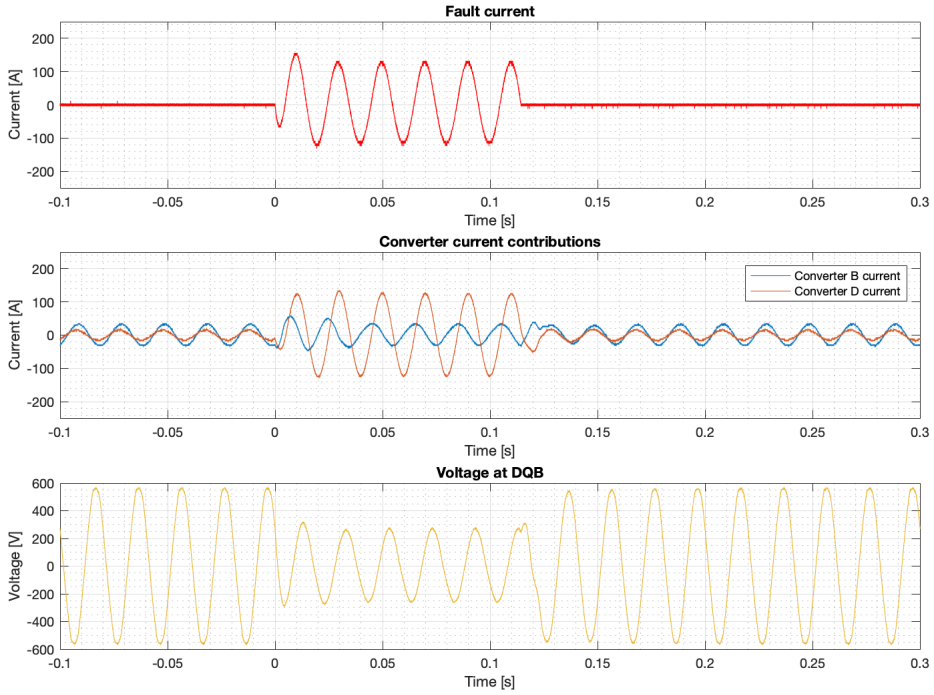

Figure 6.26: Control strategy 1 when the current limit is ± 250 [pu], I reg $K_P = 100\%$, and $P_{ref} = 300$ pu

Parameter	Value
I_{B_normal}	23 RMS [A]
I_{D_normal}	13 RMS [A]
I_{B_SC}	$\frac{1}{\sqrt{2}} \cdot 32 = 22.6$ RMS [A]
I_{D_SC}	$\frac{1}{\sqrt{2}} \cdot 126 = 89.1$ RMS [A]
I_{fault}	$\frac{1}{\sqrt{2}} \cdot \frac{132+124}{2} = 90.5$ RMS [A]
V_{drop}	$[1 - \frac{192.3}{396}] \cdot 100\% = 51.4$ %
$R_{\frac{I_{B\_SC}}{I_{D\_SC}}}$	$\frac{22.6}{137.2} = 0.25$

Table 6.16: Comparison parameters for control strategy 1 when the current limit is ± 250 [pu] and I reg $K_P = 100\%$

After the short-circuit is applied, the converter B current is still limited to approximately $I_{B\_SC} = 22.6$ RMS A, whereas the RMS-value of the converter D current is $I_{D\_SC} = 89.1$ A at the end of the short-circuit. Compared to the test case with I reg $K_p = 100$ % and current limit of ± 1000 pu in figure 6.15 and table 6.5, the voltage drop and the fault current are hardly affected by the decreased converter B current limit. Nevertheless, this test case differs from the base case in figure 6.10 due to the changed proportional gain parameter. The influence of the proportional gain value on the voltage and fault current level is therefore further confirmed. Subsequently, the I reg K_p parameter is of great importance regarding the protection scheme.

Based on the test cases above, it is evident that the current limit does not affect the protection measurements during control strategy 1. The only difference between figure 6.10 and figure 6.25 is the reduced current limit in the latter figure. As illustrated, the voltage and fault current level are equivalent for both converter controls, so it is clear that the influence of the current limit is negligible during control strategy 1.

Control strategy 2

Figure 6.27 shows the fault current, the converter currents, and the voltage drop during the short-circuit for the original settings in table 5.10, but the current limit for converter B is reduced to ± 250 pu. Moreover, table 6.17 summarizes the comparison parameters.

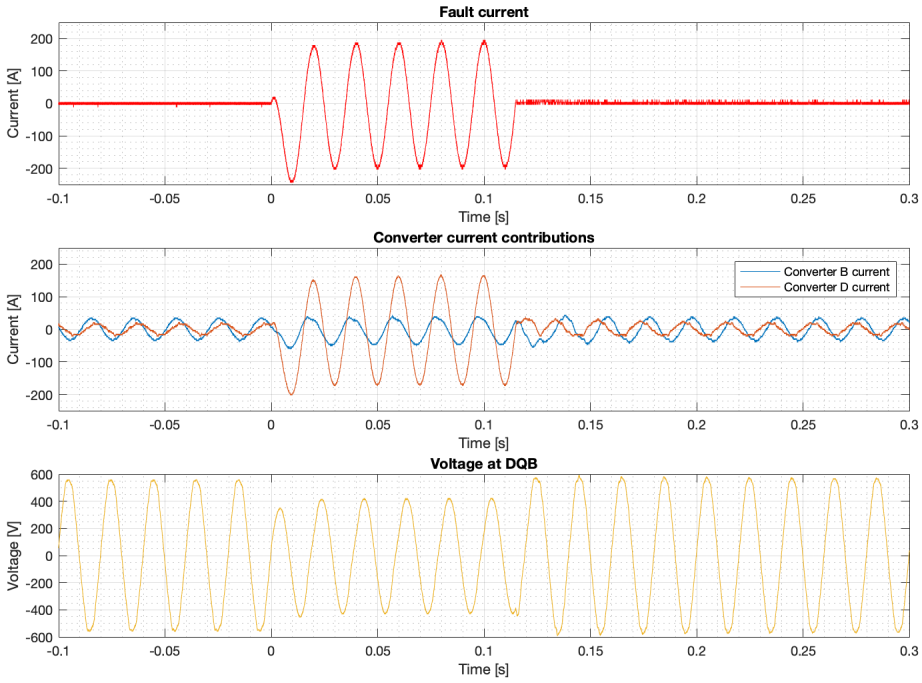

Figure 6.27: Control strategy 2 when the current limit is ± 250 [pu] and I reg $K_P = 25\%$

Parameter	Value
I_{B_normal}	23 RMS [A]
I_{D_normal}	13 RMS [A]
I_{B_SC}	$\frac{1}{\sqrt{2}} \cdot 36 = 25.5$ RMS [A]
I_{D_SC}	$\frac{1}{\sqrt{2}} \cdot \frac{166+170}{2} = 118.8$ RMS [A]
I_{fault}	$\frac{1}{\sqrt{2}} \cdot 196 = 138.6$ RMS [A]
V_{drop}	$[1 - \frac{302.6}{402}] \cdot 100\% = 24.7$ %
$R_{\frac{I_{B\_SC}}{I_{D\_SC}}}$	$\frac{25.5}{118.8} = 0.21$

Table 6.17: Comparison parameters for control strategy 2 when the current limit is ± 250 [pu] and I reg $K_P = 25\%$

After the short-circuit is applied, the converter B current is limited to approximately $I_{B\_SC} = 25.5$ RMS A, whereas the RMS-value of the converter D current increases to $I_{D\_SC} = 118.8$ A at the end

of the short-circuit. Compared to the base case, the decreased current limit of converter B affects the voltage and the fault current level. The AC voltage regulator controls the reactive current because converter B is now grid-supporting. However, the output current is limited to 250 pu, so it does not offer the same support compared to the base case. Moreover, the fault current is decreased due to limited current output from converter B. In contrast, the current limit control parameter is important for control strategy 2. As a result, the ± 500 pu current limit of converter B is tested in figure 6.28 to examine the voltage when the reactive current output from converter B is less restraint.

Figure 6.28 shows the fault current, the converter currents, and the voltage drop during the short-circuit for the original settings in table 5.10, but the current limit for converter B is reduced to ± 500 pu. Consequently, the AC RMS current limit is around ± 45 A. Note that the signals are scaled in a per-unit system with 1000 as 1 pu.

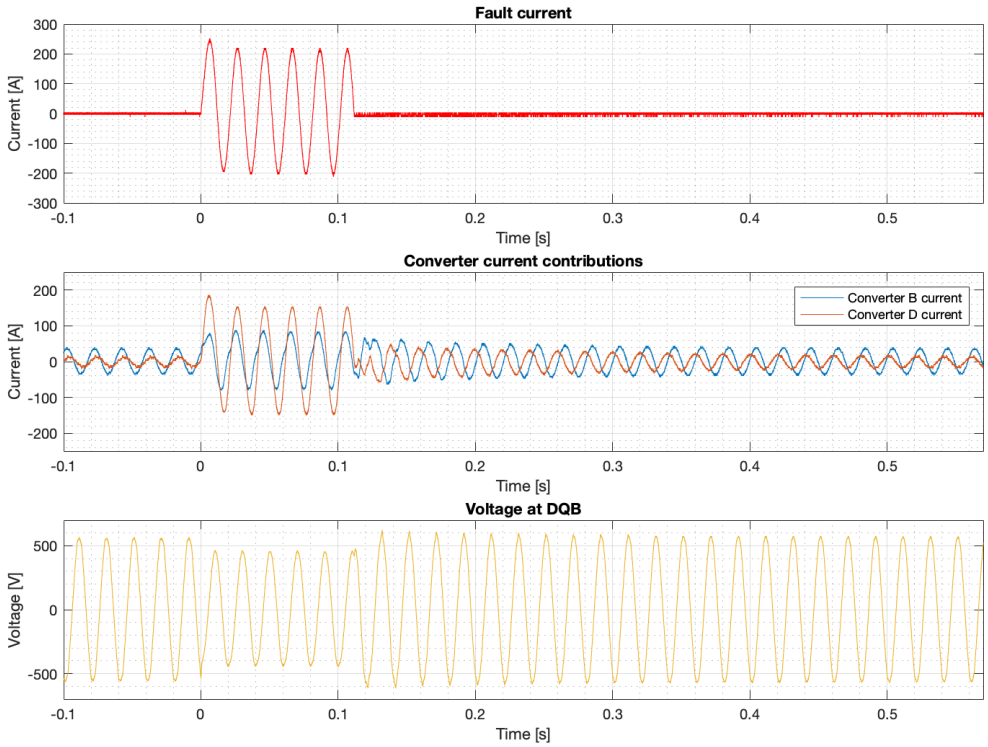

Figure 6.28: Control strategy 2 when the current limit is ± 500 [pu] and I reg $K_P = 25\%$

During normal operation, the converter currents are equal to the base case in figure 6.11. However, the current limit of converter B is exceeded during the short-circuit, so the current is reduced in the event of faults. Table 6.18 summarizes the comparison parameters.

Parameter	Value
I_{B_normal}	25 RMS [A]
I_{D_normal}	10 RMS [A]
I_{B_SC}	$\frac{1}{\sqrt{2}} \cdot 76 = 53.7$ RMS [A]
I_{D_SC}	$\frac{1}{\sqrt{2}} \cdot 150 = 106.1$ RMS [A]
I_{fault}	$\frac{1}{\sqrt{2}} \cdot \frac{220+204}{2} = 149.9$ RMS [A]
V_{drop}	$[1 - \frac{319.6}{396}] \cdot 100\% = 19.3$ %
$R_{\frac{I_{B\_SC}}{I_{D\_SC}}}$	$\frac{53.7}{106.1} = 0.51$

Table 6.18: Comparison parameters for control strategy 2 when the current limit is ± 500 [pu] and I reg $K_P = 25\%$

The voltage and fault current level are similar to the base case of control strategy 2 when the current limit is ± 500 pu. The offered voltage support indicates that the current limit of 500 pu does not restrain the reactive current from converter B. Hence, the current limit does not prevent the voltage-support.

Figure 6.29 shows the fault current, the converter currents, and the voltage drop when I reg K_p is 100 % to examine the influence of the current limit during a higher proportional gain value. The active power reference and the current limit of converter B are 300 pu and ± 250 pu, respectively. Moreover, table 6.19 summarizes the comparison parameters.

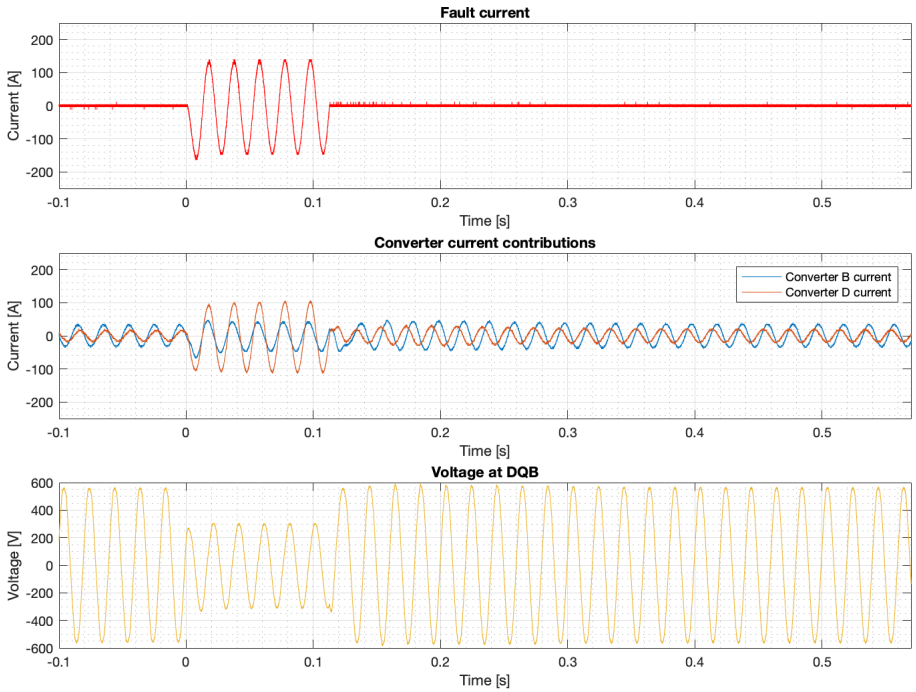

Figure 6.29: Control strategy 2 when the current limit is ± 250 [pu], I reg $K_P = 100\%$, and $P_{ref} =$ 300 pu

Parameter	Value
I_{B_normal}	23 RMS [A]
I_{D_normal}	13 RMS [A]
I_{B_SC}	$\frac{1}{\sqrt{2}} \cdot \frac{40+44}{2} = 29.7$ RMS [A]
I_{D_SC}	$\frac{1}{\sqrt{2}} \cdot \frac{106+114}{2} = 77.8$ RMS [A]
I_{fault}	$\frac{1}{\sqrt{2}} \cdot 140 = 99.0$ RMS [A]
V_{drop}	$[1 - \frac{217.8}{402}] \cdot 100\% = 45.8$ %
$R_{\frac{I_{B\_SC}}{I_{D\_SC}}}$	$\frac{29.7}{77.8} = 0.38$

Table 6.19: Comparison parameters for control strategy 2 when the current limit is ± 250 [pu] and I reg $K_P = 100\%$

After the short-circuit is applied, the converter B current is still limited to approximately $I_{B\_SC} = 22.6$ RMS A, whereas the RMS-value of the converter D current is $I_{D\_SC} = 77.8$ A at the end of the short-circuit. Compared to the case with I reg $K_p = 100$ % and current limit of ± 1000 pu in figure 6.20 and table 6.10, the converter B current is substantial reduced due to the current limit. Subsequently, the voltage is reduced due to the limited voltage support from converter B during the short-circuit. Moreover, the fault current is reduced from 135.8 to 99.0 RMS A. Thus, the current limit affects the input measurement signals to the protective relays, and must accordingly be considered when developing the protection scheme.

Based on the test cases above, it is evident that the current limit affects the protection parameters for control strategy 2, in contrast to control strategy 1. The current limit affects the voltage and fault current level, which are important parameters regarding the protection scheme. All comparison parameters are listed in table 6.21. Overall, the limited current output from the grip-supporting converter affects the voltage due to the restricted reactive current that normally supports the voltage. Moreover, the fault current decreases due to limited converter B current. Subsequently, the protection scheme needs to consider the current limit parameter for control strategy 2.

6.4 Summary of the results

The main findings from the laboratory tests are presented in section 6.4.1, while section 6.4.2 summarizes the influence of converter control separately for each control strategy.

6.4.1 The main findings

One of the main findings from the laboratory testing is that the grid-forming converter does not maintain the voltage magnitude constant at 400 RMS V during load changes. Consequently, the passive islanding detection method based on local voltage measurements does not differentiate between islanding, increased load, and short-circuit events. Moreover, the voltage drop during the islanding event also depends on the power contribution from the "grid-emulating" converter C. The undervoltage digital relay may also misinterpret the voltage drop during islanding and increased load as a fault condition. As a result, an active islanding detection method based on the direct transfer signal is implemented. The relays communicate via IEC61850 GOOSE communication, and the relays can remotely control the contactors on the AC bus-bars. Communication and external control of switches is fundamental in order to implement a protection scheme applicable in both microgrid operation modes.

Another important finding is that the fault current magnitude differs in grid-connected mode and

islanded mode. The fault current level is of particular interest regarding the over-current relay protection. Consequently, the over-current relay only trips during grid-connected mode for the converter settings in section 6.2. In other words, the relay does not operate in islanded mode when the pick-up setting in the over-current relay is configured based on short-circuit contribution from the utility grid. Thus, the need for adaptive microgrid protection is demonstrated, and the digital relay must switch to the under-voltage protection function during the islanded microgrid.

However, the over-current relay does not operate for every short-circuit even if the microgrid is grid-connected as discussed in section 6.2. The main reason for this is that the main supply is represented by another power electronic converter which does not contribute with large short-circuits compared to large synchronous generators. Additionally, the fault currents are significantly affected by the implemented control scheme and its control settings. However, the under-voltage relay operates to every short-circuit during islanded mode throughout section 6.3. In this laboratory testing, the voltage always drops during short-circuits, while the converter currents are unpredictable and highly affected by the converter control. Consequently, the short-circuit is always detected by the under-voltage relay, whereas the over-current is not always operating. Thus, the under-voltage protection function seems more suitable in inverter-dominated microgrids compared to the over-current relays with only one group setting.

The tripping of the internal protection functions within the converters, e.g., the over-current or over-frequency function, is strongly related to the converter settings. In other words, specific converter settings are necessary in order to avoid the immediate disconnection of the converter. The current trip level of the grid-forming converter is directly linked to its tolerance of high fault currents, and an increased trip level enables the converter to stay connected during faults. The grid-forming converter sets the amplitude and frequency of the reference voltage, so the rest of the system will lose the voltage reference if the grid-forming converter disconnects.

An important finding is that the fault current and voltage level, which are of particular interest concerning the over-current and under-voltage relay, depend on the implemented converter control. The implemented control scheme, i.e., the grid-following and grid-supporting control, are based on different active and reactive controllers that affect the currents and voltages in different ways. Additionally, the control settings within each converter strategy influence the converter behavior during faults. Section 6.4.2 summarizes the influences of the converter control on the fault current and voltage level during short-circuits.

6.4.2 Summary of the influence of converter control

This section summarizes the comparison parameters obtained through the laboratory testing of the converter control during the islanded mode. The results are presented in section 5.3 and accordingly, the results are already discussed throughout that section. However, essential correlations between the control settings and converter behavior are summarized in this section for each control strategy.

Control strategy 1

Table 6.20 summarizes the comparison parameters of control strategy 1 for the results in section 6.3. Important correlations between the control parameters and converter behavior during control strategy 1 are:

1. The current output from converter D is based on the change in voltage (see equation 6.13), and the voltage drop during faults is accordingly determined by the proportional gain parameter K_P.

2. The active current output from converter B is based on the active power reference because converter B is active power controlled. The reactive control consists of the reactive power control, but the reactive power reference is always zero, so converter B will not supply any reactive current. If the voltage level or the active power reference change, converter B will adjust its current output to deliver constant active power. Moreover, the current from converter B is also restricted by the currents.

3. Changing the proportional gain in the PI current regulator significantly affects the behavior of the converters. When the proportional gain value is increased, the current output from converter D decreases, while the current output from converter B increases. The droop effect from the proportional gain makes the grid-forming converter softer and increases the power-sharing between the converters. The I reg K_p parameter is equivalent to a resistance in series with the converter, so the voltage decreases significantly during short-circuits when the proportional gain is high. Moreover, the fault current level decreases if the proportional gain parameter is increased due to reduced current contribution from converter D.

4. Changing the active power reference of converter B does not affect the fault current and voltage level during short-circuits. Converter B is P/Q controlled for Q = 0, so converter B will not supply any reactive current to the inductive short-circuit or to support the voltage if the active power reference increases.

5. The increased load leads to a higher active current output from converter D. Nevertheless, the fault current and voltage level, which are essential parameters concerning the protective scheme, are not affected. The increase in active power demand will not lead to higher reactive currents in the system. Therefore, the inductive short-circuit is not supplied with more reactive currents, and the fault current is unaffected. Moreover, the voltage is unchanged due to constant reactive currents.

6. The reduced current limit of converter B does not affect the fault current and voltage level during control strategy 1. Converter B is P/Q controlled for Q = 0, so regardless of any current limit, its reactive current output is always zero to keep the reactive power output at zero.

Variations	I_B [A]	I_D [A]	I_{fault} [A]	$R_{\frac{I_{B\_SC}}{I_{D\_SC}}}$ [A]	V_{drop} [%]	Figure
Original settings	32.5	137.2	138.6	0.24	26.4	6.10
Case Kp						
Kp = 0 % I trip level = 445 A	31.1	149.9	149.9	0.21	19.3	6.12
Kp = 15 % I trip level = 345 A	32.5	145.7	147.1	0.22	23.2	6.13
Kp = 50 % I trip level = 245 A	36.8	120.9	121.6	0.30	34.5	6.14
Kp = 100 % I trip level = 245 A	48.1	97.6	93.3	0.49	49.3	6.15
Kp = 150 % I trip level = 245 A	56.6	78.5	76.4	0.72	59.2	C.5
Kp = 200 % I trip level = 245 A	93.3	74.2	53.7	1.26	71.4	6.16
Case P ref						
Pref = 500 pu	56.6	137.2	138.6	0.41	26.4	6.21
Case High load						
High load Kp = 25 % P ref = 300 pu I trip level = 345 A	31.1	154.1	138.6	0.2	25.4	6.23
Case I limit						
I limit: ± 250 pu Kp = 25 % P ref = 300 pu	22.6	137.2	135.8	0.16	27.1	6.25
I limit: ± 500 pu Kp = 25 % P ref = 300 pu	36.8	139.3	138.6	0.26	25.7	C.6
I limit: ± 250 pu Kp = 25 % P ref = 1000 pu	22.6	140.0	132.9	0.16	27.1	C.7
I limit: ± 250 pu Kp = 100 % P ref = 300 pu	22.6	89.1	90.5	0.25	51.4	6.26

Table 6.20: Summary of the comparison parameters for control strategy 1

Control strategy 2

Table 6.21 summarizes the comparison parameters of control strategy 2 for the results in section 6.3. Important correlations between the control parameters and converter behavior during control strategy 2 are:

1. The current output from converter D is based on the change in voltage (see equation 6.13), and the voltage drop during faults is accordingly determined by the proportional gain parameter K_P.

2. The active current output from converter B is based on the active power reference because converter B is active power controlled. The reactive control consists of an AC voltage regulator, so the supply of reactive current varies under generic conditions. If the voltage level or the active power reference change, converter B will adjust its current output to deliver constant active power. During short-circuits, converter B will supply reactive current to feed the inductive short-circuit and to support the voltage. Moreover, the active and reactive current from converter B are also restricted by the current limits.

3. Changing the proportional gain in the PI current regulator significantly affects the behavior of the converters, and the same results of increasing I reg K_p are observed during control strategy 2. When the proportional gain value is increased, the current output from converter D decreases, while the current output from converter B increases. The I reg K_p parameter is equivalent to a resistance in series with the converter, so the voltage decreases significantly during short-circuits when the proportional gain is high. Moreover, the fault current level decreases if the proportional gain parameter is increased due to smaller converter D currents. The proportional gain parameter gives a droop effect and increases the power-sharing between the converters. However, the power-sharing between the converters are already enabled due to the grid-supporting control strategy of converter B.

4. Changing the active power reference of converter B does not affect the fault current and voltage level during short-circuits. The increased active power output does not influence the reactive regulation of converter B. Thus, the reactive current output from converter B which supports the voltage is not increased even though the active power output increases.

5. The increased load leads to a higher active current output from converter D. Nevertheless, the fault current and voltage level, which are important parameters concerning the protective scheme, are not affected. The increased active power demand only requires more active currents, so the reactive control of converter B is not affected.

6. The reduced current limit of converter B affects the fault current and voltage level during control strategy 2. If the current limit reduces the reactive current output from converter B, less voltage support is offered. Moreover, the reactive current fed to the inductive fault is also limited.

Variations	I_B [A]	I_D [A]	I_{fault} [A]	$R_{\frac{I_{B\_SC}}{I_{D\_SC}}}$ [A]	V_{drop} [%]	Figure
Original settings	70.7	93.3	152.7	0.76	19.1	6.11
Case Kp						
Kp = 0 % I trip level = 345 A	62.2	108.9	164.0	0.57	14.3	6.17
Kp = 15 % I trip level = 345 A	66.5	100.4	161.2	0.66	17.1	6.18
Kp = 50 % I trip level = 245 A	84.9	76.4	149.9	1.11	19.8	6.19
Kp = 100 % I trip level = 245 A	91.9	55.2	135.8	1.66	26.8	6.20
Case P ref						
Pref = 500 pu	79.2	96.2	155.6	0.82	18.4	6.22
Case High load						
High load Kp = 25 % P ref = 300 pu I trip level = 345 A	69.3	111.7	158.4	0.62	17.6	6.24
Case I limit						
I limit: ± 250 pu Kp = 25 % P ref = 300 pu	25.5	118.8	138.6	0.21	24.7	6.27
I limit: ± 500 pu Kp = 25 % P ref = 300 pu	53.7	106.1	149.9	0.51	19.3	6.28
I limit: ± 250 pu Kp = 25 % P ref = 1000 pu	32.5	120.2	138.6	0.27	24.7	C.8
I limit: ± 250 pu Kp = 100 % P ref = 300 pu	29.7	77.8	99.0	0.38	45.8	6.29

Table 6.21: Summary of the comparison parameters for control strategy 2

Chapter 7

Summary and Conclusion

The implementation of microgrids affects the reliability of conventional protection schemes, so adaptive protection schemes which consider the dynamic changes in microgrids are needed. The main objective of this master's thesis is to implement an inverter-dominated microgrid with an adaptive protection scheme at the Smart Grid Laboratory at NTNU. First, the main achievements regarding the performance of the implemented microgrid are listed below:

- The active islanding detection method based on a transfer signal from the contactor in the bus-bar cabinet to the ABB digital relay is working.
- The digital relay adapts between over-current and under-voltage protective functions according to the binary input signal with information about the operation mode of the microgrid. Thus, the adaptive protection scheme is working.
- The digital relay can with binary output signals remotely control the contactor in the bus-bar cabinet.
- The laboratory converters are configured with grid-forming, grid-following, and grid-supporting control strategies.

Several topics related to microgrid protection and converter control were subsequently investigated. This research led to the main findings:

- The fault current level differs during grid-connected and islanded microgrid configuration. Consequently, the over-current relay only trips during grid-connected mode because the relay is configured with a pick-up setting based on the short-circuit contribution from the utility grid. The over-current relay will therefore not operate in the islanded configuration, so the digital relay must switch to the under-voltage protection function.
- The converter settings are crucial in order to avoid an immediate disconnection of the converter during short-circuits due to tripping of the internal protection functions.
- The implemented converter control affects the converter behavior and the power-sharing between converters. Consequently, the impact on fault current and voltage level must be strongly considered when designing the protection scheme.
- The implemented control strategy affects the converter behavior during short-circuits.
- The specific control settings within each control strategy affects the converter behavior during short-circuits.

- In this laboratory testing, the voltage always dropped below the pick-up limit during short-circuits, while the converter currents were unpredictable and highly affected by the converter control. Consequently, the under-voltage relay operated to every short-circuit, whereas the over-current relay did not always operate. Thus, the under-voltage protection function seems more suitable in inverter-dominated microgrids compared to the over-current relays with only one group setting.

The laboratory testing showed that the fault current level is reduced in islanded mode and that the control strategies and control parameters may affect the behavior of IIDG units during short-circuits. Subsequently, the converter control schemes determine the current contribution of each converter, and the regulations must be strongly considered when designing microgrid protection schemes. Still, the results from these tests are not enough to make a general conclusion regarding the exact converter behavior during short-circuits. A conclusion regarding the impact of converter control cannot be drawn without more research and extensive testing.

7.1 Recommendations for future work

The testing opportunities at the Smart Grid laboratory are enormous. The advanced control system of the laboratory converters and the complex digital relays enable numerous of test possibilities. However, the number of tests was unfortunately limited due time constrains. Recommendations for future work are therefore suggested.

- Investigate the impact of external factors, like type of short-circuits, fault impedance, and fault location, on fault current and voltage level.
- Examine several islanding detection methods and the transition between the microgrid operation modes.
- Expand the protection scheme to also adapt to the operating status of the DG sources in the system.
- Implement more advanced digital protection relays constructed with more protective functions and group settings within each function.
- Implement protection of the other network components, e.g., line protection.
- Investigate the impact of more control strategies on the voltage and fault current level. For example, the DC-link voltage regulator was not examined in this experiment.
- Investigate the impact of more control settings on the voltage and fault current level. Control parameters like active and reactive droop control and time constants would be interesting to test.

Bibliography

[1] ABB. *RELION® 670 SERIES Transformer protection RET670 Version 2.1 Product Guide*. 2019.

[2] Thomas Ackermann, Göran Andersson, and Lennart Söder. "Distributed generation: a definition". In: *Electric Power Systems Research* 57.3 (2001), pp. 195–204.

[3] I. Almutairy. "A review of coordination strategies and techniques for overcoming challenges to microgrid protection". In: *Saudi Arabia Smart Grid (SASG)*. IEEE, 2016, pp. 1–4.

[4] Yavuz Ates et al. "Adaptive Protection Scheme for a Distribution System Considering Grid-Connected and Islanded Modes of Operation". eng. In: *Energies* 9.5 (2016). URL: `https://doaj.org/article/99796d73781340f3ba9c0b859ad9262d`.

[5] R. Aujla. *Generator Stator Protection, under/over voltage, under /over frequency and unbalanced loading*. 2008.

[6] BDEW. *Technical Guideline: Generating Plants Connected to the Medium-Voltage Network*. 2008.

[7] B. P. Bhattarai et al. "An adaptive overcurrent protection in smart distribution grid". In: *2015 IEEE Eindhoven PowerTech*. 2015, pp. 1–6.

[8] A. Bidram and A. Davoudi. "Hierarchical Structure of Microgrids Control System". In: *Smart Grid, IEEE Transactions on* 3.4 (2012), pp. 1963–1976.

[9] F. Blaabjerg et al. "Overview of Control and Grid Synchronization for Distributed Power Generation Systems". In: *IEEE Transactions on Industrial Electronics* 53.5 (2006), pp. 1398–1409.

[10] J. Lewis Blackburn. *Protective relaying : principles and applications*. eng. Boca Raton, Fla, 2007.

[11] Allal M. Bouzid et al. "A survey on control of electric power distributed generation systems for microgrid applications". eng. In: *Renewable and Sustainable Energy Reviews* 44.C (2015), pp. 751–766.

[12] Belwin J. Brearley and R. Raja Prabu. "A review on issues and approaches for microgrid protection". eng. In: *Renewable and Sustainable Energy Reviews* 67 (2017), pp. 988–997.

[13] G. Chown et al. *System inertia and Rate of Change of Frequency (RoCoF) with increasing non-synchronous renewable energy penetration*. 2017.

[14] CIGRE & CIRED. *613: Protection of Distribution Systems with Distributed Energy Resources*. Joint Working Group: B5/C6.26/CIRED. 2015.

[15] M. Dewadasa, A. Ghosh, and G. Ledwich. "Protection of microgrids using differential relays". In: *AUPEC 2011*. Sept. 2011, pp. 1–6.

[16] G. Ding et al. "Coordinate control of distributed generation and active power electronics loads in islanding microgrid". In: *2017 IEEE 3rd International Future Energy Electronics Conference and ECCE Asia (IFEEC 2017 - ECCE Asia)*. June 2017, pp. 1581–1585.

[17] E. Dyrstad. "Relay Lab at NTNU". MA thesis. NTNU Trondheim, 2014.

[18] Helder Lopes Ferreira et al. "Characterisation of electrical energy storage technologies". eng. In: *Energy* 53.C (2013), pp. 288–298.

[19] B. Fossen. "Relay Protection of DG-units in Norway". MA thesis. NTNU Trondheim, 2017.

[20] Synne Garnås. "Short Circuit Current Contribution from Converters". MA thesis. NTNU Trondheim, 2017.

[21] J. Duncan Glover. *Power system analysis and design*. Stamford, Conn, 2012.

[22] P. Gupta, R. S. Bhatia, and D. K. Jain. "Adaptive protection schemes for the microgrid in a Smart Grid scenario: Technical challenges". In: *2013 IEEE Innovative Smart Grid Technologies-Asia (ISGT Asia)*. Nov. 2013, pp. 1–5. DOI: 10.1109/ISGT-Asia.2013.6698729.

[23] M. A. Haj-ahmed and M. S. Illindala. "The Influence of Inverter-Based DGs and Their Controllers on Distribution Network Protection". In: *IEEE Transactions on Industry Applications* 50.4 (July 2014), pp. 2928–2937. ISSN: 0093-9994. DOI: 10.1109/TIA.2013.2297452.

[24] Edited By Professor Nikos Hatziargyriou. *Microgrids: Architectures and Control*. eng. Wiley - IEEE. IEEE Press, 2013.

[25] Rakel Alice Utne Holt. "Device-level control of microgrids with Master-Slave structure". MA thesis. Norwegian University of Science and Technology, 2018.

[26] Anders Bergheim Holvik. "Virtual Impedance Techniques for Power Sharing Control in AC Islanded Microgrids". MA thesis. Norwegian University of Science and Technology, 2018.

[27] Ali Hooshyar and Reza Iravani. "Microgrid Protection". eng. In: *Proceedings of the IEEE* 105.7 (2017), pp. 1332–1353.

[28] Seyed Amir Hosseini et al. "An overview of microgrid protection methods and the factors involved". eng. In: *Renewable and Sustainable Energy Reviews* 64 (2016), pp. 174–186.

[29] A.M. Ibrahim et al. "Adaptive protection coordination scheme for distribution network with distributed generation using ABC". eng. In: *Journal of Electrical Systems and Information Technology* 3.2 (2016), pp. 320–332.

[30] P. Jadeja and A. Shrivastava. "Effects of DC Components on Circuit Breaker". In: *International Journal of Science and Research* ().

[31] Z. Kai-Hui and X. Ming-Chao. "Impacts of microgrid on protection of distribution networks and protection strategy of microgrid". In: *2011 International Conference on Advanced Power System Automation and Protection*. Vol. 1. Oct. 2011, pp. 356–359. DOI: 10.1109/APAP.2011.6180426.

[32] X. Kang et al. "Protection of micro-grid systems: a comprehensive survey". In: *The Journal of Engineering* 2017.13 (2017), pp. 1515–1518. DOI: 10.1049/joe.2017.0584.

[33] B. Kasztenny and D. Finney. "Fundamentals of Distance Protection". In: IEEE, 2008, pp. 1–34.

[34] Brigitte Knopf, Paul Nahmmacher, and Eva Schmid. "The European renewable energy target for 2030 – An impact assessment of the electricity sector". eng. In: *Energy Policy* 85 (2015), pp. 50–60.

[35] W Kramer et al. "Advanced Power Electronic Interfaces for Distributed Energy Systems Part 1: Systems and Topologies". In: (Jan. 2008).

[36] Hannu Laaksonen. "Technical Solutions for Low-Voltage Microgrid Concept". PhD thesis. May 2011.

[37] K. Ljøkelsøy. *Project memo: 60 kVA Laboratory converter unit. Documentation. Issue 2*. SINTEF, AN 11.12.10.

[38] K. Ljøkelsøy. *Project memo: Control system for a three-phase grid connected converter. 3. 28 February 2019 version. Description*. SINTEF, AN 19.12.xx.

[39] K. Ljøkelsøy. *Project memo: Short circuit emulator. Documentation and user instructions*. SINTEF, AN 11.12.25.

[40] C. Russell Mason. *The Art & Science of Protective Relaying.*

[41] J. Morren and S. W. H. D. Haan. "Impact of distributed generation units with power electronic converters on distribution network protection". In: *2008 IET 9th International Conference on Developments in Power System Protection (DPSP 2008).* Mar. 2008, pp. 664–669. DOI: 10.1049/cp:20080118.

[42] H. Nikkhajoei and R. H. Lasseter. "Microgrid Protection". In: *2007 IEEE Power Engineering Society General Meeting.* June 2007, pp. 1–6. DOI: 10.1109/PES.2007.385805.

[43] N. Nimpitiwan et al. "Fault Current Contribution From Synchronous Machine and Inverter Based Distributed Generators". In: *IEEE Transactions on Power Delivery* 22.1 (Jan. 2007), pp. 634–641. ISSN: 0885-8977. DOI: 10.1109/TPWRD.2006.881440.

[44] Y. Pan et al. "Impact of inverter interfaced distributed generation on overcurrent protection in distribution systems". eng. In: vol. 2. IEEE Publishing, 2011, pp. 371–376.

[45] Guido Pepermans et al. "Distributed generation: definition, benefits and issues". In: *Energy Policy* (2005), pp. 787–798.

[46] A. Petterteig et al. *Tekniske retningslinjer for tilknytning av produksjonsenheter, med maksimum aktiv effektproduksjon mindre enn 10 MW, til distribusjonsnettet.* SINTEF Energiforskning AS. Nov. 2006.

[47] Jayakrishnan R and Sruthy V. "Fault ride through augmentation of microgrid". In: *2015 International Conference on Technological Advancements in Power and Energy (TAP Energy).* June 2015, pp. 357–362. DOI: 10.1109/TAPENERGY.2015.7229645.

[48] J. Rocabert et al. "Control of Power Converters in AC Microgrids". In: *IEEE Transactions on Power Electronics* 27.11 (Nov. 2012), pp. 4734–4749. DOI: 10.1109/TPEL.2012.2199334.

[49] P. Rodriguez et al. "Decoupled Double Synchronous Reference Frame PLL for Power Converters Control". In: *IEEE Transactions on Power Electronics* 22.2 (2007), pp. 584–592. DOI: 10.1109/TPEL.2006.890000.

[50] Ruchika et al. "Islanding detection technique for a distributed generation with perfectly matched load condition". In: 2017, pp. 1503–1506. DOI: 10.1109/CCAA.2017.8230038.

[51] Kjersti L. Runestad. *A Review of Challenges and Methods for Microgrid Protection and Control of Power Converters in Microgrids.*

[52] S. Sanchez. "Stability Investigation of Power Electronics Systems". PhD thesis. Norwegian University of Science and Technology, 2015.

[53] S. M. (Suleiman M.) Sharkh. *Power electronic converters for microgrid.* eng. Singapore, 2014.

[54] J. Shiles et al. "Microgrid protection: An overview of protection strategies in North American microgrid projects". In: *2017 IEEE Power Energy Society General Meeting.* July 2017, pp. 1–5. DOI: 10.1109/PESGM.2017.8274519.

[55] Remus Teodorescu. *Grid converters for photovoltaic and wind power systems.* eng. Chichester, West Sussex, 2010.

[56] A. Timbus et al. "Evaluation of Current Controllers for Distributed Power Generation Systems". In: *IEEE Transactions on Power Electronics* 24.3 (Mar. 2009), pp. 654–664. DOI: 10.1109/TPEL.2009.2012527.

[57] Zhang Xi, Gui Bin Zou, and Tian Chun. "A Novel Adaptive Protection Scheme for Microgrid". eng. In: *Applied Mechanics and Materials* 541-542.Engineering and Manufacturing Technologies (2014), pp. 977–981.

[58] Amirnaser Yazdani. *Voltage-sourced converters in power systems : modeling, control, and applications.* eng. Hoboken, New Jersey, 2010.

Appendix A

Protection principles

This section explains the main principle of directional over-current protection, distance protection, and differential protection relays. This material is obtained from the specialization project "A Review of Challenges and Methods for Microgrid Protection and Control of Power Converters in Microgrids" conducted by the same author during the fall of 2018 [51].

A.1 Directional overcurrent protection

Directional overcurrent protection is the second alternative for short-circuit protection of outgoing feeders [14]. Directional overcurrent protection is capable to determine the current direction, in contrast to overcurrent protective relays. In other words, directional overcurrent protection is sensitive to both current magnitude and current direction. The directional feature increases the selectivity and the reliability of the relay [17]. The current settings in directional overcurrent relays are similar to overcurrent relays, however, the time setting depends on forward and backward current direction.

The simplified single line diagram of directional overcurrent outgoing feeder protection is shown in figure A.1. The green arrows illustrate the load currents during normal conditions, whereas the red arrows represent the fault currents during a fault in line A. Relay A and relay B are directional overcurrent protection relays with a forward tripping direction.

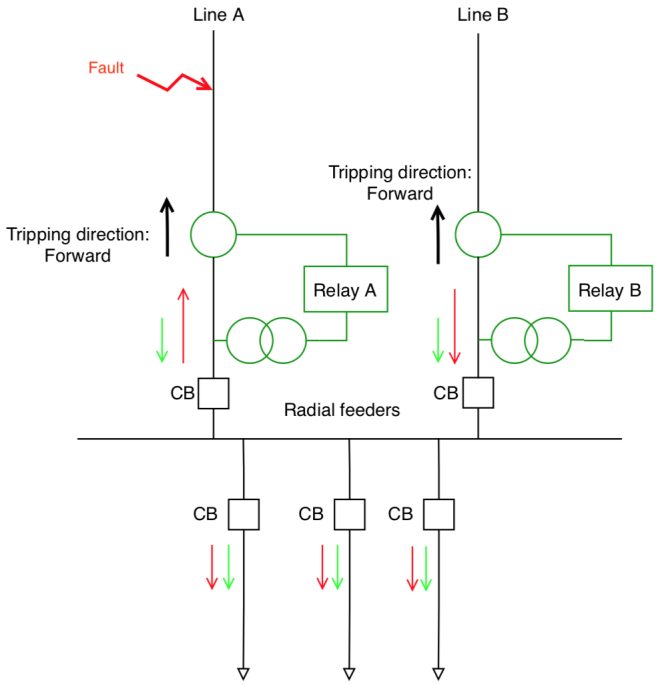

Figure A.1: Simplified single line diagram of directional overcurrent outgoing feeder protection [17]

Relay A should ideally trip before relay B to provide selectivity and minimize the isolated part of the network in the event of a fault in line A. However, relay B perceives a higher current due to the additional load current supplying the feeders. Accordingly, relay B may trip before relay A if the protective relays are not equipped with directional elements. With a forward tripping direction, however, relay B is blocked during the fault, and selectivity is thereby maintained [17].

The phase angle, ϕ, between the measured current, I_{CT}, and the voltage reference, U_{ref}, is utilized by the relay to determine the current direction. The phasor diagram of the directional overcurrent is illustrated in figure A.2 where the forward and reverse direction of I_{CT} are indicated.

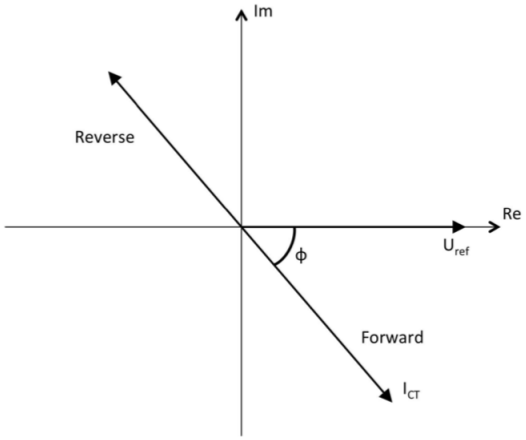

Figure A.2: Phasor diagram for directional overcurrent relays utilizing the voltage reference [17]

A.2 Distance protection

In reference [14] the third alternative for short-circuit protection is distance protection with impedance pick-up. Distance protective relays calculate the impedance from the relay to the fault occurrence by comparing the fault current against the voltage at the relay location [24]. Distance relays are a solution to the varying short-circuit capabilities during grid-connected and islanded microgrids because their operation is not only depending on current magnitude, and are thereby unaffected by the limited fault currents from IIDG units [27]. Moreover, the article [43] states that the short-circuit current contribution from inverter-based DGs is negligible so the distance protection is not affected by the in-feed currents from DERs for a inverter-dominated microgrid. In view of this, distance protection is proposed as microgrid protection in [3, 12, 28, 32].

A distance relay measures the apparent impedance derived from the voltage and the current measured locally by instrument transformers [33]. Accordingly, the distance protection relay monitors the impedance of the protected line by equation $Z = \frac{U}{I}$. Moreover, the relay provides a "zone" of protection [33] as illustrated in figure A.3. The distance relay calculates the impedance between the relay and the fault location, and thereby accurately differentiates between internal and external faults within the zone.

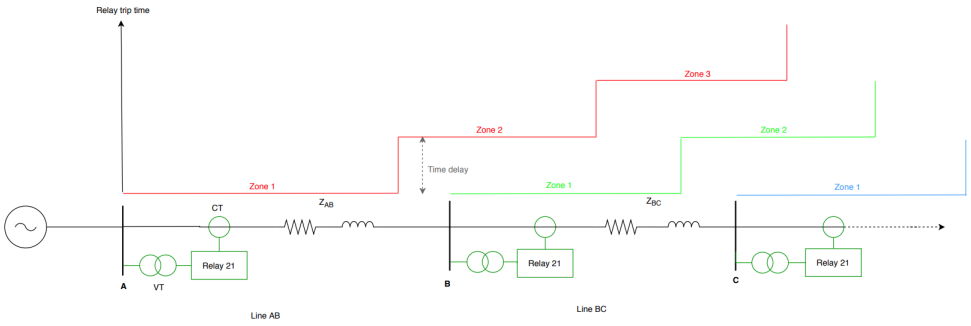

Figure A.3: Working principle of distance protection based on zones formation

Zone 1A protects the first line with 80% reach with a time delay of 0.2 seconds in order to coordinate with fuses on distribution transformers [14]. However, zone 1B with zero time delay could be utilized in the case of short-circuit during connection [14], and in a network without fuses [19]. The relay under-reach the line by 20 % so the relay does not operate before other downstream relays [17]. However, zone 2 has a 120% reach of line 1 and a time delay of 0.4-0.5 seconds [14]. The relay over-reach provides a remote back-up for the relays protecting adjacent lines [17]. The back-up scheme should only operate after a certain time delay known as coordination time interval in order to let the primary protection operate first.

Figure A.4 illustrates the event of a fault on line AB in figure A.3. During normal operations, the relay perceives the impedance of the line, Z_{line}, and the impedance of the load, $Z_{load} = \frac{U^2}{S_{load}}$, as illustrated in figure A.4. During fault conditions, however, the relay will measure the impedance of the line to the fault location, $Z_{line,F}$ and the fault impedance, Z_F [17]. The measured impedance will therefore drop significantly during a fault, and the relay will thereby detect the fault and trip the circuit breaker. Normally, the impedance settings for the different zones are illustrated by RX-diagram with a quadrilateral or circular shape illustrated in figure A.5(a) and A.5(b), respectively.

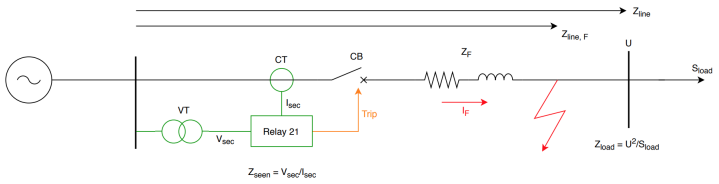

Figure A.4: Line diagram of a single line with distance relays

If distance protection is utilized for microgrids, the measured network impedance is affected by the DG unit along the line [12]. Consequently, the impedance set values have to be recalculated with an additional branch coefficient in order to reduce the impact of the current contribution from the DG source. Reference [12] lists the necessary equations for recalculating the new relay settings to enable an effective protection scheme for both grid-connected and islanded mode.

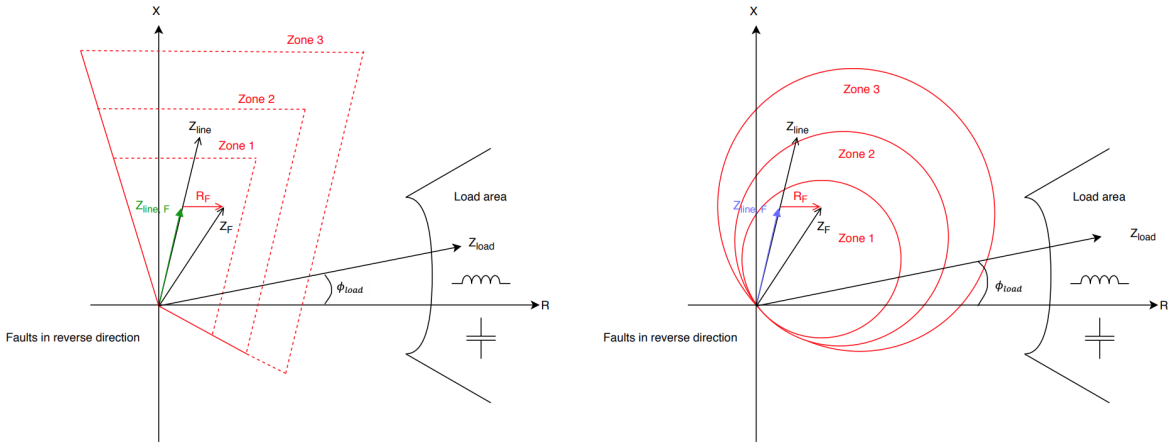

((a)) Quadrilateral zone settings

((b)) Circular (Mho) zone settings

Figure A.5: Corresponding RX-diagrams with zone settings, line, Load and fault impedances for the line in figure A.4 reproduced from [17]

A.3 Differential protection

Differential protection is a suitable microgrid relay since it is not sensitive to changing fault current level, bidirectional power flow, and the number of DG connections [15]. The differential relay principle is showed in figure A.6. Evidently, the currents flowing into the protected zone are compared with the currents flowing out of the zone. The currents should be equal during normal operation conditions, while the differential current is not zero in the event of a fault within the zone [54].

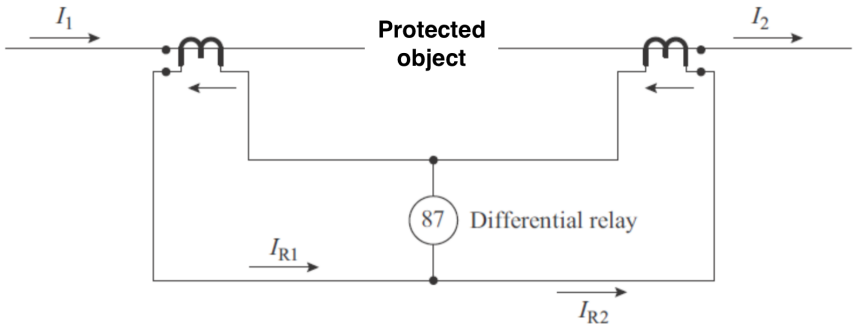

Figure A.6: Basic principle of the differential protection scheme

The relay input is the secondary currents from the CTs at both sides of the protected zone. The secondary current is expressed in equation A.1, and constitutes the primary current multiplied with the CT ratio, minus the respective excitation current [17].

$$I_s = I_p \cdot \frac{N_p}{N_s} - I_e \tag{A.1}$$

The excitation currents, I_{e1} and I_{e2}, are dependent on the resistance burdens, which is proportional to the length between the relay and the CTs [17]. Consequently, the differential protection might be limited if the distance is too long and the excitation currents differ [17]. Reference [15] therefore proposes a protection scheme with two differential relays on both ends of the feeder as shown in figure A.7. Each relay is connected to its local CT, while a communication link transfers the current values between the relays [15]. Evidently, the differential relay compares the current entering the feeder with the current leaving the feeder, and are not responding to outside faults.

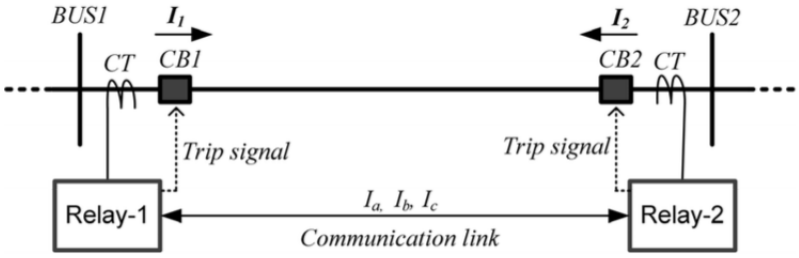

Figure A.7: Single line representation of differential feeder protection for microgrids [15]

Figure figure A.8 shows the tripping characteristic of percentage differential relays. Each relay has operating and no operation regions to avoid any false tripping. The percentage differential relay is

defined by two slopes, $K1$ and $K2$, and the dual slope characteristics is illustrated in figure A.8. The lower gradient will increase the sensitivity of the relay, while the higher gradient improves the security at high restrain currents [17]. Moreover, the $I_{threshold}$ current is the minimum differential pickup current for the relay [15]. The differential current should be zero during normal operation, however, this may not be the case since external faults cause the CTs to saturate. The threshold value is therefore necessary to ensure that relays do not trip for external faults.

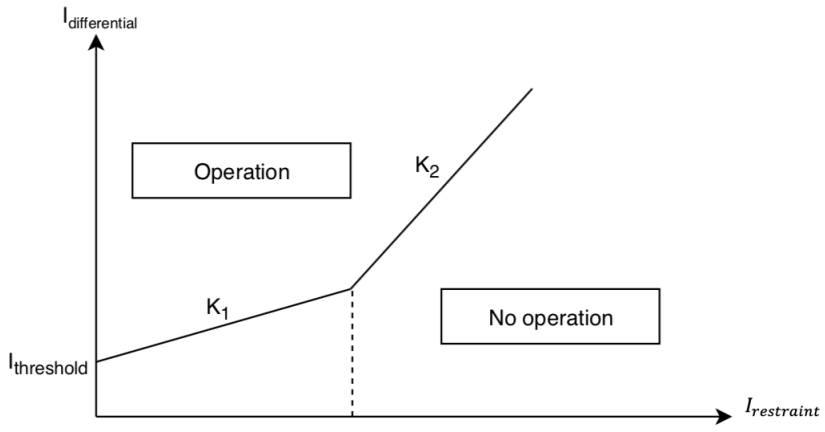

Figure A.8: Time and current characteristics of differential protection relays [15]

Appendix B

Laboratory Tests

B.1 Smart Grid Laboratory schematics

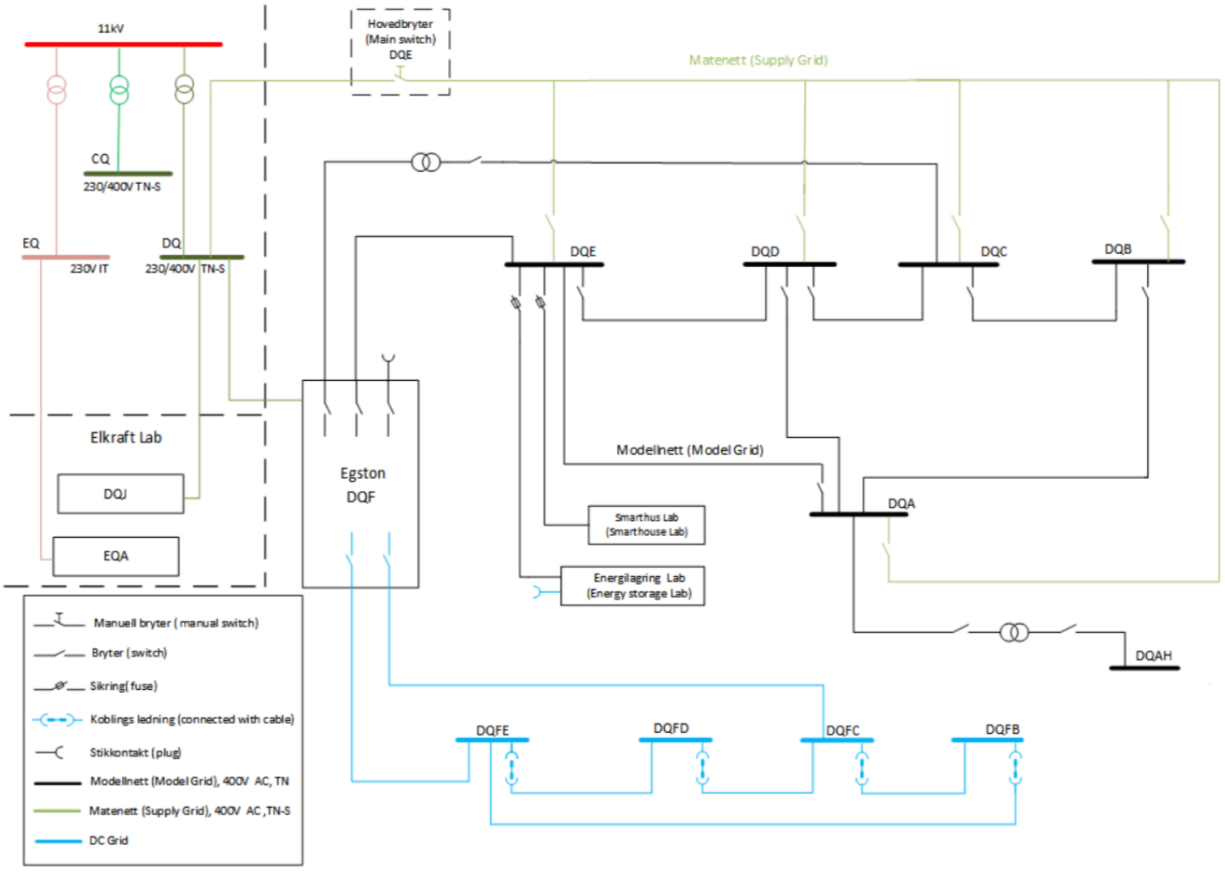

Figure B.1: Simplified hierarchical overview of the laboratory system topology

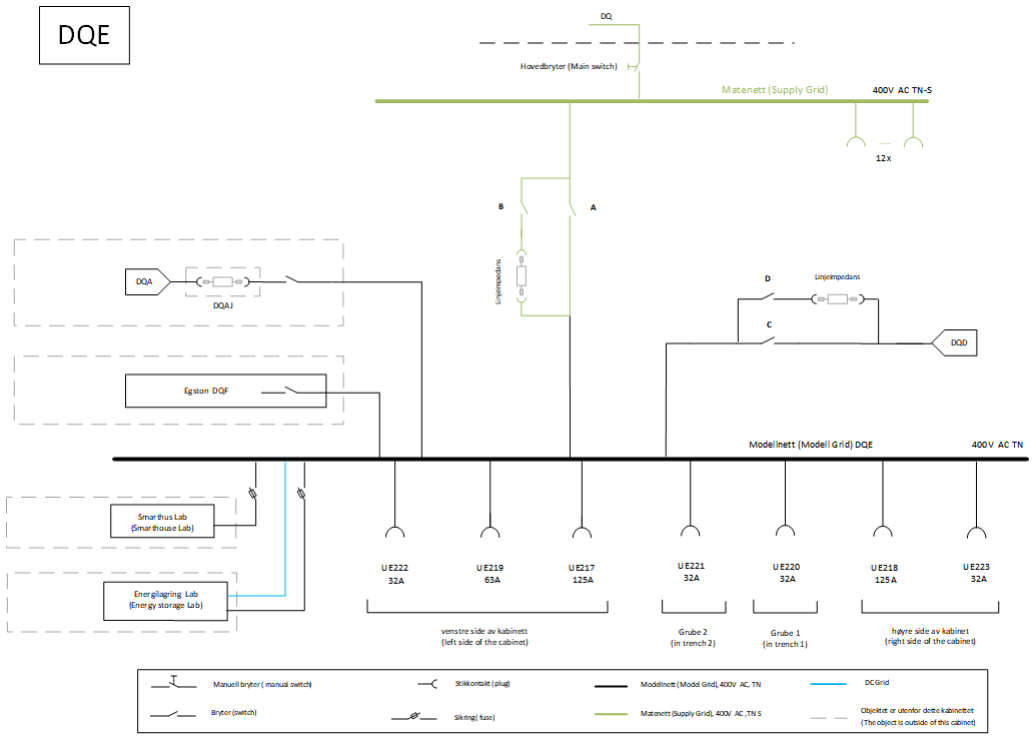

Figure B.2: Schematics of the DQE bus-bar

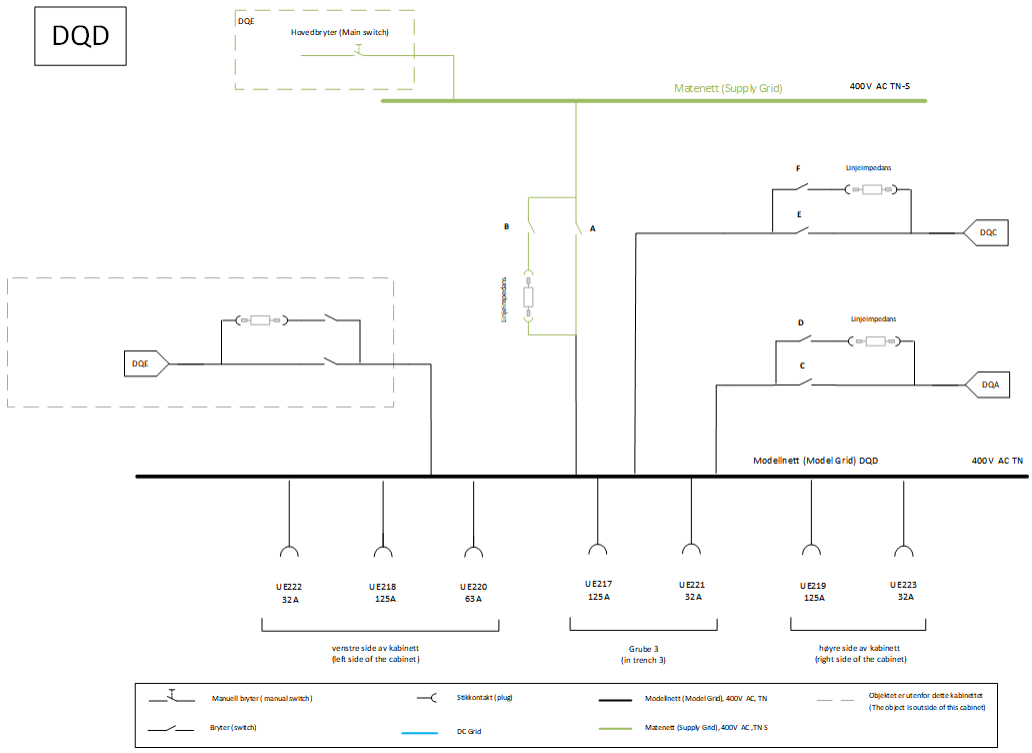

Figure B.3: Schematics of the DQD bus-bar

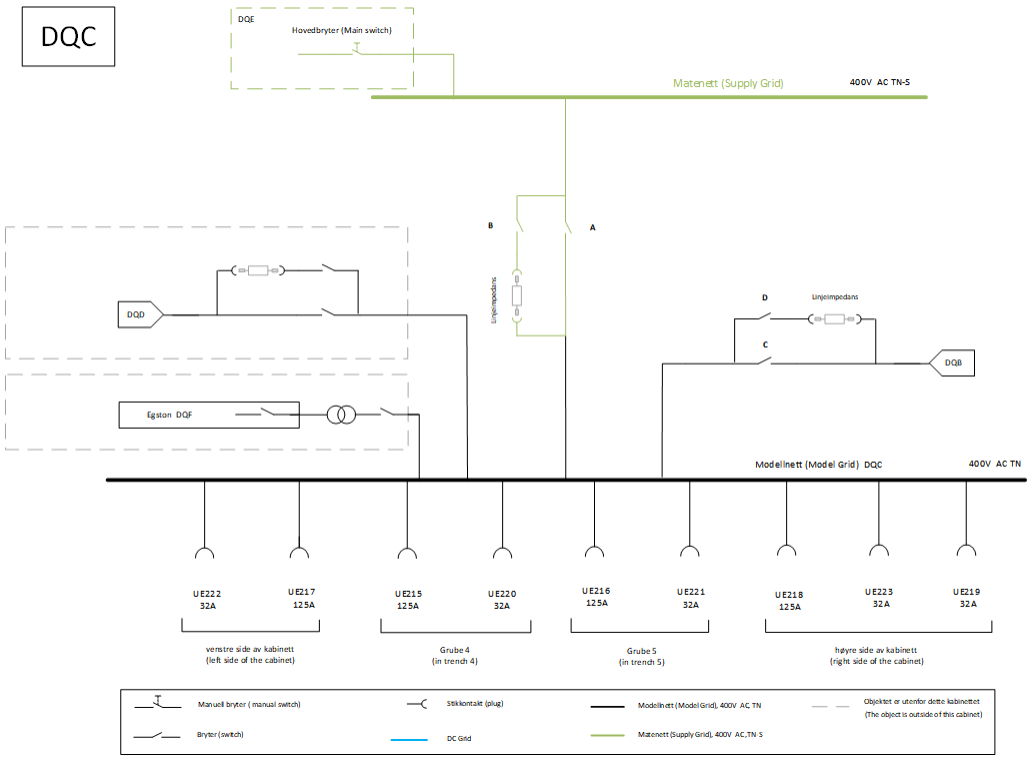

Figure B.4: Schematics of the DQC bus-bar

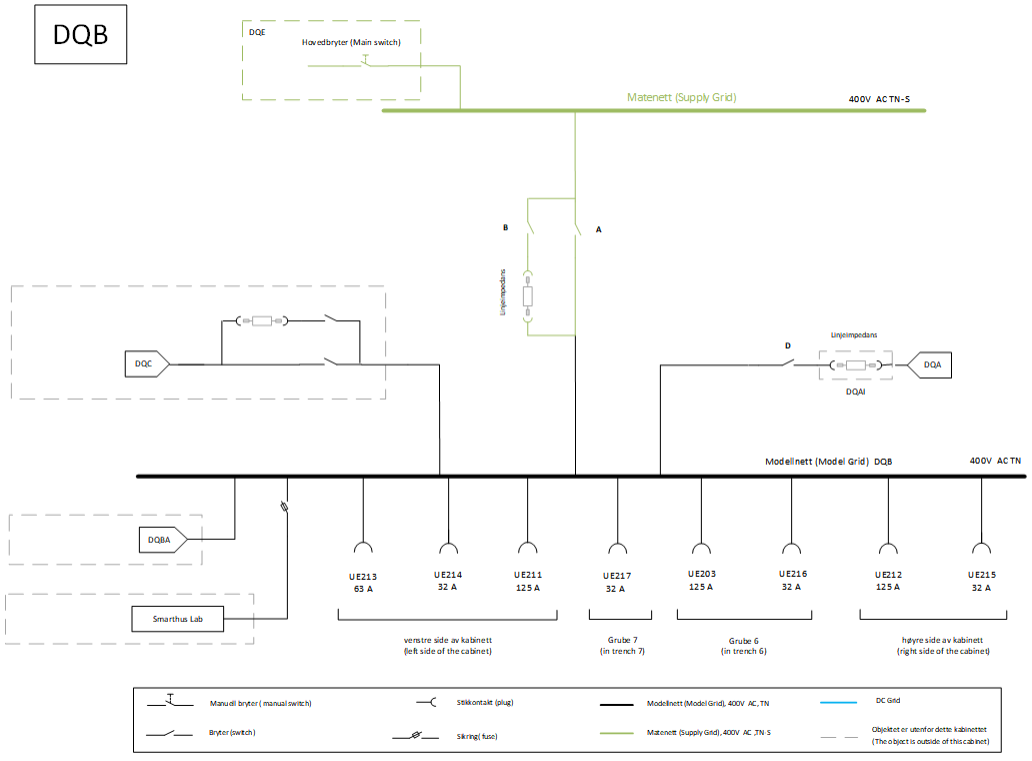

Figure B.5: Schematics of the DQB bus-bar

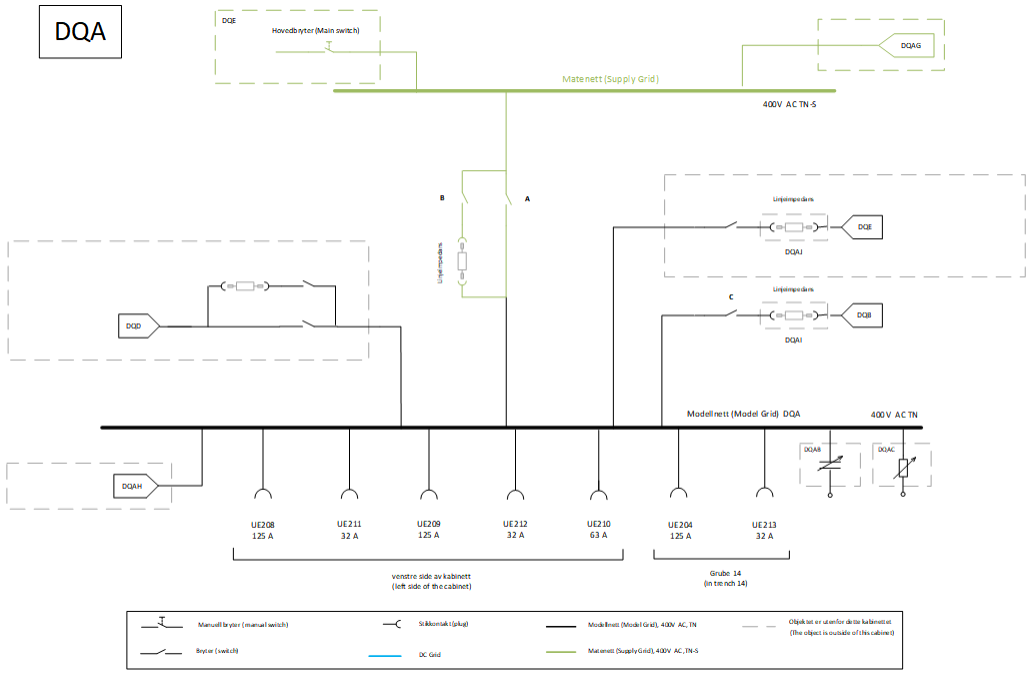

Figure B.6: Schematics of the DQA bus-bar

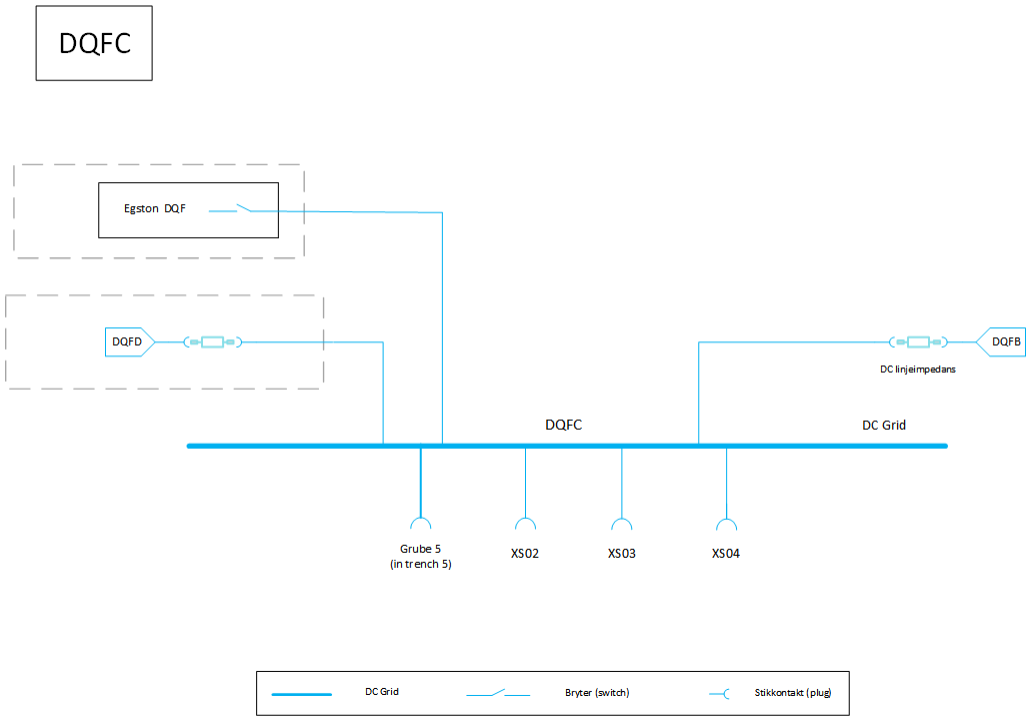

Figure B.7: Schematics of the DQFC bus-bar

B.2 Parameters lists

The available parameter values and control signal lists in the built-in control system of the laboratory VSCs are given in the list below:

1. Control Signal Parameters
2. Operation Mode Parameters
3. Current Measurement Parameters
4. Current Regulator Parameters
5. DQ Hysteresis Current Regulator
6. DC Link Voltage Regulator Parameters
7. DC Link Voltage Protection Parameter
8. AC Voltage Measurement Parameters
9. AC Voltage Regulator Parameters
10. AC Grid Voltage Protection Parameter
11. Power Regulator Parameters
12. VCO Parameters
13. PLL Parameters
14. PLL Weighting factor Parameters
15. PLL Synch Detection
16. AC Frequency Regulator Parameters
17. AC Voltage Protection Parameters
18. Active Damping Parameters
19. Temperature Parameters
20. Default Control Signals
21. CAN Bus Parameters
22. High Speed Link
23. DA Converter Parameters
24. Display Signal Configuration Menu

Additionally, table B.1 contains the converter control parameter value and control signal settings.

Parameters	Converter B Grid-supporting	Converter C Grid-following	Converter D Grid-forming
Control signal source	Menu	Menu	Menu
Ref limit max value	1000 [pu]	1000 [pu]	1000 [pu]
Limit value coupling	Separate	Separate	Separate
I trip level	245 [A]	245 [A]	245-445 [A]
Rated current	90 [A]	90 [A]	90 [A]
I reg Kp	400 [%]	400 [%]	0-200 [%]
I reg Ti	1000 μ[s]	1000 μ[s]	0 μ[s]
Angle delay comp	50 μ[s]	50 μ[s]	50 μ[s]
Driver signal source	DQ PI PWM	DQ PI PWM	DQ PI PWM
Switching freq	7000 [Hz]	7000 [Hz]	7000 [Hz]
AC rated voltage	400 [V]	400 [V]	400 [V]
U AC reg filter tc	10 [ms]	Not relevant	Not relevant
U AC reg Kp	100 [%]	Not relevant	Not relevant
U AC reg Ti	100 [ms]	Not relevant	Not relevant
U AC reg droop	100 [%%]	Not relevant	Not relevant
U AC high trip level	500 [V]	500 [V]	500 [V]
P reg filter tc	10 [ms]	10 [ms]	Not relevant
P reg Kp	1000 [%]	1000 [%]	Not relevant
P reg Ti	500 [ms]	500 [ms]	Not relevant
P reg droop	100 [%%]	100 [%%]	Not relevant
Q reg filter tc	Not relevant	10 [ms]	Not relevant
Q reg Kp	Not relevant	1000 [%]	Not relevant
Q reg Ti	Not relevant	500 [ms]	Not relevant
Q reg droop	Not relevant	100 [%%]	Not relevant
VOC operation mode	PLL	PLL	Open mode
AC rated frequency	50 [Hz]	50 [Hz]	50 [Hz]
VOC max frequency	60 [Hz]	60 [Hz]	60 [Hz]
VOC min frequency	40 [Hz]	40 [Hz]	40 [Hz]
PLL reg Kp	970 [%]	970 [%]	Not relevant
PLL reg Ti	100 [ms]	100 [ms]	Not relevant
AC freq high trip threshold	58 [Hz]	58 [Hz]	58 [Hz]
AC freq low trip threshold	42 [Hz]	42 [Hz]	42 [Hz]
Iact pos limit	250-1000 [pu]	250-1000 [pu]	1000 [pu]
Iact neg limit	- (250-1000) [pu]	- (250-1000) [pu]	- 1000 [pu]
Ireact pos limit	- 250-1000 [pu]	- 250-1000 [pu]	1000 [pu]
Ireact neg limit	- (250-1000) [pu]	- (250-1000) [pu]	- 1000 [pu]

Table B.1: Additional converter control parameters and settings for the built-in control

The signals are scaled in a per-unit system with 1000 as 1 pu

Appendix C

Additional Laboratory Results

Supplementary graphs and information from some of the test cases in chapter 6 are given in this appendix.

C.1 Different tripping characteristics of the over-current relay

Figure C.1 illustrates the fault current during grid-connected mode when converter B is grid-supporting. The proportional gain parameter I reg K_P is 100 %, and the active power references of converter B and C are 300 pu and 500 pu, respectively. Compared to figure 6.7(a), the fault current is reduced due to the grid-supporting control strategy of converter B. This demonstrates that the control strategy of the laboratory converter affects the fault current level. The lack of tripping indicates that multiple setting groups may be necessary within the over-current protective function due to the influence of converter control.

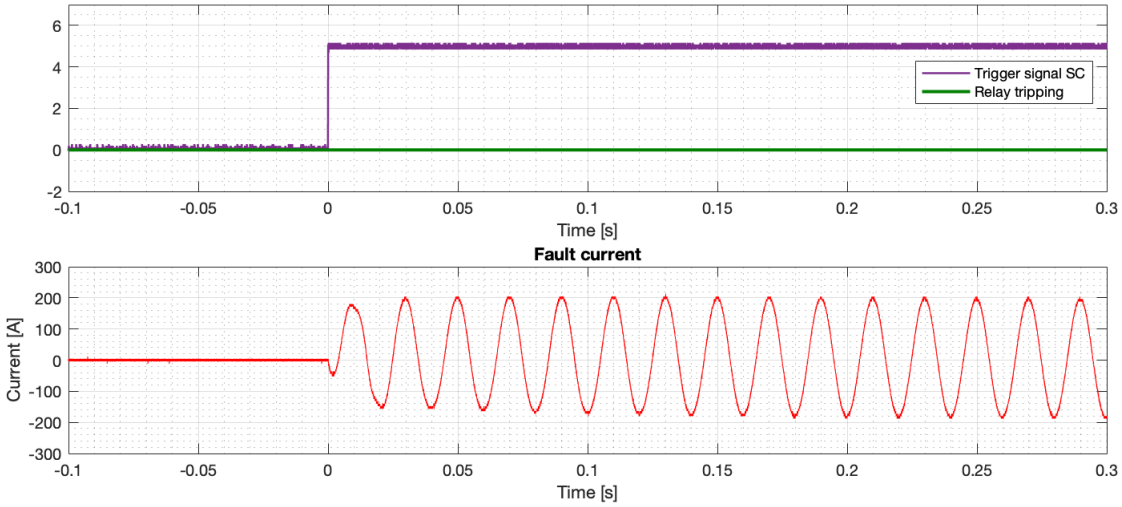

Figure C.1: Grid-connected microgrid where the over-current relay does not trip when converter B is implemented with control strategy 2

On the contrary, figure C.2(a) shows that the over-current relay trips when I reg $K_P = 50\%$ and converter B is grid-supporting, whereas figure C.2(b) shows that the relay does not trip when converter

B is grid-following for the same proportional gain value. Hence, figure C.2 demonstrates that the converter control settings affect the fault current level.

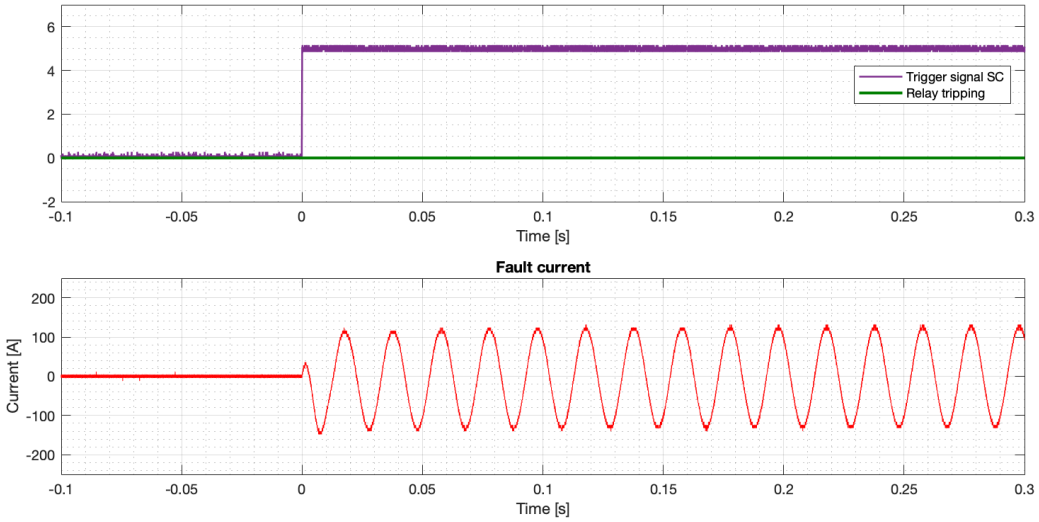

((a)) Trip of the over-current relay when converter B is grid-supporting

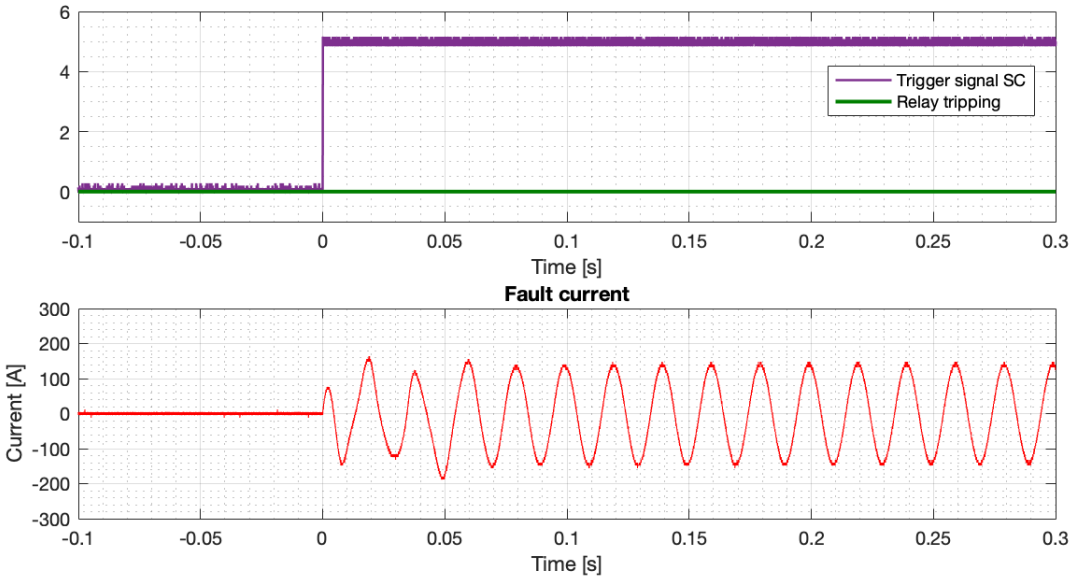

((b)) No trip of the over-current relay when converter B is grid-following

Figure C.2: Fault currents for a 1000 ms three-phase short-circuit during grid-connected mode when $K_P = 50$ % and the active power references of converter B and C are 300 pu and 500 pu, respectively.

C.2 Influence of converter control in islanded microgrid

C.2.1 Problem with immediate disconnection of converter

Figure C.3 shows the disconnection of converter B due to the over-frequency protection function. The high AC frequency trip level of converter B is reduced to 57 Hz and the grid-following converter disconnected at approximately t = 0.25 s as illustrated in figure C.3. The disconnection of converter B is illustrated by the zero current contribution after t = 0.25 s and additionally by the voltage dropping to zero after this point. The AC frequency of the voltage is approximately:

$$f = \frac{1}{T} = \frac{1}{0.2477 - 0.2323} = 65Hz \tag{C.1}$$

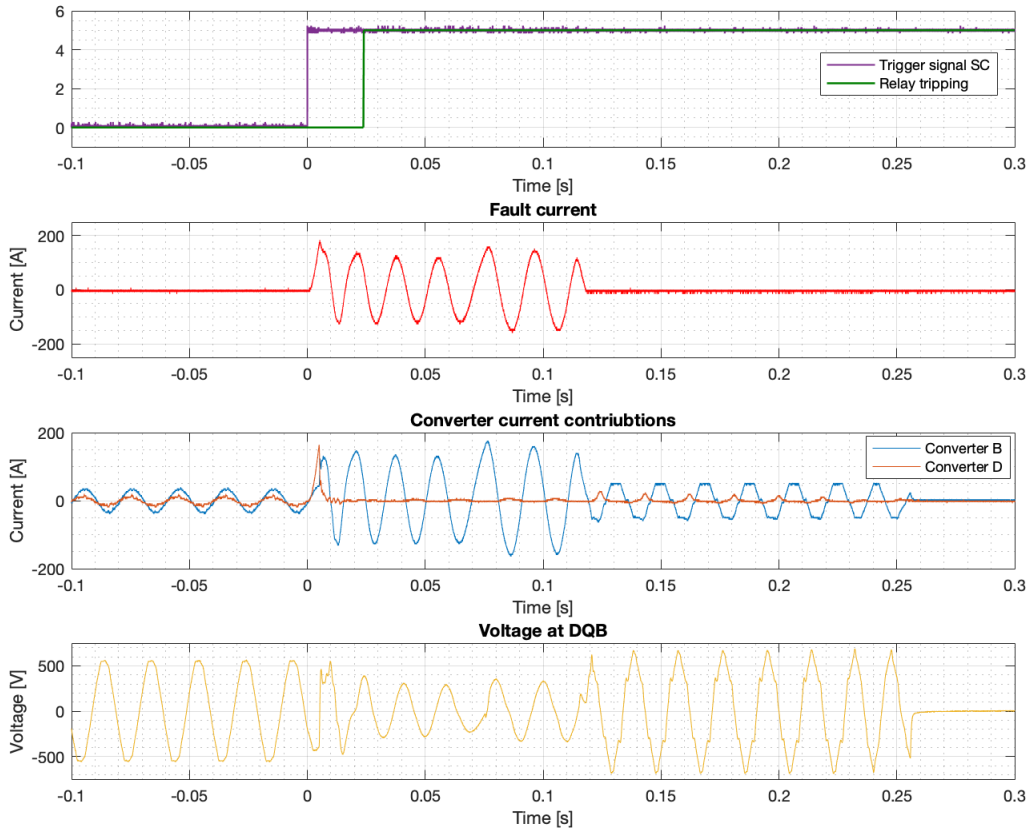

Figure C.3: Immediately disconnection of the grid-forming converter D after the fault is applied at t=0 s, whereas the grid-following converter B disconnects after 0.25 s due to over-frequency

C.2.2 Faster active and reactive control

Figure C.4 shows the base case of control strategy 2, but with faster regulation. Hence, the time constant in the PI-regulators are reduced to I reg Ti = 10 ms and P reg Ti = 10 ms. The short-circuit is made persistent by disconnecting the protection scheme so the relay will not isolate the fault.

Consequently, it is possible to investigate the current output from converter B longer into the short-circuit. However, the short-circuit duration, T_{short}, is set to 250 ms in order to examine the converter behavior after the short-circuit is finished.

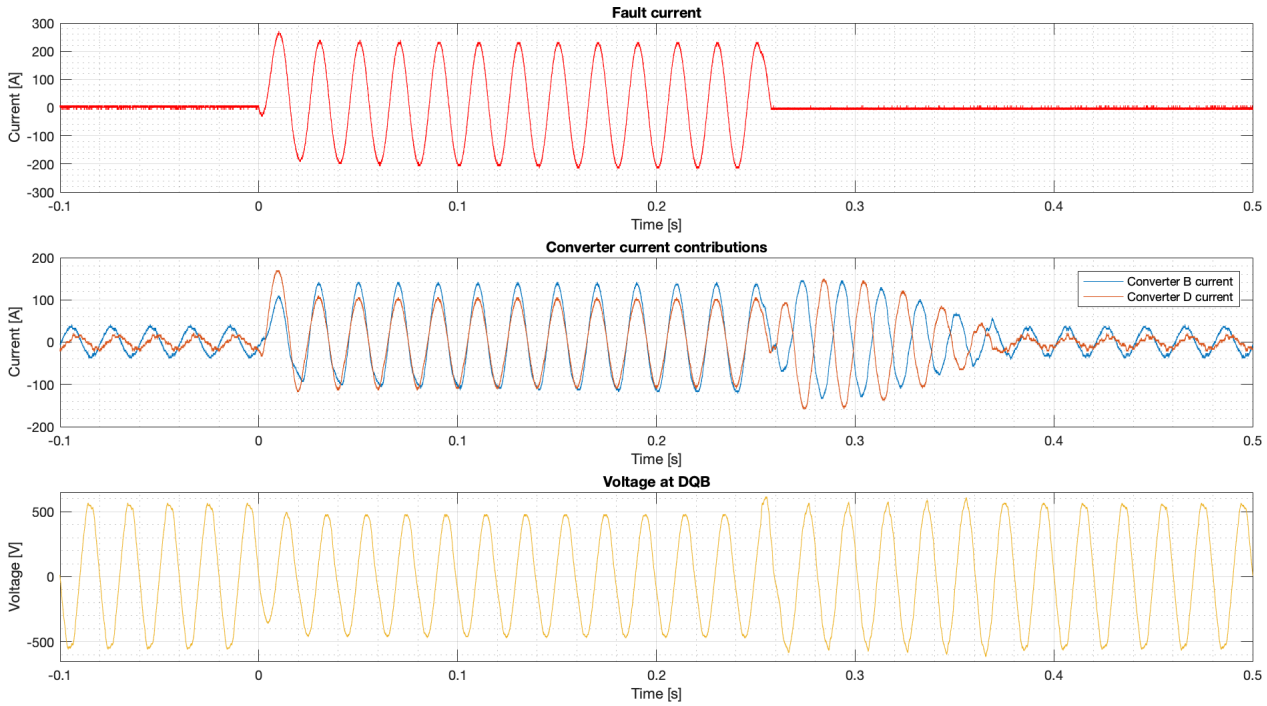

Figure C.4: Base case of control strategy 2 with I reg Ti and P reg Ti reduced to 10 [ms]

The current contribution from converter B is approximately 92 RMSA, whereas the converter D current is approximately 76 RMS A during the short-circuit. Compared to the base case in figure 6.11, the converter B current exceeds the converter D current, and the regulation of converter B is much faster.

C.2.3 Changing the proportional gain parameter

Control strategy 1

Figure C.5 illustrates the fault current, the converter currents, and the voltage drop during the short-circuit when I reg K_P is 150 %. Moreover, table C.1 summarizes the comparison parameters.

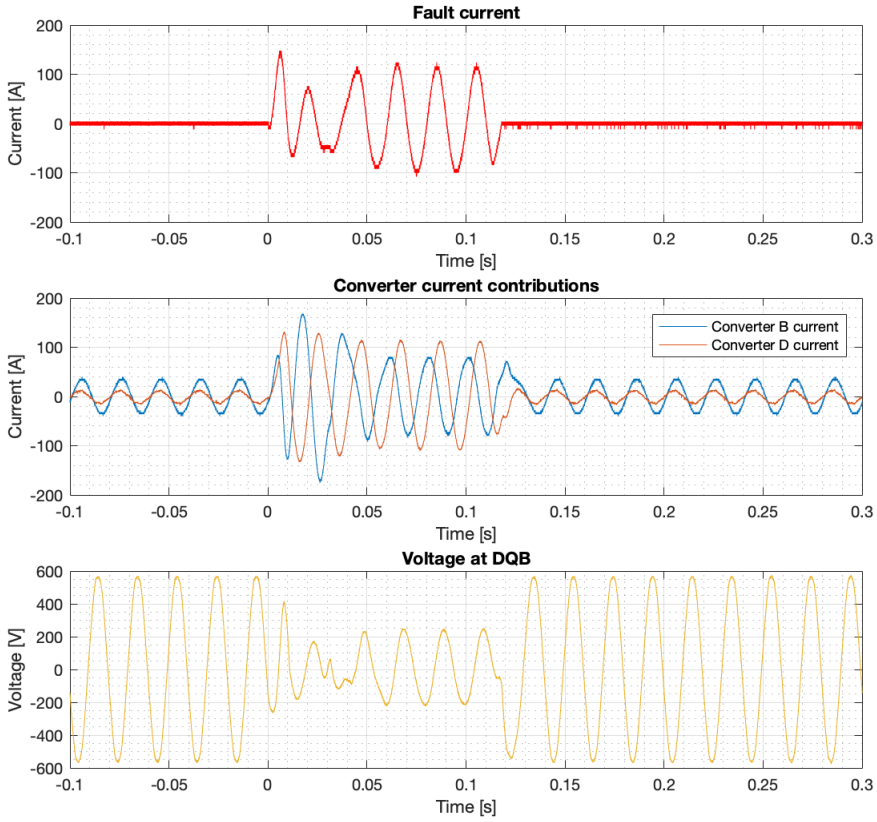

Figure C.5: Control strategy 1 with I reg $K_P = 150$ %

Parameter	Value
I_{B_normal}	25 RMS [A]
I_{D_normal}	10 RMS [A]
I_{B_SC}	$\frac{1}{\sqrt{2}} \cdot 80 = 56.6$ RMS [A]
I_{D_SC}	$\frac{1}{\sqrt{2}} \cdot \frac{113+109}{2} = 78.5$ RMS [A]
I_{fault}	$\frac{1}{\sqrt{2}} \cdot \frac{116+100}{2} = 76.4$ RMS [A]
V_{drop}	$[1 - \frac{164.1}{402}] \cdot 100\% = 59.2$ %
$R_{\frac{I_{B\_SC}}{I_{D\_SC}}}$	$\frac{56.6}{78.5} = 0.72$

Table C.1: Comparison parameters for control strategy 1 when I reg $K_P = 150\%$

C.2.4 Changing the current limit of converter B

Control strategy 1

Figure C.6 shows the fault current, the converter currents, and the voltage drop during a short-circuit for the original settings in table 5.10, but the current limit of converter B is reduced to ± 500 pu. Moreover, table C.2 summarizes the comparison parameters.

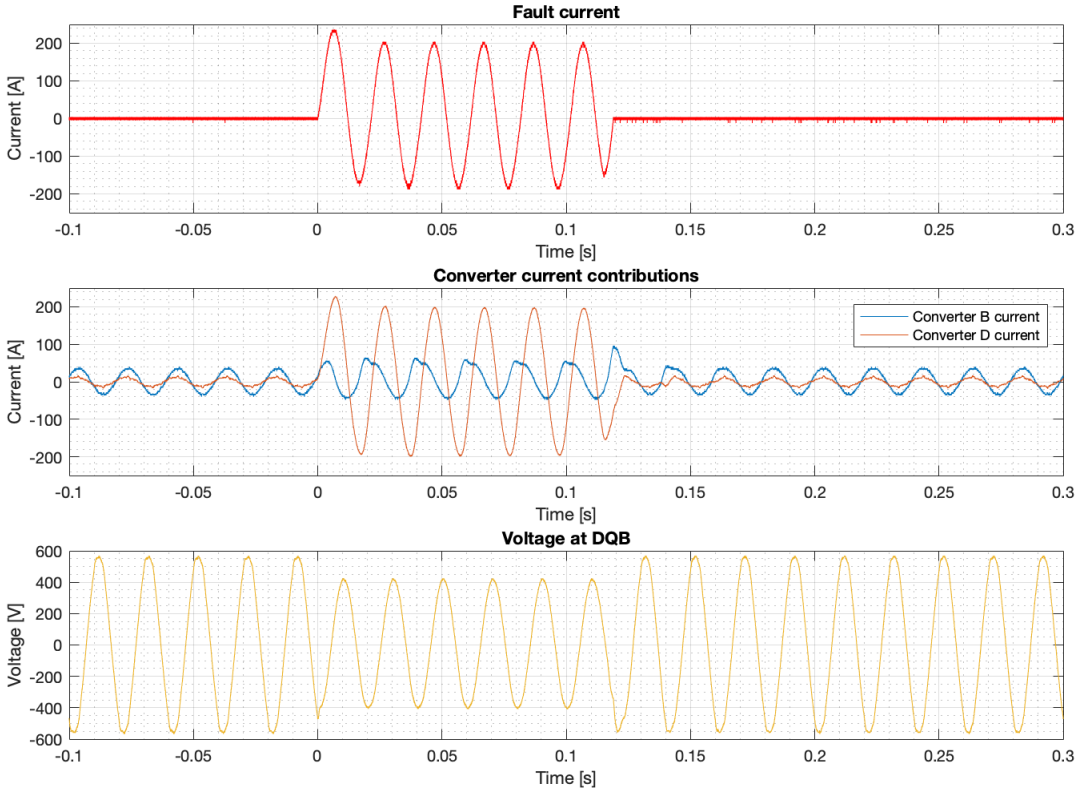

Figure C.6: Control strategy 1 when the current limit is ± 500 [pu] and I reg $K_P = 25\%$

Parameter	Value
I_{B_normal}	25 RMS [A]
I_{D_normal}	10 RMS [A]
I_{B_SC}	$\frac{1}{\sqrt{2}} \cdot \frac{56+48}{2} = 36.8$ RMS [A]
I_{D_SC}	$\frac{1}{\sqrt{2}} \cdot 197 = 139.3$ RMS [A]
I_{fault}	$\frac{1}{\sqrt{2}} \cdot \frac{204+188}{2} = 138.6$ RMS [A]
V_{drop}	$[1 - \frac{294.2}{396}] \cdot 100\% = 25.7$ %
$R_{\frac{I_{B\_SC}}{I_{D\_SC}}}$	$\frac{22.6}{137.2} = 0.26$

Table C.2: Comparison parameters for control strategy 1 when the current limit is ± 500 [pu] and I reg $K_P = 25\%$

When the current limit is ± 500 pu and the active power reference of converter B is 300 pu, the current output from converter B never exceeds the current limit during the short-circuit. Consequently, this case is more or less identical with the base case in figure 6.10.

Figure C.7 shows the fault current, the converter currents, and the voltage drop during the short-circuit when the active power reference and the current limit of converter B is 1000 pu and ± 250 pu, respectively. Nevertheless, the current output is reduced before and during the short-circuit due to the current limit of ± 250 pu, so this situation is more or less equivalent to figure 6.25 due to the same current limit. Table C.3 summarizes the comparison parameters.

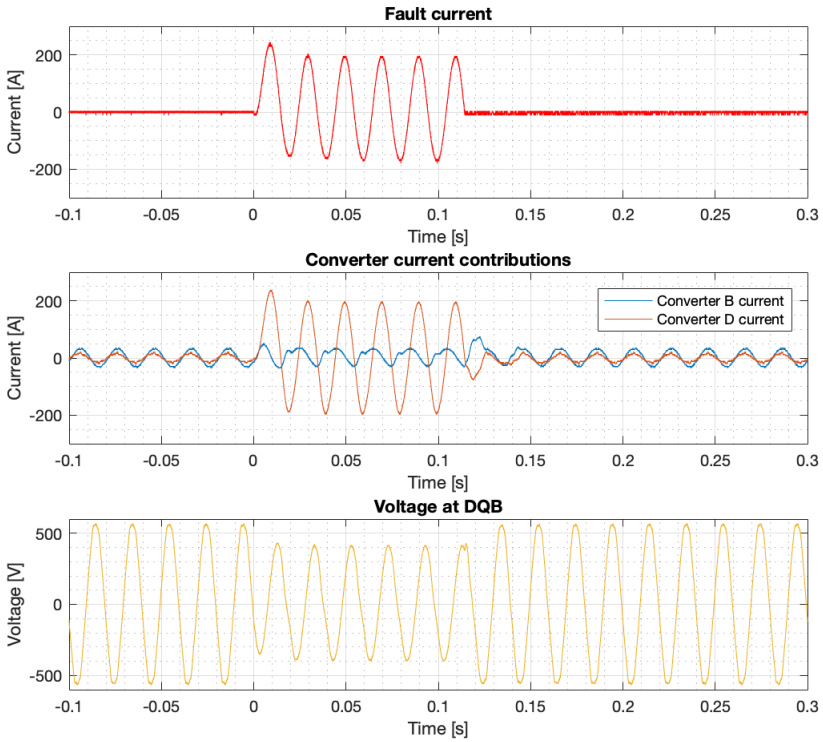

Figure C.7: Control strategy 1 when the current limit is ± 500 [pu], I reg $K_P = 25\%$, and $P_{ref} = 1000$ pu

Parameter	Value
I_{B_normal}	23 RMS [A]
I_{D_normal}	13 RMS [A]
I_{B_SC}	$\frac{1}{\sqrt{2}} \cdot 32 = 22.6$ RMS [A]
I_{D_SC}	$\frac{1}{\sqrt{2}} \cdot 198 = 140.0$ RMS [A]
I_{fault}	$\frac{1}{\sqrt{2}} \cdot \frac{196+180}{2} = 132.9$ RMS [A]
V_{drop}	$[1 - \frac{288.5}{396}] \cdot 100\% = 27.1$ %
$R_{\frac{I_{B\_SC}}{I_{D\_SC}}}$	$\frac{22.6}{140.0} = 0.16$

Table C.3: Comparison parameters for control strategy 1 when the current limit is ± 250 [pu], I reg $K_P = 25\%$, and $P_{ref} = 1000$ pu

Control strategy 2

Similarly to control strategy 1, the current limit is tested when the active power reference of converter B is to 1000 pu. Figure C.7 illustrates the test case when the active power reference and the current limit of converter B are 1000 pu and ± 250 pu, respectively. Moreover, table C.4 summarizes the comparison parameters.

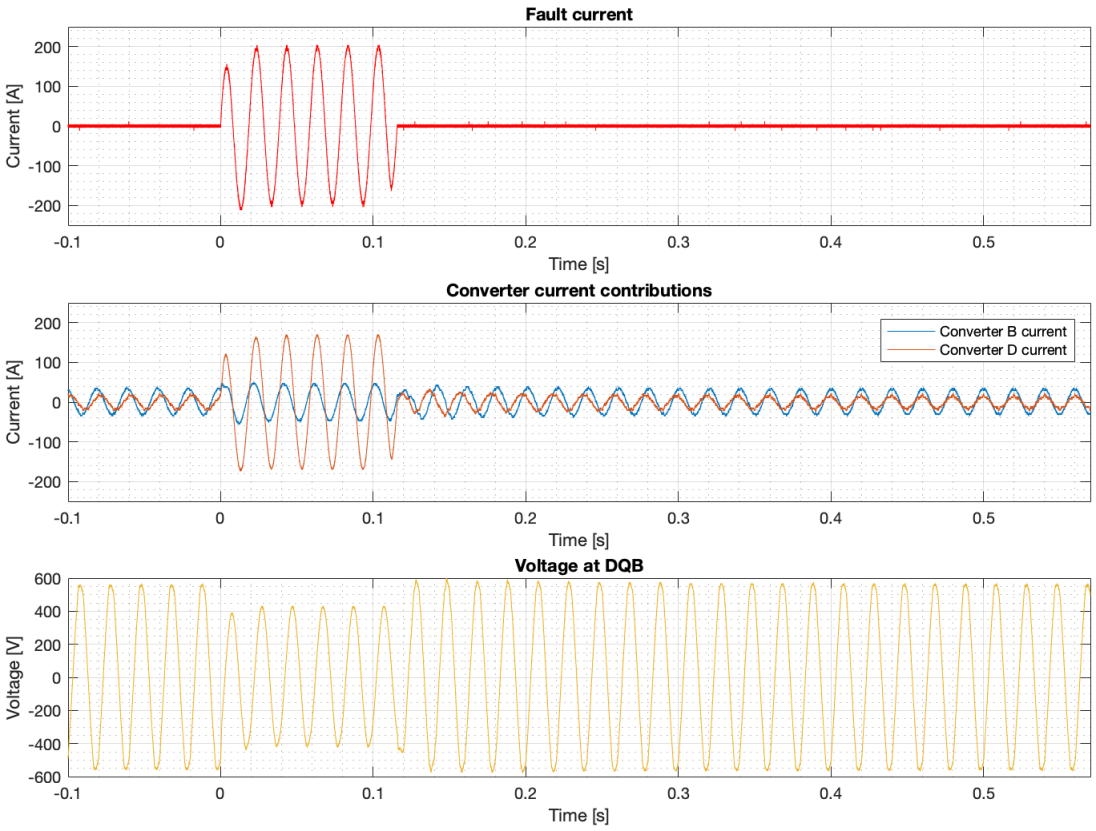

Figure C.8: Control strategy 2 when the current limit is ± 250 [pu], I reg $K_P = 25\%$, and $P_{ref} = 1000$ pu

Parameter	Value
I_{B_normal}	23 RMS [A]
I_{D_normal}	13 RMS [A]
I_{B_SC}	$\frac{1}{\sqrt{2}} \cdot \frac{44+48}{2} = 32.5$ RMS [A]
I_{D_SC}	$\frac{1}{\sqrt{2}} \cdot 170 = 120.2$ RMS [A]
I_{fault}	$\frac{1}{\sqrt{2}} \cdot 196 = 138.6$ RMS [A]
V_{drop}	$[1 - \frac{302.6}{402}] \cdot 100\% = 24.7$ %
$R_{\frac{I_{B\_SC}}{I_{D\_SC}}}$	$\frac{32.5}{120.2} = 0.27$

Table C.4: Comparison parameters for control strategy 2 when the current limit is ± 250 [pu], I reg $K_P = 25\%$, and $P_{ref} = 1000$ pu

For $Pref = 1000$ pu, the current limit of ± 250 pu is slightly exceeded during the short-circuit.

However, the increased active power reference of converter B does not affect the fault current and voltage during the short-circuit compared to figure 6.27 with equal current limit and the proportional gain parameters. In other words, the actual current output from converter B is limited to ± 250 pu for both cases, thus the test cases in figure C.8 and figure 6.27 are equivalent due to the same current limit.

Kjersti Lunde Runestad

Adaptive Protection of an Inverter-Dominated Microgrid and Testing at the Smart Grid Laboratory at NTNU

NTNU
Norwegian University of
Science and Technology